

*ATMOSPHERIC AGING OF BIOMASS-BURNING  
AEROSOL:  
OXIDANTS, OXIDATION PRODUCTS, AND  
MEASUREMENT METHODS*

Adam T. Ahern

17 February 2017

Center for Atmospheric Particle Studies

Department of Chemistry

Carnegie Mellon University

4400 Fifth Ave.

Pittsburgh, PA 15213

Thesis Committee:

Neil M. Donahue, Co-advisor

Ryan C. Sullivan, Co-advisor

Mark E. Bier

Albert A. Presto

Linda Peteanu

Submitted in partial fulfilment of the requirements for the  
degree of Doctor of Philosophy.

Copyright © 2017 Adam T. Ahern

*To my family and friends who encourage me to strive and thrive.*

*A smooth sea never made a skilled sailor.*

## ABSTRACT

We put forth in this work a multifaceted approach aimed at reducing the uncertainty regarding the effect of biomass-burning emissions on photochemical smog production and organic aerosol formation as a result of aging, including photochemical reactions and reaction with nocturnal oxidants. First, we simulated aging of authentic biomass-burning emissions from known fuels using a pair of Teflon smog chambers. We measured the evolution of the organic aerosol within the chambers as they aged, and calculated the amount of new secondary organic aerosol that was formed. The production of secondary organic aerosol could be largely predicted using extensive characterization of the major known gas-phase semi-volatile organic compounds also emitted by the burning, using two-dimensional gas chromatography and proton transfer reaction mass spectrometry.

We also determined that inorganic compounds emitted in the biomass-burning plume can have a significant effect on the atmospheric oxidant budget. Important nocturnal reservoirs of nitrogen oxides – nitryl chloride and dinitrogen pentoxide – were observed for the first time to form readily in the presence of biomass-burning emissions in dark smog chamber experiments. A positive correlation was observed between smoke emissions with high particulate chloride content and the proclivity to form nitryl chloride vapor. Acid displacement of hydrochloride acid gas by nitric acid proved to be an effective means of reducing particulate chloride, although the absorbed nitric acid did not appear to prevent the formation of nitryl chloride by the particulate chloride that remained in the particle phase.

Lastly, we performed characterization experiments on two particle mass spectrometers with the end goal of improving the accuracy of particle composition measurements using complex mixed aerosols generated in the lab, as proxies for realistic atmospheric particles. We revealed that the soot particle aerosol mass spectrometer (SP-AMS) has a variable response factor to two important inert tracers potassium and black carbon, which changes by as much as a factor of three as the

particles grow in size. The laser desorption/ionization single particle mass spectrometer (LAAPTOF) proved to have reduced sensitivity to particles less than 160 nm in diameter, due to particle beam divergence prior to reaching the laser ablation region in the mass spectrometer. During smog chamber experiments that coated authentic biomass-burning emissions with  $\alpha$ -pinene derived secondary organic aerosol, we measured a positive correlation between organic ion signal from the LAAPTOF and secondary organic mass per particle. This shows that despite the challenges associated with quantitative mass measurements from an instrument such as the LAAPTOF, the fundamental relationship between detected signal and analysed mass exists even for a complex sample like biomass-burning particles.

## ACKNOWLEDGEMENTS

This section represents an opportunity to express in a formal way, the gratitude I feel for all the people who have contributed to this dissertation. Fortunately I have many people to thank, but unfortunately I am limited by space, time, and my own sense of propriety to lay bare the many aspects which people have assisted me. I will write what I can, and know it is insufficient.

I am extremely grateful for the attention and patience of my co-advisors Neil Donahue and Ryan Sullivan, who despite having me as a student have maintained their open-door policies. I could not ask for advisors who were more supportive of independent inquiry. They have taught me in equal parts both humility and curiosity. They go above and beyond in terms of caring for their students. It manifests in small, but important ways; Neil reminding me to wear my bicycling helmet, and Ryan calling to make sure I was alright while traveling for work to Karlsruhe, Germany.

I am grateful for my thesis committee who helped guide me through the PhD process. Mark Bier and Albert Presto, their questions during my PhD furthered my understanding of the work, and by extension improved its final quality. Their insight into what the time and effort required to finish a thesis of quality, and their insistence that the product being one of quality, contributes substantial gravity to this project for me. Peter Adams, even though he officially joined my committee near the end of the process, has been present for my annual CAPS talks and always shown interest and given insightful feedback.

My colleagues during my PhD have come and gone, but all of them shared the process of inquiry and discovery with me, and been good friends. At Boston College, I was supported by Eben Cross, Andy Lambe, Paul Davidovits, and many other Aerodyne colleagues; they were the ones who inspired my love of research. I was welcomed to CAPS by many kind people to whom a simple “thank you” is woefully insufficient; but especially so for Andrea Paciga, Ellis Robinson, Daniel Tkacik, Rawad Saleh, Ben Murphy, and Andy May. There have since been many members of CAPS with whom I have truly enjoyed working. Even if I seemed scowly, serious, and stressed, often your interruptions were a source of joy for me. I love getting visits to my desk, despite my sighs of exasperation. I’d like to especially recognize the Sullivan group for their support and camaraderie: Hassan Beydoun, Kyle Gorkowski, Peter Leeman, Leif Jahn, Qing Ye, Michael Polen, and Lydia Jahl.

My mother and father, Nancy and Bill Ahern, have provided me with everything I ever wanted or needed in life. Besides life itself, they have always and continue to lend their unwavering support. They encouraged me emotionally and financially to pursue higher education and gave me every opportunity to pursue my life’s passion. The thing I am most grateful to them for is my brother. Michael has taught me many things in my life, but with respect to professional pursuits he taught me two important lessons: the value of hustle and the value of people. I also need to thank my aunt Sally and uncle Marcel who have spoiled and indulged their nephews at every opportunity.

There are many ways that my life is made fuller and more satisfying by the grace of Kristen Kruszewski, but for the sake of brevity I’ll limit myself to recognizing her contribution to my PhD work. One could not imagine a more sympathetic and caring partner. She is my anchor during the crests and valleys of doing intensive efforts. She is supportive when I need to work, but encourages me to maintain perspective and find joy. All of my work was done better, faster, and more thoughtfully for having a partner who can and would (at length) discuss research topics.

Finally, I’d like to acknowledge everyone who contributed to the research. The co-author list of this document and other publications it encompasses, past and planned, is more extensive than I can do justice in the limited space I can reasonably allocate. The following people helped

with the conception of the work, the execution of the actual project, and the coherent analysis of the data:

For the fourth Fire Lab at Missoula Experiment: the FLAME-IV CMU core-team, Rawad Saleh, Ellis Robinson, and Daniel Tkacik; the FLAME-IV CMU primary investigators/construction crew; Allen Robinson, Albert Presto, Ryan Sullivan, and Neil Donahue; and the FLAME-IV collaborators; Lindsay Hatch, Bob Yokelson, and Chelsea Stockwell.

For April 2014 lab intensive investigating monodisperse soot: R. Subramanian (Subu), Georges Saliba, Joel Corbin, Neil Donahue and Ryan Sullivan.

For the April 2016 lab intensive investigating chloride in biomass burning emissions: Lexie Goldberger, Lydia Jahl, Leif Jahn, Joel Thornton and Ryan Sullivan.

For work related to the LAAPTOF: Leif Jahn, Sören Zorn, Philip Croteau, Achim Trimborn, Peter Leeman, Joanna Sokolowski, and Ryan Sullivan.

As I said in the start, these paltry words do not express the full debt of gratitude I owe you all, but they are a good place to start.

# CONTENTS

<b>1. INTRODUCTION .....</b>	<b>1</b>
1.1. BACKGROUND AND MOTIVATION .....	1
1.1.1. <i>Chemical components of biomass-burning emissions .....</i>	<i>2</i>
1.1.2. <i>Component Volatility.....</i>	<i>4</i>
1.1.3. <i>Atmospheric oxidation.....</i>	<i>7</i>
1.1.4. <i>Conversion of dinitrogen pentoxide to nitryl chloride through                 heterogeneous chemistry on particles.....</i>	<i>8</i>
1.2. EXPERIMENTAL METHODS: SMOG CHAMBERS AND MASS SPECTROMETRY.....	10
1.3. OUTLINE OF DISSERTATION .....	13
1.4. REFERENCES .....	16
<b>2. SMOG CHAMBER STUDY OF SECONDARY ORGANIC AEROSOL FORMATION FROM BIOMASS BURNING .....</b>	<b>27</b>
2.1. INTRODUCTION .....	28
2.2. METHODS .....	31
2.2.1. <i>Experimental methods.....</i>	<i>31</i>
2.2.2. <i>Characterizing the particulate phase.....</i>	<i>34</i>
2.2.3. <i>Characterizing particle wall loss.....</i>	<i>35</i>
2.2.4. <i>Characterizing the gas phase.....</i>	<i>36</i>
2.3. RESULTS AND DISCUSSION .....	38
2.3.1. <i>Mass spectra of organic aerosol .....</i>	<i>38</i>
2.3.2. <i>Composition changes due to simulated atmospheric aging .....</i>	<i>42</i>
2.3.3. <i>Determining the SOA mass produced during an aging experiment .....</i>	<i>48</i>
2.3.4. <i>OA enhancement from various fuels and perturbations.....</i>	<i>54</i>
2.3.5. <i>Predicting the amount of SOA formed .....</i>	<i>55</i>
2.3.6. <i>Trends in oxidized VOCs with aging .....</i>	<i>61</i>
2.4. CONCLUSIONS.....	62
2.5. REFERENCES .....	64
<b>3. MULTIPHASE CHLORINE CHEMISTRY IN BIOMASS BURNING AEROSOL.....</b>	<b>76</b>
3.1. INTRODUCTION .....	77



3.2. EXPERIMENT METHODS.....	82
3.2.1. <i>Experimental overview</i> .....	82
3.2.2. <i>Particle characterization</i> .....	85
3.2.3. <i>Gas-phase characterization</i> .....	87
3.3. RESULTS AND DISCUSSION .....	88
3.3.1. <i>Particle composition from biomass-burning</i> .....	88
3.3.2. <i>Formation of N<sub>2</sub>O<sub>5</sub> and ClNO<sub>2</sub> in smog chamber experiments</i> .....	90
3.3.3. <i>Observed acid displacement in biomass burning aerosol</i> .....	95
3.4. CONCLUSION .....	98
3.5. REFERENCES .....	100
<b>4. DEVELOPMENT, LABORATORY CHARACTERIZATION, AND FIELD DEPLOYMENT OF THE LASER ABLATION AEROSOL PARTICLE MASS SPECTROMETER.....</b>	<b>ERROR!</b>
BOOKMARK NOT DEFINED.	
4.1. INTRODUCTION .....	111
4.2. EXPERIMENTAL.....	118
4.3. RESULTS AND DISCUSSION: .....	121
4.4. FUTURE WORK .....	132
4.5. CONCLUSION .....	121
4.6. REFERENCES .....	140
<b>5. EFFECT OF SECONDARY ORGANIC AEROSOL COATING THICKNESS ON THE REAL-TIME DETECTION AND CHARACTERIZATION OF BIOMASS BURNING SOOT BY TWO PARTICLE MASS SPECTROMETERS .....</b>	<b>148</b>
5.1. INTRODUCTION .....	149
5.1.1. <i>Characterization of carbonaceous aerosol by SP-AMS</i> .....	151
5.1.2. <i>Characterization of carbonaceous aerosol by LDI-SP-MS</i> .....	153
5.2. EXPERIMENTAL METHODS .....	155
5.2.1. <i>Experimental particle generation and conditioning</i> .....	155
5.2.2. <i>Particle component mass measurements</i> .....	156
5.2.3. <i>Particle mobility measurements and calculations</i> .....	161
5.3. RESULTS AND DISCUSSION .....	164
5.3.1. <i>Effect of SOA condensation on soot particle shape</i> .....	164

5.3.2. Sequential coating of monodisperse soot in a smog chamber.....	165
5.3.3. Particle composition from mass spectrometry .....	167
5.3.4. SP-AMS sensitivity to refractory species .....	173
5.3.5. LAAPTOF quantification of OM on externally mixed soot particles..	180
5.4. CONCLUSIONS.....	184
5.5. REFERENCES .....	187
<b>6. CONCLUSIONS.....</b>	<b>202</b>
6.1. REFERENCES .....	209

## LIST OF TABLES

TABLE 2.1 EXPERIMENTAL DETAILS FOR EACH PAIR OF SMOG CHAMBER EXPERIMENTS.....	33
TABLE 3.1 -SUMMARY OF CHAMBER EXPERIMENT CONDITIONS FOR MEASURING $\text{N}_2\text{O}_5$ AND $\text{ClNO}_2$ FORMATION IN THE SMOG CHAMBER. REPORED VALUES ARE THE AVERAGE FOR 10 MINUTES AFTER INJECTION OF OZONE.....	89

## LIST OF FIGURES

FIGURE 1.1. AN OIL-BURNING LAMP.....	5
FIGURE 2.1 THE EXPERIMENTAL SETUP AT THE FIRE LABORATORY IN MISSOULA EXPERIMENTS, FLAME-IV.. .....	32
FIGURE 2.2 THE NORMALIZED HIGH RESOLUTION MASS SPECTRA OF ORGANIC AEROSOL FROM BURNING BLACK SPRUCE. ....	39
FIGURE 2.3. CHANGES IN ION ABUNDANCE RELATIVE TO THE POA-TRACER ION, $C_7H_{11}^+$ , BEFORE AND AFTER TWO TYPES OF SIMULATED AGING.. .....	43
FIGURE 2.4 CALCULATED OA ENHANCEMENTS ARE PLOTTED VERSUS THE FLAME-IV BURN NUMBER .....	45
FIGURE 2.5 THE RATIO OF CERTAIN AMS OA ION FRAGMENTS TO THE TOTAL ORGANIC AEROSOL ION SIGNAL ( $F_i$ ) PROVIDE A USEFUL COMPARISON AGAINST AMBIENT OBSERVATIONS (DASHED LINES).. .....	47
FIGURE 2.6 PARTICLE MASS AND COMPOSITION MEASUREMENTS DURING A TYPICAL BBOA AGING EXPERIMENT.....	48
FIGURE 2.7 MEASURED AND CALCULATED VALUES REQUIRED FOR ESTIMATING THE TOTAL SOA <sub>51</sub>	
FIGURE 2.8 SOA MASS PREDICTED USING SPECIATED AND SCALED VOC MEASUREMENTS IS PLOTTED VERSUS SOA MASS OBSERVED IN AMS MEASUREMENTS USING THE $C_7H_{11}^+$ (m/z 95) POA TRACER.....	52
FIGURE 2.9 PREDICTED SOA MASS USING SPECIATED VOC MEASUREMENTS, FOLLOWING THE AGING OF BLACK SPRUCE SMOKE BY $\cdot OH$ OXIDATION. ....	57
FIGURE 2.10 THE CUMULATIVE SOA FORMED BY EACH VOC FOR THE AGING OF PONDEROSA PINE SMOKE. ....	58
FIGURE 2.11 THE CUMULATIVE SOA FORMED BY EACH VOC FOR THE AGING OF WIREGRASS SMOKE. .....	60
FIGURE 2.12 THE DIFFERENCE IN ACETONE CONCENTRATIONS MEASURED BY THE PTR-MS BEFORE AND AFTER AGING CORRELATES WELL WITH $\cdot OH$ EXPOSURE. ....	61

FIGURE 3.1 MAJOR CHEMICAL REACTIONS IN THE REACTIVE UPTAKE OF $N_2O_5$ BY AN AQUEOUS PARTICLE. ....	77
FIGURE 3.2 EXPERIMENTAL SETUP FOR SMOG CHAMBER EXPERIMENTS TO MEASURE THE EFFECT OF BIOMASS-BURNING AEROSOL ON NOCTURNAL NITROGEN OXIDE SPECIES AND CHLORINE CHEMISTRY. ....	83
FIGURE 3.3 PRODUCTION OF $N_2O_5(g)$ AND $ClNO_2(g)$ , MEASURED BY THE UW-CIMS, DURING DARK CHAMBER AGING OF BIOMASS-BURNING AEROSOL OR AMMONIUM BISULFATE AEROSOL. ....	91
FIGURE 3.4 MEASURED $ClNO_2$ CONCENTRATIONS 1.7 HOURS AFTER OZONE INJECTION AS A FUNCTION OF INITIAL PARTICULATE CHLORIDE MASS CONCENTRATION.....	92
FIGURE 3.5 THE RATIO OF MEASURED MAXIMUM CONCENTRATION OF $ClNO_2$ TO THE MAXIMUM CONCENTRATION OF $N_2O_5$ SHOWN AS A FUNCTION OF THE CHLORIDE FRACTION OF NONREFRACTORY PARTICULATE MASS ( $F_{Cl}$ ). ....	93
FIGURE 3.6 GAS AND PARTICLE-PHASE TIME SEQUENCES FOR A BIOMASS BURNING EXPERIMENT USING SAWGRASS WHERE RELATIVE HUMIDITY WAS INCREASED AFTER SMOKE AND $O_3$ HAD BEEN INJECTED.....	96
FIGURE 3.7 CHLORIDE FRACTION OF NON-REFRACTORY PARTICULATE MASS ( $F_{Cl}$ ) AS A FUNCTION OF RELATIVE HUMIDITY.....	97
FIGURE 4.1. SCHEMATIC OF THE LAAPTOF SINGLE-PARTICLE MASS SPECTROMETER.....	119
FIGURE 4.2. DETECTION EFFICIENCIES OF AMMONIUM AND NITRATE FOR THE LAAPTOF AND THE AMS VS. MOBILITY DIAMETER.....	122
FIGURE 4.3. A SOLUTION OF DIHYDROXYBENZOIC ACID (DHBA) WAS ATOMIZED AND THE RESULTING PARTICLES WERE DRIED AND SIZE SELECTED.....	124
FIGURE 4.4. WEIGHTED AVERAGE MASS SPECTRA FOR THREE OF THE TEN CALCULATED CLUSTERS FROM DHBA-KCL MIXING EXPERIMENT .....	125
FIGURE 4.5. THE HIGHEST VALUE OF EACH PARTICLE IN THE PARTITION MATRIX CALCULATED BY FUZZY C-MEANS CLUSTERING.....	127

FIGURE 4.6. STANDARD DEVIATION AND ABSOLUTE DEVIATION OF SHOT-TO-SHOT VARIATION AT DIFFERENT AVERAGE LASER POWERS. AND THE ENERGY PROFILE OF THE UNFOCUSED EXCIMER PULSE. ....	128
FIGURE 4.7. TWO SINGLE-PARTICLE MASS SPECTRA FROM SIZE-SELECTED 300 NM DHBA PARTICLES.....	129
FIGURE 4.8. INDIVIDUAL PARTICLE MASS SPECTRA FOR POSITIVE IONS COLLECTED DURING A BIOMASS SMOKE AND SOA MIXING EXPERIMENT. ....	130
FIGURE 4.9. ONE OF THE RESULTING CLUSTERS FROM A FUZZY CLUSTERING ALGORITHM WHICH CORRELATES WELL WITH THE INTRODUCTION OF $\alpha$ -PINENE SOA. ....	131
FIGURE 4.10. PERCENT OF PARTICLES DETECTED BY LIGHT SCATTERING AS A FUNCTION OF PARTICLE DIAMETER FOR DIFFERENT SINGLE PARTICLE MASS SPECTROMETERS.....	1314
FIGURE 4.11. SCHEMATIC OF CARNEGIE MELLON UNIVERSITY SCATTERING LASERS .....	1316
FIGURE 5.1. EXPERIMENTAL SETUP INCLUDING SIZE-SELECTED BIOMASS-BURNING AEROSOL	155
FIGURE 5.2 THE PARTICLE BEAM-WIDTH PROBE BLOCKS A FRACTION OF THE PARTICLES THAT WOULD HAVE BEEN VAPORIZED BY THE IR LASER AND THUS THE PROBE ATTENUATES THE ELEMENTAL CARBON ION SIGNAL. ....	159
FIGURE 5.3. NORMALIZED PARTICLE SIZE DISTRIBUTIONS FOR COATING EXPERIMENTS FROM TWO INSTRUMENTS.....	162
FIGURE 5.4. DYNAMIC SHAPE FACTOR ( $\chi$ ) OF SOOT PARTICLES BECAME MORE SPHERICAL ( $\chi \rightarrow 1$ ) WITH INCREASING SOA MASS.....	165
FIGURE 5.5. MONODISPERSE BIOMASS SOOT PARTICLES TO WHICH TWO SUCCESSIVE ADDITIONS OF SOA WERE APPLIED. ....	166
FIGURE 5.6. STICK INTEGRATED HIGH-RESOLUTION MASS SPECTRA FROM THE SP-AMS FOR NASCENT (TOP) AND THICKLY SOA-COATED SOOT (BOTTOM). ....	168
FIGURE 5.7. SP-AMS MEASUREMENTS OF CARBON ION FAMILY ( $C_x^+$ ) PEAK AREA RATIOS VERSUS SOA COATING MASS ON THREE DIFFERENT BBA SOOT-CORE SIZES. ....	170

FIGURE 5.8. POSITIVE POLARITY MASS SPECTRA AND ION ASSIGNMENTS FOR TWO REPRESENTATIVE PARTICLES ANALYZED BY THE LAAPTOF .....	172
FIGURE 5.9. SP-AMS-MEASURED BIOMASS-BURNING ION SIGNALS FOR $C_3^+$ (TOP) AND $K^+$ (BOTTOM) FOR THREE MOBILITY SELECTED CORE PARTICLE SIZES VERSUS FOUR DIFFERENT METRICS.....	175
FIGURE 5.10. CORRELATION OF REFRACTORY ION SIGNALS FROM THE SP-AMS DURING SOA COATING EXPERIMENTS.....	177
FIGURE 5.11. WALL-LOSS CORRECTED SP-AMS SIGNAL FROM RBC $C_x^+$ (PANEL A) AND $K^+$ (PANEL B) HAVE BEEN NORMALIZED TO THEIR NASCENT VALUES (BEFORE SOA COATING) AND ARE SHOWN AS A FUNCTION OF WALL-LOSS CORRECTED SP-AMS OM SIGNAL. MARKER ....	179
FIGURE 5.12. AVERAGED OM SIGNAL ( $m/z + 28$ ; $CO^+$ ) FROM NASCENT AND SOA-COATED SOOT PARTICLES MEASURED BY THE LAAPTOF DURING SOA COATING EXPERIMENTS VS. SOA MASS PER PARTICLE. ....	181
FIGURE 5.13. LAAPTOF-MEASURED OM ION SIGNAL ( $m/z + 28$ ; $CO^+$ ) NORMALIZED BY LAAPTOF EC ION SIGNAL (SUM OF $m/z + 24$ , $+36$ , $+48$ , $+60$ ; $C_{2-5}^+$ ) FOR UNCOATED AND SOA COATED SOOT PARTICLES.....	183

# 1. INTRODUCTION

## 1.1. Background and motivation

Biomass burning is the largest source of fine-particle mass on the planet, specifically for particles with a diameter less than 1  $\mu\text{m}$ . Submicron particles are small enough to penetrate deep into the lungs of humans (Kelly and Fussell, 2012). Although the exact mechanisms by which inhaling these particles harm people is not well understood, they are known to be related to conditions including ischaemic heart disease, lower respiratory infections, and chronic obstructive pulmonary disease (Lozano et al., 2012). More generally, there is convincing evidence that exposure to these small particles is causally correlated with shortened life expectancy (Dockery et al., 1993).

Submicron particles from biomass burning remain suspended in the atmosphere for days to weeks. While suspended, they reduce visibility and also have a potentially large impact on the magnitude of global warming (Albrecht, 1989; Solomon et al., 2007). I invoke the caveat “potentially” because there are large uncertainties regarding what actually happens to smoke after it is emitted, and consequently large uncertainties in the impacts of biomass burning on the environment and on climate change (Bond et al., 2013). The objective of the work presented here is to address specific questions that relate to the effects of burning biomass on the mass and composition of submicron aerosol particles in the



atmosphere. By reducing the uncertainty of the effects of atmospheric processing on the formation and key physicochemical properties of these particles, we empower decision makers to protect people from adverse air quality and hazardous climate change. However, before I address the specific questions underpinning the uncertainties, I must provide context by describing our current understanding of the effect of these biomass-burning emissions on climate.

The effect of biomass-burning emissions on climate is poorly understood for many reasons. One reason is the great variety of combustion conditions associated with the term “biomass burning”. Biomass burning includes the combustion of any organic material that is not derived from fossil fuels (i.e. natural gas, petroleum, or coal.) It includes agricultural burning, wild fires, prescribed fires, as well as residential heating and cooking (Bond et al., 2004, 2006; Reid et al., 2005). In addition to “biomass burning” encompassing a great variety of fuels, it also describes a variety of combustion conditions. The controlled combustion of a forced air residential oven and a wild fire will have varying levels of efficiency in the combustion, and thus yield different amounts of product. A perfectly combusting fire would yield only CO<sub>2</sub>, water, heat, leaving behind or emitting some inorganic material or ash. However, an imperfect fire experiencing incomplete combustion will emit a vast range of gaseous and particulate materials, organic and inorganic, that is collectively referred to as “biomass-burning emissions” or simply “smoke”.

#### 1.1.1. Chemical components of biomass-burning emissions

The smoke from burning biomass is comprised of particulate (both liquid and solid) and gas phase species. One is CO<sub>2</sub>(g), which along with CO(g) accounts for 90% of the initial carbon present in the biomass when it is combusted. The remaining carbon is emitted as either particles or gases, some of which have been transformed by the heat of combustion and some who have simply been volatilized (remained chemically unchanged) (Andreae et al., 1998; Ferek et al., 1998). Black carbon is an example of a particulate emission of biomass burning which has undergone significant chemical changes due to the high temperatures present in combustion flames. However,

whereas most of the carbon mass has been oxidized to CO<sub>2</sub>, molecules in hot, but O<sub>2</sub> deprived sections of the flame are oxidized in a way that results in a very different product. As high heat drives off oxygen and hydrogen atoms from organic molecules, the remaining carbon radicals begin to self-react, forming a graphitic structure that condenses into primary spherules ~10 nm in diameter (Haynes and Wagner, 1981; Mansurov, 2011; Qamar et al., 2011). These spherules cool and coagulate forming fractal-like structures that contain highly conjugated material. The high degree of conjugation means that the black carbon readily absorbs light; thus its moniker.

Black carbon is the most significant aerosol species that absorbs light and warms the planet. However, it is often co-emitted with other organic compounds as well. If these organic compounds condense into or onto a particle, they can effectively scatter light (Bond et al., 2013; Li et al., 2003; Pósfai and Buseck, 2010). This can result in a cooling effect on climate which has been hypothesized to offset the warming effect of black carbon (Bond et al., 2013). Thus we must look at the types of compounds that are emitted from biomass burning, and their respective physical and chemical properties to determine whether they will exist in the particle phase or gas phase.

The compounds that are emitted vary widely depending on the fuel that is burned (Hays et al., 2002). In some cases compounds undergo a process similar to the formation of black carbon, but do not form large enough molecules to condense. Instead, polyaromatic hydrocarbons and branched aromatic gases are emitted. These include carcinogenic molecules like naphthalene, toluene, and benzene (Nisbet and LaGoy, 1992). Some of the organic compounds present in biomass are only partially combusted. Levoglucosan is an anhydrosugar that results from the combustion of cellulose and hemicellulose, two important structural components of plant matter (Simoneit et al., 1993). Some compounds are evaporated and undergo relatively little chemical changes. Tar balls are formed from resin that was superheated and then rapidly cooled to form submicron droplets.

Another important class of compound that is emitted from biomass burning is ash. Ash is the technical term for inorganic components that result from

combustion. This material may undergo chemical changes (e.g. sulfur from biomass can be converted to  $\text{SO}_2$ ), or be emitted as it was. Salts (e.g.  $\text{KCl}$ ) that were present in the plant have been confirmed to be present on soot particles (Li et al., 2003; Pósfai and Buseck, 2010). As a result, potassium is a commonly used tracer species for biomass-burning emissions (Andreae, 1983), and chloride can have important effects on the oxidant budget in the atmosphere, as I will discuss in section 1.1.4.

### 1.1.2. Component Volatility

One important attribute of the various materials emitted from a fire is their volatility. Volatility describes the phase partitioning behavior of a compound (Donahue et al., 2006). A very volatile material, like  $\text{CO}_2$ , will exist in the gas phase under almost all conditions on Earth. Black carbon (BC) is a product of incomplete combustion, and exists in the particle phase under almost all conditions on Earth. BC is graphitic, consisting almost entirely of carbon with many double bonds, and relatively little hydrogen and oxygen mixed in (Haynes and Wagner, 1981). There exists between the highly oxygenated  $\text{CO}_2$  gas and this highly conjugated BC a wide range of products, and correspondingly a range of volatilities. Some for example will only partition into the particle phase when there are very high concentrations, such as when they are emitted from a smoky fire. However, at background concentrations, as one would find far removed from a smoke-plume source, these compounds exist entirely in the gas phase.

An example of the effect of volatility on the phase of organic compounds is a wicking lamp and lamp oil, as shown in Figure 1.1. The oil in the wick of a lamp exists in the liquid phase under high concentrations, but as the fumes become diluted with clean background air, the liquid will evaporate. The evaporated lamp oil is what burns, not the liquid. When lamp oil is in the reservoir in the base of the lamp, the vapors are not able to be diluted with outside air, and thus the gas phase reaches equilibrium with the particle phase. This is true of all organic compounds. There is some amount of the compound that will exist in equilibrium in the vapor phase at the same as the liquid or solid phase. In some cases, the amount of vapor is so small as to

be essentially non-existent, and thus the material is described as non-volatile. In other cases that amount of vapor required to reach equilibrium at normal temperatures and pressures is so large that the compound is essentially entirely in the gas-phase, and thus described as volatile. However, a basic tenant of thermodynamics is that, when multiple phases exist in a system at equilibrium, the activity of each species in the system will be the same in each phase; there will be some amount of the species in each phase.



Figure 1.1. An oil-burning lamp (Leon, 2014). The fuel in the bottom of the lamp exists in the liquid and gas phase. Because it is enclosed, the fuel vapors have reached an equilibrium with the liquid phase. However, fuel that is wicked up the wick attempts to equilibrate with the background air, and thus some of the fuel evaporates. When the lamp is not lit, some fuel slowly evaporates as background air mixes around the wick, but it is a slow process with a small saturation gradient expanding around the tip of the wick. When the lamp is lit however, the gas-phase fuel is rapidly depleted, and the gradient is large, which causes fuel to evaporate rapidly to try to reach equilibrium. This removes liquid from the base of the lamp, much as gas-phase oxidation of semi-volatile organics can rapidly deplete the particle phase, even if the bulk of the mass exists in the particle phase.

The amount of material present in the gas versus the particle phase is determined by the saturation vapor pressure and the activity of the compound in the condensed phase (Donahue et al., 2011; Pankow, 1994). For complex mixtures like organic aerosols, which can contain thousands of different compounds, it is useful to consider the effect of Raoult's law on the amount of material that will exist in the gas phase. Essentially, the vapor pressure of a compound over a mixture of many organic compounds, as in lamp oil or in organic aerosol, will be lower in the mixture than it would be over a condensed phase that consists of only that molecule (the inherent chemical property saturation vapor pressure). While the saturation vapor pressure is directly related to an inherent property of a molecule—the enthalpy of vaporization—the abundance and diversity of organic molecules makes empirical parameterizations of these properties and the associated effect on gas-particle partitioning more effective than explicit measurements and modeling of individual compounds behavior (Donahue et al., 2011; Jimenez et al., 2009; Pankow, 1994; Robinson et al., 2007). However, the degree to which organic aerosols can be assumed to be a single mixture versus phase-separated, or even reach an equilibrium partitioning state is an area of active research (Renbaum-Wolff et al., 2013; Robinson et al., 2016b; Saleh et al., 2013; Shiraiwa and Seinfeld, 2012; Ye et al., 2016).

The products of biomass burning span a range of volatilities, which results in large uncertainty with respect to the mass of the particles, and therefore their climate and health effects (Grieshop et al., 2009; Huffman et al., 2009; May et al., 2013). Some of these incomplete combustion products exist with significant portions in both the particle phase and gas phase when they are initially emitted. I will describe these as semi-volatile organic compounds (SVOCs), although a more comprehensive framework has been established and is widely used (Donahue et al., 2006, 2011). As SVOCs are mixed with the background air, which has no or low concentrations of these compounds, they are diluted and vaporize. Because we care more about the size and mass of submicron particles (due to their human health and climate effects), the task of evaluating the mass of submicron particles emitted becomes more complicated than a simple organic aerosol (OA) emission factor. We must account for

the particle mass that vaporizes due to dilution, and to do this we characterize the volatility of the bulk material. However, this is not the only mechanism by which particulate mass may transition from a condensed phase to a vapor.

### 1.1.3. Atmospheric oxidation

When smoke is emitted, it mixes with more than clean air. Besides water, molecular nitrogen, molecular oxygen, and some other relatively inert chemicals, the atmosphere of Earth contains a number of powerful oxidants. One of these powerful oxidant is ozone ( $O_3$ ). This compound can react quickly with organic compounds that contain carbon-carbon double bonds, resulting in the formation of a new organic molecule. Although the original carbon backbone is not destroyed, it is transformed into a new molecule which can have different properties (i.e. enthalpy of vaporization and therefore volatility) than the one which was initially formed.  $O_3$  can also react with NO to form  $NO_2$ , and  $O_3$  can react with  $NO_2$  to form the radical  $\cdot NO_3$ .  $\cdot NO_3$  reacts with most compounds, regardless of whether they possess a double bond, to form new organic molecules. During the daytime,  $O_3$  can be photolyzed to form  $O(^1D)$ , which in turn can react with water. This reaction will create two hydroxyl radicals (OH), which are the dominant oxidant in the troposphere during the daytime. The hydroxyl radical is extremely reactive, rapidly abstracting a hydrogen atom from organic compounds or adding to double bonds. This creates an alkyl radical which rapidly reacts with the abundant  $O_2$  in the atmosphere to form a peroxy radical. From here, the organic compound can react with a number of species in the atmosphere, but for now we are mostly concerned with the fact that these atmospheric oxidants will react rapidly with organic compounds in the gas phase and transform them into a different compound.

If these compounds are in equilibrium in the particle phase, then some of the mass that was in the particle phase will now partition into the gas phase to replace what was oxidized. To go back to the analogy of the lamp oil, this atmospheric oxidation is much like the burning lamp wick. When there is no flame (atmospheric oxidants) the lamp oil is vaporized slowly, motivated only by dilution in the

background. It is slowly evaporating, but most of the material is in the particle phase and slow to be diluted sufficiently to cause it to vaporize. However, when the lamp is lit, then the gas phase is being quickly removed. This generates a larger gradient and therefore the lamp oil vaporizes rapidly to replace it. The same thing happens with particles that exist even partially in the gas phase. Gas-phase oxidants consume the material in the vapor phase, which is then replaced from the particle phase. As the lamp oil is depleted by the burning wick, so is the particle-phase mass by the atmospheric oxidants. This multi-phase oxidation has been observed for specific species in biomass-burning emissions, and is believed to extend to all semi-volatile compounds (Donahue et al., 2012; Hennigan et al., 2010, 2011).

We can take this analogy one step further even to describe what happens to the material after the oxidation of organic material. The vapors that are emitted during incomplete combustion can be separated into two classes: the vaporized preexisting “primary” organic compounds (e.g. terpenes) and those “secondary” components that were chemically altered as a part of the combustion process (e.g. aromatics, aliphatics, polyaromatic hydrocarbons, etc.) These compounds tend to exist entirely in the gas phase, and thus are called volatile organic compounds (VOCs). Like the SVOCs, they can also be oxidized and form new products with different physical properties, including a lower vapor pressure. The lower volatility products may condense onto existing particles, or may nucleate to form new particles (onto which additional mass may then condense). These new particulate products are commonly referred to as secondary organic aerosol (SOA). Primary organic aerosol (POA) refers to the compounds as they are initially emitted from the combustion source, and SOA refers to the compounds that result from the oxidation of the POA (Donahue et al., 2012; Jimenez et al., 2009).

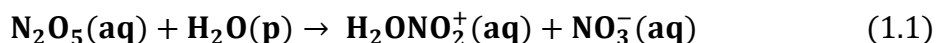
#### 1.1.4. Conversion of dinitrogen pentoxide to nitryl chloride through heterogeneous chemistry on particles

The rate of SOA formation and POA oxidation are both dependent on the concentration of atmospheric oxidants. Nitrogen oxides ( $\text{NO}_x = \text{NO} + \text{NO}_2$ ) can result

in a catalytic production of  $O_3$  and thus of  $\cdot OH$  radicals, therefore increasing the rate of SOA formation.  $NO_x$  is generated by high temperature combustion (including biomass burning), and is lost primarily by conversion to nitric acid ( $HNO_3$ ) by the oxidation of  $NO_2$  by the  $\cdot OH$  radical.  $HNO_3$  is a major component of the  $NO_y$  chemical family ( $NO_y = NO_x + HNO_2 + HNO_3 + HO_2NO_2 + \cdot NO_3 + 2N_2O_5 + \text{peroxyacetyl nitrate}$ ). The uncertainty in predicting  $NO_x$  concentrations, and therefore the oxidation budget, is mostly due to uncertainty in how quickly  $NO_x$  is converted to  $NO_y$  species and thus readily removed from the atmosphere (Dentener and Crutzen, 1993; Gao et al., 1999).

One way  $NO_x$  is converted into  $NO_y$  is through production of  $N_2O_5$ . At night,  $NO_x$  can react with ozone to form the nitrate radical ( $\cdot NO_3$ ). This radical, if it survives long enough, can react with  $NO_2$  to form  $N_2O_5$ .  $N_2O_5$  is thermally unstable, but can exist in a pseudo-steady state at night. This is because the nitrate radical ( $\cdot NO_3$ ) is photolabile and rapidly photolyzes back to  $NO_2$  in the presence of sunlight, preventing formation of  $N_2O_5$ . At night however, the  $\cdot NO_3$  survives long enough to react with other species. As previously mentioned before, this can include organic molecules, water, or in some cases  $NO_2$ . The product of  $NO_2$  and  $\cdot NO_3$  is dinitrogen pentoxide ( $N_2O_5$ .) This molecule is fairly stable at night and can prevent  $NO_x$  from being removed from the atmosphere as  $HNO_3$ . If  $N_2O_5$  survives until sunrise, it will photolyze and regenerate 2  $NO_x$  molecules. These molecules will catalytically produce  $\cdot OH$  during the daylight hours, and increase the oxidation budget that drives SOA formation and POA oxidation. Thus it is necessary to understand the formation and loss of  $N_2O_5$  to predict the oxidation budget in biomass-burning plumes (Sarwar et al., 2012; Simon et al., 2009).

Not all of the  $N_2O_5$  that is formed at night survives until sunrise. If a  $N_2O_5$  molecule encounters an aqueous particle surface, it may partition into the particle and form a reversible, solvated nitric acid product through hydrolysis (Equation 1.1).



In pure water, this  $H_2ONO_2^+$  intermediate species would then react with water to form  $HNO_3$ , which effectively removes the  $NO_x$  from the atmosphere (Dentener and



Crutzen, 1993). However, if the aqueous phase also contains sufficient chloride, nitryl chloride ( $\text{ClNO}_2$ ) can be formed.  $\text{ClNO}_2$  rapidly partitions out of the aqueous phase and remains in the atmosphere until sunrise, when it photodissociates. Formation and subsequent photodissociation of  $\text{ClNO}_2$  affects the oxidant budget by both regenerating  $\text{NO}_2$ , similar to  $\text{N}_2\text{O}_5$ , but also by converting chloride into chlorine. Atomic chlorine is an aggressive atmospheric radical oxidant similar to  $\text{OH}$ , but is two orders of magnitude more reactive than  $\text{OH}$  for noncyclic alkanes (Atkinson and Arey, 2003; Simon et al., 2009). The ability to abstract hydrogen from hydrocarbons can lead to the formation of ozone via the cyclic formation of  $\text{NO}_2$  (Reeves et al., 2002).

The formation of  $\text{ClNO}_2$  has traditionally been considered a coastal phenomenon associated with sea spray (Osthoff et al., 2008; Spicer et al., 1998). However, multiple ambient observations far removed from sea spray have observed enhanced concentrations of  $\text{ClNO}_2$  (Tham et al., 2016; Thornton et al., 2010; Wang et al., 2016). This suggests there may be other important sources of  $\text{ClNO}_2$ . Since biomass burning is ubiquitous and has been observed to generate  $\text{NO}_x$ ,  $\text{O}_3$ , and particulate chloride in high concentrations, it is a likely source of  $\text{ClNO}_2$  which has yet to be investigated (Levin et al., 2010; Pósfai and Buseck, 2010). The ability of biomass burning aerosol to transform  $\text{N}_2\text{O}_5$  into  $\text{ClNO}_2$  could have important effects on the multi-day  $\text{NO}_x$  and oxidation budget of an evolving and dispersing biomass burning plume. This could result in faster oxidation of VOCs and production of SOA.

## 1.2. Experimental methods: Smog chambers and mass spectrometry

The formation of particulate organic aerosol from gas-phase precursors has been known for a long time and has been studied extensively for different SOA precursors using batch reactors commonly referred to as smog chambers (Heisler and Friedlander, 1977; Kamens et al., 1984; Pitts et al., 1978). Smog chambers are used to generate in the lab an air parcel similar to what would be found in the atmosphere. Air parcels generated in the lab are, relative to ambient, more reproducible and can be limited with respect to the reactive species. This allows researchers to quantify the

SOA mass yield is when a given amount of VOC is reacted with a chosen oxidant. For example, Presto et al. (2005) injected an aliquot of  $\alpha$ -pinene into a clean 12 m<sup>3</sup> Teflon smog chamber and allowed it to react with O<sub>3</sub> in the dark.  $\alpha$ -pinene is a VOC that is known to be emitted by trees in huge amounts, thus quantifying the SOA yield from this species has had a significant effect on understanding the global production of OA (Hallquist et al., 2009). In this work, they identified the range of volatilities from  $\alpha$ -pinene ozonolysis products and helped to explain the production of SOA observed in the environment.

We can apply a similar technique to the analysis of more complex systems, such as biomass-burning emissions. Grieshop et al. (2009) attempted to explain the formation of SOA through the aging of biomass-burning emissions using SOA precursors measured using proton transfer reaction mass spectrometry (PTR-MS). PTR-MS is a very rapid but selective method for measuring VOC concentrations. For these experiments, they measured 10 compounds directly and inferred the presence of 67 other VOCs based on the work of Weitkamp et al. (2007). However, they were only able to account for less than 20% of the total SOA mass measured based on the VOC emissions measured and inferred. More recent work using two-dimensional gas chromatography suggests that there may be important SOA precursors that were not measured. The gas-phase characterization by Hatch et al. (Hatch et al., 2015) shows that biomass burning can emit over 400 distinct VOCs. More recent studies have revisited this question. Both Bruns et al. (2016) and Tiitta et al. (2016) used smog chambers to study the effect of aging on OA from burning hardwood fuels in a stove. They found that simple models for the oxidation of traditional pyrogenic VOCs (e.g. branched aromatics, polyaromatic hydrocarbons, etc.) were able to predict the SOA formation that was observed in the aging experiments. Their results however were limited in terms of fuel and combustion conditions, and therefore can only reliably be extrapolated to emissions from residential stoves burning hardwood.

Hennigan et al. (2011) used smog chamber aging experiments to investigate a wider variety of fuels and burn conditions, more akin to what would be found in wild-fires and agricultural burning scenarios. They reported the effect of aging on

biomass-burning emission as the OA enhancement, defined as the total amount of OA after aging normalized by the amount of OA present before aging. In this case, change in OA enhancement was found to be highly variable, including both large increases in OA mass (SOA formation) and total decreases in OA mass (multi-phase oxidation). This variability is consistent with what has been observed in ambient measurements, but there was a large degree of variability even when burning the same fuel. Therefore, additional work is required to discern the relative contributions of SOA condensation and POA multi-phase oxidation, and to improve our ability to accurately predict the OA enhancement during the chemical aging of biomass-burning aerosol.

In addition to using smog chambers to create simplified surrogates of the atmosphere, we also strive to improve the methods by which we measure and compare the aerosol in the ambient to that generated in the smog chambers. Mass spectrometry is a powerful technique that allows high time resolution measurements of aerosol composition (Canagaratna et al., 2007; Sullivan and Prather, 2005). However, there are important sources of uncertainty associated with this widely used method of measuring organic aerosol mass. To understand these limitations, we must describe how the Aerodyne Aerosol Mass Spectrometer quantitatively measures non-refractory aerosol mass (Decarlo et al., 2006; Jayne et al., 2000).

As particles enter the Aerosol Mass Spectrometer through an aerodynamic lens inlet, they strike a 600 °C tungsten heater that vaporizes the sample in the  $10^{-7}$  torr vacuum of the instrument. Once vaporized, the molecules are ionized by 70 eV electrons, resulting in a reproducible distribution of ions. High resolution ( $\sim 2100$  at  $m/z$  200) time-of-flight mass spectrometry enables the identification and quantification of the chemical formulae of the ions generated with sufficient resolution to distinguish most major isobars. We calibrate the efficiency of the electron ionization with a known compound, ammonium nitrate, and thus the digital ion signal measured by the mass spectrometer is directly calibrated to the mass of the particles that are vaporized. The caveats with this widely used online aerosol measurement technique directly affect the measurement of biomass-burning aerosols: 1) Black carbon (BC), important due to its light absorbing properties, does

not vaporize at 600 °C, even in high vacuum. Thus it is not detected by traditional aerosol mass spectrometry. 2) In general, aerosol mass spectrometry has a very low ionization efficiency ( $\sim 10^{-6}$  ions generated per molecule vaporized) and thus many particles must be vaporized and ionized to have sufficient signal. Single particle analysis is possible, but the number of detected ions per particle can limit detection and identification (Cross et al., 2007). 3) The ability of the 600 °C heater to vaporize particles is dependent on their composition and phase (i.e. solid or liquid) (Middlebrook et al., 2012). Past measurements of biomass-burning emissions have compared AMS measurements against other instruments to show that all the organic particles vaporize (Hennigan et al., 2011; Ortega et al., 2013; Tiitta et al., 2016). However, other studies of SOA have found that in some cases three out of four particles bounce off the vaporizer and are never detected (Docherty et al., 2013; Robinson et al., 2016a; Tiitta et al., 2016).

The other particle mass spectrometry technique I used in this work was a laser desorption/ionization single particle mass spectrometer. This instrument uses a vacuum ultraviolet laser to simultaneously ablate and ionize individual particles. As a result, it provides a very different type of compositional data compared to the AMS. It can measure refractory species, generates abundant ions, and can produce softer ion fragmentation (Gross et al., 2000; Spencer and Prather, 2006; Steele et al., 2003; Sullivan and Prather, 2005). However, there are considerable quantitative challenges associated with this method that requires careful calibration and testing to ensure the single particle measurements can be interpreted in a useful way.

### 1.3. Outline of Dissertation

In this work, I take three separate approaches to addressing the uncertainties involved with the atmospheric aging of biomass burning emissions and their resulting impacts on the environment and on climate change.

- In Chapter 2, I used a smog chamber to explore changes in biomass-burning OA mass as result of aging. I separated the processes of multi-phase oxidation of POA from the gas-phase oxidation of VOCs to product SOA using aerosol

mass spectrometry. The extensive VOC characterization by 2D-GC-MS from Hatch et al. (2015) allowed us to accurately predict the amount of SOA that is produced for a variety of fuels burned in conditions similar to what would be expected for woodland and agricultural burning.

- In the work described in Chapter 3, I investigated the effect of biomass burning on the atmospheric oxidant budget and lifetime of nitrogen oxides ( $\text{NO}_x$ ). The oxidant budget will dictate how quickly VOCs may be oxidized to form SOA, the production of tropospheric ozone, and are also important air pollutant toxins. Nitryl chloride ( $\text{ClNO}_2$ ) is an important nocturnal reservoir for  $\text{NO}_x$  in the atmosphere, which prevents the  $\text{NO}_x$  from being efficiently removed by precipitation as  $\text{HNO}_3$ . This alone can result in an increased  $\text{O}_3$  and  $\cdot\text{OH}$  radical production. Furthermore, when the  $\text{ClNO}_2$  is photolyzed at sunrise, it releases atomic chlorine radicals, a very powerful oxidant. I have shown for the first time that nocturnal biomass-burning plumes are suitable conditions for the formation of  $\text{ClNO}_2$ . Aerosols with high chloride content tend to produce  $\text{ClNO}_2$  more efficiently. However, a modest increase in relative humidity can result in accelerated acid displacement by nitric acid, liberating the particulate chloride as hydrochloric acid ( $\text{HCl}$ ) gas rather than nitryl chloride. Acid displacement of the particulate chloride by nitric acid can reduce the production of  $\text{ClNO}_2$ , but does not prevent it entirely.
- A new commercial single particle aerosol mass spectrometer (LAAPTOF) is developed and characterized in Chapter 4. Key performance variables such as particle-size dependent detection, variability in excimer laser power (both spatially and shot-to-shot), and analyte specific sensitivity are addressed. The LAAPTOF was deployed for a unique organic aerosol mixing experiment which showed the effective uptake of  $\alpha$ -pinene SOA vapors by externally mixed biomass-burning aerosol.
- In the work described in Chapter 5, I investigated the ability of two relatively new mass spectrometers to detect different species associated with biomass-burning aerosol. The Soot Particle Aerosol Mass Spectrometer (SP-AMS,

Aerodyne Research, Inc.) uses an intracavity infrared (IR) laser to vaporize refractory black carbon, an important light-absorbing species that is also a useful tracer for biomass-burning emissions. However, I have shown that to use the SP-AMS to measure particle mass accurately, one must carefully evaluate the fraction of particles that are vaporized incompletely by the IR laser. I also evaluated the ability of the LAAPTOF laser desorption-ionization single particle mass spectrometer to measure the amount of SOA condensed on biomass-burning aerosol particles. Despite the challenges associated with the inhomogeneity of biomass-burning aerosols, there appeared to be a positive correlation between the averaged LAAPTOF-measured OA ion signal and the calculated SOA mass per particle.

The body of work presented here is unified by the concept of improving our understanding of atmospheric processes that affect the atmospheric oxidant budget, particulate mass burdens, and key physicochemical aerosol properties related to biomass burning. In Chapters 2 and 3 I will discuss precursors for SOA formation: VOCs and oxidants respectively. Chapters 4 and 5 will be focused on improving the online measurement methods we use to evaluate particle composition in the lab and in ambient measurements. Improved measurements of particle composition (more comprehensive speciation, single particle resolution, and improved mass quantitation) are necessary for testing chemical transport models that represent our best understanding of atmospheric processes that affect the atmospheric oxidant budget, particulate mass burdens, and key physicochemical aerosol properties related to biomass burning (Alexander, 2004; Alvarado et al., 2015; Heald et al., 2011; Hodzic et al., 2016).

## 1.4. References

Albrecht, B. A.: Aerosols, cloud microphysics, and fractional cloudiness., *Science*, 245(4923), 1227–1230, doi:10.1126/science.245.4923.1227, 1989.

Alexander, B.: Impact of preindustrial biomass-burning emissions on the oxidation pathways of tropospheric sulfur and nitrogen, *J. Geophys. Res.*, 109(D8), D08303, doi:10.1029/2003JD004218, 2004.

Alvarado, M. J., Lonsdale, C. R., Yokelson, R. J., Akagi, S. K., Coe, H., Craven, J. S., Fischer, E. V., McMeeking, G. R., Seinfeld, J. H., Soni, T., Taylor, J. W., Weise, D. R. and Wold, C. E.: Investigating the links between ozone and organic aerosol chemistry in a biomass burning plume from a prescribed fire in California chaparral, *Atmos. Chem. Phys.*, 15(12), 6667–6688, doi:10.5194/acp-15-6667-2015, 2015.

Andreae, M. O.: Soot carbon and excess fine potassium: long-range transport of combustion-derived aerosols., *Science*, 220(4602), 1148–51, doi:10.1126/science.220.4602.1148, 1983.

Andreae, M. O., Andreae, T. W., Annegarn, H., Beer, J., Cachier, H., Canut, P. Le, Elbert, W., Maenhaut, W., Salma, I., Wienhold, F. G. and Zenker, T.: Airborne studies of aerosol emissions from savanna fires in southern Africa, *J. Geophys. Res. Sp. Phys.*, 103(D24), 32119–32128, 1998.

Atkinson, R. and Arey, J.: Atmospheric degradation of volatile organic compounds., *Chem. Rev.*, 103(12), 4605–38, doi:10.1021/cr0206420, 2003.

Bond, T. C., Streets, D. G., Yarber, K. F., Nelson, S. M., Woo, J. H. and Klimont, Z.: A technology-based global inventory of black and organic carbon emissions from combustion, *J. Geophys. Res. D Atmos.*, 109(14), 44, doi:10.1029/2003JD003697, 2004.

Bond, T. C., Habib, G. and Bergstrom, R. W.: Limitations in the enhancement of visible light absorption due to mixing state, *J. Geophys. Res. Atmos.*, 111(20), 1–13, doi:10.1029/2006JD007315, 2006.

Bond, T. C., Doherty, S. J., Fahey, D. W., Forster, P. M., Berntsen, T., DeAngelo, B. J., Flanner, M. G., Ghan, S., Kärcher, B., Koch, D., Kinne, S., Kondo, Y., Quinn, P. K., Sarofim, M. C., Schultz, M. G., Schulz, M., Venkataraman, C., Zhang, H., Zhang, S., Bellouin, N., Guttikunda, S. K., Hopke, P. K., Jacobson, M. Z., Kaiser, J. W., Klimont, Z., Lohmann, U., Schwarz, J. P., Shindell, D., Storelvmo, T., Warren, S. G. and Zender, C. S.: Bounding the role of black carbon in the climate system: A scientific assessment, *J. Geophys. Res. Atmos.*, 118(11), 5380–5552, doi:10.1002/jgrd.50171, 2013.

Bruns, E. A., El Haddad, I., Slowik, J. G., Kilic, D., Klein, F., Baltensperger, U. and Prévôt, A. S. H.: Identification of significant precursor gases of secondary organic aerosols from residential wood combustion, *Sci. Rep.*, 6, 27881, doi:10.1038/srep27881, 2016.

Canagaratna, M. R., Jayne, J. T., Jimenez, J. L., Allan, J. D., Alfarra, M. R., Zhang, Q., Onasch, T. B., Drewnick, F., Coe, H., Middlebrook, A., Delia, A., Williams, L. R., Trimborn, A. M., Northway, M. J., DeCarlo, P. F., Kolb, C. E., Davidovits, P. and Worsnop, D. R.: Chemical and microphysical characterization of ambient aerosols with the aerodyne aerosol mass spectrometer, *Mass Spectrom. Rev.*, 26(2), 185–222, doi:10.1002/mas.20115, 2007.

Cross, E. S., Slowik, J. G., Davidovits, P., Allan, J. D., Worsnop, D. R., Jayne, J. T., Lewis †, D. K., Canagaratna, M. and Onasch, T. B.: Laboratory and Ambient Particle Density Determinations using Light Scattering in Conjunction with Aerosol Mass Spectrometry, *Aerosol Sci. Technol.*, 41(4), 343–359, doi:10.1080/02786820701199736, 2007.

Decarlo, P. F., Kimmel, J. R., Trimborn, A., Northway, M. J., Jayne, J. T., Aiken, A. C., Gonin, M., Fuhrer, K., Horvath, T., Docherty, K. S., Worsnop, D. R. and Jimenez, J. L.: Field-deployable, high-resolution, time-of-flight aerosol mass spectrometer, *Anal. Chem.*, 78(24), 8281–8289, doi:10.1029/2001JD001213, 2006.

Dentener, F. J. and Crutzen, P. J.: Reaction of  $\text{N}_2\text{O}_5$  on tropospheric aerosols: Impact on the global distributions of  $\text{NO}_x$ ,  $\text{O}_3$ , and OH, *J. Geophys. Res.*, 98(D4), 7149, doi:10.1029/92JD02979, 1993.



Docherty, K. S., Jaoui, M., Corse, E., Jimenez, J. L., Offenberg, J. H., Lewandowski, M. and Kleindienst, T. E.: Collection Efficiency of the Aerosol Mass Spectrometer for Chamber-Generated Secondary Organic Aerosols, *Aerosol Sci. Technol.*, 47, 294–309, doi:10.1080/02786826.2012.752572, 2013.

Dockery, D. W., Pope, C. A., Xu, X., Spengler, J. D., Ware, J. H., Fay, M. E., Ferris, B. G. and Speizer, F. E.: An Association between Air Pollution and Mortality in Six U.S. Cities, *N. Engl. J. Med.*, 329(24), 1753–1759, doi:10.1056/NEJM199312093292401, 1993.

Donahue, N. M., Robinson, A. L., Stanier, C. O. and Pandis, S. N.: Coupled Partitioning, Dilution, and Chemical Aging of Semivolatile Organics, *Environ. Sci. Technol.*, 40(8), 2635–2643, doi:10.1021/es052297c, 2006.

Donahue, N. M., Epstein, S. A., Pandis, S. N. and Robinson, A. L.: A two-dimensional volatility basis set: 1. organic-aerosol mixing thermodynamics, *Atmos. Chem. Phys.*, 11(7), 3303–3318, doi:10.5194/acp-11-3303-2011, 2011.

Donahue, N. M., Robinson, A. L., Trump, E. R., Riipinen, I. and Kroll, J. H.: Volatility and Aging of Atmospheric Organic Aerosol, pp. 97–143, Springer Berlin Heidelberg, 2012.

Ferek, R. J., Reid, J. S., Hobbs, P. V., Blake, D. R. and Lioussé, C.: Emission factors of hydrocarbons, halocarbons, trace gases and particles from biomass burning in Brazil, *J. Geophys. Res.*, 103(D24), 32107, doi:10.1029/98JD00692, 1998.

Gao, R. S., Fahey, D. W., Del Negro, L. A., Donnelly, S. G., Keim, E. R., Neuman, J. A., Teverovskaia, E., Wennberg, P. O., Hanisco, T. F., Lanzendorf, E. J., Proffitt, M. H., Margitan, J. J., Wilson, J. C., Elkins, J. W., Stimpfle, R. M., Cohen, R. C., McElroy, C. T., Bui, T. P., Salawitch, R. J., Brown, S. S., Ravishankara, A. R., Portmann, R. W., Ko, M. K. W., Weisenstein, D. K. and Newman, P. A.: A comparison of observations and model simulations of  $\text{NO}_x/\text{NO}_y$  in the lower stratosphere, *Geophys. Res. Lett.*, 26(8), 1153–1156, doi:10.1029/1999GL900162, 1999.

Grieshop, A. P., Donahue, N. M. and Robinson, A. L.: Laboratory investigation of photochemical oxidation of organic aerosol from wood fires 2: analysis of aerosol mass spectrometer data, *Atmos. Chem. Phys.*, 9(6), 2227–2240, doi:10.5194/acp-9-2227-2009, 2009.

Gross, D. S., Gälli, M. E., Silva, P. J. and Prather, K. A.: Relative Sensitivity Factors for Alkali Metal and Ammonium Cations in Single-Particle Aerosol Time-of-Flight Mass Spectra, *Anal. Chem.*, 72(2), 416–422, doi:10.1021/ac990434g, 2000.

Hallquist, M., Wenger, J. C., Baltensperger, U., Rudich, Y., Simpson, D., Claeys, M., Dommen, J., Donahue, N. M., George, C., Goldstein, A. H., Hamilton, J. F., Herrmann, H., Hoffmann, T., Iinuma, Y., Jang, M., Jenkin, M. E., Jimenez, J. L., Kiendler-Scharr, A., Maenhaut, W., McFiggans, G., Mentel, T. F., Monod, A., Prévôt, A. S. H., Seinfeld, J. H., Surratt, J. D., Szmigielski, R. and Wildt, J.: The formation, properties and impact of secondary organic aerosol: current and emerging issues, *Atmos. Chem. Phys.*, 9(14), 5155–5236, doi:10.5194/acp-9-5155-2009, 2009.

Hatch, L. E., Luo, W., Pankow, J. F., Yokelson, R. J., Stockwell, C. E. and Barsanti, K. C.: Identification and quantification of gaseous organic compounds emitted from biomass burning using two-dimensional gas chromatography–time-of-flight mass spectrometry, *Atmos. Chem. Phys.*, 15(4), 1865–1899, doi:10.5194/acp-15-1865-2015, 2015.

Haynes, B. S. and Wagner, H. G.: Soot Formation, *Prog. Energy Combust. Sci.*, 7(4), 229–273, 1981.

Hays, M. D., Geron, C. D., Linna, K. J., Smith, N. D. and Schauer, J. J.: Speciation of Gas-Phase and Fine Particle Emissions from Burning of Foliar Fuels, *Environ. Sci. Technol.*, 36(11), 2281–2295, doi:10.1021/es0111683, 2002.

Heald, C. L., Coe, H., Jimenez, J. L., Weber, R. J., Bahreini, R., Middlebrook, A. M., Russell, L. M., Jolleys, M., Fu, T.-M., Allan, J. D., Bower, K. N., Capes, G., Crosier, J., Morgan, W. T., Robinson, N. H., Williams, P. I., Cubison, M. J., DeCarlo, P. F. and Dunlea, E. J.: Exploring the vertical profile of atmospheric organic aerosol: comparing 17 aircraft field campaigns with a global model, *Atmos. Chem. Phys.*, 11(24), 12673–12696, doi:10.5194/acp-11-12673-2011, 2011.

Heisler, S. L. and Friedlander, S. K.: Gas-to-particle conversion in photochemical smog: Aerosol growth laws and mechanisms for organics, *Atmos. Environ.*, 11(2), 157–168, doi:10.1016/0004-6981(77)90220-7, 1977.

Hennigan, C. J., Sullivan, A. P., Collett, J. L. and Robinson, A. L.: Levoglucosan stability in biomass burning particles exposed to hydroxyl radicals, *Geophys. Res. Lett.*, 37(9), 2–5, doi:10.1029/2010GL043088, 2010.

Hennigan, C. J., Miracolo, M. A., Engelhart, G. J., May, A. A., Presto, A. A., Lee, T., Sullivan, A. P., McMeeking, G. R., Coe, H., Wold, C. E., Hao, W.-M., Gilman, J. B., Kuster, W. C., de Gouw, J. A., Schichtel, B. A., Kreidenweis, S. M. and Robinson, A. L.: Chemical and physical transformations of organic aerosol from the photo-oxidation of open biomass burning emissions in an environmental chamber, *Atmos. Chem. Phys.*, 11(15), 7669–7686, doi:10.5194/acp-11-7669-2011, 2011.

Hodzic, A., Kasibhatla, P. S., Jo, D. S., Cappa, C. D., Jimenez, J. L., Madronich, S. and Park, R. J.: Rethinking the global secondary organic aerosol (SOA) budget: stronger production, faster removal, shorter lifetime, *Atmos. Chem. Phys.*, 16, 7917–7941, doi:10.5194/acp-16-7917-2016, 2016.

Huffman, J. A., Docherty, K. S., Mohr, C., Cubison, M. J., Ulbrich, I. M., Ziemann, P. J., Onasch, T. B. and Jimenez, J. L.: Chemically-Resolved Volatility Measurements of Organic Aerosol from Different Sources, *Environ. Sci. Technol.*, 43(14), 5351–5357, doi:10.1021/es803539d, 2009.

Jayne, J. T., Leard, D. C., Zhang, X., Davidovits, P., Smith, K. A., Kolb, C. E. and Worsnop, D. R.: Development of an Aerosol Mass Spectrometer for Size and Composition Analysis of Submicron Particles, *Aerosol Sci. Technol.*, 33(1–2), 49–70, doi:10.1080/027868200410840, 2000.

Jimenez, J. L., Canagaratna, M. R., Donahue, N. M., Prevot, A. S. H., Zhang, Q., Kroll, J. H., DeCarlo, P. F., Allan, J. D., Coe, H., Ng, N. L., Aiken, A. C., Docherty, K. S., Ulbrich, I. M., Grieshop, A. P., Robinson, A. L., Duplissy, J., Smith, J. D., Wilson, K. R., Lanz, V. A., Hueglin, C., Sun, Y. L., Tian, J., Laaksonen, A., Raatikainen, T., Rautiainen, J., Vaattovaara, P., Ehn, M., Kulmala, M., Tomlinson, J. M., Collins, D. R., Cubison, M. J., Dunlea, J., Huffman, J. A., Onasch, T. B., Alfarra, M. R., Williams, P. I., Bower, K., Kondo, Y., Schneider, J., Drewnick, F., Borrmann, S., Weimer, S., Demerjian, K., Salcedo, D., Cottrell, L., Griffin, R., Takami, A., Miyoshi, T., Hatakeyama, S., Shimono, A., Sun, J. Y.,

Zhang, Y. M., Dzepina, K., Kimmel, J. R., Sueper, D., Jayne, J. T., Herndon, S. C., Trimborn, A. M., Williams, L. R., Wood, E. C., Middlebrook, A. M., Kolb, C. E., Baltensperger, U. and Worsnop, D. R.: Evolution of Organic Aerosols in the Atmosphere, *Science* (80-. ), 326(5959), 1525–1529, doi:10.1126/science.1180353, 2009.

Kamens, R. M., Rives, G. D., Perry, J. M., Bell, D. A., Paylo, R. F., Goodman, R. G. and Claxton, L. D.: Mutagenic changes in dilute wood smoke as it ages and reacts with ozone and nitrogen dioxide. An outdoor chamber study, *Environ. Sci. Technol.*, 18(7), 523–530, doi:10.1021/es00125a008, 1984.

Kelly, F. J. and Fussell, J. C.: Size, source and chemical composition as determinants of toxicity attributable to ambient particulate matter, *Atmos. Environ.*, 60, 504–526, doi:10.1016/j.atmosenv.2012.06.039, 2012.

Levin, E. J. T., McMeeking, G. R., Carrico, C. M., Mack, L. E., Kreidenweis, S. M., Wold, C. E., Moosmüller, H., Arnott, W. P., Hao, W. M., Collett, J. L. and Malm, W. C.: Biomass burning smoke aerosol properties measured during Fire Laboratory at Missoula Experiments (FLAME), *J. Geophys. Res. Atmos.*, 115(18), 1–15, doi:10.1029/2009JD013601, 2010.

Leon, Alexis: lamp-939639\_960\_720.jpg Retrieved January 31, 2017 from <https://pixabay.com/en/lamp-sailing-oil-939639/>, 2014.

Li, J., Pósfai, M., Hobbs, P. V. and Buseck, P. R.: Individual aerosol particles from biomass burning in southern Africa: 2, Compositions and aging of inorganic particles, *J. Geophys. Res. Atmos.*, 108(D13), n/a-n/a, doi:10.1029/2002JD002310, 2003.

Lozano, R., Naghavi, M., Foreman, K., Lim, S., Shibuya, K., Aboyans, V., Abraham, J., Adair, T., Aggarwal, R., Ahn, S. Y., AlMazroa, M. A., Alvarado, M., Anderson, H. R., Anderson, L. M., Andrews, K. G., Atkinson, C., Baddour, L. M., Barker-Collo, S., Bartels, D. H., Bell, M. L., Benjamin, E. J., Bennett, D., Bhalla, K., Bikbov, B., Abdulhak, A. Bin, Birbeck, G., Blyth, F., Bolliger, I., Boufous, S., Bucello, C., Burch, M., Burney, P., Carapetis, J., Chen, H., Chou, D., Chugh, S. S., Coffeng, L. E., Colan, S. D., Colquhoun, S., Colson, K. E., Condon, J., Connor, M. D., Cooper, L. T., Corriere, M., Cortinovis, M., de Vaccaro, K. C., Couser, W., Cowie, B. C., Criqui, M. H., Cross, M., Dabhadkar, K. C.,

Dahodwala, N., De Leo, D., Degenhardt, L., Delossantos, A., Denenberg, J., Des Jarlais, D. C., Dharmaratne, S. D., Dorsey, E. R., Driscoll, T., Duber, H., Ebel, B., Erwin, P. J., Espindola, P., Ezzati, M., Feigin, V., Flaxman, A. D., Forouzanfar, M. H., Fowkes, F. G. R., Franklin, R., Fransen, M., Freeman, M. K., Gabriel, S. E., Gakidou, E., Gaspari, F., Gillum, R. F., Gonzalez-Medina, D., Halasa, Y. A., Haring, D., Harrison, J. E., Havmoeller, R., Hay, R. J., Hoen, B., Hotez, P. J., Hoy, D., Jacobsen, K. H., James, S. L., Jasrasaria, R., Jayaraman, S., Johns, N., Karthikeyan, G., Kassebaum, N., Keren, A., Khoo, J.-P., Knowlton, L. M., Kobusingye, O., Koranteng, A., Krishnamurthi, R., Lipnick, M., et al.: Global and regional mortality from 235 causes of death for 20 age groups in 1990 and 2010: a systematic analysis for the Global Burden of Disease Study 2010, *Lancet*, 380(9859), 2095–2128, doi:10.1016/S0140-6736(12)61728-0, 2012.

Mansurov, Z. A.: Formation of soot from polycyclic aromatic hydrocarbons as well as fullerenes and carbon nanotubes in the combustion of hydrocarbon, *J. Eng. Phys. Thermophys.*, 84(1), 125–159, doi:10.1007/s10891-011-0459-y, 2011.

May, A. A., Levin, E. J. T., Hennigan, C. J., Riipinen, I., Lee, T., Collett, J. L., Jimenez, J. L., Kreidenweis, S. M. and Robinson, A. L.: Gas-particle partitioning of primary organic aerosol emissions: 3. Biomass burning, *J. Geophys. Res. Atmos.*, 118(19), 11,327–11,338, doi:10.1002/jgrd.50828, 2013.

Middlebrook, A. M., Bahreini, R., Jimenez, J. L. and Canagaratna, M. R.: Evaluation of Composition-Dependent Collection Efficiencies for the Aerodyne Aerosol Mass Spectrometer using Field Data, *Aerosol Sci. Technol.*, 46(3), 258–271, doi:10.1080/02786826.2011.620041, 2012.

Nisbet, I. C. T. and LaGoy, P. K.: Toxic equivalency factors (TEFs) for polycyclic aromatic hydrocarbons (PAHs), *Regul. Toxicol. Pharmacol.*, 16(3), 290–300, doi:10.1016/0273-2300(92)90009-X, 1992.

Ortega, A. M., Day, D. A., Cubison, M. J., Brune, W. H., Bon, D., de Gouw, J. A. and Jimenez, J. L.: Secondary organic aerosol formation and primary organic aerosol oxidation from biomass-burning smoke in a flow reactor during FLAME-3, *Atmos. Chem. Phys.*, 13(22), 11551–11571, doi:10.5194/acp-13-11551-2013, 2013.

Osthoff, H. D., Roberts, J. M., Ravishankara, A. R., Williams, E. J., Lerner, B. M., Sommariva, R., Bates, T. S., Coffman, D., Quinn, P. K., Dibb, J. E., Stark, H., Burkholder, J. B., Talukdar, R. K., Meagher, J., Fehsenfeld, F. C. and Brown, S. S.: High levels of nitryl chloride in the polluted subtropical marine boundary layer, *Nat. Geosci.*, 1(5), 324–328, doi:10.1038/ngeo177, 2008.

Pankow, J. F.: An absorption model of the gas/aerosol partitioning involved in the formation of secondary organic aerosol, *Atmos. Environ.*, 28(2), 189–193, doi:10.1016/1352-2310(94)90094-9, 1994.

Pitts, J. N., Grosjean, D., Van Cauwenberghe, K., Schmid, J. P. and Fitz, D. R.: Photooxidation of aliphatic amines under simulated atmospheric conditions: formation of nitrosamines, nitramines, amides, and photochemical oxidant, *Environ. Sci. Technol.*, 12(8), 946–953, doi:10.1021/es60144a009, 1978.

Pósfai, M. and Buseck, P. R.: Nature and Climate Effects of Individual Tropospheric Aerosol Particles, *Annu. Rev. Earth Planet. Sci.*, 38(1), 17–43, doi:10.1146/annurev.earth.031208.100032, 2010.

Presto, A. A., Huff Hartz, K. E. and Donahue, N. M.: Secondary Organic Aerosol Production from Terpene Ozonolysis. 2. Effect of NO<sub>x</sub> Concentration, *Environ. Sci. Technol.*, 39(18), 7046–7054, doi:10.1021/es050400s, 2005.

Qamar, N. H., Nathan, G. J., Alwahabi, Z. T. and Chan, Q. N.: Soot sheet dimensions in turbulent nonpremixed flames, *Combust. Flame*, 158(12), 2458–2464, doi:10.1016/j.combustflame.2011.04.017, 2011.

Reeves, C. E., Penkett, S. A., Bauguitte, S., Law, K. S., Evans, M. J., Bandy, B. J., Monks, P. S., Edwards, G. D., Phillips, G., Barjat, H., Kent, J., Dewey, K., Schmitgen, S. and Kley, D.: Potential for photochemical ozone formation in the troposphere over the North Atlantic as derived from aircraft observations during ACSOE, *J. Geophys. Res. Atmos.*, 107(D23), 4707, doi:10.1029/2002JD002415, 2002.

Reid, J. S., Koppmann, R., Eck, T. F. and Eleuterio, D. P.: A review of biomass burning emissions part II: intensive physical properties of biomass burning particles, *Atmos. Chem. Phys.*, 5(3), 799–825, doi:10.5194/acp-5-799-2005, 2005.

Renbaum-Wolff, L., Grayson, J. W., Bateman, A. P., Kuwata, M., Sellier, M., Murray, B. J., Shilling, J. E., Martin, S. T. and Bertram, A. K.: Viscosity of  $\alpha$ -pinene secondary organic material and implications for particle growth and reactivity., *Proc. Natl. Acad. Sci. U. S. A.*, 110(20), 8014–9, doi:10.1073/pnas.1219548110, 2013.

Robinson, A. L., Donahue, N. M., Shrivastava, M. K., Weitkamp, E. A., Sage, A. M., Grieshop, A. P., Lane, T. E., Pierce, J. R. and Pandis, S. N.: Rethinking Organic Aerosols: Semivolatile Emissions and Photochemical Aging, *Science* (80-. ), 315(5816), 1259–1262, doi:10.1126/science.1133061, 2007.

Robinson, E. S., Onasch, T. B., Worsnop, D. and Donahue, N. M.: Collection efficiency of alpha-pinene secondary organic aerosol particles explored via light scattering single particle aerosol mass spectrometry, *Atmos. Meas. Tech. Discuss.*, 1–29, doi:10.5194/amt-2016-271, 2016a.

Robinson, E. S., Donahue, N. M., Ahern, A. T., Ye, Q. and Lipsky, E.: Single-particle measurements of phase partitioning between primary and secondary organic aerosols, *Faraday Discuss.*, 189, 31–49, doi:10.1039/C5FD00214A, 2016b.

Saleh, R., Donahue, N. M. and Robinson, A. L.: Time Scales for Gas-Particle Partitioning Equilibration of Secondary Organic Aerosol Formed from Alpha-Pinene Ozonolysis, *Environ. Sci. Technol.*, 47(11), 5588–5594, doi:10.1021/es400078d, 2013.

Sarwar, G., Simon, H., Bhave, P. and Yarwood, G.: Examining the impact of heterogeneous nitryl chloride production on air quality across the United States, *Atmos. Chem. Phys.*, 12(14), 6455–6473, doi:10.5194/acp-12-6455-2012, 2012.

Shiraiwa, M. and Seinfeld, J. H.: Equilibration timescale of atmospheric secondary organic aerosol partitioning, *Geophys. Res. Lett.*, 39(24), n/a-n/a, doi:10.1029/2012GL054008, 2012.

Simon, H., Kimura, Y., McGaughey, G., Allen, D. T., Brown, S. S., Osthoff, H. D., Roberts, J. M., Byun, D. and Lee, D.: Modeling the impact of ClNO<sub>2</sub> on ozone formation in the Houston area, *J. Geophys. Res.*, 114(D7), D00F03, doi:10.1029/2008JD010732, 2009.

Simoneit, B. R. T., Rogge, W. F., Mazurek, M. A., Standley, L. J., Hildemann, L. L. M. and Cass, G. R.: Lignin Pyrolysis Products, Lignans, and Resin Acids as Specific Tracers of Plant Classes in Emissions from Biomass Combustion, *Environ. Sci. Technol.*, 27, 2533–2541, 1993.

Solomon, S., Qin, D., Manning, M., Chen, Z., Marquis, M., Averyt, K. B., Tignor, M. and Miller, H. L.: Climate change 2007: The physical science basis, contribution of working group 1 to the fourth assessment report of the Intergovernmental Panel on Climate Change, Cambridge University Press, Cambridge, United Kingdom and New York, NY, USA., 2007.

Spencer, M. T. and Prather, K. A.: Using ATOFMS to Determine OC/EC Mass Fractions in Particles, *Aerosol Sci. Technol.*, 40(8), 585–594, doi:10.1080/02786820600729138, 2006.

Spicer, C. W., Chapman, E. G., Finlayson-Pitts, B. J., Plastridge, R. A., Hubbe, J. M., Fast, J. D. and Berkowitz, C. M.: Unexpectedly high concentrations of molecular chlorine in coastal air, *Nature*, 394(6691), 353–356, doi:10.1038/28584, 1998.

Steele, P. T., Tobias, H. J., Fergenson, D. P., Pitesky, M. E., Horn, J. M., Czerwieniec, G. a, Russell, S. C., Lebrilla, C. B., Gard, E. E. and Frank, M.: Laser Power Dependence of Mass Spectral Signatures from Individual Bacterial Spores in Bioaerosol Mass Spectrometry, *Anal. Chem.*, 75(20), 5480–5487, doi:10.1021/ac034419u, 2003.

Sullivan, R. C. and Prather, K. A.: Recent Advances in Our Understanding of Atmospheric Chemistry and Climate Made Possible by On-Line Aerosol Analysis Instrumentation, *Anal. Chem.*, 77(12), 3861–3886, doi:10.1021/ac050716i, 2005.

Tham, Y. J., Wang, Z., Li, Q., Yun, H., Wang, W., Wang, X., Xue, L., Lu, K., Ma, N., Bohn, B., Li, X., Kecorius, S., Größ, J., Shao, M., Wiedensohler, A. 5, Zhang, Y., Wang, T. and Wang, T.: Significant concentrations of nitryl chloride sustained in the morning: Investigations of the causes and impacts on ozone production in a polluted region of northern China, *Atmos. Chem. Phys.*, 16, 14959–14977, doi:10.5194/acp-16-14959-2016, 2016.



Thornton, J. A., Kercher, J. P., Riedel, T. P., Wagner, N. L., Cozic, J., Holloway, J. S., Dubé, W. P., Wolfe, G. M., Quinn, P. K., Middlebrook, A. M., Alexander, B. and Brown, S. S.: A large atomic chlorine source inferred from mid-continental reactive nitrogen chemistry., *Nature*, 464(7286), 271–4, doi:10.1038/nature08905, 2010.

Tiitta, P., Leskinen, A., Hao, L., Yli-Pirilä, P., Kortelainen, M., Grigonyte, J., Tissari, J., Lamberg, H., Hartikainen, A., Kuusalo, K., Kortelainen, A.-M., Virtanen, A., Lehtinen, K. E. J., Komppula, M., Pieber, S., Prévôt, A. S. H., Onasch, T. B., Worsnop, D. R., Czech, H., Zimmermann, R., Jokiniemi, J. and Sippula, O.: Transformation of logwood combustion emissions in a smog chamber: formation of secondary organic aerosol and changes in the primary organic aerosol upon daytime and nighttime aging, *Atmos. Chem. Phys.*, 16, 13251–13269, doi:10.5194/acp-16-13251-2016, 2016.

Wang, T., Tham, Y. J., Xue, L., Li, Q., Zha, Q., Wang, Z., Poon, S. C. N., Dubé, W. P., Blake, D. R., Louie, P. K. K., Luk, C. W. Y., Tsui, W. and Brown, S. S.: Observations of nitryl chloride and modeling its source and effect on ozone in the planetary boundary layer of southern China, *J. Geophys. Res. Atmos.*, 121(5), 2476–2489, doi:10.1002/2015JD024556, 2016.

Weitkamp, E. A, Sage, A. M., Pierce, J. R., Donahue, N. M. and Robinson, A. L.: Organic Aerosol Formation from Photochemical Oxidation of Diesel Exhaust in a Smog Chamber, *Environ. Sci. Technol.*, 41(20), 6969–6975, doi:10.1021/es070193r, 2007.

Ye, Q., Robinson, E. S., Ding, X., Ye, P., Sullivan, R. C. and Donahue, N. M.: Mixing of secondary organic aerosols versus relative humidity., *Proc. Natl. Acad. Sci. U. S. A.*, 113(45), 12649–12654, doi:10.1073/pnas.1604536113, 2016.

## 2. SMOG CHAMBER STUDY OF SECONDARY ORGANIC AEROSOL FORMATION FROM BIOMASS BURNING

After smoke from burning biomass is emitted into the atmosphere, chemical and physical processes change the amount of organic aerosol present in the aged, diluted plume. During the fourth Fire Lab At Missoula Experiment (FLAME-IV), we used smog chambers to investigate two of these processes, specifically condensation of secondary organic aerosol (SOA) and multi-phase oxidation of primary organic aerosol (POA). We simulated atmospheric aging on diluted smoke from a variety of biomass fuels while measuring particle composition using high resolution ( $R = \sim 2100$  at  $m/z$  200) aerosol mass spectrometry. These smoke aging experiments revealed variable organic aerosol (OA) enhancements, even for smoke from similar fuels and aging mechanisms. This variable OA enhancement was best explained by measured differences in the amount of VOCs that were emitted which can be oxidized to form SOA. For some experiments, we were able to accurately model SOA production in the aging experiments using a fuel-specific VOC emission inventory that was scaled by burn-specific toluene measurements. We measured the condensation of SOA using a new proposed conserved tracer ion for low-volatility POA,  $C_7H_{11}^+$  ( $m/z$  95). We used the same tracer ion to calculate the amount of mass that is lost due to gas-phase oxidation and subsequent volatilization of POA. Less than 5% of the POA mass was lost via multi-phase oxidation-volatilization during less than two hours of simulated atmospheric oxidation. The results of these aging experiments show that although dilution of POA may have a significant effect on OA enhancement, the subsequent multi-phase oxidation mechanism has a small effect. Most of the OA enhancement can be explained by the addition of SOA from known gaseous precursors.

## 2.1. Introduction

Biomass burning is the second largest source of non-methane volatile organic compounds (VOCs) on Earth (Akagi et al., 2011; Bond et al., 2013; Reid et al., 2005). After emission, these VOCs are diluted and may be oxidized. Some of the compounds that result from the oxidation of these VOCs have sufficiently low volatility to partition into the particle phase; they are known as secondary organic aerosol (SOA) (Donahue et al., 2009; Jimenez et al., 2009). SOA affects important particle characteristics like size, optical properties, and atmospheric lifetimes, and contributes significantly to the burden of particulate matter mass. Thus, it is important to understand and be able to accurately predict SOA formation. As biomass smoke also contains substantial primary organic aerosol (POA), SOA formation has been measured in part by calculating the enhancement in total organic aerosol (OA) resulting from atmospheric aging. A commonly reported value in field measurements, OA enhancement is defined as the ratio of OA mass after aging to the OA mass before aging (the POA), and usually utilizes a functionally inert chemical tracer to account for dilution.

Past observations of the OA enhancement from biomass burning using both field measurements and laboratory studies span a very wide range. Yokelson et al. (2009) measured the OA mass in a biomass burning plume in the Yucatan, Mexico. After 1.5 hours of aging, and accounting for dilution using carbon monoxide, they reported a doubling of organic aerosol (OA) mass, suggesting significant condensation of SOA. Other field measurements have observed little or no increase in OA mass, although the OA almost invariably becomes much more oxidized with aging (Akagi et al., 2012; Jolleys et al., 2012; Reid and Hobbs, 1998). In an effort to identify the cause of the observed variability in SOA production from aged biomass-burning emissions, smog chambers have been used to allow sampling of emissions from specific fuels with reproducible oxidation chemistry that simulates atmospheric aging (Bruns et al., 2016; Grieshop et al., 2008; Hennigan et al., 2011; Tiitta et al., 2016). The injection into a large smog chamber also dilutes the smoke, simulating atmospheric plume dynamics.

Dilution is necessary to simulate because it significantly alters the amount of OA present in the smoke, beyond the effect of just dilution. This is because at lower mass concentrations of OA material, a larger fraction of compounds partition more into the gas phase versus the particle phase, depending on their vapor pressure and activity in the condensed phase (Donahue et al., 2006, 2011a). Some of the primary organic aerosol (POA) is semi-volatile under OA concentrations relevant to biomass-burning plumes and background ambient conditions (Grieshop et al., 2008; Hennigan et al., 2011; May et al., 2013; Robinson et al., 2007). Furthermore, photochemical processing is greatly accelerated when semi-volatile POA molecules are in the gas-phase as they are more accessible to atmospheric oxidants than when they reside in the condensed aerosol phase (Donahue et al., 2013; Hennigan et al., 2010, 2011). In order to understand the SOA production in ambient biomass-burning plumes, both the dilution and oxidation processes must be investigated. Our goal is thus to determine the contributions of both SOA mass formation and POA mass loss to the total OA enhancement. We thus participated in the collaborative Fourth Fire Lab At Missoula Experiment (FLAME-IV) (Hatch et al., 2015; Stockwell et al., 2014, 2015; Tkacik et al., 2017), studying biomass smoke aging through dilution and oxidation in dual 7 m<sup>3</sup> smog chambers after dilution of the nascent smoke by a factor of about 25.

Aerosol mass spectrometry provides both quantitative mass measurements and compositional information, albeit with extensive fragmentation of organic compounds. This extensive fragmentation causes the identification of POA mass versus SOA mass to typically be constrained by individual measured ions, and is then scaled based on a reference mass spectrum. For example, both Sage et al. (2008) and Grieshop et al. (2008) used the mass spectrum of POA prior to aging to calculate SOA mass produced in smog-chamber aging experiments. However, this method of calculating SOA mass assumes that POA is only lost via particle-to-wall deposition (neglecting POA vaporization or oxidation) and also that the contribution of SOA to the chosen POA-marker ions is negligible. For example, the marker ion used by Sage et al. (2008) was  $m/z$  57, an ion that has been identified as a dominant feature in SOA mass spectra as well (Ulbrich et al., 2009). Thus, the calculated SOA mass may be

underestimated if the POA mass spectrum is scaled by an ion also produced from the fragmentation of SOA components. Alternatively, the calculated SOA mass may be overestimated if the POA mass spectrum is scaled by an ion produced by a semi-volatile or reactive/non-conserved POA compound. Hennigan et al. (2011) calculated an upper estimate of POA that may be oxidized, assuming that levoglucosan – a product of cellulose pyrolysis – is a conserved tracer for POA. They found that for their smog-chamber experiments using biomass-burning emissions, only 17% of the OA mass after aging was POA. However, levoglucosan is a small fraction of POA and it is also semi-volatile. Thus in this work, we identified a novel POA tracer ion ( $C_7H_{11}^+$ ,  $m/z$  95) produced by low-volatility POA compounds with minimal influence from compounds present in SOA. We used this conserved POA tracer ion to calculate both the POA mass lost through evaporation/oxidation and the new SOA mass condensed.

Having measured the amount of SOA formed in FLAME-IV experiments, we compared the measured SOA with the amount predicted based on the extensive gas-phase characterization of VOCs understood to contribute to SOA formation through oxidation and condensation. Recent studies have investigated the emissions of logwood fires in residential woodstoves, which have much more consistent combustion conditions. They were able to predict the amount of SOA measured in their smog-chamber experiments using relatively few traditional VOC SOA precursors (e.g. toluene, benzene,  $\alpha$ -pinene, etc. (Bruns et al., 2016; Tiitta et al., 2016)). However, the biomass burned in our experiments typically contained more than just logwood, and was burned in an open, scattered arrangement rather than in a residential woodstove. Stockwell et al. (2014, 2015) showed that the VOC mass emissions from simple cookstoves were much lower than those from uncontained fires. Furthermore, Hatch et al. (2015) showed, unsurprisingly, that the composition of the VOCs emitted in FLAME-IV varied significantly depending on the fuel burned.

We conducted smog-chamber aging experiments using smoke from fuels and burn conditions representative of open biomass burning. We then analyzed the varying composition of the organic aerosol as a result of aging, using a POA tracer ion to more precisely measure the counterbalancing effects of POA evaporation and SOA

condensation on total OA mass. The remarkable gas-phase characterization of emissions available for the burns during FLAME-IV give a good estimate of SOA production from the oxidation of 674 identified VOCs.

## 2.2. Methods

### 2.2.1. Experimental methods

We performed smog-chamber experiments during FLAME-IV using dual smog chambers that enabled paired experiments on the same smoke aerosol from the same biomass fuel burn. Tkacik et al. (2017) provides a detailed description of the Dual Chamber Experiment method, and Stockwell et al. (2013) provides a comprehensive description of the fuels burned and the combustion conditions used. Thus, we provide only a brief description here.

We burned a variety of biomass fuels and injected the resulting smoke into a pair of identical 7 m<sup>3</sup> Teflon environmental chambers, located inside the 3,000 m<sup>3</sup> combustion chamber at the Missoula Fire Sciences Lab. Globally relevant fuels discussed in this paper include agricultural cuttings, tree debris, and peat (Stockwell et al., 2014) collected from North America, Africa, and Asia. Before each burn, we loosely scattered or propped up the biomass fuel on the ignition platform, similar to what one might expect to occur in open burning. We then ignited the fuel using a resistive heating element.

We show a schematic of the experimental setup in Figure 2.1. Prior to each experiment, we purged the twin smog chambers for 12 hours with dry, particle-free and VOC-scrubbed air. We used UV radiation from black lights (GE model 10526) positioned underneath the chambers to assist in cleaning the chambers. At the beginning of an experiment, we filled the two darkened chambers with smoke. Smoke was pulled through heated, passivated, and smoke-conditioned transfer lines by four Dekati eductor diluters (Tkacik et al., 2017). For some experiments, smoke

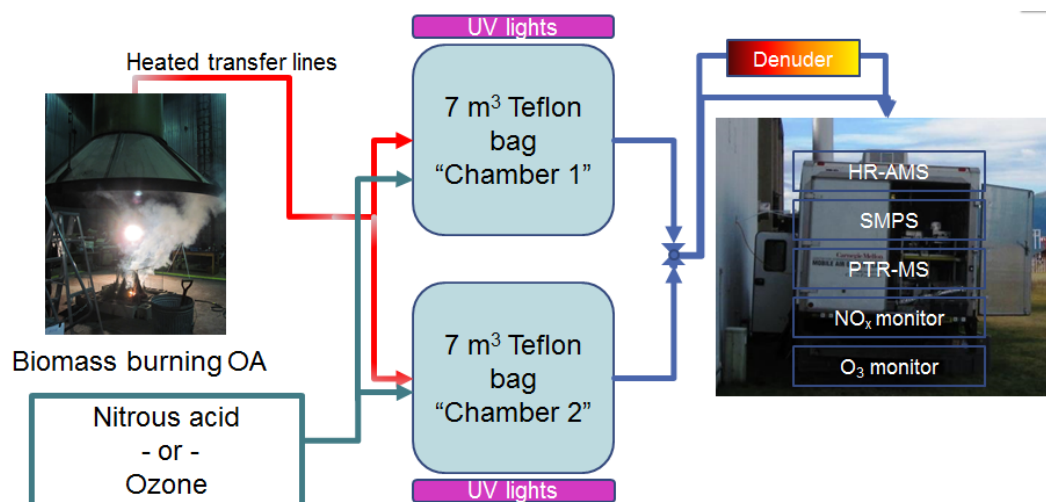


Figure 2.1 The experimental setup at the Fire Laboratory in Missoula Experiments, FLAME-IV. Biomass was burned in the Missoula Fire Lab facility and transferred via heated transfer lines to two identical smog chambers. The smog chambers could independently simulate three types of aging: UV photolysis, UV photolysis with nitrous acid (HONO), or dark ozonolysis. Instrumentation in the CMU mobile lab characterized the emissions during the experiments using an automated valve system to switch between the two chambers.

was sampled from the well-mixed plume in the Fire Lab smoke stack. These experiments are identified as “stack” burns. Alternatively, the chimney, or stack, was sealed and the ignited biomass was allowed to burn completely, filling the entire Fire Lab combustion chamber. These experiments are called “chamber” burns, and for these cases the smoke was sampled from 5’ off the ground, reducing the transfer line from 50’ (for stack burns) to 10’ (for chamber burns). 15 to 45 minutes after smoke injection, we perturbed the contents of a chamber in one of three ways: 1) using UV lights to generate hydroxyl radicals (OH) from existing precursors, 2) adding nitrous acid (HONO) in addition to the UV lights to augment the  $\cdot\text{OH}$  concentration, or 3) injecting an excess of ozone (>500 ppbv). We generated and injected HONO from a solution of H<sub>2</sub>SO<sub>4</sub> and NaNO<sub>2</sub> via the method described in Ng et al. (2007). We generated ozone separately via corona discharge in the presence of pure oxygen. We also conducted control experiments periodically with no

Table 2.1 Experimental details for each pair of smog chamber experiments.

Burn Number - chamber	Date	Fuel	Perturbation Type	Organic Aerosol <sup>1</sup> μg/m <sup>3</sup>	O:C	NO+NO <sub>2</sub> ppb
84-1	10/21/2012	Ponderosa pine	HONO + UV	65	0.21	
84-2	10/21/2012	Ponderosa pine	UV only	57	0.21	
115-1	10/23/2012	Okote	UV only	1	0.16	1
115-2	10/23/2012	Okote	Ozone	1	0.13	0
126-1	10/24/2012	Black spruce	HONO + UV	5	0.16	100
126-2	10/24/2012	Black spruce	UV only	4	0.17	11
127-1	10/25/2012	Ponderosa pine	Dark	60	0.16	11
127-2	10/25/2012	Ponderosa pine	UV only	56	0.17	13
131-1	10/28/2012	Black spruce	Dark	16	0.20	3
131-2	10/28/2012	Black spruce	UV only	11	0.20	2
134-1	10/29/2012	Black spruce	Dark	105	0.22	32
134-2	10/29/2012	Black spruce	Ozone	64	0.22	24
137-1	10/30/2012	Black spruce	Dark	67	0.23	29
137-2	10/30/2012	Black spruce	UV only	47	0.23	26
140-1	10/31/2012	Ponderosa pine	HONO + UV	184	0.21	643
140-2	10/31/2012	Ponderosa pine	UV only	121	0.22	12
142-1	11/1/2012	Ponderosa pine	Dark	39	0.23	18
142-2	11/1/2012	Ponderosa pine	Ozone	36	0.23	19
144-1	11/3/2012	Ponderosa pine	UV only	117	0.22	10
144-2	11/3/2012	Ponderosa pine	Ozone	137	0.21	12
146-1	11/4/2012	Organic hay	Dark	130	0.14	19
146-2	11/4/2012	Organic hay	UV only	145	0.14	23
148-1	11/5/2012	Giant cutgrass	Dark	7	0.26	20
148-2	11/5/2012	Giant cutgrass	UV only	9	0.24	24
151-1	11/6/2012	Wiregrass	UV only	15	0.43	21
151-2	11/6/2012	Wiregrass	Dark	15	0.41	23
153-1	11/7/2012	Rice straw	Dark	19	0.22	46
153-2	11/7/2012	Rice straw	UV only	16	0.23	45
154-1	11/8/2012	Peat	Ozone	28	0.10	2
154-2	11/8/2012	Peat	UV only	27	0.10	2
155-1	11/10/2012	Black spruce	HONO + UV	84	0.25	1386
155-2	11/10/2012	Black spruce	UV only	91	0.24	10
156-1	11/11/2012	Black spruce	Ozone	66	0.26	50
156-2	11/11/2012	Black spruce	Ozone	67	0.26	12
157-1	11/12/2012	Black spruce	UV only	85	0.27	13
157-2	11/12/2012	Black spruce	Ozone	76	0.27	13

<sup>1</sup>OA concentration after injection, but before perturbation at beginning of experiment.



perturbation to one or both chambers. In these cases, suspended particle concentrations decreased due to loss to the walls and VOC concentrations remained constant. We list each experiment in Table 2.1, indexed according to the burn identification convention in Stockwell et al. (2013). The additional hyphenated number is used to separate the different smog chambers filled with smoke diluted from the same fuel. Table 2.1 also contains details regarding initial OA concentrations and composition.

We sampled the aerosol in the dual chambers through passivated 3/8" O.D. stainless steel that was actively maintained at 20°C using a suite of instruments located outside the Fire Lab in the CMU mobile lab. Two automated 2-way ball valves allowed for the gas and particle instrumentation to switch between sampling from either one of the two chambers.

### 2.2.2. Characterizing the particulate phase

We quantified black carbon (BC) using a Single Particle Soot Photometer (SP2, Droplet Measurement Technologies) and a 7-wavelength aethalometer (McGee Scientific model AE-31) (Saleh et al., 2014). Since black carbon is inert and effectively nonvolatile, and has no other sources after smoke injection, it has been used in past chamber experiments to measure the rate at which aerosol particles were lost to the walls (Hennigan et al., 2011; Tkacik et al., 2017). However, at high concentrations (greater than 12,500 particles cm<sup>-3</sup>) the SP2 may become saturated, causing it to undercount the number of BC-containing particles. Likewise, the aethalometer sensitivity may increase due to increased OA content on particles (Heringa et al., 2011). Thus, although BC in theory makes an excellent tracer species for particle wall-loss, the difficulty associated with its accurate measurement makes it challenging to use in practice.

We measured total particle number and mobility diameter size distributions using a scanning mobility particle sizer (Model 3081: 3080 DMA and 3021 butanol CPC; TSI, Inc.), characterizing particles from 10.7 to 478 nm in mobility diameter. We measured speciated aerosol mass and chemical composition using an Aerodyne high-

resolution aerosol mass spectrometer (AMS). The AMS efficiently measures particulate matter that has a vacuum aerodynamic diameter between 70 nm and 700 nm and that vaporizes upon contact with a 600 °C heater in vacuum (Decarlo et al., 2006; Jayne et al., 2000). We performed high-resolution peak fitting and attribution of the AMS signal using PIKA 1.12 and calculated the O:C elemental ratio using the method described by Canagaratna et al. (2015). For quantitative mass measurements of organic aerosol for the AMS, the collection efficiency with respect to particle bounce is very important. For fresh biomass-burning aerosol, we used a collection efficiency of 1.0, consistent with past observations of primary and aged emissions from biomass burning (Hennigan et al., 2011; Heringa et al., 2011). However, composition measurements indicate that aging of the organic aerosol can increase O:C, indicating condensation of SOA. The SOA may reduce the collection efficiency toward a lower value as reported for highly oxidized ambient aerosol. This may shift the collection efficiency of the AMS from 1.0 to as low as 0.5, as is observed for smog-chamber SOA measurements (Docherty et al., 2013; Robinson et al., 2016).

### 2.2.3. Characterizing particle wall loss

Calculating OA enhancements in smog-chamber experiments requires that one account for particles and vapors that are lost to the Teflon walls. When possible, it is common to calculate the particle wall loss using black carbon as a conserved tracer, and the total aerosol mass concentration from measurements made by either a scanning mobility particle sizer or an aerosol mass spectrometer (Grieshop et al., 2009; Hennigan et al., 2011; Heringa et al., 2011; Tiitta et al., 2016).

However, during the aging process physicochemical properties of the particles are changing, and this may lead to bias in calculated OA enhancements. For example, particle density may change due to the condensation of SOA, or the particle collection efficiency of the AMS may change, due to changes in the fraction of particles that bounce off the heated vaporizer (Docherty et al., 2013; Robinson et al., 2016). Primary biomass-burning emissions are typically quantified assuming no particle bounce (collection efficiency = 1.0), but secondary organic aerosol can have a

collection efficiency of 0.5 or lower (Docherty et al., 2013; Hennigan et al., 2011; Robinson et al., 2016).

While a changing collection efficiency can affect the total signal from an ion in the mass spectrum, it will not change the *fraction* of the total ion signal it contributes. Thus, if one uses the relative contribution of ions in the organic aerosol mass spectra, changes in particle density and collection efficiency are internally corrected. In this work, we identify a primary OA tracer ion that is generated from molecules that are detected in POA, that have a low volatility, and that are unlikely to have a significant contribution from SOA. We then use the changing relative contribution of this ion's signal to the total OA ion signal to calculate both the SOA mass condensed and POA mass evaporated during the chamber experiment. Additional wall-loss corrections are required to account for particle and vapor deposition, but our new method for calculating changes in OA composition using the POA tracer self-corrects for any changes in both AMS collection efficiency and particle density. It also reduces the dependence on notoriously inaccurate black-carbon mass measurements.

#### 2.2.4. Characterizing the gas phase

We used a proton transfer reaction mass spectrometer (PTR-MS) to measure in real-time the concentrations of selected VOCs. The PTR-MS (Ionicon, GmbH.) measures organic ions formed from charge transfer between  $\text{H}_3\text{O}^+$  produced in an isolated source and the VOCs in the sampled gas. Each VOC has a specific charge-transfer efficiency that we calibrated weekly with a premixed standard of known concentrations including toluene and acetone, which we discuss in this manuscript (Scott-Marrin, Inc., Riverside, California). We operated the quadrupole mass spectrometer of the PTR-MS in selected-ion mode, analyzing with unit mass resolution preselected volatile organic compounds, listed in the Supplemental Information. The 1 Hz time resolution of the PTR-MS is useful for calculating the  $\cdot\text{OH}$  exposure in the chamber, but cannot differentiate between isobars, such as the many monoterpene isomers that have different chemical structures but the same chemical

formula and thus same molecular weight. We used the following first-order reaction equation for toluene to calculate the  $\cdot\text{OH}$  concentration:

$$\ln \frac{C_t}{C_o} = e^{-kt[\text{OH}]} \quad (2.1)$$

Where  $C_o$  and  $C_t$  are concentrations of toluene measured at the beginning and end of a chamber aging experiment, respectively. A rate constant of  $k = 5.63 \times 10^{-12} \text{ cm}^3 \text{ molecule}^{-1} \text{ sec}^{-1}$  was used (Atkinson and Arey, 2003). When we injected HONO into the smog chambers, the estimated  $\cdot\text{OH}$  concentration was usually about  $2 \times 10^6 \text{ molecules cm}^{-3}$ , as opposed to about  $1 \times 10^6 \text{ molecules cm}^{-3}$  for UV lights only experiments. For dark ozonolysis experiments, toluene decay calculations indicated that  $\sim 2 \times 10^5 \cdot\text{OH}$  molecules  $\text{cm}^{-3}$  were generated by secondary processes.

To provide a more detailed analysis of the volatile organic compounds, we collected vapor samples adsorption-thermal desorption (ATD) cartridges for offline analysis via two-dimensional gas chromatography (2D-GC). Hatch et al. (2015) describe this analysis that used two GC columns to separate the gas samples first by volatility, and then by polarity. The dual adsorbents in the ATD cartridges allow for the collection of organic gases with a broad range of volatilities (Pankow et al., 2012). The least volatile compounds quantified in this work, sesquiterpenes ( $\text{C}_{15}\text{H}_{24}$ ), have a vapor pressure of  $\sim 1 \times 10^{-3} \text{ kPa}$  at  $25^\circ\text{C}$  (Helmig et al., 2003). Therefore, some intermediate volatility compounds (e.g. alkanes  $\text{C}_{16}\text{--C}_{22}$  and polyaromatic hydrocarbons larger than acetylnaphthalene) that are thought to contribute significantly to SOA formation in petroleum combustion emissions may not have been measured (Presto et al., 2009; Zhao et al., 2014). Besides quantitatively measuring 674 compounds, Hatch et al. also put forth a framework by which to estimate SOA production from the measured VOC precursors. We will use the same parameters to predict the amount of VOC reacted and subsequent SOA mass formed.

We measured other gas-phase species including  $\text{NO}_x$  ( $\text{NO}_x = \text{NO} + \text{NO}_2$ ), carbon dioxide, and ozone using a suite of separate instruments. The  $\text{NO}_x$  monitor was a chemiluminescent analyzer (Teledyne model 200EU), while ozone was measured

by photometry (API model 400A). Carbon dioxide was measured using non-dispersive infrared photometry (Licor Biosciences Model LI-820).

## 2.3. Results and Discussion

### 2.3.1. Mass spectra of organic aerosol

In panel A of Figure 2.2 we show the high-resolution mass spectrum for the organic aerosol component from black spruce smoke after it was diluted into one of our smog chambers, and prior to any aging. The ions are grouped into chemical families according to their oxygen content:  $C_xH_y$  (green) has no oxygen,  $C_xH_yO$  (purple) has one oxygen, and  $C_xH_yO_{>1}$  (pink) has more than one oxygen (in this case usually 2). The abundance of signal from  $C_xH_y$  is typical of fresh combustion emissions that have a low oxidation state. The presence of  $C_xH_yO_2$  –  $C_2H_4O_2$  and  $C_3H_5O_2$  in particular – is consistent with past observations of primary biomass-burning OA (Cubison et al., 2011; Hennigan et al., 2011; Ortega et al., 2013); these are fragments from carbohydrates that are major biomass combustion products.

We did not attempt to resolve nitrogen containing ions because they are not easily resolved at the V-mode resolution of  $\sim 2100$  at  $m/z$  200. Also, the nitrate group from organic nitrates typically fragments in the vaporizer, producing a characteristically high ratio of  $NO^+$  to  $NO_2^+$  ion signal ( $m/z$  30:46) compared to ammonium nitrate (Farmer et al., 2010). Our instrument has a typical 30:46 of  $\sim 0.3$  for ammonium nitrate. We measured  $NO^+$  to  $NO_2^+$  ion ratio values for diluted POA ranging from 3.6 to 12.6, suggesting significant organic nitrate content in the fresh, diluted smoke. The measured 30:46 ratio decreased with time for all chamber experiments, suggesting that pyrogenic ammonia was neutralized to form  $NH_4NO_3$ , thus diluting the relative contribution from organic nitrates to the  $NO^+$  and  $NO_2^+$  ion fragments.

Panel B in Figure 2.2 shows a mass spectrum for the organic aerosol from the same black spruce smoke experiment, after aging via UV light and  $\cdot OH$  oxidation

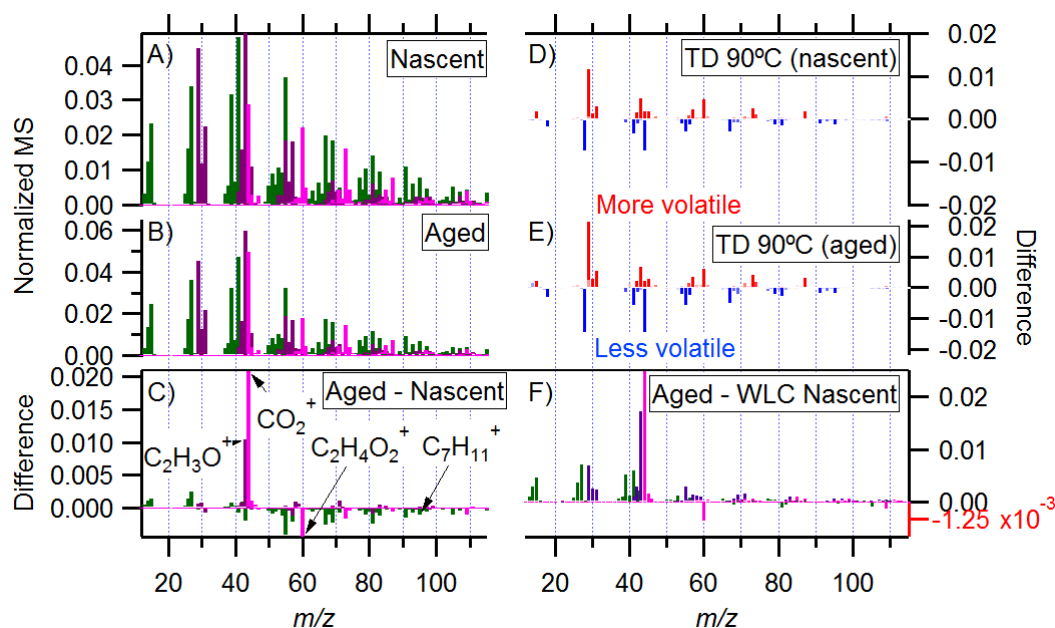


Figure 2.2 The normalized high resolution ( $\sim 2100$  at  $m/z$  200) mass spectra of organic aerosol from burning black spruce before (A) and after aging by UV light (B). Panel C) shows the difference between the normalized spectra in (A) and (B). Positive values indicate that an ion signal increased following aging, potentially due to the formation of secondary organic aerosol. Negative values may have three different explanations: evaporation of OA, oxidation of OA into VOCs or SOA, or dilution by condensation of SOA. The difference between the normalized mass spectra from thermally denuded and bypass OA are shown for nascent (D) and aged (E) aerosol. Panel (F) shows the difference between the aged OA mass spectrum (E) and the wall-loss corrected nascent OA mass spectrum (D). The positive signal, likely from the SOA, is very similar to other mass spectra for highly oxidized organic aerosol. The negative mass spectra, shown with a differently scaled axis in red (10x the positive axis), shows small changes in mass for  $\text{C}_2\text{H}_4\text{O}_2$ ,  $\text{C}_6\text{H}_9$ ,  $\text{C}_8\text{H}_9$ , and  $\text{C}_6\text{H}_5\text{O}_2$ .

(no HONO added). To illustrate the differences between the two spectra, and to correct for particle wall loss, we show the difference of the two spectra, each normalized to their total ion signal, in panel C. As this is the difference of normalized spectra, positive signals indicate ions that are more abundant in the aged spectrum, and negative signals indicate ions are more abundant in the fresh spectrum. Ions with

a positive value in panel C are therefore secondary organic aerosol products produced during the aging. For example,  $\text{CO}_2^+$  ( $m/z$  44) and  $\text{C}_2\text{H}_3\text{O}^+$  ( $m/z$  43), which contribute the bulk of the signal here and in the Ng et al. ambient OA triangle ( $f_{44}$  vs  $f_{43}$ ), are strongly associated with SOA (Ng et al., 2010). Ions with negative signals in panel C are predominantly POA, which is diluted by the SOA production during aging. However, SOA may also contribute to ions that also produced by POA components present in the fresh aerosol, and thus produce negative values in panel C. For example, toluene and  $\alpha$ -pinene are present in biomass-burning emissions and they form SOA (Yokelson et al., 2013). Previous studies have shown that secondary organic aerosol can contribute to signal at  $m/z$  55 (mostly  $\text{C}_4\text{H}_7^+$ ) and thus although most of the signal at  $m/z$  55 is from POA, the reduction may be less than one would expect after aging because of counterbalancing condensation of SOA (Chhabra et al., 2010; Hildebrandt, 2009). In addition to dilution by secondary organic aerosol, primary organic aerosol may evaporate from the particles and/or may be oxidized, which could also result in a negative difference signal.

The family  $\text{C}_x\text{H}_y\text{O}_2$  has a large negative signal in Fig. 5.2c, indicating it is present in the POA. This family includes the ion at  $m/z$  60,  $\text{C}_2\text{H}_4\text{O}_2^+$ , the dominant ion resulting from the fragmentation of levoglucosan in the AMS (Cubison et al., 2011; Hennigan et al., 2010). Levoglucosan is a common biomass-burning marker compound that results from the pyrolysis of organic polymers like cellulose (Simoneit et al., 1999). Although this marker has been shown to correlate with levoglucosan, a comparison between AMS data and filter analysis shows levoglucosan accounts for less than 10% of the total signal at  $m/z$  60 (Aiken et al., 2009; Lee et al., 2010; Sullivan et al., 2008); the rest may come from other cellulose-pyrolysis products and other OA components. Cellulose pyrolysis may also generate other products contributing to other highly oxygenated ions observed in the POA, namely  $\text{C}_3\text{H}_5\text{O}_2^+$  ( $m/z$  73) and  $\text{C}_4\text{H}_7\text{O}_2^+$  ( $m/z$  87). The AMS measured signal at  $m/z$  60 has previously been employed as a tracer ion for biomass burning (Aiken et al., 2009; Cubison et al., 2011; Hennigan et al., 2011). However, Hennigan et al. (2010, 2011) showed that levoglucosan is semi-volatile and reacts with hydroxyl radicals in the gas phase at a non-trivial rate,

though as stated previously levoglucosan only accounts for a small portion of the signal at  $m/z$  60. To our knowledge, the effect of atmospheric aging on other ions derived from cellulose pyrolysis components during AMS analysis in the family of  $C_xH_yO_2$  has not yet been investigated. Thus, if one attempts to use  $m/z$  60 as a conserved POA tracer ion, it will prove difficult to quantify the contribution of biomass burning given that it will decay due to both oxidation and dilution. Furthermore, the initial concentrations of  $m/z$  60 in OA may depend on the fuel and/or combustion conditions.

Primary organic aerosol from combustion is typically characterized by chemically reduced fragments, such as  $m/z$  55 ( $C_4H_7^+$ ) and  $m/z$  57 ( $C_4H_9^+$ ) (Ulbrich et al., 2009). This is consistent with past investigations of emissions from fossil fuel combustion as well as biomass burning. Another POA ion of interest is the signal at  $m/z$  95,  $C_7H_{11}^+$ . Due to its large mass, it is less likely to have significant interference from SOA, as this could only come from secondary molecules with a long ( $C_7$ ) aliphatic component. A general trend observed in AMS measurements is the loss of larger organic ions as the oxidation of the OA increases (Canagaratna et al., 2015).

Figure 2.2d & e show difference spectra of the fresh and aged aerosol before and after passing through a 90 °C thermodenuder. These mass spectra are normalized to the sum of their total OA ion signal before subtraction, as thermophoresis in the thermodenuder reduces particle transmission. The positive values represent ions from molecules that are relatively more abundant in the un-denuded spectra and thus more volatile, while the negative values represent ions from molecules relatively more abundant in the denuded aerosol's spectra and therefore less volatile. The signal at  $CO_2^+$  ( $m/z$  44) comes largely from compounds with very low volatility in both the unaged and aged organic aerosol. The signal from  $CO_2^+$  is greater in the aged than in the unaged OA, consistent with Figure 2.2c. The other significant SOA ion,  $C_2H_3O^+$  ( $m/z$  43), appears to be associated with molecules that are more volatile than those responsible for the  $CO_2^+$  fragment. Of the POA ions, the  $C_xH_y$  family appears to be less volatile than the  $C_xH_yO_2$  family. Again, this is consistent with the findings of Hennigan et al. (2011) regarding levoglucosan and the tracer ion  $m/z$  60. The  $C_7H_{11}^+$



( $m/z$  95) signal is associated with compounds with low volatility. It is therefore less likely to undergo gas-phase oxidation, and the relative contribution of  $C_7H_{11}^+$  to the organic aerosol mass spectrum ( $I_{C_7H_{11}}$ ) will only change due to either heterogeneous oxidation or the condensation of secondary material. We propose using this ion as a conserved POA tracer ion for biomass burning aerosol, which will allow for compositional changes to be normalized using the signal from  $C_7H_{11}^+$  ( $m/z$  95).

Figure 2.2f again shows the difference between the fresh and aged organic aerosol. However, unlike in Figure 2.2c, we have scaled the primary OA mass spectrum by the signal at  $C_7H_{11}^+$ . This allows us to correct for particle wall loss and changes in collection efficiency due to particle bounce in the AMS. In this panel, ions with positive signal likely come from SOA. The SOA includes significant oxidized ions besides  $C_2H_3O^+$  and  $CO_2^+$ , consistent with ambient observations of oxidized OA (OOA) (Ulbrich et al., 2009). Negative ions are shown on a separate axis in red that is 10x the scale. This shows that besides the condensation of SOA, there is potential for the oxidation of intermediate volatility compounds that may form more oxidized volatile organic compounds. These ions include  $C_2H_4O_2^+$ ,  $C_6H_5O_2^+$ ,  $C_6H_9^+$ , and  $C_8H_9^+$ . However, the change in mass is small, and thus we only focus on the POA mass volatilized based on the most drastically changing ion,  $C_2H_4O_2^+$  ( $m/z$  60).

### 2.3.2. Composition changes due to simulated atmospheric aging

#### 2.3.2.1. Specific ion changes with respect to a conserved POA tracer ion

The AMS provides both high mass resolution and high time resolution. In order to report changes in organic-aerosol composition with high time resolution, we correct for particle wall loss and potential changes in particle bounce in the AMS by normalizing ion signals to a conserved POA ion,  $C_7H_{11}^+$ . We show the changes in the OA mass spectrum relative to  $C_7H_{11}^+$  following UV illumination after HONO injection (Figure 2.3-1), and following ozone injection (Figure 2.3-2). We have also normalized each ion signal fraction ( $f$ ) by its initial value ( $f^t/f_i$ ), prior to any perturbation. The figures show the relative change in ion abundance as a result of

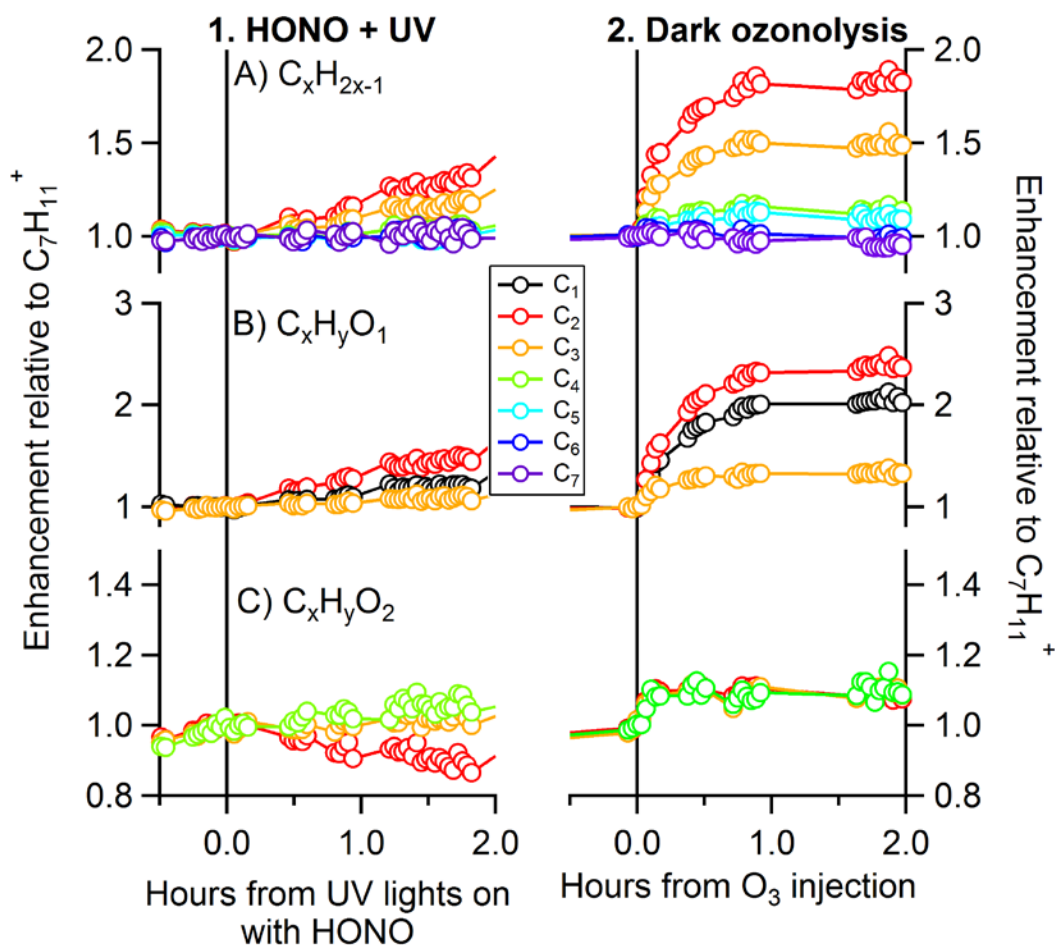


Figure 2.3. Changes in ion abundance relative to the POA-tracer ion,  $C_7H_{11}^+$ , before and after two types of simulated aging. Panel series 1 (left) shows the oxidation of black spruce smoke in the presence of HONO and UV lights. Panel series 2 (right) shows smoke from the same fire being exposed to ozone in the dark. Panels A) contain ions with the formula  $C_xH_{2x-1}$ , panels B) the formula  $C_xH_yO_1$  and panels C) the formula  $C_xH_yO_2$ , associated with the semi-volatile POA material. The greater concentrations of oxidants in the ozone aging case show a much more rapid production of SOA, and thus the  $C_xH_y$  and  $C_xH_yO_1$  ions increase rapidly. For the HONO experiment, we see a decrease in the  $C_2H_4O_2$  signal, consistent with the semi-volatile components becoming oxidized in the gas phase. However, the larger ions of  $C_xH_yO_2$  do not appear to change, suggesting they are less reactive or less volatile than the compounds that contribute to  $C_2H_4O_2$ .

the aging, and are grouped by the ion family. The a) panels show the changes in the aliphatic and aromatic derived  $C_xH_{2x-1}$  ions (typically associated with hydrocarbon-like OA (HOA), but also present in aged, oxidized OA (OOA)), the b) panels show the changes to the  $C_xH_yO$  ions, and the c) panels show the changes to the  $C_xH_yO_2$  ions, all relative to the conserved  $C_7H_{11}^+$  POA tracer.

Panel a in Figure 2.3 reveals an increase in  $C_xH_{2x-1}$  fragments relative to  $C_7H_{11}^+$  after both types of aging. If any VOCs are oxidized, resulting in condensation of SOA, those SOA products may fragment to form ions within this  $C_xH_{2x-1}$  family where  $x < 4$ . However, the ions  $C_6H_{11}^+$  and  $C_7H_{13}^+$  do not increase relative to  $C_7H_{11}^+$ . This suggests that the condensed SOA either produces fragments in equal proportion at all of these masses or instead that there is little or no contribution from SOA at any of these masses. Reference spectra for aged organic aerosol, as derived by positive matrix factorization, typically include very little contribution at higher  $m/z$ , and thus we believe that there is very little SOA contribution to  $C_7H_{11}^+$  (Ulbrich et al., 2009).

Panel b in Figure 2.3 shows the change in the singly oxygenated ions ( $C_xH_yO^+$ ) relative to  $C_7H_{11}^+$ . Both figures show an enhancement in CHO,  $C_2H_3O$ , and  $C_3H_5O$ . The experiment with  $\cdot OH$  aging from added HONO in Figure 2.3-1 shows a more gradual increase in the oxidized species compared to the ozone aging experiment in Figure 2.3-2. This is consistent with the trends observed for known SOA precursors such as monoterpenes. For ozone experiments the monoterpene signal decreases rapidly upon injection, whereas for  $\cdot OH$  oxidation experiments it is more gradual.

Panel c in Figure 2.3 shows the change in ions with two oxygen atoms ( $C_xH_yO_2^+$ ) relative to  $C_7H_{11}^+$ . We showed in panel c of Figure 2.2 that the ions of  $C_xH_yO_2^+$  are predominantly POA despite their high oxygen content as they are cellulose pyrolysis products, and more volatile than the compounds that resulted in  $C_xH_{2x-1}$  ions. For panel c in Figure 2.3-2, we see that there is

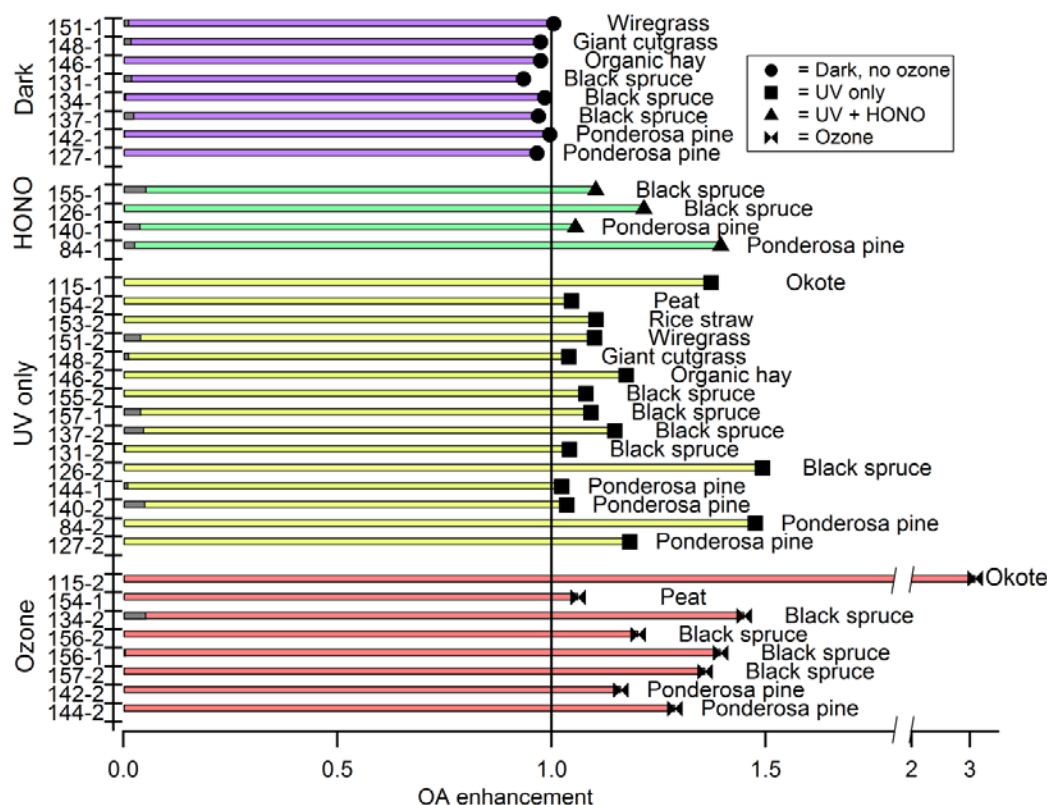


Figure 2.4 Calculated OA enhancements are plotted versus the FLAME-IV burn number (left column), and then the smog chamber number (#-1 or #-2). OA enhancements are grouped by the perturbation type, and then by fuel types. Non-coniferous canopy fuels are plotted first, and then black spruce, and ponderosa pine. SOA formation was calculated using  $f_{7H11+}$  as an indicator of new material condensing on the POA. The decrease in  $C_2H_4O_2^+$  relative to  $C_7H_{11}^+$  was used to estimate the mass of levoglucosan expected to have been volatilized from the particles. This is shown as a fraction of the initial OA mass as a grey bar in the column. In all cases this is very small.

some formation of SOA also contributing to the  $C_xH_yO_2$  family. This is consistent with the findings of Ortega et al. (2013), who observed enhancement of these ions using a photo-oxidation flow tube to age biomass-burning emissions. However, in panel c of Figure 2.3-1, the  $C_2H_4O_2^+$  ion appears to undergo gas-phase oxidation, and thus the ratio relative to  $C_7H_{11}^+$  decreases. This is consistent with the findings of Hennigan et al. (2010, 2011), who showed using gas chromatography that levoglucosan did react via gas-phase oxidation. If we assume that all wall-loss corrected  $C_2H_4O_2^+$  depletion

is due to the loss of levoglucosan, we can calculate the amount of total POA that was volatilized by using the reference spectrum of pure levoglucosan to estimate the other mass. This is shown as a fraction of the initial OA mass as gray bars in Figure 2.4. In all cases, the calculated mass loss due to evaporation of POA was less than 5% of the initial OA. However, the signals for the larger  $C_xH_yO_2^+$  ions follow the same trend as  $C_7H_{11}^+$ , and thus the ratio stays constant. This suggests that the compounds contributing to these ions are effectively non-volatile, or conceivably there is equivalent simultaneous production and loss of these compounds.

#### 2.3.2.2. Changes in characteristic AMS tracer ions

The ratio of characteristic AMS fragments to the total organic spectrum (expressed as  $f_{m/z}$ ) provides a useful comparison against ambient observations. Such ratios are plotted in Figure 2.5a & b. The green symbols indicate fresh emissions, and the red symbols indicate the OA after aging. Closed symbols are coniferous canopy fuels (i.e. black spruce and ponderosa pine), and open symbols are other fuels (e.g. grasses, peat, etc.) In panel a we plot  $f_{44}$  (mostly  $CO_2^+$ ) against  $f_{43}$  ( $C_3H_7^+$  and  $C_2H_3O^+$ ). The triangle indicates the portion of this space observed by Ng et al. (2010) for most ambient OA. They show that fresh emissions have a range of  $f_{43}$  values and relatively low  $f_{44}$ ; with increased atmospheric aging,  $f_{44}$  approaches a maximum of 0.3, and  $f_{43}$  converges to 0.035. We show the data from Hennigan et al. (2011) study of BBA aging from the FLAME-III study, with fresh OA plotted as black crosses, and aged OA plotted as blue circles. Consistent with FLAME-III OA, our smoke has low  $f_{43}$ , though it is somewhat higher than reported by Hennigan et al. Our fresh smoke also has low  $f_{44}$ , especially for the coniferous canopy fuels (i.e. Black Spruce and Ponderosa Pine). The grasses have a higher initial  $f_{44}$ , around 0.06. Peat smoke has a relatively low  $f_{44}$ , similar to that of coniferous-canopy smoke.

After oxidation, we observed an increase in both  $f_{44}$  and  $f_{43}$ . However, because we did not age our aerosol as long as Hennigan et al. did, our aged smoke also did not reach as high  $f_{44}$  values. Note that ozonolysis forms significantly more

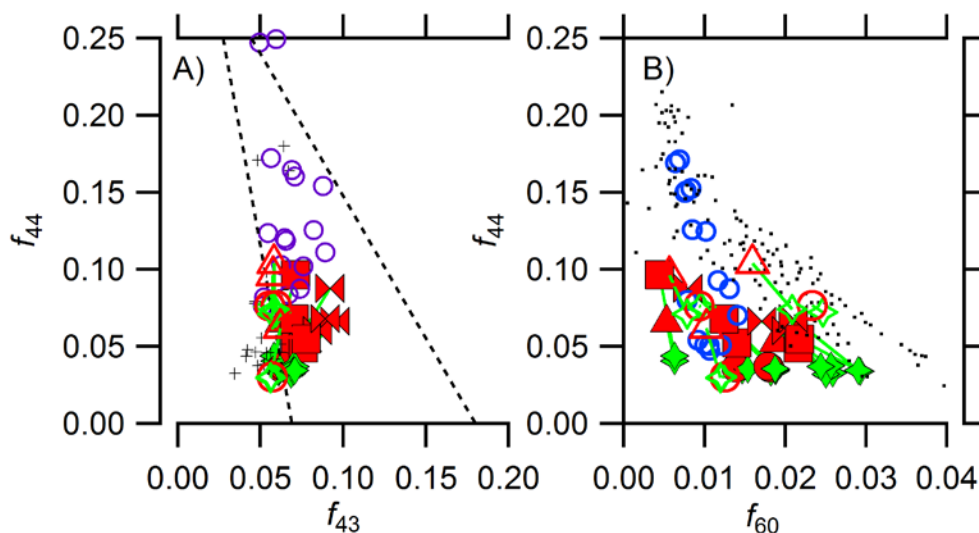


Figure 2.5 The ratio of certain AMS OA ion fragments to the total organic aerosol ion signal ( $f_i$ ) provide a useful comparison against ambient observations (dashed lines). In both panels, green symbols indicate emission prior to oxidation, and red indicates the OA after aging. Closed symbols are coniferous canopy fuels (i.e. Black Spruce and Ponderosa Pine), and the open symbols are the other fuels (e.g. grasses, peat, etc.). In panel a)  $f_{44}$  (OOA marker) is plotted against  $f_{43}$  (less oxidized). Consistent with Hennigan et al. (purple circles are aged experiments, black crosses are fresh emissions), the initial burns have relatively little  $f_{43}$  or  $f_{44}$ , but increase in both as a result of oxidation (Hennigan et al., 2011). In panel b) the OOA tracer  $f_{44}$  is plotted against the typical biomass-burning tracer  $f_{60}$ . Measurements of ambient biomass-burning plumes are shown for comparison. Data from Cubison et al. (2011) is shown as black dots and the data from Aiken et al. (2010) are shown as blue circles.

total organic mass, and thus increases significantly in both  $f_{44}$  and  $f_{43}$ . In contrast,  $\cdot\text{OH}$  oxidation driven by the UV lights and HONO photolysis increases  $f_{44}$  relatively more, and the slope of the  $\cdot\text{OH}$  oxidation experiments (triangles and squares) in Figure 2.5a reflects this.

In Figure 2.5b we plot the OOA tracer  $f_{44}$  against the biomass-burning tracer  $f_{60}$  (Cubison et al., 2011; Hennigan et al., 2011). Coniferous-canopy fuels produced a wide range of initial  $f_{60}$  values. Although we conducted replicate burns of similar fuels,

even those show a wide range of initial  $f_{60}$  values. POA from coniferous-canopy fuels span a range from 0.005 to 0.03 in initial  $f_{60}$ , suggesting that fire-to-fire variability is more important than the fuel with respect to initial  $f_{60}$  values. However, in all cases, aging of biomass-burning OA causes  $f_{44}$  to increase and  $f_{60}$  to decrease. This was most pronounced when significant SOA was formed, although dark control experiments also revealed a small decrease in  $f_{60}$  as well, potentially due to absorption of gas-phase levoglucosan into the Teflon chamber walls, which would promote further evaporation of POA.

### 2.3.3. Determining the SOA mass produced during an aging experiment

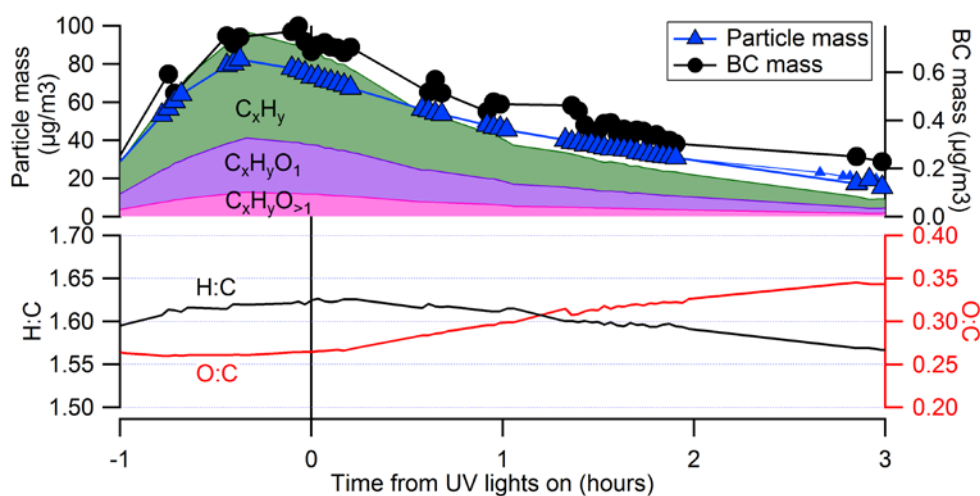


Figure 2.6 Particle mass and composition measurements during a typical BBOA aging experiment. Smoke from black spruce was aged using UV lights with no added oxidant (157-1 from Table 2.1). Total particle mass (blue triangles) is calculated from the particle volume determined by the SMPS assuming a density of  $1.3 \text{ g cm}^{-3}$ . Black carbon (black circles) was measured by the SP2. AMS measurements of particle organic carbon mass and OA chemical families are the solid filled traces. In all cases, particle mass increases when smoke is injected at  $t = -1$  hours, and then decreases around  $t = 0$  as particles begin to be lost to the chamber walls. The H:C and O:C elemental ratios of the OA derived from the AMS measurements are plotted in the lower panel.

We have already seen that the aging experiments resulted in significant SOA formation with a mass spectrum consistent with typical SOA mass spectra (Figure

2.2c). Next we would like to estimate the absolute production of SOA mass. Broadly, this requires quantification of SOA condensation to two reservoirs – suspended particles and the wall region (whether to wall deposited particles or to the Teflon itself) – and also the deposition of suspended SOA particulate mass to the walls. The process is conceptually straightforward but technically challenging (Matsunaga and Ziemann, 2010; Trump et al., 2016; Ye et al., 2016; Zhang et al., 2014). It involves quantifying both the total suspended OA mass concentration and changes to it and then attributing those changes to net condensation and the various wall losses. All measurements of the suspended OA concentration suffer from systematic challenges (e.g. unknown particle mixing state or morphology), which are amplified when determining differences, but we also have very precise measurements of the aerosol composition from the AMS. As much as possible we shall exploit those precise measurements.

Figure 2.6 shows mass and composition measurements of a typical biomass-burning aerosol aging experiment. After we start to inject the smoke at  $t = -1.0$  h, the BC mass concentration measured by the SP2 increases. After injection is complete, the BC mass decreases as particles are lost to the walls. The particle volume measured by the SMPS follows the same general trend. Using particle mobility diameter (from SMPS) and vacuum aerodynamic diameter (from AMS), one can calculate the average effective particle density (DeCarlo et al., 2004; Jayne et al., 2000). We use this effective density,  $\sim 1.3 \text{ g cm}^{-3}$ , to convert SMPS-determined integrated particle volume into total particle mass. The AMS-measured organic mass, separated into ion families as previously discussed, is also shown in Figure 2.6 and follows the same general trend. Since the particle mass is mostly organic material ( $\text{BC} < 10\%$  of total mass), one might expect a closer correlation between SMPS measured particle mass and AMS measured mass. However, although biomass-burning POA is typically assumed not to bounce off the AMS vaporizer (collection efficiency = 1.0), smog-chamber SOA and ambient OOA typically have been reported to have a particle bounce with a collection efficiency as low as 0.3 (Docherty et al., 2013; Robinson et al., 2016). This complicates the direct comparison of the SMPS-derived particle mass and the AMS-derived particle mass.



As all of the external corrections for wall loss have biases, we use the low-volatility, primary organic ion  $C_7H_{11}^+$  tracer we identified here as an internal standard for POA within the AMS mass spectrum (Hennigan et al., 2010; Heringa et al., 2011). This approach requires that we assume that the organic aerosol is homogeneous in composition (i.e.  $f_{C_7H_{11}}$  is independent of particle size) and that heterogeneous oxidation of the particles is slow. The consistent ratio of  $C_7H_{11}^+$  with the larger ( $C_x > 5$ )  $C_xH_{2x-1}$  ions supports the assumption that any contribution to  $C_7H_{11}^+$  from SOA is negligible (Figure 2.3a). We feel that the precision gained from removing the uncertainty in variable AMS collection efficiencies more than compensates for the smaller uncertainties associated with these assumptions regarding the  $C_7H_{11}^+$  POA tracer.

With an internal standard for non-volatile POA in the mass spectrum, we can precisely measure the relative amount of SOA condensed on the particles during an experiment. However, we must also account for any SOA that condenses directly onto the smog chamber walls. For each chamber experiment, we averaged data for each 5-minute interval defined by the switching period between the two smog chambers. We show an example of the SOA calculation in Figure 2.7 We calculate the amount of SOA condensed onto the remaining suspended particles for each interval based on the composition change. The change in the amount of SOA on the particles is defined in Equation. 2.2:

$$dSOA_{particles} = \left( \frac{Org(t) + Org(t-1)}{2} \right) * \left( \left( 1 - \frac{f_{C_7H_{11}}(t)}{f_{C_7H_{11}}(init)} \right) - \left( 1 - \frac{f_{C_7H_{11}}(t-1)}{f_{C_7H_{11}}(init)} \right) \right) \quad (2.2)$$

where  $dSOA_{particles}$  is the change in the amount of suspended SOA from time  $t$  relative to  $t-1$ , and  $Org$  is the organic aerosol mass concentration ( $\mu g\ m^{-3}$ ).  $f_{C_7H_{11}}(init)$  indicates the initial contribution of  $C_7H_{11}^+$  to the total OA signal, prior to

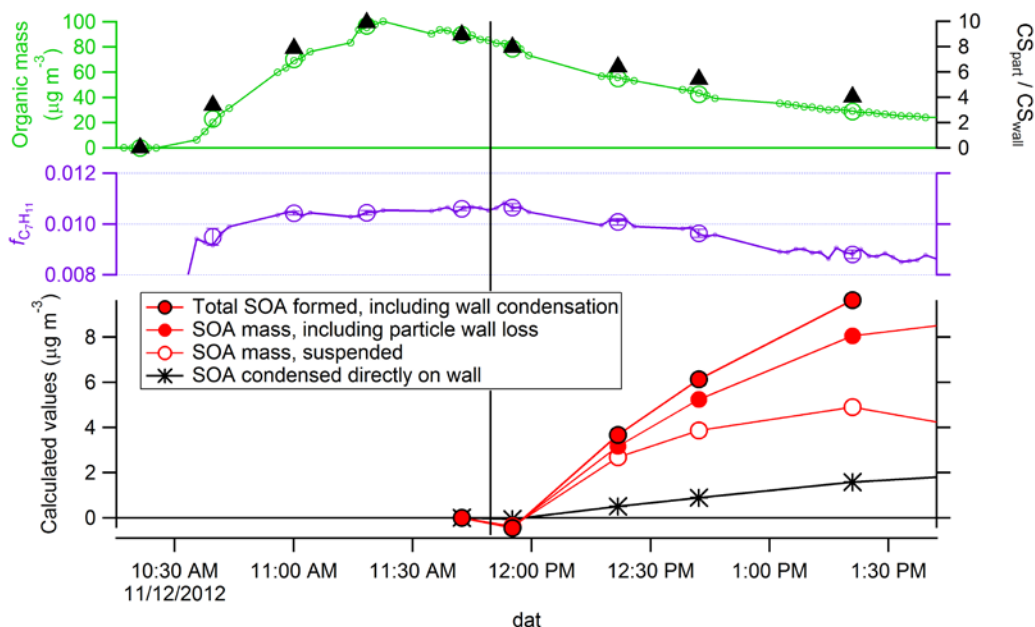


Figure 2.7 Measured and calculated values required for estimating the total SOA produced by accounting for SOA mass that is lost to the walls either by condensing directly or by deposition as a particle. The experiment shown as an example is the photooxidation of black spruce smoke (157-1 from Table 2.1). The top panel shows that injecting smoke causes an increase in organic aerosol (green circles), and also an increase in the ratio of the suspended condensation sink and the Teflon walls condensation sink (black triangles). The middle panel shows the evolution of the mass spectra, represented as the fraction of organic signal contributed by the ion  $\text{C}_7\text{H}_{11}^+$ ,  $f_{\text{C}_7\text{H}_{11}}$ . Once aging begins and SOA condenses (black vertical line),  $f_{\text{C}_7\text{H}_{11}}$  decreases. The final plot on the bottom shows the evolution of the SOA with time, described in Section 2.3.3.

aging, while  $f_{\text{C}_7\text{H}_{11}}(t)$  and  $f_{\text{C}_7\text{H}_{11}}(t-1)$  are its contribution at those two respective times. The integral of  $d\text{SOA}_{\text{particles}}$  is the total amount of SOA condensed on the particles, including particle wall loss. If we were to neglect vapor condensation directly to the walls, this would conclude the calculation; it is thus a lower limit to the total SOA production. This set of assumptions is referred to as the  $\omega = 0$  case in earlier work (Hennigan et al., 2011; Weitkamp et al., 2007), where  $\omega$  is the proportionality factor that describes the ability of vapors to partition to the walls and to particles. When  $\omega = 0$ , then condensable products only partition to suspended particles. When

there is perfect equilibrium between the bulk phase and the particles on the wall,  $\omega = 1$  (Weitkamp et al., 2007).

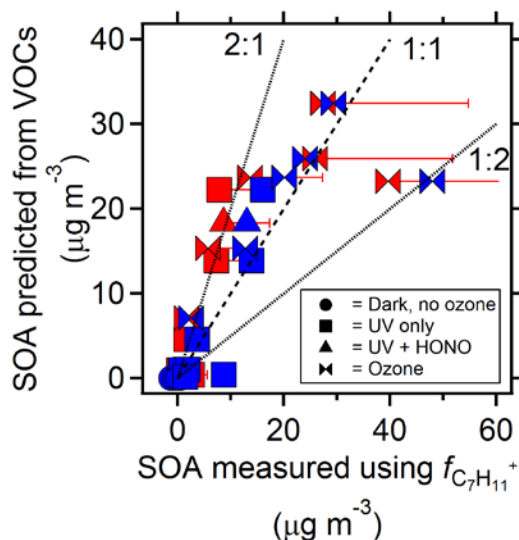


Figure 2.8. SOA mass predicted using speciated and scaled VOC measurements is plotted versus SOA mass observed in AMS measurements using the  $C_7H_{11}^+$  ( $m/z$  95) POA tracer. Blue symbols indicate SOA mass calculated assuming that particles on the wall are in equilibrium with the suspended particles. Red symbols indicate SOA mass calculated assuming an irreversible condensation sink on the wall of  $0.8 \text{ min}^{-1}$ . The error bars on the red points indicate the SOA mass that would result from assuming that after SOA condenses on the particle, the probability of a particle bouncing off the AMS vaporizer goes from 0 to 50%. Symbol shapes indicate the aging perturbation used in that experiment.

To estimate the amount of SOA condensed directly on the walls, we first need to know the collision frequency of vapors with the walls and with the suspended particles. We then calculate the loss frequency (the condensation sink) to each of those two reservoirs and assume that the condensation fluxes are proportional to those condensation sinks. This is accurate in the limit when the condensing vapors are effectively non-volatile, meaning that the saturation ratios are very high (Donahue et al., 2011b; Trump et al., 2016). For the walls, we assume that the condensation sink is the collision frequency and that the deposition is effectively irreversible, consistent with observations of semi-volatile organics (Krechmer et al.,

2016; Ye et al., 2016). For these chambers, based on the surface to volume ratio, that gives a constant wall condensation sink of  $8 \text{ min}^{-1}$  (McMurry and Grosjean, 1985). For the suspended particles, we need to know the Fuchs corrected surface area, modified by the mass accommodation coefficient (Saleh et al., 2013; Seinfeld J.H., 1998). After we stop injecting smoke and begin oxidation, the Fuchs corrected surface area increases as the particles grow, but decreases as the particles diffuse to the walls. We use the method described in Sinha et al. (2017), who found a mass accommodation coefficient of 0.3 for particles in FLAME-IV. We then calculate the mass of SOA condensation directly on the walls:

$$dSOA_{walls} = dSOA_{particles} * \frac{CS_{walls}}{CS_{particles}} \quad (2.3)$$

Equation 2.3 shows that when the suspended condensation sink is high, the contribution of the wall loss of SOA is very small relative to the total SOA produced. The average ratio of the condensation sink for suspended particles to the condensation sink of the Teflon walls for our experiments was 5, and thus the correction of vapors lost to the walls is small, typically 15% or less of  $dSOA_{particles}$ . Figure 2.8 also shows an upper-limit calculation for SOA produced. In this scenario, we assume that by partitioning through the gas phase, all suspended particles are in equilibrium with particles that have deposited on the walls (the  $\omega = 1$  case). We show the results of this assumption with blue markers in Figure 2.8. This assumption can increase the calculated SOA by about a factor of two, although it is unlikely that the very low volatility products would quickly reach equilibrium with the suspended phase, and thus we treat this as an upper limit for SOA production. With the wall condensation constrained, the sum of the SOA on the walls and the SOA condensed on the particles represents the total SOA formed from the oxidized VOCs in the smog chamber. We show contributions to each reservoir in Figure 2.7. It should also be noted that for these experiments a minimal amount of time was allowed between filling the chamber and perturbing it. This was to reduce the amount of semi-volatile vapors that would be absorbed into the Teflon walls.

### 2.3.4. OA enhancement from various fuels and perturbations

In Figure 2.4 we show the calculated OA enhancements for all the chamber experiments. We calculated the OA enhancements using Equation 2.4:

$$OA\ enhancement = \left( \frac{SOA + POA}{POA} \right) \quad (2.4)$$

Dark control experiments, where we injected the smoke into both smog chambers and then imposed no perturbation, show very little change in OA enhancement. There may be a small decrease in OA mass, consistent with what was observed in Figure 2.5 for  $f_{60}$ , but it is very small, and potentially within the precision of the method. Gray bars on the left of the OA enhancement indicate the calculated mass that would volatilize if the decrease in  $f_{60}$  was due to the volatilization of levoglucosan. This may explain some of the decreased OA enhancements for dark experiments. Broadly, the very small changes to the dark control experiments confirm the method and also the value of our novel dual-chamber experiments, as the null reference is available to compare the perturbed experiment to, for the same smoke simultaneously injected into both chambers (Tkacik et al., 2017).

For experiments where  $\cdot OH$  radicals were used to age the biomass-burning aerosol, we observed a modest OA enhancement consistent with the condensation of SOA. Even for a given fuel type (e.g. Ponderosa Pine) the enhancement was highly variable, again suggesting the importance of burn-to-burn variability. On average, experiments where ozone was added had a higher OA enhancement. In the presence of  $>500$  ppb of ozone, 66% of the measured monoterpene concentration had reacted after 1.5 hours. For an  $\cdot OH$  oxidation experiment, it took 3.8 hours to react away 66% of the measured monoterpenes. Thus for the ozone experiment, we would expect that more SOA precursors would have been oxidized after 1.5 hours.

While these OA enhancements are smaller than those reported by Hennigan et al. (2011) from FLAME-III, this is consistent with the lesser extent of aging employed during our FLAME-IV experiments that used a shorter total aging time. The OA enhancements reported by Hennigan et al. (2011) were at the end of the

experiments, after roughly 5 hours of oxidation. Our measurements report the state of aging after  $\sim 1.5$  hours. In some cases, another fire was started in the same room as our smog chambers, which was readily detected as a contamination source in our chambers. We discarded any contaminated data; all plots indicating “after aging” refer to  $\sim 1.5$  hours of aging for consistency.

### 2.3.5. Predicting the amount of SOA formed

Biomass combustion produces abundant volatile organic carbon (VOC) emissions in addition to primary organic aerosol. Some of these VOCs are the result of incomplete combustion (e.g. benzene, toluene, etc.) and some are present in the fuel itself and volatilized by the heat of combustion, but otherwise unaltered, (e.g. terpenoids) (Hays et al., 2002; Reid et al., 2005; Schauer et al., 2001). Regardless of their origin, some of these VOCs can be oxidized to produce SOA. Hatch et al. (2015) published the composition and abundance of over 400 volatile organic compounds for four of the fuels we used for our aging experiments, based on 2D-GC-MS analysis of cartridge samples from FLAME-IV. Although there may be variability in the total emissions from fire to fire, Hatch et al. showed that for two burns of the same fuel that the composition of the VOCs in the smoke was fairly consistent. Thus, we can use those speciated measurements for a given fuel and scale the absolute concentrations by the toluene measured in the chamber prior to aging as measured by our PTR-MS.

We also use the PTR-MS measurement of toluene to estimate the  $\cdot\text{OH}$  exposure after perturbation (Eqn. (2.1)) (Hennigan et al., 2011; Heringa et al., 2011). Using gas-phase rate constants for  $\cdot\text{OH}$  oxidation of a series of VOCs from Arey and Atkinson (2003), and following the guidelines of Hatch et al. (2015) where no rate constants were available for some VOCs, we calculated the fraction of individual VOCs oxidized for each experiment for that calculated  $\text{OH}$ . We followed the recommendation of Hatch et al. with respect to SOA yields resulting from each VOC's oxidation, and the full table of rate constants and assumed yields is available in the Supplemental Information. For ozonolysis experiments, we assumed compounds with carbon-carbon double bonds (principally monoterpenes) were all oxidized. One

important caveat of this method is the relatively slow reaction of terminal double bonds, present in two of the ten monoterpenes measured in these emissions. This terminal double carbon bond reacts  $\sim 30$  times slower with ozone than an internal double carbon bond (Atkinson and Arey, 2003). For black spruce emissions, camphene, which has a terminal double carbon bond, constitutes roughly 30% of the monoterpenes measured. PTR-MS measurements confirm that for ozonolysis experiments, the total monoterpene signal decreases rapidly before seeming to plateau at 30% of the initial signal, whereas our simplified model of the ozonolysis experiments predicts no monoterpene signal should remain. This may explain the slightly higher ratio of predicted vs. measured SOA mass for ozonolysis experiments, compared to the ratio of predicted vs. measured SOA mass for  $\cdot\text{OH}$  oxidation experiments. The effect of over predicting the amount of camphene reacted is small due to its relatively low SOA yield.

#### 2.3.5.1. Comparing mass of SOA formed to mass of SOA expected from VOC oxidation

In Figure 2.8 we compare the predicted and measured SOA mass for the various biomass-burning smog chamber experiments. We show the measured SOA for the  $\omega = 1$  scenario (blue) and the  $\omega = 0$  case with the wall-loss correction described in Section 2.3.3 (red). The error bars on the red markers indicate the possible SOA mass measured for a range of AMS collection efficiencies between 1 (marker) and 0.5 (error bar). The predicted SOA is on average higher than the observed SOA, but the uncertainty in the AMS collection efficiency spans the 1:1 line between measured and predicted SOA. This suggests that the majority of the SOA in these experiments was produced by the measured VOC SOA precursors, and that variability in the biomass-burning OA enhancement can be explained almost entirely by variability in those precursors rather than necessitating the inclusion of unmeasured species such as intermediate volatility organic compounds (Grieshop et al., 2008; Zhao et al., 2014). The variability ultimately relates to burn conditions and fuels.

## 2.3.5.2. Fuel dependent sources of SOA

## 2.3.5.2.1. Coniferous canopy fuels

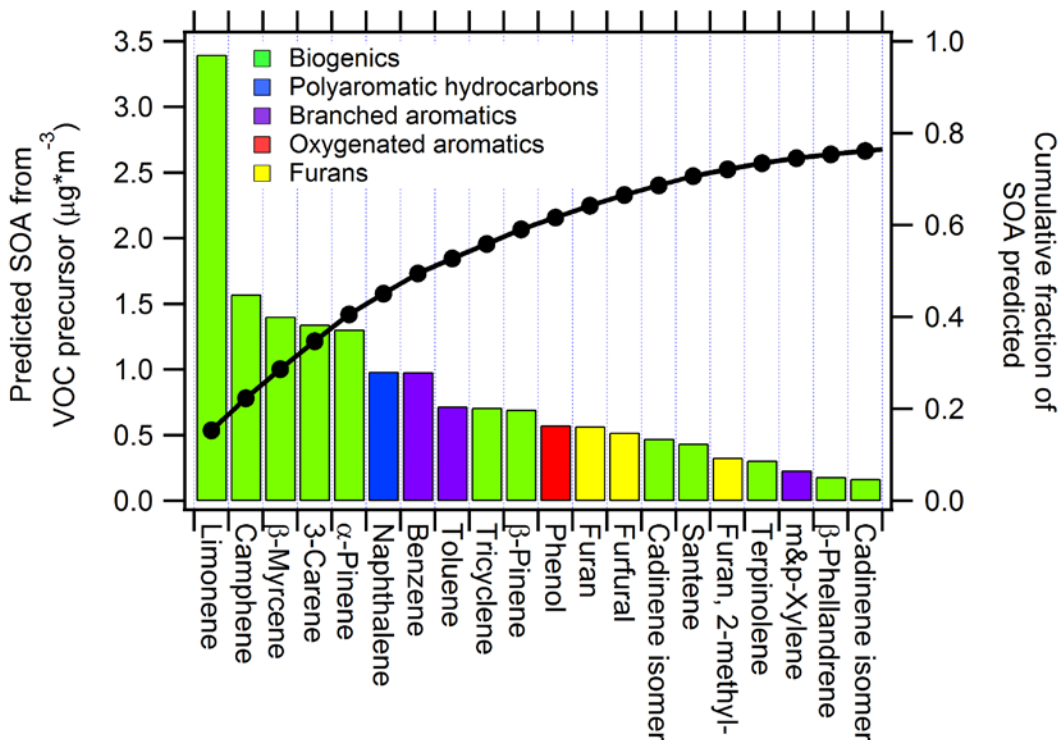


Figure 2.9. Predicted SOA mass using speciated VOC measurements, following the aging of black spruce smoke by  $\cdot\text{OH}$  oxidation. The colored bars show the absolute SOA mass. The right axis (black circles) shows the fraction of the cumulative SOA predicted to be formed,  $\sim 20 \mu\text{g m}^{-3}$ . Although only twenty VOC species are shown on the plot, over 400 total species were identified and quantified by Hatch et al. (2015).

We show the predicted SOA mass contribution of individual VOCs from a black-spruce smoke aging experiment in Figure 2.9. The precursors are colored by their types. Biogenic compounds (mostly terpenoids) are green, polyaromatic hydrocarbons are blue, branched aromatics are purple, oxygenated aromatics (including phenol and guaiacol) are red, and furans are yellow.



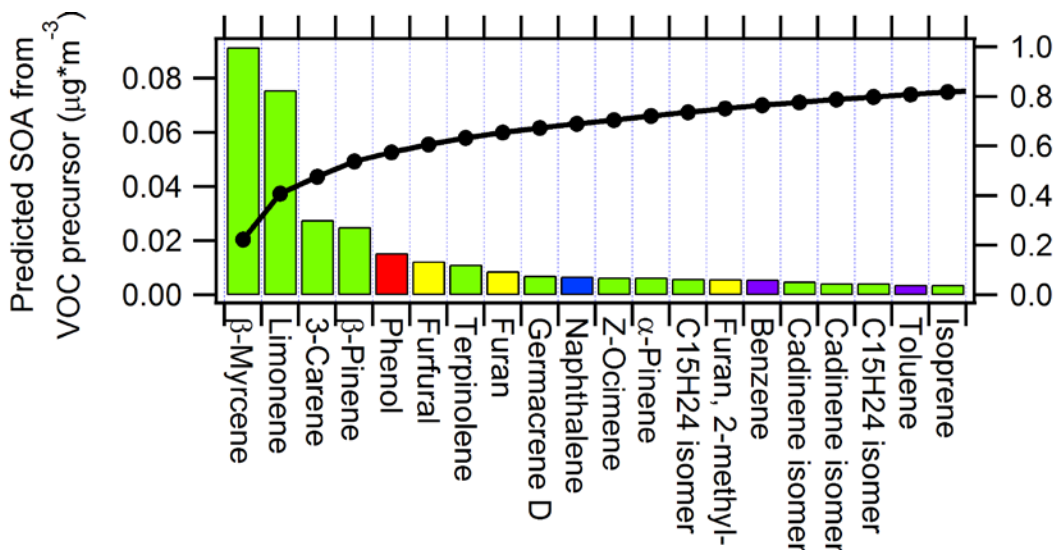


Figure 2.10. The cumulative SOA formed by each VOC for the aging of ponderosa pine smoke. The left axis is the cumulative SOA formed and the right shows the fraction of total SOA predicted. The coloring scheme is the same as in Figure 2.9.

The black traces show the same data but as a cumulative fraction, plotted on the right axis. More than 40% of the SOA produced is predicted to come from oxidation of monoterpenes. This stands in contrast to aging experiments by Bruns et al. (2016) and Tiitta et al. (2016) using logwood smoke from a residential woodstove. They observed good agreement between measured SOA mass and predictions based on the oxidation of mostly pyrogenic VOCs, i.e. benzene, naphthalene, and toluene. Tiitta et al. and Bruns et al. studied a more controlled form of combustion and burned only dried hardwood, and they did not observe any monoterpene emissions. Thus, we show that in considering coniferous fuels in wild or prescribed open burning conditions, the emissions from monoterpenes are critical for predicting the SOA formation potential. It is also possible that the monoterpenes evaporated from the hardwood studied by Bruns et al. during drying; the resulting SOA would be part of the life-cycle SOA production from the burning process much as fugitive emissions from vehicle fuels is part of the lifecycle emissions associated with transportation (Burnham et al., 2012; Curran, 2006).

The 2D-GC measurements of the smoke emissions allowed Hatch et al. to identify a dozen specific monoterpenes. In contrast, other experiments measuring monoterpenes using only PTR-MS measurements can only determine the total amount of monoterpenes without speciation, and must make assumptions about speciation and thus their reactivity with  $\cdot\text{OH}$  and  $\text{O}_3$  and their SOA yields. Grieshop et al. (2008) represented all of the monoterpenes as  $\alpha$ -pinene. We assessed this simplification by comparing the SOA predicted from our speciated measurements with the SOA predicted when representing all of the monoterpenes as  $\alpha$ -pinene. Our detailed model predicts that  $\alpha$ -pinene is responsible for less than one-quarter of the monoterpene-derived SOA; however, the net effect of representing all monoterpenes as  $\alpha$ -pinene is relatively small. For the  $\cdot\text{OH}$  oxidation experiments, the simplified model gives 6% less SOA mass than the fully speciated model that uses the 2D-GC measurements. For the ozonolysis experiments, the simplified model gives 15% more SOA mass.

Figure 2.9 also shows that combustion products, classified as substituted aromatics and polyaromatic hydrocarbons, are the next largest contributor to the SOA after biogenic compounds. However, their contribution is small relative to the monoterpenes. Not shown on this plot are the other 350+ VOCs that were quantified by 2D-GC and modelled. At least 75 VOCs are needed to explain 90% of the SOA mass formed.

Figure 2.10 shows a similar distribution of SOA precursors for ponderosa-pine smoke. More than 50% of the SOA formed was due to monoterpenes. Although other work has suggested that ponderosa pine produces more VOCs and therefore is likely to generate more SOA than black spruce, we observed a large degree of variability in the total amount of VOCs emitted from both fuels (Hennigan et al., 2011; Stockwell et al., 2013).

## 2.3.5.2.2. Wiregrass

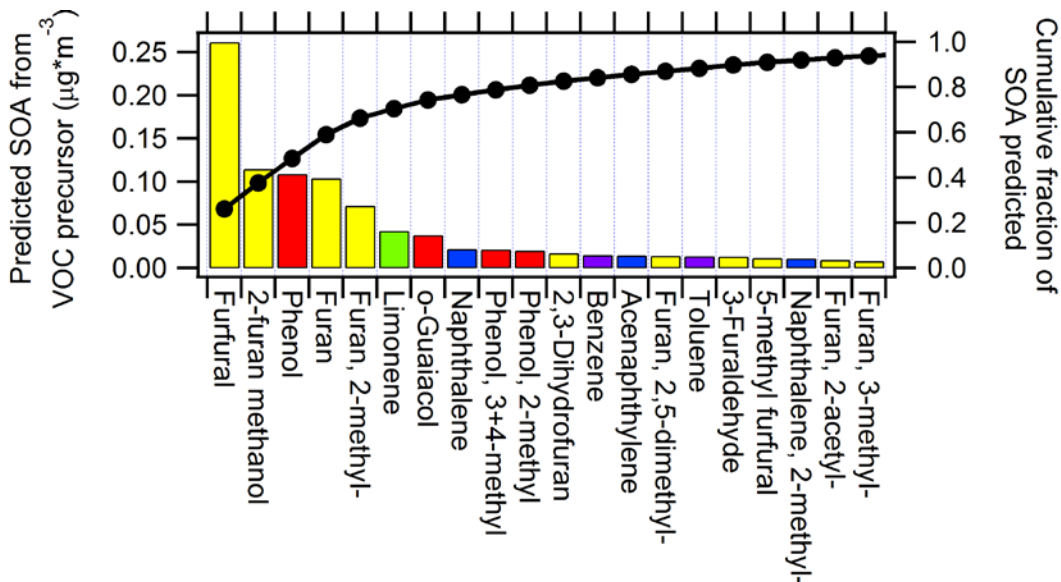


Figure 2.11. The cumulative SOA formed by each VOC for the aging of wiregrass smoke. The left axis is the cumulative SOA formed and the right shows the fraction of total SOA predicted. The coloring scheme is the same as in Figure 2.9.

We observed very little SOA production from the aging of smoke from wiregrass. In Figure 2.11 we show the VOC-specific and cumulative SOA formed from the modeled aging of wiregrass smoke, using the same convention as Figure 2.9 described in Section 2.3.5.2.1. We predict just  $1 \mu\text{g m}^{-3}$  of SOA compared to  $15 \mu\text{g m}^{-3}$  from Black Spruce smoke. This is likely due to a combination of smaller emission rates and variable amounts of total smoke injected. Monoterpenes are much less abundant in wiregrass smoke, and so contribute much less to SOA production compared to the coniferous canopy smoke. Consequently, oxygenated aromatics are relatively more important. The oxygenated aromatics are likely the product of cellulose combustion. Cellulose is a naturally occurring polymer and its structure includes many oxygenated aromatic groups (Pettersen, 1984). The combustion of this cellulose may also contribute to the large amount of furans apparent in Figure 2.11 (Paine et al., 2008).

## 2.3.6. Trends in oxidized VOCs with aging

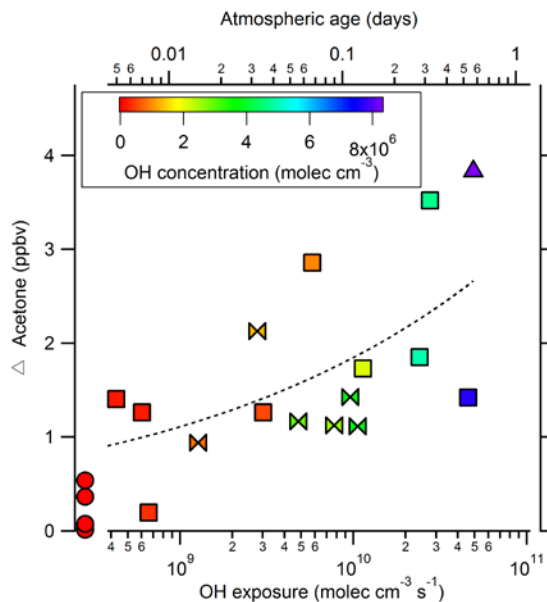


Figure 2.12. The difference in acetone concentrations measured by the PTR-MS before and after aging correlates well with  $\cdot\text{OH}$  exposure.  $\cdot\text{OH}$  concentration was calculated using the decay of toluene and a pseudo-first order reaction rate law. An offset exponential function was fit to guide the eye: the change in acetone concentration as a result of aging (ppbv) =  $0.126 + 0.00637 \cdot [\text{OH exposure}]^{0.243}$ .

In addition to the SOA precursors, we also measured the production of small oxidized VOCs that do not form SOA. Figure 2.12 shows the increase in acetone that resulted from the aging of biomass-burning aerosol as a function of  $\cdot\text{OH}$  exposure. The markers are colored by the calculated  $\cdot\text{OH}$  concentration and the marker shapes indicate the type of perturbation in the smog chamber. There is a strong positive correlation between  $\cdot\text{OH}$  exposure and the increase in acetone measured by the PTR-MS. This suggests that regardless of fuel, there is a consistent production of acetone when biomass-burning smoke is aged by  $\cdot\text{OH}$  radicals. This correlation in acetone enhancement is notable in part due to the lack of correlation we observed comparing  $\cdot\text{OH}$  exposure to other oxidized VOCs measured by the PTR-MS, including methanol, formaldehyde, or acetaldehyde. Oxidized VOCs have previously been proposed as an

indicator for SOA formation, however this work shows a strong correlation with  $\cdot\text{OH}$  exposure, rather than SOA formation (Lee et al., 2006). Our observations are consistent with recent work that shows that acetone is formed due to photodegradation of SOA. However, dark ozonolysis experiments also generated some acetone, consistent with SOA formation also having acetone as a by-product (Malecha and Nizkorodov, 2016).

## 2.4. Conclusions

Measurements of organic aerosol mass enhancement in ambient biomass-burning plumes are highly variable. We investigated SOA formation and multi-phase POA oxidation in smoke from the open burning of various whole biofuels, using aging experiments conducted in a dual smog chamber system. We have found that in the controlled environment of a smog chamber, the OA enhancement following aging of the smoke can be predicted using a fuel-specific VOC inventory that is scaled to the toluene concentration on a fire-by-fire basis. We did not observe significant mass loss associated with POA volatilization in these experiments. Multi-phase oxidation of POA contributed only a small fraction of the total OA mass or composition change, however evaporation that may have occurred when injecting smoke into the smog chambers was not measured.

We also found that for coniferous-canopy smoke, biogenic VOCs were significant precursors for SOA production. This is in contrast to the findings of Bruns et al. (2016) and Tiitta et al. (2016), who could predict the SOA formation from aged wood-burning emissions using mostly pyrogenic VOCs. Inclusion of the less volatile IVOCs (besides sesquiterpenes) was not required to obtain good agreement between the predicted and measured OA enhancement, only using more volatile VOCs measured by PTR-MS. Our results show that open-burning biofuel emissions require a more careful investigation of biogenic VOCs innate to the fuel. Given that most of the OA enhancement in aging smoke plumes can be explained by oxidation of well-studied biogenic VOC SOA precursors, we propose that future work should focus on VOC emission profiles. Identifying parameterizations for VOC emission profiles of

open-burning biofuels under different combustion conditions is likely the best way to predict OA enhancement of smoke plumes in ambient measurements and in dynamically evolving smoke plumes.

## 2.5. References

- Aiken, A. C., Salcedo, D., Cubison, M. J., Huffman, J. A., DeCarlo, P. F., Ulbrich, I. M., Docherty, K. S., Sueper, D., Kimmel, J. R., Worsnop, D. R., Trimborn, A., Northway, M., Stone, E. A., Schauer, J. J., Volkamer, R. M., Fortner, E., de Foy, B., Wang, J., Laskin, A., Shutthanandan, V., Zheng, J., Zhang, R., Gaffney, J., Marley, N. A., Paredes-Miranda, G., Arnott, W. P., Molina, L. T., Sosa, G. and Jimenez, J. L.: Mexico City aerosol analysis during MILAGRO using high resolution aerosol mass spectrometry at the urban supersite (T0) – Part 1: Fine particle composition and organic source apportionment, *Atmos. Chem. Phys.*, 9(17), 6633–6653, doi:10.5194/acp-9-6633-2009, 2009.
- Aiken, A. C., de Foy, B., Wiedinmyer, C., DeCarlo, P. F., Ulbrich, I. M., Wehrli, M. N., Szidat, S., Prevot, A. S. H., Noda, J., Wacker, L., Volkamer, R., Fortner, E., Wang, J., Laskin, A., Shutthanandan, V., Zheng, J., Zhang, R., Paredes-Miranda, G., Arnott, W. P., Molina, L. T., Sosa, G., Querol, X. and Jimenez, J. L.: Mexico city aerosol analysis during MILAGRO using high resolution aerosol mass spectrometry at the urban supersite (T0) – Part 2: Analysis of the biomass burning contribution and the non-fossil carbon fraction, *Atmos. Chem. Phys.*, 10(12), 5315–5341, doi:10.5194/acp-10-5315-2010, 2010.
- Akagi, S. K., Yokelson, R. J., Wiedinmyer, C., Alvarado, M. J., Reid, J. S., Karl, T., Crounse, J. D. and Wennberg, P. O.: Emission factors for open and domestic biomass burning for use in atmospheric models, *Atmos. Chem. Phys.*, 11(9), 4039–4072, doi:10.5194/acp-11-4039-2011, 2011.
- Akagi, S. K., Craven, J. S., Taylor, J. W., McMeeking, G. R., Yokelson, R. J., Burling, I. R., Urbanski, S. P., Wold, C. E., Seinfeld, J. H., Coe, H., Alvarado, M. J. and Weise, D. R.: Evolution of trace gases and particles emitted by a chaparral fire in California, *Atmos. Chem. Phys.*, 12(3), 1397–1421, doi:10.5194/acp-12-1397-2012, 2012.
- Atkinson, R. and Arey, J.: Atmospheric degradation of volatile organic compounds., *Chem. Rev.*, 103(12), 4605–38, doi:10.1021/cr0206420, 2003.
- Bond, T. C., Doherty, S. J., Fahey, D. W., Forster, P. M., Berntsen, T., DeAngelo, B. J., Flanner, M. G., Ghan, S., Kärcher, B., Koch, D., Kinne, S., Kondo, Y., Quinn, P. K., Sarofim,

M. C., Schultz, M. G., Schulz, M., Venkataraman, C., Zhang, H., Zhang, S., Bellouin, N., Guttikunda, S. K., Hopke, P. K., Jacobson, M. Z., Kaiser, J. W., Klimont, Z., Lohmann, U., Schwarz, J. P., Shindell, D., Storelvmo, T., Warren, S. G. and Zender, C. S.: Bounding the role of black carbon in the climate system: A scientific assessment, *J. Geophys. Res. Atmos.*, 118(11), 5380–5552, doi:10.1002/jgrd.50171, 2013.

Bruns, E. A., El Haddad, I., Slowik, J. G., Kilic, D., Klein, F., Baltensperger, U. and Prévôt, A. S. H.: Identification of significant precursor gases of secondary organic aerosols from residential wood combustion, *Sci. Rep.*, 6, 27881, doi:10.1038/srep27881, 2016.

Burnham, A., Han, J., Clark, C. E., Wang, M., Dunn, J. B. and Palou-Rivera, I.: Life-Cycle Greenhouse Gas Emissions of Shale Gas, Natural Gas, Coal, and Petroleum, *Environ. Sci. Technol.*, 46(2), 619–627, doi:10.1021/es201942m, 2012.

Canagaratna, M. R., Jimenez, J. L., Kroll, J. H., Chen, Q., Kessler, S. H., Massoli, P., Hildebrandt Ruiz, L., Fortner, E., Williams, L. R., Wilson, K. R., Surratt, J. D., Donahue, N. M., Jayne, J. T. and Worsnop, D. R.: Elemental ratio measurements of organic compounds using aerosol mass spectrometry: characterization, improved calibration, and implications, *Atmos. Chem. Phys.*, 15(1), 253–272, doi:10.5194/acp-15-253-2015, 2015.

Chhabra, P. S., Flagan, R. C. and Seinfeld, J. H.: Elemental analysis of chamber organic aerosol using an aerodyne high-resolution aerosol mass spectrometer, *Atmos. Chem. Phys.*, 10(9), 4111–4131, doi:10.5194/acp-10-4111-2010, 2010.

Cubison, M. J., Ortega, A. M., Hayes, P. L., Farmer, D. K., Day, D., Lechner, M. J., Brune, W. H., Apel, E., Diskin, G. S., Fisher, J. A., Fuelberg, H. E., Hecobian, A., Knapp, D. J., Mikoviny, T., Riemer, D., Sachse, G. W., Sessions, W., Weber, R. J., Weinheimer, A. J., Wisthaler, A. and Jimenez, J. L.: Effects of aging on organic aerosol from open biomass burning smoke in aircraft and laboratory studies, *Atmos. Chem. Phys.*, 11(23), 12049–12064, doi:10.5194/acp-11-12049-2011, 2011.

Curran, M. A.: US EPA Life Cycle Assessment: Principles and Practice, Paper No. EPA/600/R-06/060, Cincinnati, US, 2006.



Decarlo, P. F., Kimmel, J. R., Trimborn, A., Northway, M. J., Jayne, J. T., Aiken, A. C., Gonin, M., Fuhrer, K., Horvath, T., Docherty, K. S., Worsnop, D. R. and Jimenez, J. L.: Field-deployable, high-resolution, time-of-flight aerosol mass spectrometer, *Anal. Chem.*, 78(24), 8281–8289, doi:10.1029/2001JD001213, 2006.

DeCarlo, P. F., Slowik, J. G., Worsnop, D. R., Davidovits, P. and Jimenez, J. L.: Particle Morphology and Density Characterization by Combined Mobility and Aerodynamic Diameter Measurements. Part 1: Theory, *Aerosol Sci. Technol.*, 38(12), 1185–1205, doi:10.1080/027868290903907, 2004.

Docherty, K. S., Jaoui, M., Corse, E., Jimenez, J. L., Offenberg, J. H., Lewandowski, M. and Kleindienst, T. E.: Collection Efficiency of the Aerosol Mass Spectrometer for Chamber-Generated Secondary Organic Aerosols, *Aerosol Sci. Technol.*, 47, 294–309, doi:10.1080/02786826.2012.752572, 2013.

Donahue, N. M., Robinson, A. L., Stanier, C. O. and Pandis, S. N.: Coupled Partitioning, Dilution, and Chemical Aging of Semivolatile Organics, *Environ. Sci. Technol.*, 40(8), 2635–2643, doi:10.1021/es052297c, 2006.

Donahue, N. M., Robinson, A. L. and Pandis, S. N.: Atmospheric organic particulate matter: From smoke to secondary organic aerosol, *Atmos. Environ.*, 43(1), 94–106, doi:10.1016/j.atmosenv.2008.09.055, 2009.

Donahue, N. M., Epstein, S. A., Pandis, S. N. and Robinson, A. L.: A two-dimensional volatility basis set: 1. organic-aerosol mixing thermodynamics, *Atmos. Chem. Phys.*, 11(7), 3303–3318, doi:10.5194/acp-11-3303-2011, 2011a.

Donahue, N. M., Trump, E. R., Pierce, J. R. and Riipinen, I.: Theoretical constraints on pure vapor-pressure driven condensation of organics to ultrafine particles, *Geophys. Res. Lett.*, 38(16), n/a–n/a, doi:10.1029/2011GL048115, 2011b.

Donahue, N. M., Chuang, W., Epstein, S. A., Kroll, J. H., Worsnop, D. R., Robinson, A. L., Adams, P. J., Pandis, S. N., Kroll, J. H., Donahue, N. M., Jimenez, J. L., Kessler, S., Canagaratna, M. R., Wilson, K., Alteri, K. E., Mazzoleni, L. R., Wozniak, A. S., Bluhm, H., Mysak, E. R., Smith, J. D., Kolb, C. E., Worsnop, D. R., Guenther, A. B., Jiang, X., Heald, C. L., Sakulyanontvittaya, T., Duhl, T., Emmons, L. K., Wang, X., Kamens, R., Jeffries, H.,

Gery, M., Wiener, R., Sexton, K., Howe, G., Jeffries, H., Tonnesen, S., Kamens, R. M., Jaoui, M., Vizuete, W., Jeffries, H. E., Tesche, T. W., Olaguer, E. P., Couzo, E., Atkinson, R., Prinn, R., Huang, J., Weiss, R., Cunnold, D., Fraser, P., Simmonds, P., McCulloch, A., Harth, C., Reimann, S., Salameh, P., O'Doherty, S., Wang, R., Porter, L., Miller, B., Krummel, P., Goldstein, A. H., Galbally, I. E., Aumont, B., Szopa, S., Madronich, S., Donahue, N. M., Epstein, S. A., Pandis, S. N., Robinson, A. L., Donahue, N. M., Kroll, J. H., Robinson, A. L., Pandis, S. N., Zobrist, B., Marcolli, C., Pedernera, D. A., Koop, T., Virtanen, A., Joutsensaari, J., Koop, T., Kannosto, J., Yli-Pirila, P., Leskinen, J., Makela, J. M., Holopainen, J. K., Poeschl, U., Kulmala, M., Worsnop, D. R., Laaksonen, A., Koop, T., Bookhold, J., Shiraiwa, M., Poeschl, U., Vaden, T. D., Imre, D., Ber'aneek, J., Shrivastava, M., Zelenyuk, A., Shiraiwa, M., et al.: Why do organic aerosols exist? Understanding aerosol lifetimes using the two-dimensional volatility basis set, *Environ. Chem.*, 10(3), 151, doi:10.1071/EN13022, 2013.

Farmer, D. K., Matsunaga, A., Docherty, K. S., Surratt, J. D., Seinfeld, J. H., Ziemann, P. J. and Jimenez, J. L.: Response of an aerosol mass spectrometer to organonitrates and organosulfates and implications for atmospheric chemistry, *Proc. Natl. Acad. Sci.*, 107(15), 6670–6675, doi:10.1073/pnas.0912340107, 2010.

Grieshop, A. P., Logue, J. M., Donahue, N. M. and Robinson, A. L.: Laboratory investigation of photochemical oxidation of organic aerosol from wood fires – Part 1: Measurement and simulation of organic aerosol evolution, *Atmos. Chem. Phys. Discuss.*, 8(4), 15699–15737, doi:10.5194/acpd-8-15699-2008, 2008.

Grieshop, A. P., Donahue, N. M. and Robinson, A. L.: Laboratory investigation of photochemical oxidation of organic aerosol from wood fires 2: analysis of aerosol mass spectrometer data, *Atmos. Chem. Phys.*, 9(6), 2227–2240, doi:10.5194/acp-9-2227-2009, 2009.

Hatch, L. E., Luo, W., Pankow, J. F., Yokelson, R. J., Stockwell, C. E. and Barsanti, K. C.: Identification and quantification of gaseous organic compounds emitted from biomass burning using two-dimensional gas chromatography–time-of-flight mass

spectrometry, *Atmos. Chem. Phys.*, 15(4), 1865–1899, doi:10.5194/acp-15-1865-2015, 2015.

Hays, M. D., Geron, C. D., Linna, K. J., Smith, N. D. and Schauer, J. J.: Speciation of Gas-Phase and Fine Particle Emissions from Burning of Foliar Fuels, *Environ. Sci. Technol.*, 36(11), 2281–2295, doi:10.1021/es0111683, 2002.

Helmig, D., Revermann, T., Pollmann, J., Kaltschmidt, O., Jiménez Hernández, A., Bocquet, F. and David, D.: Calibration system and analytical considerations for quantitative sesquiterpene measurements in air, *J. Chromatogr. A*, 1002(1), 193–211, doi:10.1016/S0021-9673(03)00619-8, 2003.

Hennigan, C. J., Sullivan, A. P., Collett, J. L. and Robinson, A. L.: Levoglucosan stability in biomass burning particles exposed to hydroxyl radicals, *Geophys. Res. Lett.*, 37(9), 2–5, doi:10.1029/2010GL043088, 2010.

Hennigan, C. J., Miracolo, M. A., Engelhart, G. J., May, A. A., Presto, A. A., Lee, T., Sullivan, A. P., McMeeking, G. R., Coe, H., Wold, C. E., Hao, W.-M., Gilman, J. B., Kuster, W. C., de Gouw, J. A., Schichtel, B. A., Kreidenweis, S. M. and Robinson, A. L.: Chemical and physical transformations of organic aerosol from the photo-oxidation of open biomass burning emissions in an environmental chamber, *Atmos. Chem. Phys.*, 11(15), 7669–7686, doi:10.5194/acp-11-7669-2011, 2011.

Heringa, M. F., DeCarlo, P. F., Chirico, R., Tritscher, T., Dommen, J., Weingartner, E., Richter, R., Wehrle, G., Prévôt, A. S. H. and Baltensperger, U.: Investigations of primary and secondary particulate matter of different wood combustion appliances with a high-resolution time-of-flight aerosol mass spectrometer, *Atmos. Chem. Phys.*, 11(12), 5945–5957, doi:10.5194/acp-11-5945-2011, 2011.

Hildebrandt, L., Donahue, N. M. and Pandis, S. N.: High formation of secondary organic aerosol from the photo-oxidation of toluene, *Atmos. Chem. Phys.*, 9(9), 2973–2986, doi:10.5194/acp-9-2973-2009, 2009.

Jayne, J. T., Leard, D. C., Zhang, X., Davidovits, P., Smith, K. A., Kolb, C. E. and Worsnop, D. R.: Development of an Aerosol Mass Spectrometer for Size and Composition

Analysis of Submicron Particles, *Aerosol Sci. Technol.*, 33(1-2), 49-70, doi:10.1080/027868200410840, 2000.

Jimenez, J. L., Canagaratna, M. R., Donahue, N. M., Prevot, A. S. H., Zhang, Q., Kroll, J. H., DeCarlo, P. F., Allan, J. D., Coe, H., Ng, N. L., Aiken, A. C., Docherty, K. S., Ulbrich, I. M., Grieshop, A. P., Robinson, A. L., Duplissy, J., Smith, J. D., Wilson, K. R., Lanz, V. A., Hueglin, C., Sun, Y. L., Tian, J., Laaksonen, A., Raatikainen, T., Rautiainen, J., Vaattovaara, P., Ehn, M., Kulmala, M., Tomlinson, J. M., Collins, D. R., Cubison, M. J., Dunlea, J., Huffman, J. A., Onasch, T. B., Alfarra, M. R., Williams, P. I., Bower, K., Kondo, Y., Schneider, J., Drewnick, F., Borrmann, S., Weimer, S., Demerjian, K., Salcedo, D., Cottrell, L., Griffin, R., Takami, A., Miyoshi, T., Hatakeyama, S., Shimono, A., Sun, J. Y., Zhang, Y. M., Dzepina, K., Kimmel, J. R., Sueper, D., Jayne, J. T., Herndon, S. C., Trimborn, A. M., Williams, L. R., Wood, E. C., Middlebrook, A. M., Kolb, C. E., Baltensperger, U. and Worsnop, D. R.: Evolution of Organic Aerosols in the Atmosphere, *Science* (80-. ), 326(5959), 1525-1529, doi:10.1126/science.1180353, 2009.

Jolleys, M. D., Coe, H., McFiggans, G., Capes, G., Allan, J. D., Crosier, J., Williams, P. I., Allen, G., Bower, K. N., Jimenez, J. L., Russell, L. M., Grutter, M. and Baumgardner, D.: Characterizing the Aging of Biomass Burning Organic Aerosol by Use of Mixing Ratios: A Meta-analysis of Four Regions., *Environ. Sci. Technol.*, doi:10.1021/es302386v, 2012.

Krechmer, J. E., Pagonis, D., Ziemann, P. J. and Jimenez, J. L.: Quantification of Gas-Wall Partitioning in Teflon Environmental Chambers Using Rapid Bursts of Low-Volatility Oxidized Species Generated in Situ, *Environ. Sci. Technol.*, 50(11), 5757-5765, doi:10.1021/acs.est.6b00606, 2016.

Lee, A., Goldstein, A. H., Kroll, J. H., Ng, N. L., Varutbangkul, V., Flagan, R. C. and Seinfeld, J. H.: Gas-phase products and secondary aerosol yields from the photooxidation of 16 different terpenes, *J. Geophys. Res. Atmos.*, 111(17), 1-25, doi:10.1029/2006JD007050, 2006.

Lee, T., Sullivan, A. P., Mack, L., Jimenez, J. L., Kreidenweis, S. M., Onasch, T. B., Worsnop, D. R., Malm, W., Wold, C. E., Hao, W. M. and Collett, J. L.: Chemical Smoke

Marker Emissions During Flaming and Smoldering Phases of Laboratory Open Burning of Wildland Fuels, *Aerosol Sci. Technol.*, 44(9), i–v, doi:10.1080/02786826.2010.499884, 2010.

Malecha, K. T. and Nizkorodov, S. A.: Photodegradation of Secondary Organic Aerosol Particles as a Source of Small, Oxygenated Volatile Organic Compounds, *Environ. Sci. Technol.*, 50(18), 9990–9997, doi:10.1021/acs.est.6b02313, 2016.

Matsunaga, A. and Ziemann, P. J.: Gas-Wall Partitioning of Organic Compounds in a Teflon Film Chamber and Potential Effects on Reaction Product and Aerosol Yield Measurements, *Aerosol Sci. Technol.*, 44(10), 881–892, doi:10.1080/02786826.2010.501044, 2010.

May, A. A., Levin, E. J. T., Hennigan, C. J., Riipinen, I., Lee, T., Collett, J. L., Jimenez, J. L., Kreidenweis, S. M. and Robinson, A. L.: Gas-particle partitioning of primary organic aerosol emissions: 3. Biomass burning, *J. Geophys. Res. Atmos.*, 118(19), 11,327–11,338, doi:10.1002/jgrd.50828, 2013.

McMurry, P. H. and Grosjean, D.: Gas and aerosol wall losses in Teflon film smog chambers, *Environ. Sci. Technol.*, 19(12), 1176–1182, doi:10.1021/es00142a006, 1985.

Ng, N. L., Chhabra, P. S., Chan, A. W. H., Surratt, J. D., Kroll, J. H., Kwan, A. J., McCabe, D. C., Wennberg, P. O., Sorooshian, A., Murphy, S. M., Dalleska, N. F., Flagan, R. C. and Seinfeld, J. H.: Effect of NO<sub>x</sub> level on secondary organic aerosol (SOA) formation from the photooxidation of terpenes, *Atmos. Chem. Phys.*, 7(19), 5159–5174, doi:10.5194/acp-7-5159-2007, 2007.

Ng, N. L., Canagaratna, M. R., Zhang, Q., Jimenez, J. L., Tian, J., Ulbrich, I. M., Kroll, J. H., Docherty, K. S., Chhabra, P. S., Bahreini, R., Murphy, S. M., Seinfeld, J. H., Hildebrandt, L., Donahue, N. M., DeCarlo, P. F., Lanz, V. A., Prévôt, A. S. H., Dinar, E., Rudich, Y. and Worsnop, D. R.: Organic aerosol components observed in Northern Hemispheric datasets from Aerosol Mass Spectrometry, *Atmos. Chem. Phys.*, 10(10), 4625–4641, doi:10.5194/acp-10-4625-2010, 2010.

Ortega, A. M., Day, D. A., Cubison, M. J., Brune, W. H., Bon, D., de Gouw, J. A. and Jimenez, J. L.: Secondary organic aerosol formation and primary organic aerosol oxidation from biomass-burning smoke in a flow reactor during FLAME-3, *Atmos. Chem. Phys.*, 13(22), 11551–11571, doi:10.5194/acp-13-11551-2013, 2013.

Paine, J. B., Pithawalla, Y. B. and Naworal, J. D.: Carbohydrate pyrolysis mechanisms from isotopic labeling: Part 4. The pyrolysis of d-glucose: The formation of furans, *J. Anal. Appl. Pyrolysis*, 83(1), 37–63, doi:10.1016/j.jaap.2008.05.008, 2008.

Pankow, J. F., Luo, W., Melnychenko, A. N., Barsanti, K. C., Isabelle, L. M., Chen, C., Guenther, A. B. and Rosenstiel, T. N.: Volatilizable Biogenic Organic Compounds (VBOCs) with two dimensional Gas Chromatography-Time of Flight Mass Spectrometry (GC  $\times$  GC-TOFMS): sampling methods, VBOC complexity, and chromatographic retention data, *Atmos. Meas. Tech.*, 5, 345–361, doi:10.5194/amt-5-345-2012, 2012.

Petterson, R. C.: The chemical composition of wood, in *Chemistry of Solid Wood*, Adv. Chem. Series, 207, edited by R. Rowell, pp. 57–126, American Chemical Society, Washington DC., 1984.

Presto, A. A., Miracolo, M. A., Kroll, J. H., Worsnop, D. R., Robinson, A. L. and Donahue, N. M.: Intermediate-Volatility Organic Compounds: A Potential Source of Ambient Oxidized Organic Aerosol, *Environ. Sci. Technol.*, 43(13), 4744–4749, doi:10.1021/es803219q, 2009.

Reid, J. S. and Hobbs, P. V.: Physical and optical properties of young smoke from individual biomass fires in Brazil, *J. Geophys. Res. Atmos.*, 103(D24), 32013–32030, doi:10.1029/98JD00159, 1998.

Reid, J. S., Koppmann, R., Eck, T. F. and Eleuterio, D. P.: A review of biomass burning emissions part II: intensive physical properties of biomass burning particles, *Atmos. Chem. Phys.*, 5(3), 799–825, doi:10.5194/acp-5-799-2005, 2005.

Robinson, A. L., Donahue, N. M., Shrivastava, M. K., Weitkamp, E. A., Sage, A. M., Grieshop, A. P., Lane, T. E., Pierce, J. R. and Pandis, S. N.: Rethinking Organic Aerosols: Semivolatile Emissions and Photochemical Aging, *Science* (80-. ), 315(5816), 2007.

Robinson, E. S., Onasch, T. B., Worsnop, D. and Donahue, N. M.: Collection efficiency of alpha-pinene secondary organic aerosol particles explored via light scattering single particle aerosol mass spectrometry, *Atmos. Meas. Tech. Discuss.*, 1–29, doi:10.5194/amt-2016-271, 2016.

Sage, A. M., Weitkamp, E. A., Robinson, A. L. and Donahue, N. M.: Evolving mass spectra of the oxidized component of organic aerosol: results from aerosol mass spectrometer analyses of aged diesel emissions, *Atmos. Chem. Phys.*, 8(5), 1139–1152, doi:10.5194/acp-8-1139-2008, 2008.

Saleh, R., Donahue, N. M. and Robinson, A. L.: Time Scales for Gas-Particle Partitioning Equilibration of Secondary Organic Aerosol Formed from Alpha-Pinene Ozonolysis, *Environ. Sci. Technol.*, 47(11), 5588–5594, doi:10.1021/es400078d, 2013.

Saleh, R., Robinson, E. S., Tkacik, D. S., Ahern, A. T., Liu, S., Aiken, A. C., Sullivan, R. C., Presto, A. A., Dubey, M. K., Yokelson, R. J., Donahue, N. M. and Robinson, A. L.: Brownness of organics in aerosols from biomass burning linked to their black carbon content, *Nat. Geosci.*, 7(9), 647–650, doi:10.1038/ngeo2220, 2014.

Schauer, J. J., Kleeman, M. J., Cass, G. R. and Simoneit, B. R. T.: Measurement of Emissions from Air Pollution Sources. 3. C 1 –C 29 Organic Compounds from Fireplace Combustion of Wood, *Environ. Sci. Technol.*, 35(9), 1716–1728, doi:10.1021/es001331e, 2001.

Seinfeld J.H., P. S. N.: *Atmospheric Chemistry and Physics from Air Pollution to Climate Change*, 1998.

Simoneit, B. R. T., Schauer, J. J., Nolte, C. G., Oros, D. R., Elias, V. O., Fraser, M. P., Rogge, W. F. and Cass, G. R.: Levoglucosan, a tracer for cellulose in biomass burning and atmospheric particles, *Atmos. Environ.*, 33(2), 173–182, doi:10.1016/S1352-2310(98)00145-9, 1999.

Stockwell, C. E., Veres, P. R., Williams, J. and Yokelson, R. J.: Characterization of biomass burning smoke from cooking fires , peat , crop residue and other fuels with high resolution proton-transfer- reaction time-of-flight mass spectrometry, , 845–865, doi:10.5194/acp-15-845-2015, 2013.

Stockwell, C. E., Yokelson, R. J., Kreidenweis, S. M., Robinson, A. L., DeMott, P. J., Sullivan, R. C., Reardon, J., Ryan, K. C., Griffith, D. W. T. and Stevens, L.: Trace gas emissions from combustion of peat, crop residue, domestic biofuels, grasses, and other fuels: configuration and Fourier transform infrared (FTIR) component of the fourth Fire Lab at Missoula Experiment (FLAME-4), *Atmos. Chem. Phys.*, 14(18), 9727–9754, doi:10.5194/acp-14-9727-2014, 2014.

Stockwell, C. E., Veres, P. R., Williams, J. and Yokelson, R. J.: Characterization of biomass burning emissions from cooking fires, peat, crop residue, and other fuels with high-resolution proton-transfer-reaction time-of-flight mass spectrometry, *Atmos. Chem. Phys.*, 15(2), 845–865, doi:10.5194/acp-15-845-2015, 2015.

Sullivan, A. P., Holden, A. S., Patterson, L. A., Mcmeeking, G. R., Kreidenweis, S. M., Malm, W. C., Hao, W. M., Wold, C. E. and Collett, J. L.: A method for smoke marker measurements and its potential application for determining the contribution of biomass burning from wildfires and prescribed fires to ambient PM 2.5 organic carbon, *J. Geophys. Res.*, 113, doi:10.1029/2008JD010216, 2008.

Tiitta, P., Leskinen, A., Hao, L., Yli-Pirilä, P., Kortelainen, M., Grigonyte, J., Tissari, J., Lamberg, H., Hartikainen, A., Kuusalo, K., Kortelainen, A.-M., Virtanen, A., Lehtinen, K. E. J., Komppula, M., Pieber, S., Prévôt, A. S. H., Onasch, T. B., Worsnop, D. R., Czech, H., Zimmermann, R., Jokiniemi, J. and Sippula, O.: Transformation of logwood combustion emissions in a smog chamber: formation of secondary organic aerosol and changes in the primary organic aerosol upon daytime and nighttime aging, *Atmos. Chem. Phys.*, 16, 13251–13269, doi:10.5194/acp-16-13251-2016, 2016.

Tkacik, D. S., Robinson, E. S., Ahern, A. T., Saleh, R., Stockwell, C. E., Simpson, I., Meinardi, S., Blake, D. R., Yokelson, R. J., Presto, A. A., Sullivan, R. C., Donahue, N. M. and Robinson, A. L.: A dual-chamber enhancement method for quantifying effects of atmospheric perturbations on secondary organic aerosol formation from biomass burning emissions, *J. Geophys. Res.*, submitted 2017.



Trump, E. R., Epstein, S. A., Riipinen, I. and Donahue, N. M.: Wall effects in smog chamber experiments: A model study, *Aerosol Sci. Technol.*, 50(11), 1180–1200, doi:10.1080/02786826.2016.1232858, 2016.

Ulbrich, I. M., Canagaratna, M. R., Zhang, Q., Worsnop, D. R. and Jimenez, J. L.: Interpretation of organic components from Positive Matrix Factorization of aerosol mass spectrometric data, *Atmos. Chem. Phys.*, 9(9), 2891–2918, doi:10.5194/acp-9-2891-2009, 2009.

Weitkamp, E. a, Sage, A. M., Pierce, J. R., Donahue, N. M. and Robinson, A. L.: Organic Aerosol Formation from Photochemical Oxidation of Diesel Exhaust in a Smog Chamber, *Environ. Sci. Technol.*, 41(20), 6969–6975, doi:10.1021/es070193r, 2007.

Ye, P., Ding, X., Hakala, J., Hofbauer, V., Robinson, E. S. and Donahue, N. M.: Vapor wall loss of semi-volatile organic compounds in a Teflon chamber, *Aerosol Sci. Technol.*, 50(8), 822–834, doi:10.1080/02786826.2016.1195905, 2016.

Yokelson, R. J., Crounse, J. D., DeCarlo, P. F., Karl, T., Urbanski, S., Atlas, E., Campos, T., Shinozuka, Y., Kapustin, V., Clarke, A. D., Weinheimer, A., Knapp, D. J., Montzka, D. D., Holloway, J., Weibring, P., Flocke, F., Zheng, W., Toohey, D., Wennberg, P. O., Wiedinmyer, C., Mauldin, L., Fried, A., Richter, D., Walega, J., Jimenez, J. L., Adachi, K., Buseck, P. R., Hall, S. R. and Shetter, R.: Emissions from biomass burning in the Yucatan, *Atmos. Chem. Phys.*, 9(15), 5785–5812, doi:10.5194/acp-9-5785-2009, 2009.

Yokelson, R. J., Burling, I. R., Gilman, J. B., Warneke, C., Stockwell, C. E., de Gouw, J., Akagi, S. K., Urbanski, S. P., Veres, P., Roberts, J. M., Kuster, W. C., Reardon, J., Griffith, D. W. T., Johnson, T. J., Hosseini, S., Miller, J. W., Cocker III, D. R., Jung, H. and Weise, D. R.: Coupling field and laboratory measurements to estimate the emission factors of identified and unidentified trace gases for prescribed fires, *Atmos. Chem. Phys.*, 13(1), 89–116, doi:10.5194/acp-13-89-2013, 2013.

Zhang, X., Cappa, C. D., Jathar, S. H., McVay, R. C., Ensberg, J. J., Kleeman, M. J. and Seinfeld, J. H.: Influence of vapor wall loss in laboratory chambers on yields of

secondary organic aerosol., *Proc. Natl. Acad. Sci. U. S. A.*, 111(16), 5802–7, doi:10.1073/pnas.1404727111, 2014.

Zhao, Y., Hennigan, C. J., May, A. A., Tkacik, D. S., de Gouw, J. A., Gilman, J. B., Kuster, W. C., Borbon, A. and Robinson, A. L.: Intermediate-Volatility Organic Compounds: A Large Source of Secondary Organic Aerosol, *Environ. Sci. Technol.*, 48(23), 13743–13750, doi:10.1021/es5035188, 2014.

### 3. MULTIPHASE CHLORINE CHEMISTRY IN BIOMASS BURNING AEROSOL

Biomass burning is a source of both particulate chloride and nitrogen oxides, two important precursors for the formation of nitryl chloride ( $\text{ClNO}_2$ ), which perturbs the atmospheric oxidant budget. In this work, we investigated the ability of biomass burning to produce  $\text{ClNO}_2(\text{g})$  through nocturnal dark chemistry using authentic biomass burning emissions in a smog chamber. Fuels that emitted chloride-rich smoke in turn produced more  $\text{ClNO}_2$  than those that did not emit substantial chloride. There was a positive relationship between the amount of  $\text{ClNO}_2$  formed and the total amount of particulate chloride in the chamber, and with the chloride fraction of non-refractory (non-BC) particle mass. Dinitrogen pentoxide ( $\text{N}_2\text{O}_5$ ) was observed to form promptly following the addition of ozone to the smoke aerosol. The uptake of  $\text{N}_2\text{O}_5(\text{g})$  onto the aerosol in turn released  $\text{ClNO}_2(\text{g})$ , but the reactive uptake probability is significantly smaller than that observed on deliquesced ammonium bisulfate aerosol. At atmospherically relevant elevated relative humidity levels, the particulate chloride in the biomass burning aerosol was rapidly but incompletely displaced by nitric acid, produced largely by the heterogeneous uptake of dinitrogen pentoxide. Despite this chloride acid displacement, the biomass burning aerosol still converted a fraction of  $\text{N}_2\text{O}_5(\text{g})$  into  $\text{ClNO}_2(\text{g})$ , suggesting that the chloride that wasn't displaced was still available in an aqueous phase. We believe that this acid displacement of aqueous chloride is limited by the availability of  $\text{HNO}_3$  that forms in the smoke plume.

### 3.1. Introduction

An accurate budget of atmospheric oxidants is necessary to predict the formation and loss of atmospheric pollutants and climate-forcing agents (e.g. methane and particulate matter). Atomic chlorine and nitrogen oxides ( $\text{NO}_x = \text{NO} + \text{NO}_2$ ) are three gases that contribute significantly to the oxidation budget of the atmosphere, and whose lifetime is directly impacted by the formation and fate of  $\text{N}_2\text{O}_5(\text{g})$  (Brown et al., 2006; Dentener and Crutzen, 1993).  $\text{N}_2\text{O}_5$  forms at night via reactions (R1-R3), shown below.  $\text{NO}_2$  reacts with  $\text{O}_3$  to form  $\cdot\text{NO}_3$ . At night,  $\cdot\text{NO}_3$  can live long enough to react with  $\text{NO}_2$  and form  $\text{N}_2\text{O}_5$ .  $\text{N}_2\text{O}_5$  is thermally unstable and exists in a temperature-dependent equilibrium with  $\text{NO}_2 + \cdot\text{NO}_3$ . Typically at sunrise,  $\text{N}_2\text{O}_5$  photolyzes rapidly regenerating  $\text{NO}_2$  and  $\cdot\text{NO}_3$  (Atkinson et al., 2003; Cox and Derwent, 1976; Hecht and Seinfeld, 1972).

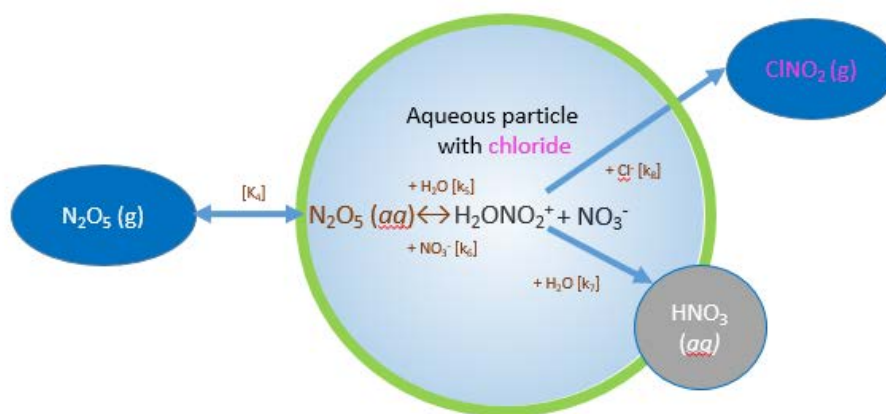
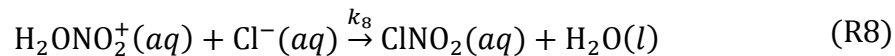
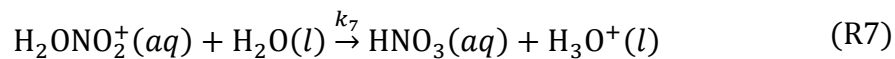
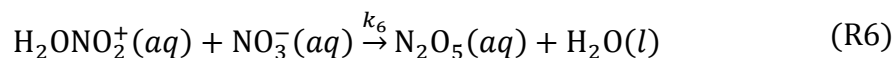
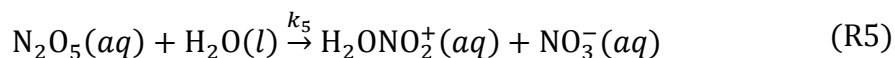


Figure 3.1 Major chemical reactions in the reactive uptake of  $\text{N}_2\text{O}_5$  by an aqueous particle. Based on Fig. 1 from Bertram and Thornton (2009). After  $\text{N}_2\text{O}_5$  is formed in the gas phase, it may be removed from the atmosphere at  $\text{HNO}_3(\text{aq})$  or persist in the nocturnal reservoir  $\text{ClONO}_2(\text{g})$ . The fate of the  $\text{N}_2\text{O}_5$  depends largely on particle morphology and composition.

This extends the atmospheric lifetime of the NO<sub>x</sub> family, which otherwise would be efficiently removed from the atmosphere through oxidation of NO<sub>2</sub> to HNO<sub>3</sub>. The extended NO<sub>x</sub> lifetime allows for more cycles of catalytic ozone (O<sub>3</sub>) production, an important oxidant in the atmosphere. However, the fate of N<sub>2</sub>O<sub>5</sub> can be altered through heterogeneous hydrolysis reactions with aerosol particles. The composition of the particle will affect both the reactive uptake probability ( $\gamma_{\text{N}_2\text{O}_5}$ ) and thus the rate of heterogeneous loss, and also the chemical fate of N<sub>2</sub>O<sub>5</sub> that is taken up by the particle phase. Figure 3.1, reproduced from Bertram and Thornton (2009), shows the potential chemical pathways available for N<sub>2</sub>O<sub>5</sub> in the presence of a particle phase. Reactions (R4-R8) illustrate the individual chemical reactions, including the formation of a solvated reactive intermediate [H<sub>2</sub>ONO<sub>2</sub>]<sup>+</sup>, that may lead to the removal of N<sub>2</sub>O<sub>5</sub> from the atmosphere as HNO<sub>3</sub>(aq), or to the formation of ClNO<sub>2</sub>(aq), which will rapidly partition into the gas phase. Competition between H<sub>2</sub>O and Cl<sup>-</sup> for reaction with the [H<sub>2</sub>ONO<sub>2</sub>]<sup>+</sup> intermediate is the key step for determining the product branching ratio between HNO<sub>3</sub>(aq) and ClNO<sub>2</sub>(aq) (Bertram and Thornton, 2009; Roberts et al., 2009).



Formation of ClNO<sub>2</sub>(g) can have a significant impact on the atmospheric oxidant budget. ClNO<sub>2</sub> is formed in the particle-phase, but then rapidly evaporates to the gas-phase where it is stable in the dark but quickly photo-dissociates into NO<sub>2</sub> and <sup>•</sup>Cl. Atomic chlorine is a potent radical similar to the hydroxyl radical. <sup>•</sup>Cl can oxidize typically long-lived greenhouse gases like methane, initiate the free radical oxidation of volatile organic compounds (VOCs) that catalytically produces ozone, smog, and hydroxyl radicals (Young et al., 2012). ClNO<sub>2</sub> has previously been observed in coastal

regions where sea spray provides ample particulate chloride, a critical precursor to  $\text{ClNO}_2$  formation (Mielke et al., 2013; Osthoff et al., 2008). However, observations of  $\text{ClNO}_2$  have recently been observed in a number of inland regions, suggesting other important sources (Brown et al., 2016; Mielke et al., 2016; Tham et al., 2016; Thornton et al., 2010; Wang et al., 2016). Production of  $\text{ClNO}_2$  far from non-marine chloride sources represents an important but previously unrecognized perturbation to the atmospheric oxidant budget. This perturbation affects production of ozone, particulate matter, and other air pollutants, as well as the lifetime of VOCs.

Biomass-burning aerosol (BBA) is a likely candidate for formation of  $\text{ClNO}_2$  because smoke plumes contain all the necessary precursors:  $\text{NO}_x$ ,  $\text{O}_3$ , water, and often particulate chloride. In contrast to the oceanic sources of  $\text{ClNO}_2$ , where  $\text{NO}_x$  and  $\text{O}_3$  from anthropogenic sources mix with natural sea spray, biomass-burning generates the  $\text{NO}_x$ ,  $\text{O}_3$ , and particulate chloride from a point source, increasing the likelihood of  $\text{N}_2\text{O}_5$  and  $\text{ClNO}_2$  formation within the evolving smoke plume. Biomass burning also emits substantial amounts of VOCs, which will be a sink for the nitrate radical and could therefore prevent the formation of  $\text{N}_2\text{O}_5(\text{g})$ . The propensity for  $\text{N}_2\text{O}_5$  to form in realistic biomass burning plumes is not well known, and this is a prerequisite for the subsequent production of  $\text{ClNO}_2(\text{g})$  (Alexander, 2004). Understanding biomass burning as a source of particulate chloride is of particular interest because it will allow for a better quantification of  $\text{ClNO}_2$  production from other, more readily regulated sources such as coal burning power plants (Graedel and Keene, 1995; Riedel et al., 2013; Wang et al., 2016). Furthermore, wildfires have both natural and anthropogenic causes, and so understanding the effect of these wildfires on the oxidant budget during the pre-industrial era may provide better estimates of the lifetimes of climate-forcing agents, allowing us to better determine the anthropogenic climate forcing, and thus more accurately predict the future impacts of human activities on climate change.

$\text{ClNO}_2$  production from biomass-burning has yet to be investigated explicitly, despite the significant potential impacts on current and pre-industrial atmospheric oxidants, air quality, and climate change. In these experiments, we measured the

ClNO<sub>2</sub> production potential of authentic biomass-burning aerosol in smoke plume conditions. Although formation of N<sub>2</sub>O<sub>5</sub> is fairly well understood, its heterogeneous uptake on authentic biomass burning aerosol has not been explored through laboratory kinetics experiments. The two critical steps, reactive uptake of N<sub>2</sub>O<sub>5</sub> ( $\gamma_{\text{N}_2\text{O}_5}$ ) and the yield of ClNO<sub>2</sub> from N<sub>2</sub>O<sub>5</sub> uptake ( $\phi_{\text{ClNO}_2}$ ) are both highly dependent on particle composition and morphology. Knopf et al. (2011) have previously measured the reactive uptake of nitrate radicals by organic compounds proxies that are abundant in biomass burning aerosol. They found that the organic proxies had a very low  $\gamma_{\text{N}_2\text{O}_5}$  ( $4\text{--}6 \times 10^{-5}$ ) regardless of relative humidity. However, these measurements have potential shortcomings with respect to their application to surface reactivity of authentic biomass-burning aerosol, which varies in composition and morphology from particle to particle, as well as depending on the type of fuel burned. Thus, we suspect that these two key parameters,  $\gamma_{\text{N}_2\text{O}_5}$  and  $\phi_{\text{ClNO}_2}$ , might be significantly different from that previously determined for pure and mixed inorganic and organic aerosol (OA) particles (Abbatt et al., 2012; Escorcia et al., 2010; McNeill et al., 2006; Ryder et al., 2015; Thornton et al., 2003).

Past studies have investigated the effect of particle composition on the reactive uptake coefficient or heterogeneous reaction probability of N<sub>2</sub>O<sub>5</sub> ( $\gamma_{\text{N}_2\text{O}_5}$ ), and have found that particle composition and morphology play important roles, particularly with respect to organic aerosol (Abbatt et al., 2012; Escorcia et al., 2010; McNeill et al., 2006; Ryder et al., 2015; Thornton et al., 2003). Initial findings by Escorcia et al. (2010) showed that the measured  $\gamma_{\text{N}_2\text{O}_5}$  on ammonium bisulfate (ABS) particles decreases by an order of magnitude when coated with even thin layer of  $\alpha$ -pinene ozonolysis secondary organic aerosol. Ryder et al. (2015) reported that organic material had no measureable effect on the  $\gamma_{\text{N}_2\text{O}_5}$  on sea-spray aerosol. These results are consistent with reactive uptake being dependent on the particle morphology, as this controls what chemical phase is available at the surface for heterogeneous reaction. The composition and morphology of biomass-burning aerosol is difficult to predict because of the variability in combustion fuels and conditions, the wide variety of inorganic and carbonaceous components emitted, the

complexity and vast variability in individual particle morphology, composition, and mixing state, and because of the potential for secondary organic and inorganic aerosol formation as a result of atmospheric oxidation and aging (Akagi et al., 2012; Alvarado et al., 2015; Levin et al., 2010; Li et al., 2003; Reid et al., 2005; Yokelson et al., 2009).

Independent of the potential reactive uptake suppression by organic surfactants, the parameterization proposed by Bertram and Thornton (2009) synthesizes Reactions (R4-R8) to describe uptake of  $N_2O_5$  by an aqueous phase  $\gamma_{N_2O_5}$  and the yield of  $ClNO_2$  per  $N_2O_5$  molecule taken up by the aqueous phase ( $\phi_{ClNO_2}$ ):

$$\gamma_{N_2O_5} = \frac{4}{\omega} \frac{V}{S_a} K_H k'_5 \left( 1 - \frac{1}{\left( \frac{k_7 [H_2O]}{k_6 [NO_3^-]} \right) + 1 + \left( \frac{k_8 [Cl^-]}{k_6 [NO_3^-]} \right)} \right) \quad (3.1)$$

$$\phi_{ClNO_2} = \left( 1 + \frac{k_7 [H_2O(l)]}{k_8 [Cl^-]} \right)^{-1} \quad (3.2)$$

where  $V$  = total particle volume concentration ( $m^3 m^{-3} air$ ),  $S_a$  = total particle surface area concentration ( $m^2 m^{-3}$ ),  $\omega$  = mean molecular speed of  $N_2O_5$  ( $m s^{-1}$ ),  $K_H$  = dimensionless Henry's law coefficient for  $N_2O_5$ ,  $H_2O$  = liquid particulate water,  $NO_3^-$  = particulate nitrate, and  $Cl^-$  = particulate chloride. Three aerosol components are identified as having an important effect on the ability of particles to convert  $N_2O_5$  into  $ClNO_2$ : water, nitrate, and chloride.

Equation 3.1 shows that low water content reduces  $N_2O_5$  uptake, as it is a hydrolysis reaction. Lower water content also implies a higher concentration of  $NO_3^-$ , which can inhibit  $\gamma_{N_2O_5}$  and is known as the nitrate effect. The nitrate effect refers to the decrease in  $N_2O_5$  reactive uptake due to an increased concentration of  $NO_3^-$ , and therefore a faster rate for the decomposition of the  $[H_2ONO_2]^+$  intermediate (R6).

Empirical measurements have shown that the ratio of  $k_8/k_7$  (R8/R7), is large ( $483 \pm 175$ ; Bertram and Thornton, 2009), favoring the formation of  $ClNO_2$  instead of  $HNO_3$  in solutions where there is even a modest amount of chloride,  $< 5 M$  (Behnke et al., 1997; Bertram and Thornton, 2009; Kercher et al., 2009). Equation 3.2 shows that an increased chloride concentration will also increase the yield of  $ClNO_2$ , in



addition to increasing reactive uptake of  $\text{N}_2\text{O}_5$ . Thus, in these experiments we used biomass fuels with different expected chloride contents to investigate the effect of initial particulate chloride concentration on  $\phi_{\text{ClNO}_2}$ .

Water is a critical component for the heterogeneous uptake of  $\text{N}_2\text{O}_5$  and subsequent production of  $\text{ClNO}_2$ . Water is necessary to generate an aqueous phase to promote the efficient hydrolysis of  $\text{N}_2\text{O}_5$ , and simultaneously dilutes the particle nitrate (thus enhancing  $\gamma_{\text{N}_2\text{O}_5}$ ) and particle chloride (decreasing  $\phi_{\text{ClNO}_2}$ ) concentrations. Increased water content can also affect particle morphology (i.e. liquid-liquid phase separation) and potentially allow for acid displacement chemistry (Gard et al., 1998; Li et al., 2003), shown in reaction (R9):



where M is a cation (e.g. potassium, sodium, etc.) This mechanism can have the two-fold effect of increasing  $\text{NO}_3^-$  (decreasing  $\gamma_{\text{N}_2\text{O}_5}$ ) and decreasing chloride (reducing  $\phi_{\text{ClNO}_2}$ ), while releasing substantial HCl to the gas phase. In our smog chamber experiments, we investigated the effect of relative humidity on the  $\text{ClNO}_2$  produced from authentic biomass-burning aerosol generated from various fuels to determine the influence of particle-phase water content on this multiphase chemistry.

## 3.2. Experiment Methods

### 3.2.1. Experimental overview

We investigated the fate of chloride in biomass-burning emissions in one of the Carnegie Mellon University 12 m<sup>3</sup> Teflon smog chambers (Grieshop et al., 2009; Hennigan et al., 2010; Huff Hartz et al., 2005; Presto et al., 2005). Prior to each experiment, the chambers were purged using UV blacklights and VOC-free and particle-free air overnight to ensure the particle concentrations were < 10 p/cc.

We used four types of aerosol in these experiments. Ammonium bisulfate was selected as a test particle that did not contain chloride and that has a well-characterized  $\gamma_{\text{N}_2\text{O}_5}$  (Abbatt et al., 2012; Bertram and Thornton, 2009; Thornton et al., 2003). The three biomass fuels burned were sawgrass, cutgrass, and birch wood.

Sawgrass and cutgrass smoke have previously been observed to have high-chloride content, likely due to the brackish water where they grow (Stockwell et al., 2014). These tall grasses were obtained for us from near Savannah, Georgia by the U.S. Fish and Wildlife Service, while the birch was bought as firewood at a local grocery store in Pittsburgh, PA.

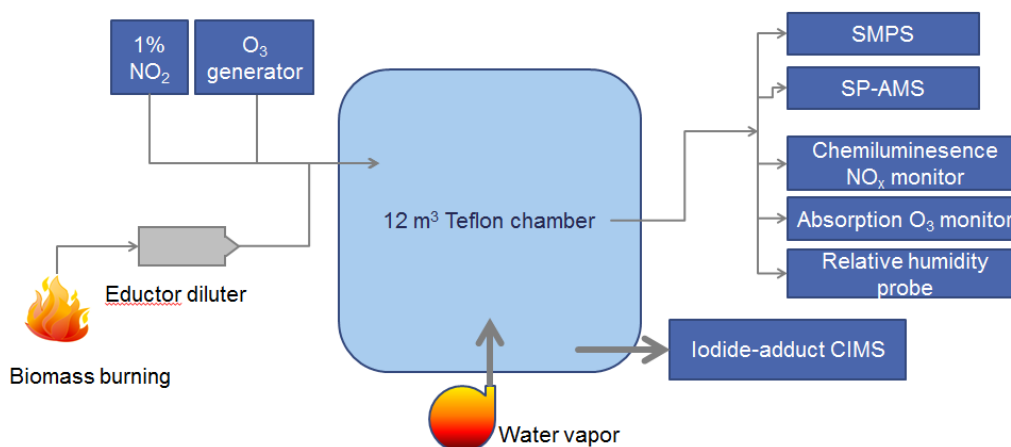


Figure 3.2. Experimental setup for smog chamber experiments to measure the effect of biomass-burning aerosol on nocturnal nitrogen oxide species and chlorine chemistry. The CMU smog chamber was filled with precursors for N<sub>2</sub>O<sub>5</sub> formation, either from biomass burning or from a compressed gas cylinder. Gas and particle phase instrumentation sampled air from the chamber reactor whose relative humidity was adjusted using steam.

We prepared a 1 g L<sup>-1</sup> solution of ammonium bisulfate in MilliQ water that we nebulized directly into the smog chamber using a TSI model 3076 Aerosol Generator. In some experiments the aerosol was passed through a diffusion drier, and in others the aerosol was not dried and remained deliquesced before being injected into the pre-humidified smog chamber. We scattered tall grass samples in an aluminium pan and ignited them using a butane lighter. We added fuel by hand to maintain visual flaming combustion conditions while we filled the smog chamber using a pair of Dekati eductor diluters. The diluters pulled flow from a 1/2" stainless steel inlet positioned 1 m above the fire on the side of the exhaust chimney, as shown in Figure 3.2. The diluters then injected the sampled smoke into the smog chamber via a room-

temperature 3/8" o.d. copper transfer line. The inlet sampled smoke after it had mixed with room air, but before being removed by the exhaust hood. Contamination due to any entrained room particles is assumed to be small relative to the extremely high concentrations of smoke particles entering the chimney. We used the same sampling set up for the birch-wood smoke, except that the birch wood was burned in a naturally aspirated cast-iron woodstove with the door left open. The birch wood was split into kindling about 2 cm in diameter before being lit with the butane lighter. It was allowed to burn for about 5 minutes before chamber filling was started. The fires were fed until the smog chamber contained a sufficient particle concentration. We aimed for a particle surface area concentration of  $\sim 2 \times 10^9 \text{ nm}^2 \text{ cm}^{-3}$ , which was typically achieved after 20 to 40 minutes of particle injection. This corresponded to a particle number concentration of  $3.5 \times 10^5$  to  $2.0 \times 10^5 \text{ cm}^{-3}$ , but varied significantly for each experiment. Details for each experiment are provided in Table 3.1.

$\text{N}_2\text{O}_5$  was formed in the smoke from a series of gas-phase reactions that begin with  $\text{NO}_x$  and ozone. During our experiments, the smoke injection increased the chamber concentration of  $\text{NO}_x$  to an average concentration of 72 ppb, as indicated in Table 3.1. For experiments where smoke was not used, small aliquots of 1%  $\text{NO}_2$  (Liquid Technologies, Co.) were added to the chamber to achieve  $\text{NO}_x$  levels similar to those in the burn experiments. After  $\text{NO}_2$  had been added, either from the compressed-gas cylinder or from the nascent smoke, we injected ozone generated from pure oxygen gas flowing through a corona discharge source (HTU500AC, Azco). Initial ozone concentrations were typically 95 ppbv.

As the conversion of  $\text{N}_2\text{O}_5$  into  $\text{ClNO}_2$  is understood to occur in the aqueous phase, we also explored the effect of relative humidity on  $\text{ClNO}_2$  formation. We achieved a relative humidity as high as 60% with minimal air dilution by injecting steam into the smog chamber. We heated approximately 300 mL of MilliQ water in a 3-neck 500 mL glass flask using an electric mantel (Robinson et al., 2016b; Ye et al., 2016). We purged the water of volatile impurities by flushing clean air over the heated system for 10 mins before connecting the flask to the heated steam-injection line. We mixed the steam using pulses of clean, dry air from a nearby inlet connected

to the chamber to prevent thermal stratification in the chamber. Relative humidity was measured from near the top of the chamber using a temperature and humidity probe (Vaisala, model HNP-233).

### 3.2.2. Particle characterization

We measured particle composition using the Aerodyne Soot Particle high resolution Aerosol Mass Spectrometer (SP-AMS, Aerodyne Research Inc.) (Onasch et al., 2012). The SP-AMS uses a high-power infrared (IR) laser to evaporate black-carbon containing aerosol, facilitating the measurement of refractory black carbon (rBC) aerosol mass by the AMS. Particles that do not contain rBC, and therefore do not efficiently absorb the IR laser, are evaporated by the conventional 600 °C tungsten thermal vaporizer that sits behind the IR laser beam. The vapors produced by either the IR laser or vaporizer are subsequently ionized by a 70 eV electron source, and the resulting ions are analyzed by a high-resolution ( $R \sim 2100$  at  $m/z 200$ ) time-of-flight mass spectrometer. Data was analyzed using SQUIRREL v1.57I and high-resolution ion peak fitting using PIKA v1.16I. Ion signal from  $C_1^+$  was apportioned to rBC using the relationship:  $rBC-C_1^+ = 0.625 \times C_3^+$ . This is the relative ion abundance we observed in the rBC calibrant aerosol, Regal Black (Onasch et al., 2012). Any additional signal from  $C_1^+$  was apportioned as organic aerosol mass that had fragmented to just  $C_1^+$ . We report both refractory (i.e. rBC) and non-refractory aerosol components.

We used the automated menu switching function of the SP-AMS data acquisition program to alternate between measurements with the IR laser on and the IR laser off. Unless specified otherwise, refractory species were measured with the SP-AMS infrared (IR) laser on, using particle beam-width probe measurements to estimate the rBC collection efficiency ( $E_{IR,rBC} = 0.4 \pm 0.15$ ) (Ahern et al., 2016; Willis et al., 2014). Due to uncertainty associated with the relative ionization efficiencies of non-refractory species vaporized with the SP-AMS using the IR laser, we report non-refractory species as measured when only using the conventional 600 °C vaporizer with the IR laser off (Carbone et al., 2015; Decarlo et al., 2006; Jayne et al., 2000; Willis

et al., 2014). With the conventional vaporizer, the largest source of uncertainty for quantitative mass measurements is due to particles bouncing off the vaporizer and thus not being detected (Docherty et al., 2013; Robinson et al., 2016a). However, with biomass-burning aerosol there are assumptions we describe below that allow us to estimate particle bounce by comparing SP-AMS mass measurements with the laser on versus with the laser off.

For the non-refractory species, we use two reasonable assumptions that allow us to calculate the particle bounce collection efficiency of the SP-AMS: 1) We assume that all particles contain some black carbon. Given the visually observed flaming nature of the fires, and single particle measurements of other flaming emissions, we believe this to be likely (Ahern et al., 2016); 2) We assume the relative ionization efficiency of chloride is the same regardless of being vaporized by the IR laser or the tungsten vaporizer. While there is some evidence that organic molecules may ionize more readily when vaporized by the IR laser of the SP-AMS, the evidence regarding chloride suggests that it has the same relative ionization efficiency in both cases (Lee et al., 2016).

Based on these assumptions, the increase in chloride signal when the IR laser is on versus off allows one to solve for the fraction of particles that bounce off the tungsten vaporizer. Solving this equation results in a particle bounce collection efficiency of 0.49 for particles not vaporized by the IR laser for fresh biomass burning aerosol. This value is reasonable and commonly used for AMS ambient aerosol measurements (Middlebrook et al., 2012). Using this collection efficiency and the standard fragmentation table in PIKA v1.16I, we report the remaining non-refractory species measured with the IR laser off. We assume that the dominant form of chloride in biomass burning aerosol is ammonium chloride and therefore is measured effectively by the SP-AMS in laser off mode, as has been previously reported (Decarlo et al., 2008; Huffman et al., 2008; Salcedo et al., 2006). However, if the form of chloride is a semi-refractory form with a higher boiling temperature (e.g. NaCl, PbCl, etc.) then some of the material may not be promptly vaporized, and thus the stated Cl<sup>-</sup> concentration may be underreported (Ovadnevaite et al., 2012; Salcedo et al., 2010).

Past work has shown that elevated relative humidity, can induce a transition for some particle from solids to liquids, thereby increasing their collection efficiency, with the most significant effect taking place at very high relative humidity (greater than 80%) (Matthew et al., 2008; Middlebrook et al., 2012; Ng et al., 2011). Given that the relative humidity in the smog chamber was always less than 65% RH, we believe that the particle bounce collection efficiency was not significantly affected by changes in relative humidity.

We measured particle size and number using a polonium neutralizer and a Scanning Mobility Particle Sizer (SMPS, TSI, Inc., model 3081; 3080 Long DMA and 3772 CPC) sampling directly from the chamber. The SMPS sheath flow was set to 5.0 L min<sup>-1</sup> and the aerosol sample flow was reduced to 0.5 L min<sup>-1</sup> using a mass flow controller to supply a particle-free makeup flow for the CPC's 1.0 L min<sup>-1</sup> total flow rate. We calculated the particle surface area assuming all particles are spherical.

### 3.2.3. Gas-phase characterization

We measured the gas-phase composition using an absorption-based ozone monitor (Dasibi, 1008-PC), a chemiluminescence NO<sub>x</sub> monitor with a molybdenum catalyst (Advance Pollution Instrumentation, model 200A), and a relative humidity probe (Vaisala, HNP-233). It should be noted that the NO<sub>x</sub> data will be biased high due to unconstrained conversions of nitrogen oxides (e.g. N<sub>2</sub>O<sub>5</sub>) to NO (Villena et al., 2012; Winer et al., 1974). At most this would bias NO<sub>x</sub> 10% high, and would not influence our results significantly.

We measured iodide ion adducts of N<sub>2</sub>O<sub>5</sub>, ClNO<sub>2</sub>, and other gases using the University of Washington chemical ionization time of flight mass spectrometer (UW-CIMS) (Gaston et al., 2016; Kercher et al., 2009; Lopez-Hilfiker et al., 2014). The UW-CIMS pulled 8.0 Lpm of flow through a 3/8" o.d. Teflon sampling inlet to limit the loss of reactive species. Laminar flow was calculated for these conditions with a 15% loss rate to the walls to limit the loss of reactive gases. A <sup>210</sup>Po ionizer (Staticmaster, model P-2021) was used to create reagent ions (I<sup>-</sup>) from methyl iodide. The mass spectrometer was tuned for weak declustering and N<sub>2</sub>O<sub>5</sub> was sampled at the collision

limit in the ion molecular reaction (IMR) reactor. The IMR was also humidified to 35% RH to control for variable sensitivity to water vapour of any species. We humidified the inlet zeroes to 35% RH to maintain constant sensitivity. Iodide clusters were measured with a resolution of 4000.

We quantified the loss of  $\text{N}_2\text{O}_5$  in the inlet using a  $\text{N}_2\text{O}_5$  flow-reactor placed in front of the inlet, similar in principle to that described by Bertram et al. (2009) to generate a constant flowing concentration of  $\text{N}_2\text{O}_5$  by reacting a stream of  $\text{NO}_2$  with an excess of  $\text{O}_3$ . A dynamic gas-calibrator (Thermo Electron Co., model 146C) supplied a variable flow of NO from a compressed-gas cylinder (1500 ppb NO, Liquid Technologies Co.) and also generated a constant flow of  $\text{O}_3$  from compressed zero air. We used a passivated 4 L glass bottle reservoir to allow ample reaction time for the  $\text{NO}_2$  and  $\text{O}_3$  to generate a steady source of  $\text{N}_2\text{O}_5$ .  $\text{ClNO}_2$  was calibrated by flowing  $\text{N}_2\text{O}_5$  over a NaCl bed and assuming 1:1 conversion from  $\text{N}_2\text{O}_5$  to  $\text{ClNO}_2$  (Kercher et al., 2009).

### 3.3. Results and Discussion

#### 3.3.1. Particle composition from biomass-burning

The initial particle composition of the smoke varied from burn-to-burn but there were some trends based on the fuel burned. We list the particle composition for each chamber experiment in Table 3.1, including the chloride fraction of non-refractory aerosol mass ( $f_{\text{Cl}} = \text{Cl}^- / (\text{Cl}^- + \text{NO}_3^- + \text{OA} + \text{NH}_4^+ + \text{SO}_4^{2-})$ ). Burning sawgrass produced the aerosol with the highest  $f_{\text{Cl}}$ , 0.32. Cutgrass burning could also generate high  $f_{\text{Cl}}$  aerosol, but in one instance had a very low  $f_{\text{Cl}}$  of 0.03. Birch-wood smoke consistently had the lowest chloride content with  $f_{\text{Cl}} = 0.01$ , with one exception where  $f_{\text{Cl}} = 0.09$ . It should be noted however, that although the birch wood had low chloride content, other parts of the plant that we did not burn may have contained elevated chloride concentrations. The greens of trees, which are readily burned in wildfires, can produce higher concentrations of chloride when burned than the lignin-rich wood (Hays et al., 2002; Schauer et al., 2001). In addition to particle composition, Table 3.1 also lists the relative humidity at the time of the aerosol measurement. For

Table 3.1. Summary of chamber experiment conditions for measuring  $\text{N}_2\text{O}_5$  and  $\text{ClNO}_2$  formation in the smog chamber. Reported values are the average for 10 minutes after injection of ozone.

Aerosol/ Fuel	rBC	Cl	$f\text{Cl}^1$	$\text{NO}_x$	$\text{O}_3$	Surface Area	R H	Number Conc <sup>2</sup> (t = 0 hrs)	Number Conc <sup>3</sup> (t = 1.7 hrs)
	$\mu\text{g m}^{-3}$	$\mu\text{g m}^{-3}$		ppb	ppb	$\text{nm}^2 \text{cm}^{-3}$	%	$\text{nm}^2 \text{cm}^{-3}$	$\text{nm}^2 \text{cm}^{-3}$
ABS <sup>4</sup>		0.01	0.00	33	78	4.08E+03	1	0.00E+00	3.98E-01
ABS <sup>4</sup>		0.02	0.00	105	102	2.23E+09	3	8.26E+04	4.22E+04
ABS <sup>4</sup>		0.01	0.00	74	73	3.30E+05	38	1.24E+01	1.19E+05
ABS <sup>4</sup>		0.01	0.00	320	161	1.45E+05	35	5.14E+00	2.35E+04
Sawgrass	1.39	0.89	0.32	72	91	3.86E+08	1	2.11E+04	1.15E+04
Sawgrass	5.93	3.24	0.19	152	88	1.58E+09	5	8.27E+04	6.06E+04
Sawgrass	8.82	2.21	0.12	102	143	2.16E+09	3	7.85E+04	4.15E+04
Birch	16.5	0.05	0.01	57	107	1.52E+09	39	2.40E+04	1.80E+04
Birch	6.19	0.05	0.01	69	114	6.49E+08	2	1.29E+04	1.03E+04
Birch	10.9	0.02	0.00	96	140	1.06E+09	21	1.62E+04	1.25E+04
Birch	20.2	0.13	0.01	67	130		2		
Birch		0.01	0.09	10	105	4.32E+04	1	6.36E+04	2.90E+04
Birch	15.5	0.14	0.01	76	118	1.39E+09	2	3.91E+04	1.67E+04
Cutgrass				116	140	1.45E+09	2	4.63E+04	1.21E+04
Cutgrass	9.99	0.19	0.02	108	2	1.17E+09	35	3.31E+04	2.20E+04
Cutgrass	6.34	0.36	0.05	0		9.55E+08	14	1.66E+04	1.24E+04
Cutgrass	2.12	0.15	0.03	15	54	3.25E+08	4	7.83E+03	6.32E+03
Cutgrass	6.77	0.79	0.12	90	84	7.27E+08	2	1.37E+04	6.11E+03
Cutgrass	0.13			88	101	1.06E+09	35	1.94E+04	7.84E+03
Denuded	14.8	2.73	0.10	78	52	1.28E+09	1	3.75E+04	2.34E+04
Cutgrass	0.03	0.17	0.17	24	40	8.64E+07	1	2.78E+03	2.07E+03
Denuded	9.41	1.54	0.07	71	60	1.04E+09	2	2.53E+04	7.87E+03

<sup>1</sup>  $f\text{Cl}$  = mass chloride / (mass sulfate + nitrate + organic + ammonium + chloride)

<sup>2</sup> SMPS-measured particle number concentration when the ozone was injected (sometimes no particles had yet been injected)

<sup>3</sup> SMPS-measured particle concentration 1.7 hours after ozone injection. Decreased particle concentration compared to the number concentration at t = 0 hours is due to particle wall loss. Increased particulate concentration is due to the injection of ammonium bisulfate particles after ozone injection.

<sup>4</sup> ABS = ammonium bisulfate



cutgrass smoke experiments, the  $f_{Cl}$  was consistently lower when the chamber was humidified. This will be discussed in greater detail in the context of gas-phase measurements in Section 3.3.3.

### 3.3.2. Formation of $N_2O_5$ and $ClNO_2$ in smog chamber experiments

Substantial  $N_2O_5$  was quickly produced in all our biomass smoke chamber experiments from the nascent smoke following the injection of ozone, but exhibited a wide degree of variability. We show in Figure 3.3a the concentration of  $N_2O_5$  formed during various smog chamber experiments. We injected ozone at  $t = 0$  hours, and thus initiated reactions (R1)-(R3), which produce  $N_2O_5$ . The formation of  $N_2O_5$  in a biomass-burning plume is not necessarily a given. The  $\cdot NO_3$  radical reacts rapidly with volatile organic compounds, which are abundant in biomass burning plumes and may out compete  $NO_2$  (R2), and thus limit the formation of  $N_2O_5$ . However, the  $N_2O_5$  formation we observed was prompt and through comparison to the ammonium bisulfate experiments, which are devoid of volatile organic compounds, does not appear to be impeded by the presence of the organic vapors emitted in the smoke.

Using the UW-CIMS we measured significant variability with respect to the maximum amount of  $N_2O_5$  observed, and also the temporal trends of  $N_2O_5$  formation and loss. This variability was likely due to different initial concentrations of  $NO_x$  and ozone in the chamber (listed in Table 3.1), as well as the 10 minute mixing time associated with the  $12\text{ m}^3$  smog chamber volume. At  $t = \sim 0.5$  hour, the  $N_2O_5$  concentrations began to decrease for two likely reasons: 1) production of  $N_2O_5$  decreases due to consumption of the precursors  $NO_x$  and  $O_3$ ; 2)  $N_2O_5$  is also being lost by uptake to the particles and walls, where it may decompose and liberate  $NO_x$ , or be converted to either  $HNO_3$  or  $ClNO_2$  (Wahner et al., 1998a, 1998b).

If  $N_2O_5$  is converted to  $ClNO_2$  in the aerosol aqueous phase following reactive uptake,  $ClNO_2$  rapidly partitions into the gas phase. Figure 3.3b shows the concentration of  $ClNO_2(g)$  measured by the UW-CIMS.  $ClNO_2$  is stable in the dark smog chamber, and thus has no significant sinks in these experiments. The

concentration of  $\text{ClNO}_2$  only increases, unless the UV lights in the smog chamber are turned on.

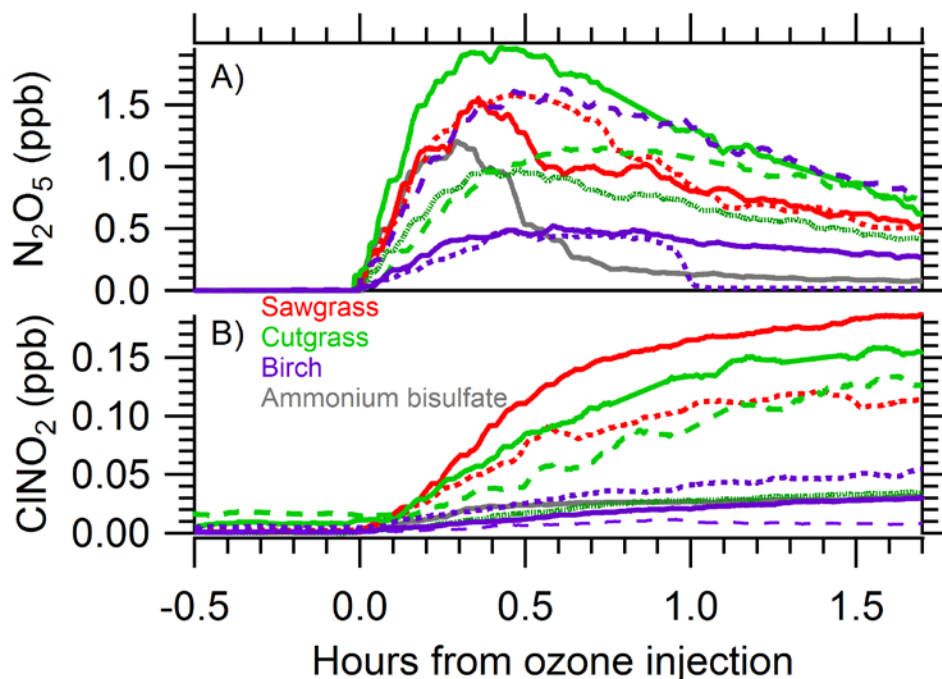


Figure 3.3. Production of  $\text{N}_2\text{O}_5(\text{g})$  and  $\text{ClNO}_2(\text{g})$ , measured by the UW-CIMS, during dark chamber aging of biomass-burning aerosol or ammonium bisulfate aerosol. Panel a) shows the formation of  $\text{N}_2\text{O}_5$  from the reaction of  $\text{NO}_x$  and  $\text{O}_3$  for chamber experiments with different particles. Initial production is very fast, but after  $\sim 0.5$  hours the loss of the  $\text{N}_2\text{O}_5$  either to the chamber walls or particle surfaces becomes faster than the formation of  $\text{N}_2\text{O}_5$ . Panel b) shows the formation of  $\text{ClNO}_2$ . Grass burns appear to generate the most  $\text{ClNO}_2$ , but they also tend to have the most  $\text{N}_2\text{O}_5$  available to be converted.

Figure 3.3b shows that smoke from sawgrass (red) and cutgrass (green) generate more  $\text{ClNO}_2$  than smoke from birch wood (purple) or ammonium bisulfate (black). We did observe the formation of  $\text{ClNO}_2$  in nominally chloride-free control experiments: the ammonium bisulfate seeded experiments (Figure 3.3), and also in aerosol-free experiments (not shown). This is presumably due to chloride that was already present on – or subsequently partitioned to – the chamber walls. In most cases the effect of injecting biomass-burning emissions resulted in a higher

concentration of  $\text{ClNO}_2$  being formed than what was observed when similar amounts of  $\text{N}_2\text{O}_5$  precursors ( $\text{NO}_x + \text{O}_3$ ) were injected in the control experiments (ammonium bisulfate aerosol or aerosol free) without biomass-burning emissions.

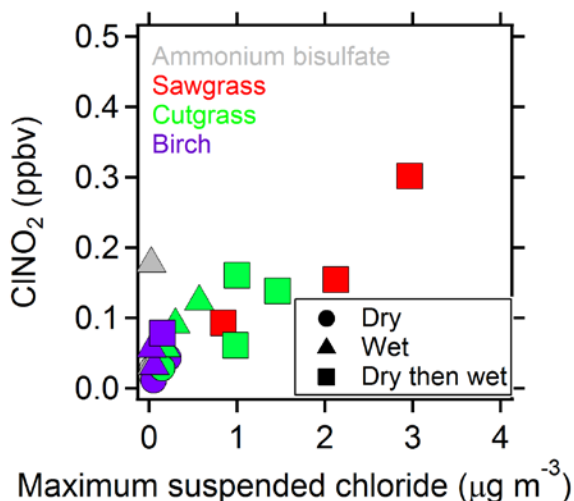


Figure 3.4. Measured  $\text{ClNO}_2$  concentrations 1.7 hours after ozone injection as a function of initial particulate chloride mass concentration. Markers are colored by the fuel that generated the smoke for a given experiment. Circles indicate dry experiments ( $\text{RH} < 2\%$ ) and triangles indicate wet experiments ( $\text{RH} > 10\%$ ). This is an effective synthesis of the trends shown in Figure 3.3, which is that chlorine rich fuels lead to an enhancement of  $\text{ClNO}_2$  production. While this plot suggests that increased chloride content in smoke leads to an increase in  $\text{ClNO}_2$  production, it neglects to account for the simultaneous increase in the  $\text{ClNO}_2$  precursor  $\text{N}_2\text{O}_5$ . Injecting more smoke will lead to more  $\text{N}_2\text{O}_5$  production as well as more particulate chloride, and could result in a higher total amount of  $\text{ClNO}_2$  produced.

In Figure 3.4, we used the same color convention as in Figure 3.3 to show the maximum concentration of  $\text{ClNO}_2$  measured as a function of the maximum particulate chloride mass concentration that we observed in each chamber experiment. Figure 3.4 shows a positive correlation between the total particulate chloride emitted in the biomass-burning emissions and the subsequent  $\text{ClNO}_2$  formation. However, there is significant scatter in the relationship between particle chloride mass and  $\text{ClNO}_2$  formed. This scatter can be easily explained by the burn-to-burn variability in  $\text{N}_2\text{O}_5$

precursors, and therefore  $\text{N}_2\text{O}_5$  production. I.e. it is obvious that injecting more smoke will result in higher initial concentrations of  $\text{NO}_x$ , which will in turn result in more  $\text{N}_2\text{O}_5$  being formed, which means there is greater potential for  $\text{ClNO}_2$  formation. This explanation for the positive correlation in Figure 3.4 between particulate chloride and  $\text{ClNO}_2$  production is independent of the potential of the smoke particles to convert  $\text{N}_2\text{O}_5$  into  $\text{ClNO}_2$ , i.e.  $\gamma_{\text{N}_2\text{O}_5}$  and  $\phi_{\text{ClNO}_2}$ .

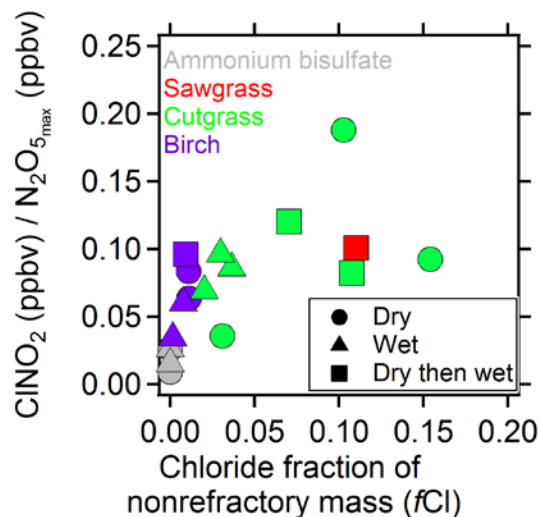


Figure 3.5. The ratio of measured maximum concentration of  $\text{ClNO}_2$  to the maximum concentration of  $\text{N}_2\text{O}_5$  shown as a function of the chloride fraction of nonrefractory particulate mass ( $f\text{Cl}$ ).

To isolate the  $\text{ClNO}_2$  formation potential of the biomass-burning particles from the influence of chamber wall chemistry, in Figure 3.5 we plot the normalized, maximum  $\text{ClNO}_2$  concentration observed as a function of  $f\text{Cl}$ , the maximum (initial) particulate chloride non-refractory mass fraction. Using  $f\text{Cl}$  reveals the effect of particle composition rather than the effect of total particle concentration on the production of  $\text{ClNO}_2$ . Furthermore, we normalized the maximum  $\text{ClNO}_2$  by the maximum  $\text{N}_2\text{O}_5$  observed to reduce the influence of simply having more  $\text{ClNO}_2$  precursor available for reaction, caused by variability in the initial concentrations of  $\text{NO}_x$ ,  $\text{O}_3$ , and VOCs (that scavenge  $\text{NO}_3$ ) in the nascent smoke. Figure 3.5 reveals a much more robust relationship between particle composition and  $\text{ClNO}_2$  produced. Even aerosol systems with low-chloride content ( $f\text{Cl} = 0.01$ ), such as the birch-wood

smoke, may result in an enhanced formation of  $\text{ClNO}_2$  relative to what we observed from chloride-free experiments. With increasing particulate chloride mass fraction, there is an increase in  $\text{ClNO}_2$  produced per  $\text{N}_2\text{O}_5$  molecule available for reaction. More extensive modelling is required to extract the  $\gamma_{\text{N}_2\text{O}_5}$  and  $\phi_{\text{ClNO}_2}$  kinetic parameters for heterogeneous uptake of  $\text{N}_2\text{O}_5$  and subsequent  $\text{ClNO}_2$  production on biomass burning particles. With this analysis, we have demonstrated for the first time that biomass-burning plumes may be a source of atmospheric  $\text{ClNO}_2$ , and that the efficacy with which  $\text{N}_2\text{O}_5$  is converted to  $\text{ClNO}_2$  is correlated with the particulate chloride mass fraction,  $f_{\text{Cl}}$ .

One limitation of smog chamber experiments is the potential for reactants to interact with the smog chamber walls. In an ideal experiment,  $\text{N}_2\text{O}_5$  would only be lost by thermolysis through (R3) or by reactive uptake on the particles (R4), as occurs in the atmosphere. This would allow us to directly calculate  $\gamma_{\text{N}_2\text{O}_5}$  of the biomass-burning aerosol using just the measured particle surface area and loss rate of  $\text{N}_2\text{O}_5(\text{g})$ , which would then lead to a precise calculation of  $\phi_{\text{ClNO}_2}$  from the observed increase in  $\text{ClNO}_2(\text{g})$ . However, for our conditions it appears that the loss of  $\text{N}_2\text{O}_5$  was strongly influenced by interactions with the chamber walls. We confirmed this by injecting  $\text{NO}_2$  and  $\text{O}_3$  into the smog chamber without any particles; the  $\text{N}_2\text{O}_5$  concentration had the same temporal profile as in the experiments with biomass-burning aerosol (Figure 3.3). From this we conclude that the  $\text{N}_2\text{O}_5$  is diffusing to the walls and being taken up with some efficiency, which in turn may produce some  $\text{ClNO}_2$  from whatever particles exist on the smog chamber walls from past experiments. While the aerosol-free experiments and ammonium bisulfate experiments do allow us to calculate the  $\gamma_{\text{N}_2\text{O}_5}$  and  $\phi_{\text{ClNO}_2}$  for reactions of  $\text{N}_2\text{O}_5$  with the chamber walls, to do so requires detailed modeling of the gas phase kinetics. This will be the subject of a future manuscript, but for now we can draw some conclusions about  $\gamma_{\text{N}_2\text{O}_5}$  and  $\phi_{\text{ClNO}_2}$  by comparing with the ammonium bisulfate experiments, for which these heterogeneous kinetics parameters are known (Abbatt et al., 2012; Bertram et al., 2009; Bertram and Thornton, 2009).

We can compare the evolution of  $\text{N}_2\text{O}_5$  and  $\text{ClNO}_2$  for the BBA smoke experiments to the experiments where deliquesced ammonium bisulfate aerosol was injected into the smog chamber. In Figure 3.3a the ammonium bisulfate experiments are shown in grey, and we see that for a similar particle surface area as the biomass burning experiments, there is a much faster  $\text{N}_2\text{O}_5$  decay at  $t = 0.4$  hours. We don't differentiate between humidified and non-humidified biomass-burning aerosols for this comparison because in both cases, the  $\gamma_{\text{N}_2\text{O}_5}$  for the biomass burning experiments must be much smaller than that known for the deliquesced ammonium bisulfate ( $\gamma_{\text{N}_2\text{O}_5} = 0.28$ ; Bertram et al., 2009), otherwise we would see a similarly fast decay in those experiments. It is more likely the reactive uptake is 1-2 orders of magnitude lower, similar to that observed for other organic aerosol systems (Abbatt et al., 2012; Escorcia et al., 2010). This also means that humidification of the biomass burning aerosol did not significantly accelerate the reactive uptake of  $\text{N}_2\text{O}_5$ , even though particulate water content is an important driver of  $\gamma_{\text{N}_2\text{O}_5}$  based on prior studies using inorganic and organic aerosol particles (Eqn. (3.1)). Biomass-burning aerosol contains organic compounds which may inhibit reactive uptake of  $\text{N}_2\text{O}_5$  by reducing the availability of water at the gas-particle interface, but also contains significant amounts of hygroscopic inorganic salts (such as KCl) whose associated water content would facilitate the uptake of  $\text{N}_2\text{O}_5$  and formation of  $\text{ClNO}_2$ . The observed small  $\gamma_{\text{N}_2\text{O}_5}$  also confirms that the  $\phi_{\text{ClNO}_2}$  of the biomass burning aerosol may be significant given that the absolute  $\text{ClNO}_2$  concentration increases significantly over the ammonium bisulfate experiments, despite fewer molecules of  $\text{N}_2\text{O}_5$  being taken up per collision by the biomass-burning aerosol compared to the ammonium bisulfate.

### 3.3.3. Observed acid displacement in biomass burning aerosol

The effect of relative humidity on the uptake of  $\text{N}_2\text{O}_5$  and production of  $\text{ClNO}_2$  is another variable in ambient smoke plumes that we can investigate using these smog chamber experiments. It has been shown that although an aqueous phase is necessary for the production of  $\text{ClNO}_2$ , water uptake will also reduce the concentration of chloride in the particles. This can favor the production of  $\text{HNO}_3$  versus  $\text{ClNO}_2$  through

$\text{N}_2\text{O}_5$  hydrolysis as the  $\text{Cl}^-$  reactant has been diluted, and the nitrate effect from  $\text{HNO}_3$  has also been diluted, as shown in Figure 3.1 (Bertram and Thornton, 2009).

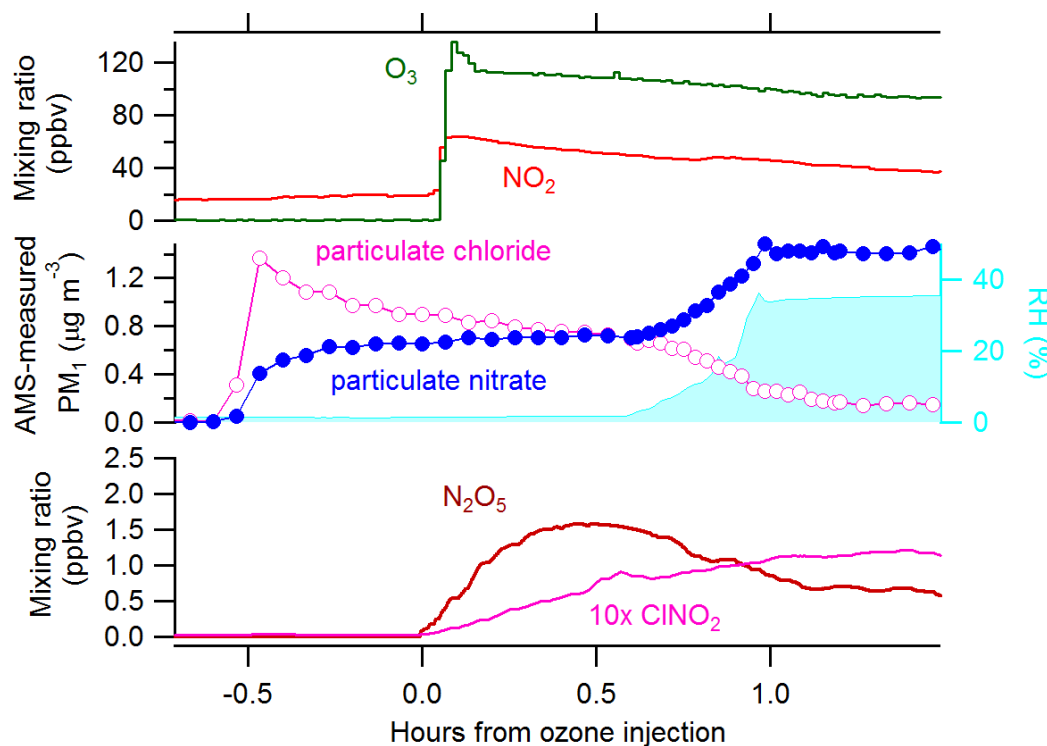


Figure 3.6. Gas and particle-phase time sequences for a biomass burning experiment using sawgrass where relative humidity was increased after smoke and  $\text{O}_3$  had been injected. The top panel shows the  $\text{O}_3$  injection and subsequent conversion of  $\text{NO}$  to  $\text{NO}_2$ . The bottom panel shows that at the time of  $\text{O}_3$  injection, both  $\text{N}_2\text{O}_5$  and  $\text{ClNO}_2$  form. Particle composition was measured by the AMS and shown in the middle panel, along with the relative humidity. The relative humidity increase has a notable and immediate effect on the particulate chloride and nitrate concentration, starting when the relative humidity was only slightly increased.

Figure 3.6 shows the effect of injecting steam into the smog chamber to elevate RH on particle composition. At  $t = 0.6$  hours, particulate chloride decreased as we increased the relative humidity. However, we see no change in the rate of  $\text{ClNO}_2$  formation, and thus we believe we are observing a rapid hydrochloric acid displacement reaction (R9). This would explain the rapid loss of chloride without the subsequent enhanced production of  $\text{ClNO}_2$ . However, the  $\text{N}_2\text{O}_5$  concentration does not

appear to decrease substantially in response to the particulate  $\text{NO}_3^-$  increase, which suggests that the displacement of  $\text{HCl(g)}$  is induced at least in part by another mechanism. Acid displacement of  $\text{Cl}^-$  as  $\text{HCl(g)}$  through uptake of  $\text{HNO}_3(\text{g})$  directly, rather than by  $\text{HNO}_3$  generated through uptake of  $\text{N}_2\text{O}_5(\text{g})$ , is another chloride-nitrate substitution mechanism that was likely occurring (Li et al., 2015; Song and Carmichael, 2001). It should be noted that in a biomass-burning plume, any displaced  $\text{HCl(g)}$  may still become neutralized by  $\text{NH}_3(\text{g})$  and recondense as  $\text{NH}_4\text{Cl}$ , as was seen in Mexico City (Decarlo et al., 2008). This chloride would then again be available for heterogeneous displacement through uptake of  $\text{N}_2\text{O}_5$ . Also,  $\text{HCl(g)}$  can be photolyzed or oxidized by  $\cdot\text{OH}$  to form atomic chlorine, a powerful atmospheric oxidant.

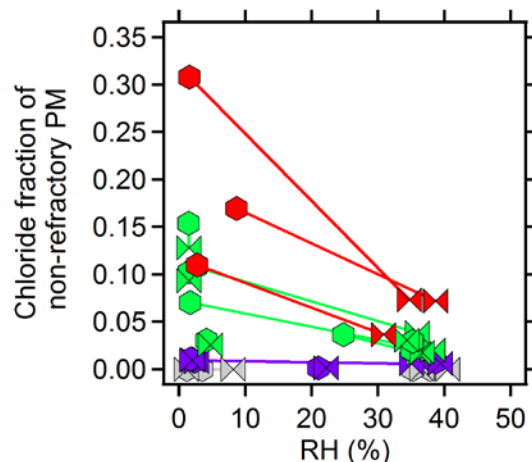


Figure 3.7. Chloride fraction of non-refractory particulate mass ( $f_{\text{Cl}}$ ) as a function of relative humidity. Hexagons indicate measurements taken at the beginning of the experiment, and bowties mark measurements at the end of the experiment. In instances where steam was injected into the smog chamber, the relative humidity increased and  $f_{\text{Cl}}$  decreased.

As shown in Figure 3.6, even a modest increase in relative humidity can cause a rapid increase in particulate nitrate and decrease in particulate chloride. Figure 3.7 shows the effect of a relative humidity ramp on the particulate chloride mass fraction,  $f_{\text{Cl}}$ . Markers are colored according to particle type, consistent with Figure 3.3 and Figure 3.4. Marker symbols indicate if the reported measurement was taken before (hexagons) or after (bow ties) steam injection. In some cases the smog chamber was



pre-humidified, or steam was never injected, and thus for those two cases both markers for the same experiment will be at the same relative humidity. Particles with low initial chloride content (i.e. birch-wood smoke and ammonium bisulfate) showed very little change in the particulate chloride fraction. However, cutgrass and sawgrass both saw significant but incomplete reduction in  $fCl$ . We observed that a higher  $fCl$  prior to acid displacement resulted in a higher  $fCl$  following acid displacement. We investigated a relative humidity of up to 60%, but we did not observe any further chloride displacement beyond what was observed at 10% RH.

This incomplete displacement of  $Cl^-$  suggests that the displacement is limited by the availability of  $N_2O_5(g)$  and  $HNO_3(g \text{ or } aq)$  that form in the smoke aerosol. An alternate explanation is that the  $Cl^-$  that is not displaced was effectively encapsulated by black carbon or other particulate components, and therefore not available for reaction. However, if this  $Cl^-$  was unavailable for acid displacement by  $HNO_3$ , then it would also be unavailable for  $ClNO_2$  formation.  $ClNO_2$  formation appears to be consistent with the observed particulate  $Cl^-$  content, regardless of whether it has undergone acid displacement (Figure 3.7). The triangle markers in Figures 3.3 & 3.4 indicate experiments where the particles were humidified during  $ClNO_2$  formation. These markers follow the same trend as other low- $fCl$  aerosol systems, independent of relative humidity. This demonstrates that after acid displacement, the nitrate effect is not inhibiting  $N_2O_5$  uptake, and that although some of the particulate chloride does not become displaced by  $HNO_3$ , it is still available for the formation of  $ClNO_2$ .

### 3.4. Conclusion

$N_2O_5(g)$  and  $ClNO_2(g)$  are important nocturnal reservoirs that affect atmospheric oxidant budgets, but whose formation is not well understood. We have found that substantial amounts of  $N_2O_5(g)$  and then  $ClNO_2(g)$  can be produced quickly under nocturnal conditions similar to ambient biomass-burning smoke plumes.  $N_2O_5$  formation was not significantly impeded by competition between volatile organic compounds and  $NO_2$  for the  $NO_3^-$  radical. More  $ClNO_2$  was formed in the presence of particles that had a higher concentration of particulate chloride, and

this correlation was even stronger between  $\text{ClNO}_2$  produced and the particulate chloride mass fraction,  $f_{\text{Cl}}$ . Uptake of  $\text{N}_2\text{O}_5$  by the smog chamber walls proved to be a significant sink of  $\text{N}_2\text{O}_5$  which complicates the calculation of the heterogeneous kinetic parameters  $\gamma_{\text{N}_2\text{O}_5}$  and  $\phi_{\text{ClNO}_2}$ . However, by comparing the temporal trends of  $\text{N}_2\text{O}_5$  with deliquesced ammonium bisulfate aerosol we can conclude that the biomass burning aerosol consistently had a  $\gamma_{\text{N}_2\text{O}_5}$  much less than 0.28 (Bertram et al., 2009), and these particles efficiently convert what  $\text{N}_2\text{O}_5$  is taken up to  $\text{ClNO}_2$ .

Furthermore, we have found that with just a modest increase in relative humidity, acid displacement of  $\text{HCl}(\text{g})$  by  $\text{HNO}_3(\text{g})$  rapidly decreases the particulate chloride content. However, this displacement is incomplete, and the remaining particulate chloride appears to be of sufficient concentration to reduce the nitrate effect and still produce  $\text{ClNO}_2$ . The incomplete loss of particulate chloride through either  $\text{ClNO}_2$  production from  $\text{N}_2\text{O}_5(\text{g})$  uptake or  $\text{HCl}$  acid displacement from  $\text{HNO}_3(\text{g})$  uptake is likely caused by a depletion of the  $\text{HNO}_3$  reactants in the smoke aerosol. Since we do not see complete chloride displacement but can confirm that the remaining  $\text{Cl}^-$  is still available for formation of  $\text{ClNO}_2$ , we believe that the displacement is limited by the availability of  $\text{N}_2\text{O}_5$  and  $\text{HNO}_3$ .

Now that we have confirmed that  $\text{N}_2\text{O}_5$  and  $\text{ClNO}_2$  are effectively formed in biomass burning plumes despite the competing chloride loss by acid displacement, future work will include a kinetic model that will allow for the quantification of the  $\text{N}_2\text{O}_5$  wall loss in these experiments. This will enable the calculation of the reactive uptake probability of  $\text{N}_2\text{O}_5$  ( $\gamma_{\text{N}_2\text{O}_5}$ ) and the yield of  $\text{ClNO}_2$  ( $\phi_{\text{ClNO}_2}$ ) for the biomass-burning aerosols we tested. These are the key parameters that have previously been implemented in chemical transport models to study the impact of  $\text{N}_2\text{O}_5$  uptake and chlorine activation chemistry on the atmospheric oxidant budget. These models can then be used to estimate the impact of the  $\text{N}_2\text{O}_5$  and  $\text{ClNO}_2$  formation that in this work have shown are likely to occur in biomass-burning plumes today and historically around the globe (Simon et al., 2009).

### 3.5. References

- Abbatt, J. P. D., Lee, A. K. Y. and Thornton, J. A.: Quantifying trace gas uptake to tropospheric aerosol: recent advances and remaining challenges, *Chem. Soc. Rev.*, 41(19), 6555, doi:10.1039/c2cs35052a, 2012.
- Ahern, A. T., Subramanian, R., Saliba, G., Lipsky, E. M., Donahue, N. M. and Sullivan, R. C.: Effect of secondary organic aerosol coating thickness on the real-time detection and characterization of biomass-burning soot by two particle mass spectrometers, *Atmos. Meas. Tech.*, 9, 6117–6137, doi:10.5194/amt-9-6117-2016, 2016.
- Akagi, S. K., Craven, J. S., Taylor, J. W., McMeeking, G. R., Yokelson, R. J., Burling, I. R., Urbanski, S. P., Wold, C. E., Seinfeld, J. H., Coe, H., Alvarado, M. J. and Weise, D. R.: Evolution of trace gases and particles emitted by a chaparral fire in California, *Atmos. Chem. Phys.*, 12(3), 1397–1421, doi:10.5194/acp-12-1397-2012, 2012.
- Alexander, B.: Impact of preindustrial biomass-burning emissions on the oxidation pathways of tropospheric sulfur and nitrogen, *J. Geophys. Res.*, 109(D8), D08303, doi:10.1029/2003JD004218, 2004.
- Alvarado, M. J., Lonsdale, C. R., Yokelson, R. J., Akagi, S. K., Coe, H., Craven, J. S., Fischer, E. V., McMeeking, G. R., Seinfeld, J. H., Soni, T., Taylor, J. W., Weise, D. R. and Wold, C. E.: Investigating the links between ozone and organic aerosol chemistry in a biomass burning plume from a prescribed fire in California chaparral, *Atmos. Chem. Phys.*, 15(12), 6667–6688, doi:10.5194/acp-15-6667-2015, 2015.
- Atkinson, R., Baulch, D. L., Cox, R. A., Crowley, J. N., Hampson, R. F., Hynes, R. G., Jenkin, M. E., Rossi, M. J. and Troe, J.: Evaluated kinetic and photochemical data for atmospheric chemistry: Volume I - gas phase reactions of O<sub>x</sub>, HO<sub>x</sub>, NO<sub>x</sub> and SO<sub>x</sub> species, *Atmos. Chem. Phys.*, 4(6), 1461–1738, doi:10.5194/acp-4-1461-2004, 2004.
- Behnke, W., George, C., Scheer, V. and Zetzsch, C.: Production and decay of ClNO<sub>2</sub> from the reaction of gaseous N<sub>2</sub>O<sub>5</sub> with NaCl solution : Bulk and aerosol experiments, *J. Geophys. Res.*, 102, 3795–3804, 1997.

Bertram, T. H. and Thornton, J. A.: Toward a general parameterization of  $\text{N}_2\text{O}_5$  reactivity on aqueous particles: the competing effects of particle liquid water, nitrate and chloride, *Atmos. Chem. Phys.*, 9(21), 8351–8363, doi:10.5194/acp-9-8351-2009, 2009.

Bertram, T. H., Thornton, J. A. and Riedel, T. P.: An experimental technique for the direct measurement of  $\text{N}_2\text{O}_5$  reactivity on ambient particles, *Atmos. Meas. Tech.*, 2(1), 231–242, doi:10.5194/amt-2-231-2009, 2009.

Brown, S. S., Ryerson, T. B., Wollny, A. G., Brock, C. A., Peltier, R., Sullivan, A. P., Weber, R. J., Dubé, W. P., Trainer, M., Meagher, J. F., Fehsenfeld, F. C. and Ravishankara, A. R.: Variability in Nocturnal Nitrogen Oxide Processing and Its Role in Regional Air Quality, *Science* (80-. ), 311(5757), 2006.

Brown, S. S., Dubé, W. P., Tham, Y. J., Zha, Q., Xue, L., Poon, S., Wang, Z., Blake, D. R., Tsui, W., Parrish, D. D. and Wang, T.: Nighttime chemistry at a high altitude site above Hong Kong, *J. Geophys. Res. Atmos.*, 121(5), 2457–2475, doi:10.1002/2015JD024566, 2016.

Carbone, S., Onasch, T., Saarikoski, S., Timonen, H., Saarnio, K., Sueper, D., Rönkkö, T., Pirjola, L., Häyriinen, A., Worsnop, D. and Hillamo, R.: Characterization of trace metals on soot aerosol particles with the SP-AMS: detection and quantification, *Atmos. Meas. Tech.*, 8, 4803–4815, doi:10.5194/amt-8-4803-2015, 2015.

Cox, R. A. and Derwent, R. G.: The ultraviolet absorption spectrum of gaseous nitrous acid, *J. Photochem.*, 6, 23–24, 1976.

Decarlo, P. F., Kimmel, J. R., Trimborn, A., Northway, M. J., Jayne, J. T., Aiken, A. C., Gonin, M., Fuhrer, K., Horvath, T., Docherty, K. S., Worsnop, D. R. and Jimenez, J. L.: Field-deployable, high-resolution, time-of-flight aerosol mass spectrometer, *Anal. Chem.*, 78(24), 8281–8289, doi:10.1029/2001JD001213, 2006.

DeCarlo, P. F., Dunlea, E. J., Kimmel, J. R., Aiken, A. C., Sueper, D., Crounse, J., Wennberg, P. O., Emmons, L., Shinozuka, Y., Clarke, A., Zhou, J., Tomlinson, J., Collins, D. R., Knapp, D., Weinheimer, A. J., Montzka, D. D., Campos, T. and Jimenez, J. L.: Fast airborne aerosol size and chemistry measurements above Mexico City and Central Mexico

during the MILAGRO campaign, *Atmos. Chem. Phys.*, 8(14), 4027–4048, doi:10.5194/acp-8-4027-2008, 2008.

Dentener, F. J. and Crutzen, P. J.: Reaction of  $\text{N}_2\text{O}_5$  on tropospheric aerosols: Impact on the global distributions of  $\text{NO}_x$ ,  $\text{O}_3$ , and OH, *J. Geophys. Res. Atmos.*, 98(D4), 7149–7163, doi:10.1029/92JD02979, 1993.

Docherty, K. S., Jaoui, M., Corse, E., Jimenez, J. L., Offenberg, J. H., Lewandowski, M. and Kleindienst, T. E.: Collection Efficiency of the Aerosol Mass Spectrometer for Chamber-Generated Secondary Organic Aerosols, *Aerosol Sci. Technol.*, 47, 294–309, doi:10.1080/02786826.2012.752572, 2013.

Escorcia, E. N., Sjostedt, S. J. and Abbatt, J. P. D.: Kinetics of  $\text{N}_2\text{O}_5$  Hydrolysis on Secondary Organic Aerosol and Mixed Ammonium Bisulfate–Secondary Organic Aerosol Particles, *J. Phys. Chem. A*, 114(50), 13113–13121, doi:10.1021/jp107721v, 2010.

Gard, E. E., Kleeman, M. J., Gross, D. S., Hughes, L. S., Allen, J. O., Morrical, B. D., Fergenson, D. P., Dienes, T., Ga, M. E., Johnson, R. J., Cass, G. R. and Prather, K. A.: Direct Observation of Heterogeneous Chemistry in the Atmosphere, *Science* (80-. ), 279(February), 1998.

Gaston, C. J., Lopez-Hilfiker, F. D., Whybrew, L. E., Hadley, O., McNair, F., Gao, H., Jaffe, D. A. and Thornton, J. A.: Online molecular characterization of fine particulate matter in Port Angeles, WA: Evidence for a major impact from residential wood smoke, *Atmos. Environ.*, 138, 99–107, doi:10.1016/j.atmosenv.2016.05.013, 2016.

Graedel, T. E. and Keene, W. C.: Tropospheric budget of reactive chlorine, *Global Biogeochem. Cycles*, 9(1), 47–77, doi:10.1029/94GB03103, 1995.

Grieshop, A. P., Donahue, N. M. and Robinson, A. L.: Laboratory investigation of photochemical oxidation of organic aerosol from wood fires 2: analysis of aerosol mass spectrometer data, *Atmos. Chem. Phys.*, 9(6), 2227–2240, doi:10.5194/acp-9-2227-2009, 2009.

Hays, M. D., Geron, C. D., Linna, K. J., Smith, N. D. and Schauer, J. J.: Speciation of Gas-Phase and Fine Particle Emissions from Burning of Foliar Fuels, *Environ. Sci. Technol.*, 36(11), 2281–2295, doi:10.1021/es0111683, 2002.

Hecht, T. A. and Seinfeld, J. H.: Development and validation of a generalized mechanism for photochemical smog, *Environ. Sci. Technol.*, 6(1), 47–57, doi:10.1021/es60060a003, 1972.

Hennigan, C. J., Sullivan, A. P., Collett, J. L. and Robinson, A. L.: Levoglucosan stability in biomass burning particles exposed to hydroxyl radicals, *Geophys. Res. Lett.*, 37(9), 2–5, doi:10.1029/2010GL043088, 2010.

Huff Hartz, K. E., Rosenørn, T., Ferchak, S. R., Raymond, T. M., Bilde, M., Donahue, N. M. and Pandis, S. N.: Cloud condensation nuclei activation of monoterpene and sesquiterpene secondary organic aerosol, *J. Geophys. Res. Atmos.*, 110(D14), n/a-n/a, doi:10.1029/2004JD005754, 2005.

Huffman, J. A., Ziemann, P. J., Jayne, J. T., Worsnop, D. R., Jimenez, J. L., Aiken, A., Docherty, K., Ulbrich, I., Decarlo, P., Kimmel, J., Dunlea, E., Cubi-Son, M., Trimborn, A., Kroll, J., Northway, M. and Salcedo, D.: Development and Characterization of a Fast-Stepping/Scanning Thermodenuder for Chemically-Resolved Aerosol Volatility Measurements, *Aerosol Sci. Technol.*, 42, 395–407, doi:10.1080/02786820802104981, 2008.

Jayne, J. T., Leard, D. C., Zhang, X., Davidovits, P., Smith, K. A., Kolb, C. E. and Worsnop, D. R.: Development of an Aerosol Mass Spectrometer for Size and Composition Analysis of Submicron Particles, *Aerosol Sci. Technol.*, 33(1–2), 49–70, doi:10.1080/027868200410840, 2000.

Kercher, J. P., Riedel, T. P. and Thornton, J. A.: Chlorine activation by N<sub>2</sub>O<sub>5</sub>: simultaneous, in situ detection of ClNO<sub>2</sub> and N<sub>2</sub>O<sub>5</sub> by chemical ionization mass spectrometry, *Atmos. Meas. Tech.*, 2(2), 193–204, 2009.

Knopf, D. A., Forrester, S. M. and Slade, J. H.: Heterogeneous oxidation kinetics of organic biomass burning aerosol surrogates by O<sub>3</sub>, NO<sub>2</sub>, N<sub>2</sub>O<sub>5</sub>, and NO<sub>3</sub>, *Phys. Chem. Chem. Phys.*, 13(47), 21050, doi:10.1039/c1cp22478f, 2011.

Lee, A. K. Y., Willis, M. D., Healy, R. M., Wang, J. M., Jeong, C.-H., Wenger, J. C., Evans, G. J. and Abbatt, J. P. D.: Single-particle characterization of biomass burning organic aerosol (BBOA): evidence for non-uniform mixing of high molecular weight organics and potassium, *Atmos. Chem. Phys.*, 16(9), 5561–5572, doi:10.5194/acp-16-5561-2016, 2016.

Levin, E. J. T., McMeeking, G. R., Carrico, C. M., Mack, L. E., Kreidenweis, S. M., Wold, C. E., Moosmüller, H., Arnott, W. P., Hao, W. M., Collett, J. L. and Malm, W. C.: Biomass burning smoke aerosol properties measured during Fire Laboratory at Missoula Experiments (FLAME), *J. Geophys. Res.*, 115(D18), 1–15, doi:10.1029/2009JD013601, 2010.

Li, C., Ma, Z., Chen, J., Wang, X., Ye, X., Wang, L., Yang, X., Kan, H., Donaldson, D. J. and Mellouki, A.: Evolution of biomass burning smoke particles in the dark, *Atmos. Environ.*, 120, 244–252, doi:10.1016/j.atmosenv.2015.09.003, 2015.

Li, J., Posfai, M., Hobbs, P. V. and Buseck, P. R.: Individual Aerosol Particles from Biomass Burning in Southern Africa Compositions and Aging of Inorganic Particles, , 108, 1–12, doi:10.1029/2002JD002310, 2003.

Lopez-Hilfiker, F. D., Mohr, C., Ehn, M., Rubach, F., Kleist, E., Wildt, J., Mentel, T. F., Lutz, A., Hallquist, M., Worsnop, D. and Thornton, J. A.: A novel method for online analysis of gas and particle composition: description and evaluation of a Filter Inlet for Gases and AEROsols (FIGAERO), *Atmos. Meas. Tech.*, 7(4), 983–1001, doi:10.5194/amt-7-983-2014, 2014.

Matthew, B. M., Middlebrook, A. M. and Onasch, T. B.: Collection efficiencies in an Aerodyne Aerosol Mass Spectrometer as a function of particle phase for laboratory generated aerosols, *Aerosol Sci. Technol.*, 42(January), 884–898, doi:10.1080/02786820802356797, 2008.

McNeill, V. F., Patterson, J., Wolfe, G. M. and Thornton, J. A.: The effect of varying levels of surfactant on the reactive uptake of  $\text{N}_2\text{O}_5$  to aqueous aerosol, *Atmos. Chem. Phys.*, 6(6), 1635–1644, doi:10.5194/acp-6-1635-2006, 2006.

Middlebrook, A. M., Bahreini, R., Jimenez, J. L. and Canagaratna, M. R.: Evaluation of Composition-Dependent Collection Efficiencies for the Aerodyne Aerosol Mass Spectrometer using Field Data, *Aerosol Sci. Technol.*, 46(3), 258–271, doi:10.1080/02786826.2011.620041, 2012.

Mielke, L. H., Stutz, J., Tsai, C., Hurlock, S. C., Roberts, J. M., Veres, P. R., Froyd, K. D., Hayes, P. L., Cubison, M. J., Jimenez, J. L., Washenfelter, R. A., Young, C. J., Gilman, J. B., de Gouw, J. A., Flynn, J. H., Grossberg, N., Lefer, B. L., Liu, J., Weber, R. J. and Osthoff, H. D.: Heterogeneous formation of nitryl chloride and its role as a nocturnal NO<sub>x</sub> reservoir species during CalNex-LA 2010, *J. Geophys. Res. Atmos.*, 118(18), 10,638–10,652, doi:10.1002/jgrd.50783, 2013.

Mielke, L. H., Furgeson, A., Odame-Ankrah, C. A. and Osthoff, H. D.: Ubiquity of ClNO<sub>2</sub> in the urban boundary layer of Calgary, Alberta, Canada, *Can. J. Chem.*, 94(4), 414–423, doi:10.1139/cjc-2015-0426, 2016.

Ng, N. L., Herndon, S. C., Trimborn, A., Canagaratna, M. R., Croteau, P. L., Onasch, T. B., Sueper, D., Worsnop, D. R., Zhang, Q., Sun, Y. L. and Jayne, J. T.: An Aerosol Chemical Speciation Monitor (ACSM) for Routine Monitoring of the Composition and Mass Concentrations of Ambient Aerosol, *Aerosol Sci. Technol.*, 45(7), 780–794, doi:10.1080/02786826.2011.560211, 2011.

Onasch, T. B., Trimborn, A., Fortner, E. C., Jayne, J. T., Kok, G. L., Williams, L. R., Davidovits, P. and Worsnop, D. R.: Soot Particle Aerosol Mass Spectrometer: Development, Validation, and Initial Application, *Aerosol Sci. Technol.*, 46(7), 804–817, doi:10.1080/02786826.2012.663948, 2012.

Osthoff, H. D., Roberts, J. M., Ravishankara, A. R., Williams, E. J., Lerner, B. M., Sommariva, R., Bates, T. S., Coffman, D., Quinn, P. K., Dibb, J. E., Stark, H., Burkholder, J. B., Talukdar, R. K., Meagher, J., Fehsenfeld, F. C. and Brown, S. S.: High levels of nitryl chloride in the polluted subtropical marine boundary layer, *Nat. Geosci.*, 1(5), 324–328, doi:10.1038/ngeo177, 2008.

Ovadnevaite, J., Ceburnis, D., Canagaratna, M., Berresheim, H., Bialek, J., Martucci, G., Worsnop, D. R. and O'Dowd, C.: On the effect of wind speed on submicron sea salt



mass concentrations and source fluxes, *J. Geophys. Res. Atmos.*, 117(16), 1–11, doi:10.1029/2011JD017379, 2012.

Presto, A. A., Huff Hartz, K. E. and Donahue, N. M.: Secondary Organic Aerosol Production from Terpene Ozonolysis. 2. Effect of NO<sub>x</sub> Concentration, *Environ. Sci. Technol.*, 39(18), 7046–7054, doi:10.1021/es050400s, 2005.

Reid, J. S., Koppmann, R., Eck, T. F. and Eleuterio, D. P.: A review of biomass burning emissions part II: intensive physical properties of biomass burning particles, *Atmos. Chem. Phys.*, 5(3), 799–825, doi:10.5194/acp-5-799-2005, 2005.

Riedel, T. P., Wagner, N. L., Dubé, W. P., Middlebrook, A. M., Young, C. J., Öztürk, F., Bahreini, R., VandenBoer, T. C., Wolfe, D. E., Williams, E. J., Roberts, J. M., Brown, S. S. and Thornton, J. A.: Chlorine activation within urban or power plant plumes: Vertically resolved ClNO<sub>2</sub> and Cl<sub>2</sub> measurements from a tall tower in a polluted continental setting, *J. Geophys. Res. Atmos.*, 118(15), 8702–8715, doi:10.1002/jgrd.50637, 2013.

Roberts, J. M., Osthoff, H. D., Brown, S. S., Ravishankara, A. R., Coffman, D., Quinn, P. and Bates, T.: Laboratory studies of products of N<sub>2</sub>O<sub>5</sub> uptake on Cl<sup>−</sup> containing substrates, *Geophys. Res. Lett.*, 36(20), L20808, doi:10.1029/2009GL040448, 2009.

Robinson, E. S., Onasch, T. B., Worsnop, D. and Donahue, N. M.: Collection efficiency of alpha-pinene secondary organic aerosol particles explored via light scattering single particle aerosol mass spectrometry, *Atmos. Meas. Tech. Discuss.*, 1–29, doi:10.5194/amt-2016-271, 2016a.

Robinson, E. S., Donahue, N. M., Ahern, A. T., Ye, Q. and Lipsky, E.: Single-particle measurements of phase partitioning between primary and secondary organic aerosols, *Faraday Discuss.*, 0, 1–19, doi:10.1039/C5FD00214A, 2016b.

Ryder, O. S., Campbell, N. R., Morris, H., Forestieri, S., Ruppel, M. J., Cappa, C., Tivanski, A., Prather, K. and Bertram, T. H.: Role of Organic Coatings in Regulating N<sub>2</sub>O<sub>5</sub> Reactive Uptake to Sea Spray Aerosol, *J. Phys. Chem. A*, 119(48), 11683–11692, doi:10.1021/acs.jpca.5b08892, 2015.

Salcedo, D., Onasch, T. B., Dzepina, K., Canagaratna, M. R., Zhang, Q., Huffman, J. A., DeCarlo, P. F., Jayne, J. T., Mortimer, P., Worsnop, D. R., Kolb, C. E., Johnson, K. S., Zuberi, B., Marr, L. C., Volkamer, R., Molina, L. T., Molina, M. J., Cardenas, B., Bernabé, R. M., Márquez, C., Gaffney, J. S., Marley, N. A., Laskin, A., Shutthanandan, V., Xie, Y., Brune, W., Leshner, R., Shirley, T. and Jimenez, J. L.: Characterization of ambient aerosols in Mexico City during the MCMA-2003 campaign with Aerosol Mass Spectrometry: results from the CENICA Supersite, *Atmos. Chem. Phys.*, 6(4), 925–946, doi:10.5194/acp-6-925-2006, 2006.

Salcedo, D., Onasch, T. B., Aiken, A. C., Williams, L. R., de Foy, B., Cubison, M. J., Worsnop, D. R., Molina, L. T. and Jimenez, J. L.: Determination of particulate lead using aerosol mass spectrometry: MILAGRO/MCMA-2006 observations, *Atmos. Chem. Phys.*, 10(12), 5371–5389, doi:10.5194/acp-10-5371-2010, 2010.

Schauer, J. J., Kleeman, M. J., Cass, G. R. and Simoneit, B. R. T.: Measurement of Emissions from Air Pollution Sources. 3. C 1 –C 29 Organic Compounds from Fireplace Combustion of Wood, *Environ. Sci. Technol.*, 35(9), 1716–1728, doi:10.1021/es001331e, 2001.

Simon, H., Kimura, Y., McGaughey, G., Allen, D. T., Brown, S. S., Osthoff, H. D., Roberts, J. M., Byun, D. and Lee, D.: Modeling the impact of ClNO<sub>2</sub> on ozone formation in the Houston area, *J. Geophys. Res.*, 114(D7), D00F03, doi:10.1029/2008JD010732, 2009.

Song, C. H. and Carmichael, G. R.: Gas-Particle Partitioning of Nitric Acid Modulated by Alkaline Aerosol, *J. Atmos. Chem.*, 40(1), 1–22, doi:10.1023/A:1010657929716, 2001.

Stockwell, C. E., Yokelson, R. J., Kreidenweis, S. M., Robinson, A. L., DeMott, P. J., Sullivan, R. C., Reardon, J., Ryan, K. C., Griffith, D. W. T. and Stevens, L.: Trace gas emissions from combustion of peat, crop residue, domestic biofuels, grasses, and other fuels: configuration and Fourier transform infrared (FTIR) component of the fourth Fire Lab at Missoula Experiment (FLAME-4), *Atmos. Chem. Phys.*, 14(18), 9727–9754, doi:10.5194/acp-14-9727-2014, 2014.

- Tham, Y. J., Wang, Z., Li, Q., Yun, H., Wang, W., Wang, X., Xue, L., Lu, K., Ma, N., Bohn, B., Li, X., Kecorius, S., Größ, J., Shao, M., Wiedensohler, A., Zhang, Y. and Wang, T.: Significant concentrations of nitryl chloride sustained in the morning: investigations of the causes and impacts on ozone production in a polluted region of northern China, *Atmos. Chem. Phys.*, 16(23), 14959–14977, doi:10.5194/acp-16-14959-2016, 2016.
- Thornton, J. A., Braban, C. F. and Abbatt, J. P. D.: N<sub>2</sub>O<sub>5</sub> hydrolysis on sub-micron organic aerosols: the effect of relative humidity, particle phase, and particle size, *Phys. Chem. Chem. Phys.*, 5(20), 4593, doi:10.1039/b307498f, 2003.
- Thornton, J. A., Kercher, J. P., Riedel, T. P., Wagner, N. L., Cozic, J., Holloway, J. S., Dubé, W. P., Wolfe, G. M., Quinn, P. K., Middlebrook, A. M., Alexander, B. and Brown, S. S.: A large atomic chlorine source inferred from mid-continental reactive nitrogen chemistry., *Nature*, 464(7286), 271–4, doi:10.1038/nature08905, 2010.
- Villena, G., Bejan, I., Kurtenbach, R., Wiesen, P. and Kleffmann, J.: Interferences of commercial NO<sub>2</sub> instruments in the urban atmosphere and in a smog chamber, *Atmos. Meas. Tech.*, 5(1), 149–159, doi:10.5194/amt-5-149-2012, 2012.
- Wahner, A., Mentel, T. F. and Sohn, M.: Gas-phase reaction of N<sub>2</sub>O<sub>5</sub> with water vapor: Importance of heterogeneous hydrolysis of N<sub>2</sub>O<sub>5</sub> and surface desorption of HNO<sub>3</sub> in a large teflon chamber, *Geophys. Res. Lett.*, 25(12), 2169–2217, 1998a.
- Wahner, A., Mentel, T. F., Sohn, M. and Stier, J.: Heterogeneous reaction of N<sub>2</sub>O<sub>5</sub> on sodium nitrate aerosol, *J. Geophys. Res. Atmos.*, 103(D23), 31103–31112, doi:10.1029/1998JD100022, 1998b.
- Wang, T., Tham, Y. J., Xue, L., Li, Q., Zha, Q., Wang, Z., Poon, S. C. N., Dubé, W. P., Blake, D. R., Louie, P. K. K., Luk, C. W. Y., Tsui, W. and Brown, S. S.: Observations of nitryl chloride and modeling its source and effect on ozone in the planetary boundary layer of southern China, *J. Geophys. Res. Atmos.*, 121(5), 2476–2489, doi:10.1002/2015JD024556, 2016.
- Willis, M. D., Lee, A. K. Y., Onasch, T. B., Fortner, E. C., Williams, L. R., Lambe, A. T., Worsnop, D. R. and Abbatt, J. P. D.: Collection efficiency of the soot-particle aerosol

mass spectrometer (SP-AMS) for internally mixed particulate black carbon, *Atmos. Meas. Tech.*, 7(12), 4507–4516, doi:10.5194/amt-7-4507-2014, 2014.

Winer, A. M., Peters, J. W., Smith, J. P. and Pitts, J. N.: Response of commercial chemiluminescent nitric oxide-nitrogen dioxide analyzers to other nitrogen-containing compounds, *Environ. Sci. Technol.*, 8(13), 1118–1121, doi:10.1021/es60098a004, 1974.

Ye, Q., Robinson, E. S., Ding, X., Ye, P., Sullivan, R. C. and Donahue, N. M.: Mixing of secondary organic aerosols versus relative humidity, *Proc. Natl. Acad. Sci. U. S. A.*, 113(45), 12649–12654, doi:10.1073/pnas.1604536113, 2016.

Yokelson, R. J., Crounse, J. D., DeCarlo, P. F., Karl, T., Urbanski, S., Atlas, E., Campos, T., Shinozuka, Y., Kapustin, V., Clarke, A. D., Weinheimer, A., Knapp, D. J., Montzka, D. D., Holloway, J., Weibring, P., Flocke, F., Zheng, W., Toohey, D., Wennberg, P. O., Wiedinmyer, C., Mauldin, L., Fried, A., Richter, D., Walega, J., Jimenez, J. L., Adachi, K., Buseck, P. R., Hall, S. R. and Shetter, R.: Emissions from biomass burning in the Yucatan, *Atmos. Chem. Phys.*, 9(15), 5785–5812, doi:10.5194/acp-9-5785-2009, 2009.

Young, C. J., Washenfelder, R. A., Roberts, J. M., Mielke, L. H., Osthoff, H. D., Tsai, C., Pikel'naya, O., Stutz, J., Veres, P. R., Cochran, A. K., VandenBoer, T. C., Flynn, J., Grossberg, N., Haman, C. L., Lefer, B., Stark, H., Graus, M., de Gouw, J., Gilman, J. B., Kuster, W. C. and Brown, S. S.: Vertically Resolved Measurements of Nighttime Radical Reservoirs in Los Angeles and Their Contribution to the Urban Radical Budget, *Environ. Sci. Technol.*, 46(20), 10965–10973, doi:10.1021/es302206a, 2012.

# 4. DEVELOPMENT, LABORATORY CHARACTERIZATION, AND FIELD DEPLOYMENT OF THE LASER ABLATION AEROSOL PARTICLE MASS SPECTROMETER

The Laser Ablation Aerosol Particle Time Of Flight (LAAPTOF) Mass Spectrometer is a new single-particle mass spectrometer that measures the size and chemical composition of individual particles between 160 nm and 1.0  $\mu\text{m}$  diameter. LAAPTOF measurements of aerosol particles in the lab and during an experimental field campaign at the Missoula Fire Sciences Lab were made to explore the detection capabilities of the new instrument. Using a free-firing excimer laser, the lower particle size of 50% transmission was found to be 160 nm, larger than that of a similar particle inlet on the Aerodyne Aerosol Mass Spectrometer (AMS). Internally mixed particles of dihydroxybenzoic acid and potassium chloride show single-particle mass spectra with only the inorganic signal, or with both inorganic and organic ions. This difference is likely due to different amounts of laser power absorbed by each particle. Single-particle composition measurements were also used to help identify the mixing state of secondary organic aerosol

components mixed with primary combustion aerosol in smog chamber reactor experiments. Methods for utilizing quantitative AMS particle measurements to calibrate for matrix effects and compound specific detection efficiencies of the LAAPTOF are discussed.

## 4.1. Introduction

Atmospheric aerosols affect human health, visibility, and climate. Particles exist in a wide range of sizes and chemical compositions in the atmosphere, and these properties determine how the particles interact with their environment. Elemental carbon particles are known to be strong absorbers of sunlight. Their absorption of sunlight increases global radiative forcing, and warms the planet, whereas non-absorbing particles (e.g. dust and sea-spray) scatter light, thus decreasing visibility and also reflecting solar light back into space. This offsets some of the warming caused by greenhouse gases (Bond et al., 2013; IPCC, 2013; White and Roberts, 1977). Furthermore, some particles larger than 50-100 nm, depending on hygroscopicity, can serve as nuclei for water condensation, producing liquid cloud droplets. Clouds composed of increased numbers of smaller cloud droplets have stronger reflective properties and also tend to take longer to precipitate. Thus, increased particle concentrations can lead to longer lasting and whiter clouds that will reflect more sunlight into space (IPCC, 2013).

Particle size and composition determine whether a particle is a potential cloud condensation nuclei (CCN) under typical atmospheric conditions. An important constituent to consider is elemental carbon, a hydrophobic and strongly light absorbing product of incomplete combustion. Being hydrophobic, it does not readily nucleate a cloud droplet. This also extends the lifetime of elemental carbon particles as their rate of wet deposition is slow. This primary elemental carbon particle in the presence of other separate particle compositions is described as an externally mixed aerosol population. However, atmospheric processing may result in the condensation of hydrophilic secondary products, such as sulfuric acid and oxidized organic species. An aerosol population in which all the particles are elemental carbon coated in secondary material is described as internally mixed. In this specific case, the light absorption of the elemental carbon core is enhanced by the refractive coating

that acts as a lens and allows the elemental carbon particle to absorb more light than it would if externally mixed (Cappa et al., 2012; Lack et al., 2009).

This conversion of a hydrophobic particle into a hydrophilic internally mixed particle increases the particle's rate of wet deposition, and this reduces particle number and mass concentrations. This has a direct effect on human health. In general, there has been evidence of increased mortality with higher particle mass concentration (Dockery and Pope, 1993). Specifically, particles with a diameter less than 2.5  $\mu\text{m}$  penetrate deep into human lungs, and even smaller particles may pass through the blood-brain barrier (Kreuter et al., 1995; Schwartz et al., 2002). The toxicological potential of these ingested particles depends on their composition, which may be harmless sodium chloride, or may include known toxins like polycyclic aromatic hydrocarbons and/or heavy metals (Carbone et al., 2015; Finlayson-Pitts, 1997). Measurement of particulate mass presents many challenges, including small amounts of mass and many chemical species. *In situ* mass spectrometry of particles has been developed as a sensitive method for the detection of many types of aerosol (Sullivan and Prather, 2005).

This chapter will discuss the development of a new instrument for single-particle mass spectrometry (SP-MS), designated the Laser Ablation Aerosol Particle Time of Flight (LAAPTOF) mass spectrometer (Gemayel et al., 2016; Marsden et al., 2016). This work includes characterizing the instrument's performance in the lab, and preliminary results from the fourth Fire Laboratory At Missoula Experiment (FLAME-IV), an experimental campaign in Missoula, MT that was discussed in Chapter 2.

Mass spectrometry is widely used to great advantage to help characterize the multitude of aerosol compositions measured in laboratory and field campaigns. Two particle mass spectrometers of note are the previously mentioned LAAPTOF SP-MS, and the commercially available Aerodyne Aerosol Mass Spectrometer (AMS) (DeCarlo et al., 2006; Jayne et al., 2000). The AMS combines thermal vaporization with electron ionization, for size-resolved measurements of aggregate non-refractory aerosol composition with time resolution on the order of minutes. SP-MS has been

developed to make use of its high sensitivity and fast measurement time of individual particles on the order of seconds. Simultaneous measurement of particle vacuum aerodynamic diameter ( $d_{va}$ ) by time-of-flight between two continuous wave laser beams enables the correlation of particle composition with particle size (Su et al., 2004). The mass spectrum is produced by laser desorption/ionization (LDI) of an individual particle with one or two separate laser pulses. The ionized fragments of the particle are then measured with a bipolar time-of-flight mass spectrometer (ToF-MS) (Carson et al., 1995; Gard et al., 1997; Hinz et al., 1996; Zelenyuk and Imre, 2005).

Laser desorption/ionization typically produces many more ions per molecule than thermal desorption coupled with electron ionization. This facilitates the measurement of a solid or liquid mass suspended in gas with very high temporal resolution. For example, SP-MS is very sensitive to the very low concentrations of heavy metals which can be present in an aerosol population that are, by mass, composed mostly of aged organic aerosol. Particle composition measurements from filter collection and analysis would likely not have the sensitivity needed to detect the presence of heavy metals in episodic events. Mercury, an important semi-volatile species and a bioaccumulative neurotoxin, was observed by Murphy et al. (1998a) in about half the particles measured at high altitude during aircraft measurements using SP-MS. This observation raised questions about the fate of atmospheric mercury, which was thought to be removed from the atmosphere via condensation on aerosol. SP-MS was also used to detect heavy metals during the ground-based MILAGRO campaign. The lead and zinc containing aerosol, combined with air parcel back-trajectories, were used to identify urban manufacturing facilities as the source of significant but transient pollution around Mexico City, Mexico (Moffet et al., 2008).

Besides the ability to measure important tracers present in small concentrations, SP-MS provides important information about mixing state and refractory material. Airborne SP-MS measurements have measured the mixing state of inorganic (usually  $\text{SO}_4^{2-}$  containing species) and carbonaceous aerosol in the upper troposphere (Murphy et al., 2006). Particle light absorption is highly sensitive to the mixing state, causing either additional reflection or absorption enhancement via a



lensing effect (Cappa et al., 2012; Lack et al., 2009). These measurements of mixing state showed an unexpectedly high concentration of carbonaceous (likely organic) aerosol. This additional organic material increases the uncertainty of the predicted lifetimes of light absorbing material in the atmosphere.

Identifying trends in thousands of individual particle spectra can be very difficult. To better characterize these trends, single-particle mass spectra can be grouped into clusters containing common ions and similar relative ion intensities using a clustering or sorting computer algorithm such as ART-2a, K-means, or Fuzzy clustering (e.g. C-means) (Rebotier and Prather, 2007; Zelenyuk et al., 2008b). This allows us to more readily understand changes in the population's composition as a function of time by classifying the particles into groups of similar composition, that reflect the sources and processing of the particles. For example, correlating the time evolution of particle classes with air parcel back-trajectories, dust particles detected with SP-MS were shown to have reached Ireland from Europe, America, and Africa (Dall'Osto et al., 2004).

SP-MS is also invaluable in airborne campaigns where the velocity of the airplane through the atmosphere demands very high temporal resolution (Creamean et al., 2013; Murphy et al., 1998b, 2006; Pratt et al., 2009). Brock et al. (2004) used SP-MS's excellent temporal resolution along with gas-phase measurements to investigate atmospheric chemical processing in clouds. The ability to temporally resolve which particles were inside or outside a cloud showed that particles were scavenged by the cloud, but that gas-phase precursors persisted to form new particles after cloud processing. These and other unique capabilities of SP-MS are outlined more extensively by Pratt & Prather (2012), Sullivan & Prather (2005) and Murphy (2007).

Although SP-MS has been utilized broadly for the identification of species within individual aerosol particles, it is limited in its ability to quantitatively determine the mass of each component in the particle. The number of ions generated and the degree of fragmentation of these ions depend on several parameters, including instrument operation, LDI laser power, laser shot-to-shot variations,

particle composition, morphology, and mixing state. In contrast, the Aerodyne Aerosol Mass Spectrometer (AMS) is commonly used to quantify submicron aerosol mass populations composed of non-refractory material. This quantitative measurement can be used to assess the response of the SP-MS instruments to individual components in pure and internally mixed single particles (Healy et al., 2010). The AMS is limited to non-refractory material because the aerosol is vaporized via impaction on a  $\sim 600$  °C surface in a high vacuum, after which the resulting vapors are subjected to electron ionization. By controlling the vaporizer temperature and the energy of the ionizing electrons (typically 70 eV), the AMS obtains reproducible ion fragmentation patterns. The inability to measure components that do not vaporize at 600 °C (known as refractory components) limits the AMS's ability to characterize aerosol composed of black carbon and minerals, both of which are important and common components of atmospheric particles (DeCarlo et al., 2006; Jayne et al., 2000). Single-particle measurements in the AMS are also limited by the low ion signal produced from individual particles via electron ionization.

Post-measurement corrections are required to perform mass quantitative measurements with the AMS. One must account for an aerosol particle's propensity to impact on (as opposed to bounce off of) the vaporizer and also its ability to form ions from electron ionization. These two properties are characterized for individual components (e.g. organic, sulfate, nitrate, etc.) with corrections defined as collection efficiency and ionization efficiency, respectively (Jayne et al., 2000; Middlebrook et al., 2012). With an Aerodyne Light-Scattering (LS) module that detects each particle optically before it hits the vaporizer, *in situ* measurements of this collection efficiency are possible with a LS-AMS (Cross et al., 2007; Robinson et al., 2016).

The LS-AMS modification also allows the thermal desorption coupled with electron ionization instrument to operate in a single-particle collection mode. The light scattering module identifies the arrival of a particle into the vaporizing region, and ions are generated by the usual thermal desorption and electron ionization process. The single-particle LS-AMS measurements, like the normal ensemble method, cannot measure refractory material and are still subject to particle bounce.

Additionally, there is poor signal-to-noise for individual particle mass spectra due to the low efficiency of electron ionization and the small amount of mass contained in a single submicron particle. The signal-to-noise ratio is typically very good for individual particle detection by SP-MS due to the more efficient laser desorption/ionization process involved.

A new data acquisition card on more recent models of the AMS also allows for single-particle measurements without optical detection. This event trigger mode can acquire single particle mass spectra more rapidly than the instruments with only the light scattering module. This mode of operation is not limited to optically detectable particles, and thus can measure mass spectra for particles with diameters less than 200 nm. However, one cannot measure the particle bounce collection efficiency, and it does require a user-determined ion threshold to trigger the recording of an ion event. This may lead to sampling biases unless the aerosol population in question has otherwise been well characterized (Ye et al., 2016).

While laser desorption/ionization (LDI) single particle mass spectrometry methods do not suffer from the issue of particles bouncing off a vaporizing surface, the particle being measured must absorb light in the wavelength of the laser used for desorption/ionization to produce ions (Thomson et al., 1997). This phenomenon may be characterized as a matrix effect, which implies that each component in the particle is ionized as a function of the absorptive properties of the entire particle. For example, two particles that are 90% by mass organic liquid may produce very different total ion intensities if the other 10% is highly light absorbing black carbon, as opposed to a non-absorbing inorganic salt. The ion signal intensity generated from each particle is also affected by shot-to-shot variability in LDI laser power received by each particle (Steele et al., 2003, Wenzel and Prather, 2004).

A combined AMS and SP-MS measurement approach may yield an improved quantitative understanding of single particle mass spectra, including particles composed of multiple components; organic and inorganic, refractory and non-refractory. The development of the LAAPTOF has been the subject of the combined efforts of Aeromegt GmbH, Aerodyne Research Inc., and Ryan Sullivan's group in the

Center for Atmospheric Particle Studies (CAPS) at Carnegie Mellon University. Using a species-specific determination of ionization efficiency and matrix effects, similar to the AMS's correction for ionization efficiency and particle bounce, and combining measurements from the AMS and the LAAPTOF, it may be possible to significantly improve the mass quantitative capabilities of the LAAPTOF. It is the ultimate goal to have a single-particle mass spectrometer for which particle light absorption, ionization efficiency, and matrix effects have been characterized sufficiently for single-particle measurements to be mass quantitative for both refractory and non-refractory material.

The first step of this development is determining the baseline capabilities of the new single particle instrument; the first instrument of its kind was delivered to CMU in June of 2012. As this is the first LAAPTOF instrument produced, it is still in the prototype stage and requires extensive testing, troubleshooting, and characterization. These tests include: 1) measuring laser power and laser power variability from shot-to-shot, 2) investigating the fragmentation patterns of the particle mass spectra as a function of laser power and particle mixing state, 3) building a library of single-particle mass spectra from different particle sources and compositions, 4) comparing spectra with existing single-particle mass spectral libraries, and 5) investigating instrument sensitivities to different substances.

The LAAPTOF was deployed with the CAPS mobile laboratory for the Fire Lab At Missoula Experiment (FLAME-IV) field campaign in Missoula, Montana in the fall of 2012. The purpose of this field campaign was to measure the chemical, physical, and optical properties of emissions from simulated forest fires before and after photochemical processing, in collaboration with over 12 institutions (Stockwell et al., 2014; Tkacik et al., 2017). CAPS scientists returned to Missoula to investigate questions which arose from the prior FLAME-III experiments, including the cause of variability in the formation of secondary organic aerosol (SOA) within our simulated atmospheric aging chambers (Hennigan et al., 2011). The results from FLAME-IV regarding the production of SOA were described in detail in Chapter 2. During FLAME-IV, the LAAPTOF supplemented the quantitative measurements of non-

refractory aggregate aerosol components by the AMS with semi-quantitative measurements of individual particles and information about the mixing state of the aerosol during an experiment involving the external mixing black spruce smoke in a smog chamber with secondary organic aerosol (SOA) formed in a separate vessel, and then injected into the smog chamber. The LAAPTOF could determine that vapors from the secondary organic aerosol population did mix with the primary organic aerosol (Robinson et al., 2013; Ye et al., 2016).

## 4.2. Experimental

The LAAPTOF, a schematic of which is shown in Figure 4.1, has a number of components that dictate which particle sizes and compositions will be detected by the mass spectrometer. The LAAPTOF uses an aerodynamic lens to accelerate particles to their terminal velocity in a collimated beam within a chamber evacuated by a differentially pumped vacuum system (Liu et al., 2007). The particle then scatters light from two continuous violet ( $\lambda=405$  nm) 100 mW lasers, placed  $\sim 117$  mm apart along the trajectory of the particles. The velocity of the particle is determined from the time-of-flight between these two light scattering events. This velocity is a function of particle size, density, and shape, and can be related to a vacuum aerodynamic diameter ( $d_{va}$ ) (DeCarlo et al., 2004).

Particle detection also triggers the firing of an excimer laser. The particle is desorbed and ionized by the VUV ( $\lambda=193$  nm) laser pulse (GAM EX5 excimer laser operating with the ArF exciplex) and the ions are extracted by orthogonal electric fields into a dual polarity ToFwerk B-ToF mass spectrometer. The LDI process generates ions with a wide distribution of kinetic energy. A reflectron is used in both time-of-flight tubes to correct for the distribution of initial velocities for ions of the same mass-to-charge ratio ( $m/z$ ), though the resolution is still typically on the order of unit mass resolution. Ions are measured by multi-channel plate (MCP) detectors.

The system is held under vacuum by a unique multi-stage turbomolecular vacuum pump (Pfeiffer), backed by a diaphragm pump. Typical pressure at the lens exit is 2 Torr, while that in the mass spectrometer's ionization region is  $2 \times 10^{-7}$  Torr.

To maximize the number of particles hit with the laser pulse, the excimer laser can be triggered by the particle light scattering event when it passes through the laser beam of the second diode, which is just before the ion extraction region. Alternatively, the excimer laser can be triggered at a constant frequency, or free-fired, to attempt to generate ions from particles too small to be detected via light scattering. This free-firing method was used for all the data shown below, unless otherwise stated.

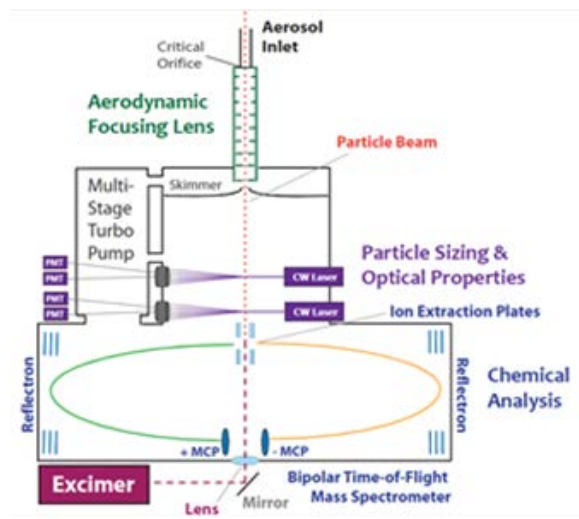


Figure 4.8. Schematic of the LAAPTOF single-particle mass spectrometer. The LAAPTOF has an aerodynamic lens aerosol inlet to focus and transmit submicron particles through a skimmer into the particle sizing region by velocimetry. The particle then passes through a second skimmer and into the mass spectrometer where ions are created with the excimer laser pulse are accelerated orthogonally into the dual polarity time-of-flight mass spectrometer.

The Aerodyne AMS is described in detail by Jayne et al. (2000). Using the same aerodynamic lens described above, the particles pass through a chopper (a spinning disc with a narrow 1% slit) that only transmits particles at a specific interval. The time between the particle passing through the slit and the detection of ions is used to derive coupled particle size and composition measurements. Impaction on a hot tungsten surface at 600 °C in vacuum vaporizes non-refractory material and the resulting gases are ionized using a 70 eV electron beam. These ions are then extracted into a high-resolution time-of-flight mass spectrometer. Light scattering may also be

used to detect the passage of a particle prior to thermal desorption (Cross et al., 2007). This allows the correlation of ion extractor pulses to a single particle and the measurement of ions which result from the thermal desorption and electron ionization from that individual particle. In the absence of this light scattering module, the extractor plates are pulsed at a predetermined frequency, which provides size-dependent aggregate composition information.

In order to correctly interpret the measurements obtained by the LAAPTOF, it is necessary to measure the efficiency with which particles of different sizes are transmitted by the lens inlet, which particles can be detected by the violet scattering lasers, and which particles are hit and generate ions with the 193 nm laser pulse (Shields et al., 2008). To generate particles of known composition, deionized water solutions of individual and mixed components are atomized and then size-selected by a TSI model 3071A differential mobility analyzer (DMA), with a sheath flow of 5.0 Lpm and a sample flow of 0.5 Lpm. Another TSI model 3071A DMA with a TSI model 3772 condensation particle counter (CPC), operating at a DMA sheath flow of 3.0 Lpm and a sample flow of 0.3 Lpm, measured the atomized particle concentration as a function of size (aerosol size distribution) by scanning the DMA's voltage. The combination of a scanning DMA size selector and a CPC particle counter is known as a scanning mobility particle sizer (SMPS). This determines particle concentration as a function of particle mobility diameter ( $d_{\text{mob}}$ ), which for spherical particles is equivalent to geometric diameter. The AMS and the LAAPTOF sampled aerosol with an inlet flow of 0.1 Lpm each, regulated by a critical orifice in the inlet of both instruments. Generated aerosol standards of known composition, size, and concentration, were used to probe the various detection limits of the LAAPTOF.

For experiments during the FLAME-IV campaign, black spruce smoke was pulled through heated stainless-steel transfer lines and diluted by a factor of 8 with Dekati eductor dilutors that injected the aerosol into a 7 m<sup>3</sup> Teflon bag (Tkacik et al., 2017). Details are provided in Chapter 2. The particle mass spectra collected during FLAME-IV will initially be useful in terms of determining aerosol mixing state and refractory components.

### 4.3. Results and Discussion

To collect and correctly interpret the mass spectra from the LAAPTOF, one must characterize the transmission of a particle through the aerodynamic lens, absorption of the excimer laser pulse by a particle, and finally the formation of ions from a particle. Diagnostics are presented below that probe the detection limits of the instrument along with preliminary results from the FLAME-IV experiments.

For a particle to be detected by the LAAPTOF, it must first be accelerated from ambient conditions into the particle sizing vacuum region, changing from ambient pressure ( $\sim 760$  Torr) to  $<10^{-1}$  Torr. After passing through a critical orifice at atmospheric pressure, the aerosol is collimated by a series of increasingly small apertures in an aerodynamic lens (Liu et al., 1995). This lens focuses the aerosol particles into a collimated beam that passes through a skimmer at its exit. This allows most of the (small and diffusive) gas molecules to be pumped away while the (more massive and inertial) particle beam is transmitted further into the instrument. However, some smaller particles diffuse out of the beam along with the gas molecules, and some of the larger particles are lost by impaction in the lens as the streamlines narrow. According to Liu et al. (2007), the lens design on the LAAPTOF has a lower and upper particle diameter limit of half-transmission of 0.075 and 0.75  $\mu\text{m}$ , respectively.

In Figure 4.2 the measured normalized rate at which size-selected particles of ammonium nitrate were detected as a function of size is displayed for the LAAPTOF and the AMS. By auto-firing the excimer laser on the LAAPTOF, we eliminate the instrument's detection dependence on particle light scattering efficiency. The LAAPTOF detected small particles less efficiently than the AMS. This is consistent with the fact that smaller particles diffuse more than larger particles due to Brownian motion during transit from the aerodynamic lens to the ionization region. While particles transmitted through the AMS need to hit a conical vaporizer with an area of  $\sim 1.149 \text{ mm}^2$  to produce vapors and ions, in the LAAPTOF particles must be hit by an excimer beam profile which is focused to a rectangular beam estimated to be 0.08



mm<sup>2</sup> in the ionization region. By determining that particles smaller than 200 nm are hit by the excimer with limited efficiency, one may apply a correction for the particle concentrations measured in the affected size (Qin et al., 2005; Marsden et al., 2016).

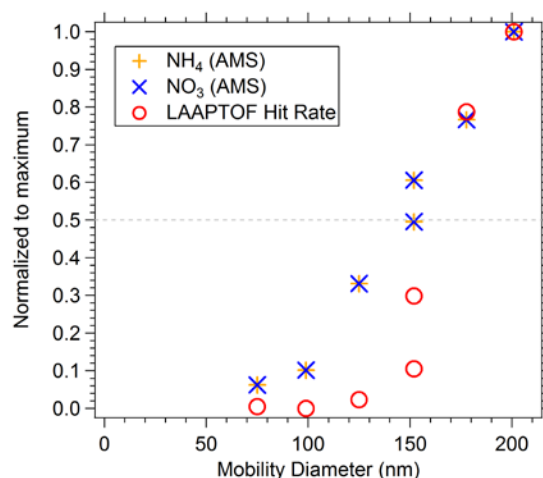


Figure 4.9. Detection efficiencies of ammonium and nitrate for the LAAPTOF and the AMS vs. particle mobility diameter. Efficiency decreases for mobility diameters smaller than 200 nm for size-selected ammonium nitrate particles. Both LAAPTOF hit-rate and AMS-measured mass have been normalized by the particle concentration determined by the SMPS and assuming unity transmission at  $d_{mob} = 200$  nm, which is supported by calculations and measurements from a similar lens (Liu et al., 2007).

In the LAAPTOF's light scattering region, the particle must pass through and scatter light from two 405 nm diode lasers so that the time delay between two scattered light pulses can be used to determine the particle velocity (and thus aerodynamic size), and also to trigger the desorption/ionization laser. The two scattered light detectors are composed of two sets of three optical fibers that form a circle with the incident laser beam passing between them into a beam dump. The forward scattered light from the particle is collected by the surrounding fibers, and transmitted to a photomultiplier tube (PMT). Each pair of fibers is measured by one PMT, so two PMTs are used for scattered light detection from each scattering laser. Two PMTs allows for the use of coincidence to separate scattering events from electronic noise.

From the flight time between the two lasers, a vacuum aerodynamic diameter may be derived with  $\sim 2\%$  uncertainty from the measured particle velocity. This particle diameter-velocity relationship is typically calibrated using polystyrene latex spheres – an aerosol of precisely known size, shape, and density. The amount of laser light scattered by a submicron particle is a function of the laser intensity, laser wavelength, particle size, particle shape, and the position of the particle's flight path in relation to the laser beam's energy profile. To minimize the light noise within the spectrometer, apertures are used to shape the scattering laser profile, and beam traps eliminate much of the unscattered incident light. These beam shaping apertures reduce the laser power from 100 mW to  $\sim 40$  mW, but allow for operation of the PMTs at a higher gain and increase sensitivity to light scattered by the particles. Small particles provide the two-fold challenge of not scattering much light when in the laser beam, and also having a greater proclivity to drifting out of the collimated particle beam as a result of Brownian diffusion. Irregularly shaped particles (e.g. cubic NaCl particles and fractal-like black carbon particles) also have a greater likelihood of diverging off the particle flight path from the aerodynamic lens than spherical particles do (e.g. liquid organic and aqueous particles) (Zelenyuk et al., 2008a).

Having determined the sampling biases between the inlet and the ionization region, we can begin to calculate the ratio of particles that were detected by the mass spectrometer to the number of particles that were drawn into the mass spectrometer. If a particle has triggered the scattering lasers, then the excimer laser will fire and this may result in the formation of ions that are extracted into the time-of-flight mass spectrometer. A particle will only be detected if it contains components that absorb the laser energy, and if the laser pulse has sufficient energy to desorb and ionize the material comprising the particle. The LAAPTOF uses a vacuum ultraviolet laser because each 193 nm VUV photon has more energy (6.425 eV) than longer wavelengths and because absorption cross-sections typically increase with decreasing wavelength. A rare example of a poorly light absorbing substance at  $\lambda=193$  nm is ammonium sulfate – a common component of atmospheric aerosol (Thomson et al., 1997). Fortunately, atmospheric aerosols larger than about 100 nm

are rarely composed of pure compounds. Atmospheric processing quickly oxidizes gas-phase precursors whose less volatile products will condense on the previously pure compounds. Therefore, submicron particles are likely to contain some component that will absorb the 193 nm photons.

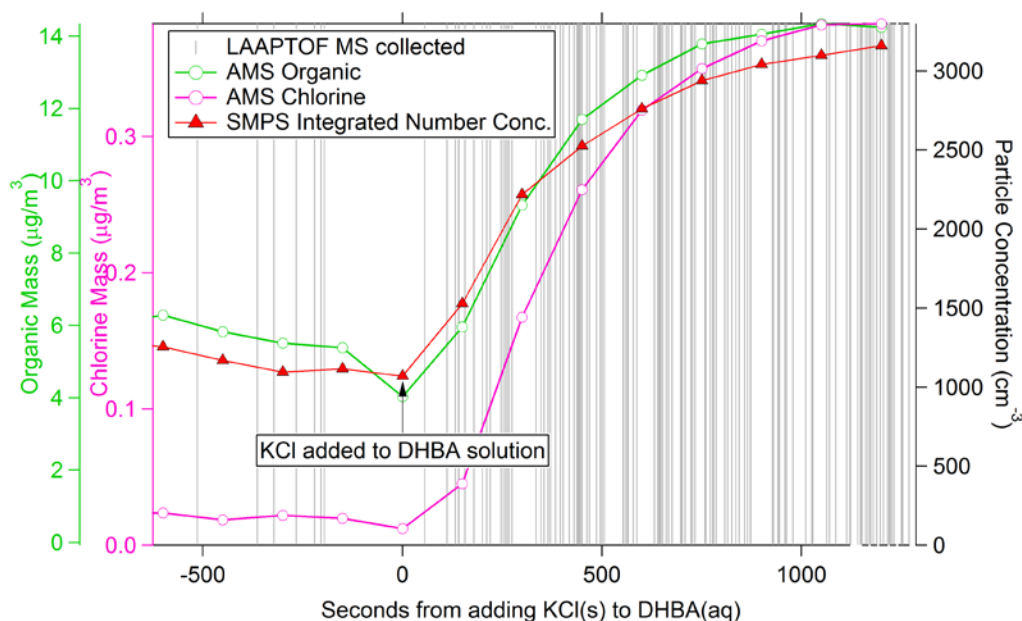


Figure 4.10. A solution of dihydroxybenzoic acid (DHBA) was atomized and the resulting particles were dried and size selected. At time zero, potassium chloride was added to the solution. The frequency of particle detection events from the LAAPTOF increase with the addition of KCl to the atomized dihydroxybenzoic acid solution at time = 0. Number concentration, organic mass, and chlorine mass also increased.

Pure organic aerosol was generated and measured to determine the LAAPTOF's sensitivity to size-selected pure dihydroxybenzoic acid, an organic molecule with a wide range of absorption due to its multiply substituted aromatic ring. Figure 4.3 shows the effect of changes in particle composition on instrument sensitivity. At time = 0, potassium chloride (KCl) was added to the atomized solution. Before time = 0, the 300 nm dihydroxybenzoic acid (DHBA) particles were rarely detected by the free-firing LAAPTOF. However, upon the addition of KCl to the solution at time = 0, the LAAPTOF particle hits (illustrated in Figure 4.3 by the

vertical gray lines) increased in frequency. This increase was due to the increase in particle number concentration and also sensitivity to the KCl now present in the particles.

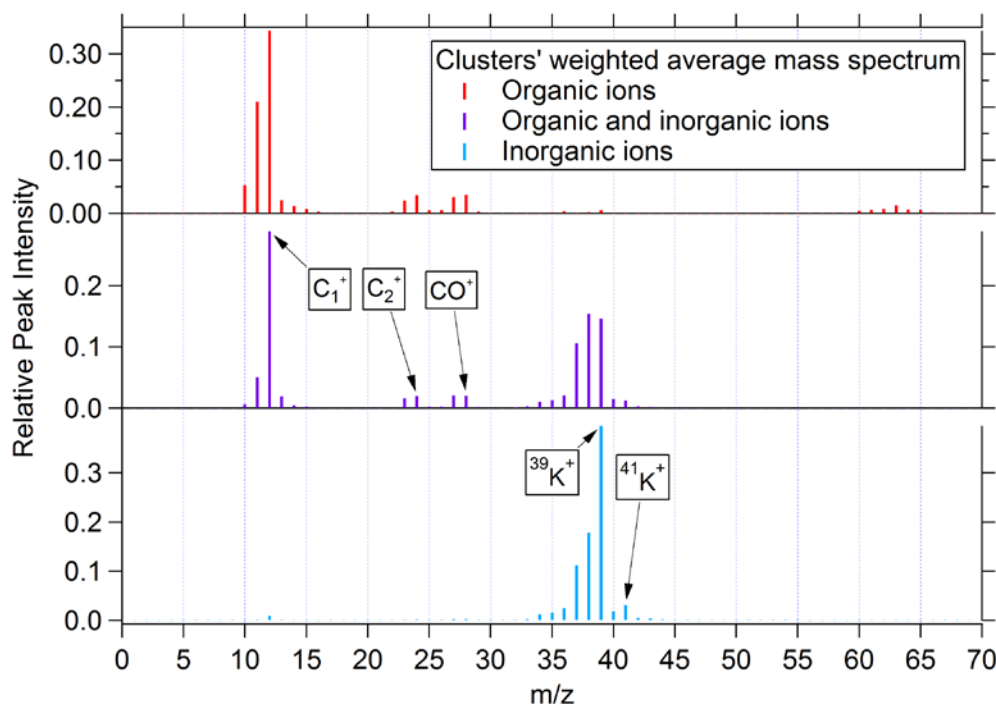


Figure 4.11. Weighted average mass spectra for three of the ten calculated clusters from DHBA-KCl mixing experiment. Organic cations include  $C_1^+$ ,  $C_2^+$ , and  $CO^+$ . Inorganic cations include  $^{39}K^+$  and  $^{41}K^+$ .

The particle detection frequency (normalized by particle concentration) increased by a factor of three with the addition of KCl to the DHBA solution. This could be due to either more efficient laser absorption of the mixture compared to the pure DHBA, or the low ionization energy of  $K^+$ . The latter is more likely, as the DHBA has an aromatic ring, which should absorb well at 193 nm. It is worth noting that the addition of KCl to the solution also increased the frequency of the detection of negative ions, likely due to electrons liberated from  $K^+$  and the high electron affinity of Cl.

The Fuzzy C-Means non-exclusive clustering algorithm (Bezdek, 1981) was used to classify the mass spectra into groups of similar particles. This algorithm

generates a user-designated number of clusters by initially assigning a random degree of belonging between the individual spectra and the clusters, referred to as the partition matrix. In fuzzy clustering a particle can belong to multiple clusters, and the partitioning matrix quantifies its degree of belonging for each cluster ranging from 0 to 1. The cluster's center, or representative mass spectrum, is then computed by averaging the mass spectra, weighed by the partitioning matrix, which for the first iteration is randomly generated. The partition matrix is then calculated, and the cluster center is recalculated with the new partition matrix. This process is iterated until the change in the partition matrix between iterations reaches a user-designated limit. The Fuzzy nature of the C-means algorithm means that particles can mathematically contribute to multiple cluster centers if they have ion signal values that are similar. As an example, consider if the algorithm identifies a cluster dominated by organic ions and a cluster dominated by sulfate ions. What will be the partitioning value of a particle that has both? In a non-fuzzy algorithm, the particle would be allocated into the single cluster it is most similar to. In the Fuzzy C-Means algorithm, the particle will belong equally (or inequally) to both clusters.

Ten clusters were calculated for the DHBA-KCl mixing experiment. The different degrees of fragmentation and magnitude (as well as integration and calibration errors from small total signal mass spectra) are included in the weighted average mass spectra in Figure 4.4, which represent three clusters of the ten identified. The top spectrum likely represents a pure organic particle, while the middle spectrum shows both organic cations and inorganic cations, and is therefore internally mixed. Finally, the bottom spectrum is dominated by inorganic peaks, namely potassium, which is readily ionized by LDI.

The ten clusters that were retrieved by the fuzzy clustering algorithm were then manually recombined into three groups based on their spectral characteristics; those containing only organic ion fragments, those containing only inorganic fragments, and those with both types of fragments. Figure 4.5 shows a particle's highest value from the partition matrix, which tells the degree to which each particle mass spectrum belongs to a group,

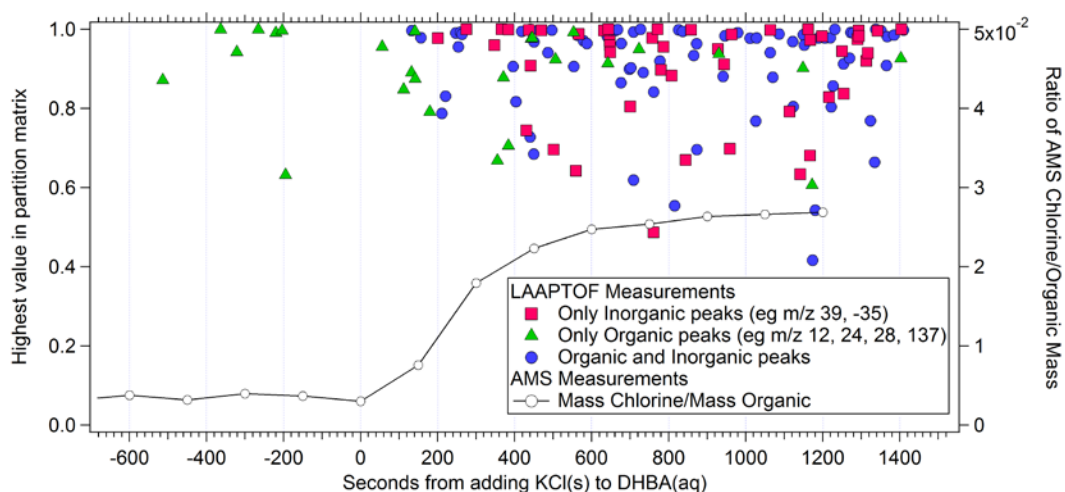


Figure 4.12. The highest value of each particle in the partition matrix calculated by Fuzzy C-Means clustering. A calculated metric for comparison between the similarity of individual particle mass spectra and the weighted average mass spectra of three groups of clusters: a group dominated by organic ions (tentatively identified as  $C^+$ ,  $C_2^+$ ,  $CO^+$ , and dehydrated DHBA), a group dominated by inorganic ions ( $K^+$ ,  $Cl^-$ ), and a group with strong contributions from both organic and inorganic components.

with values from 0 to 1. A value near 1 for a cluster means that the individual particle mass spectrum had the same  $m/z$  intensities as the calculated weighted average; the cluster average mass spectra or weight matrix shown in Figure 4.4. A change in mass composition is measured as a function of time by the LAAPTOF and the AMS from near pure organic to a mix of organic and inorganic salt. The left abscissa shows how similar an individual particle's mass spectrum is to the weight matrix of each of the three reference mass spectra. Values less than 1 suggest that although a particle may have similar  $m/z$  to the cluster's weighted average spectrum, but also deviate significantly. This could indicate the absence of key ions, or the presence of additional ions not present in the reference spectrum.

Identical particles that are exposed to different laser intensities will generate different mass spectra, both in degree of fragmentation and magnitude. An excimer laser's power is determined by the population inversion of metastable multiplexes (in this case, ArF). The standard deviation of the power of each laser

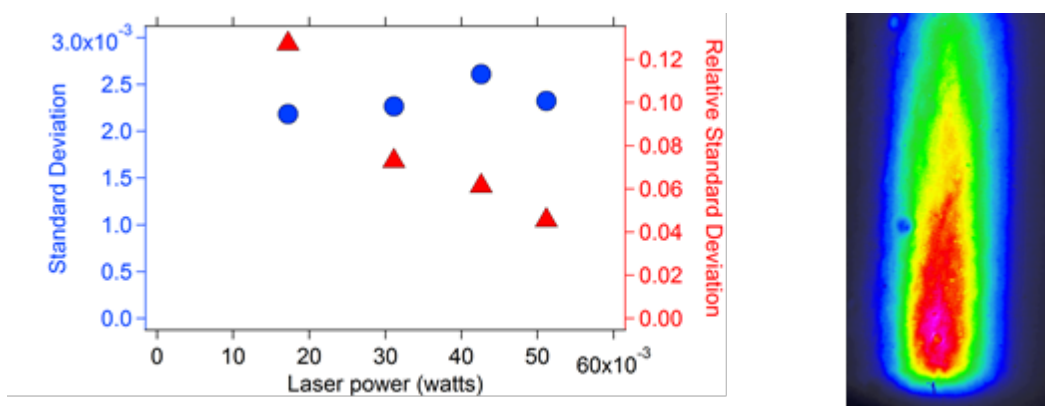


Figure 4.13. (left, a) Standard deviation (blue) and absolute deviation (red) shot-to-shot variation at different average laser powers. (right, b) The energy profile of the unfocused excimer pulse, which is colored by energy intensity from blue (low) to red (high). Within the ionization region, the beam is focused to 200  $\mu\text{m}$  by 400  $\mu\text{m}$ . Thus the submicron particles can receive a wide range of laser energy across the LDI laser beam's profile.

shot was found to be consistent as a function of average laser power (Figure 4.6a). The relative standard deviation decreases with increasing laser power, which suggests external attenuation of the laser beam's power with the laser operating near maximum power may decrease absolute shot-to-shot variation, while reducing the laser power to the appropriate levels that avoid excessive ion fragmentation. The operation of the instrument at high laser power results in the increased fragmentation of molecules within the particle, and in some cases the creation of new ions within the ion plume that do not reflect the original particle composition (e.g. a mass spectrum from  $\text{NH}_4^+$  containing aerosol has been observed to form  $[\text{N}_2\text{H}]^+$ ). Particles may also encounter different laser energies depending on where in the laser profile they are ablated. Figure 4.6b displays an image of the unfocused excimer laser's profile from a single laser shot. Particle diameters are usually  $<1\%$  of the total beam width, and therefore may be ablated in the shoulder of the laser profile and experience less energy transfer than a particle that is ablated in the center. The effect of different laser powers on the degree of fragmentation for the same substance, in this case DHBA, is shown in Figure 4.7. The bottom mass spectrum shows very little

fragmentation, with the only visible fragment being the dehydrated form of the original molecule ( $[M-H_2O]^+$ ,  $m/z$  136). The upper mass spectrum was from an identical particle, and is shown to be fragmented in some cases to atomic carbon at  $m/z$  12. This is likely due to increased laser power absorbed (Steele et al., 2003).

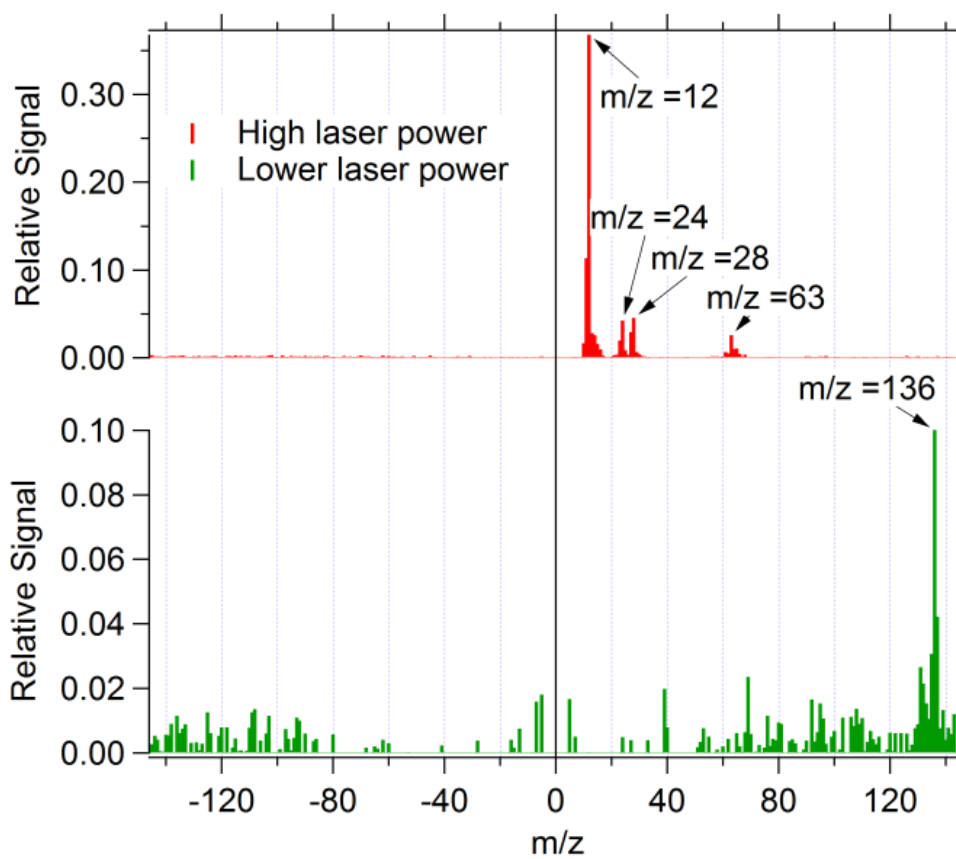


Figure 4.14. Two single-particle mass spectra from size-selected 300 nm DHBA particles. Lower laser power causes minimal fragmentation, producing a dehydrated cation ( $[M-H_2O]^+$ ,  $m/z$  136) of DHBA (MW=154), whereas higher power can cause fragmentation to atomic cations.

This variability in measured spectra from particle-to-particle was observed in a mixing experiment performed during FLAME-IV. In this dual smog chamber experiment, diluted combustion aerosol was introduced into the chamber and then experienced photochemical oxidation when the UV lights were turned on. Secondary organic aerosol (SOA) generated from oxidizing  $\alpha$ -pinene with  $O_3$  was then



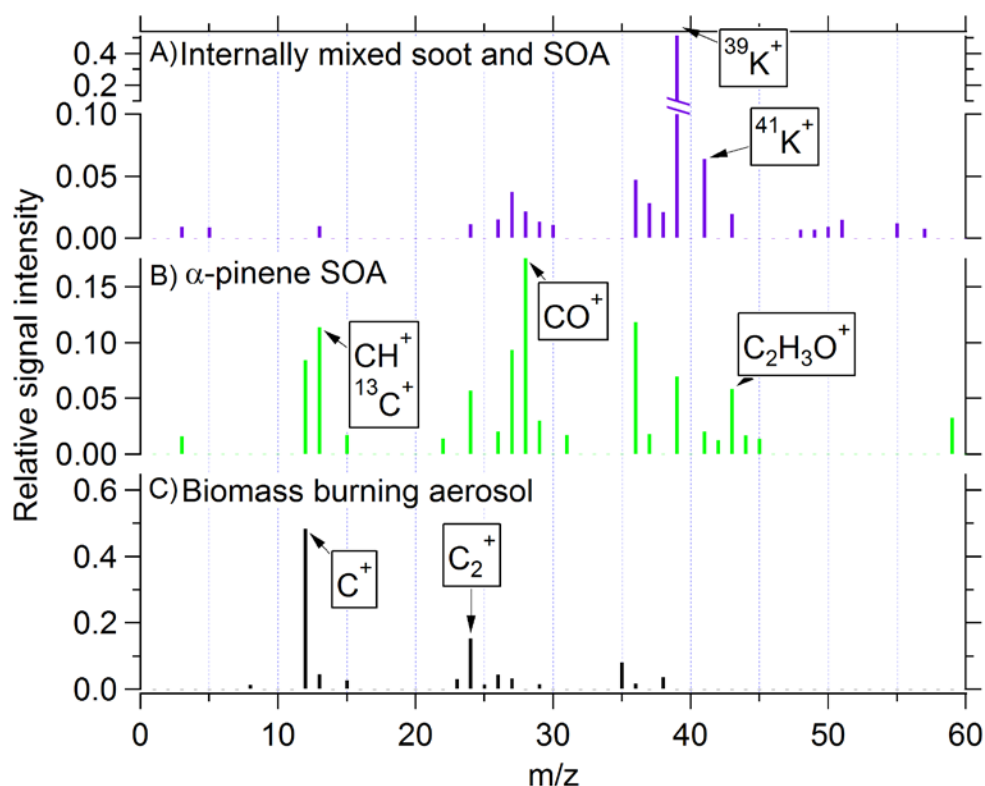


Figure 4.15. Individual particle mass spectra for positive ions collected during a biomass smoke and SOA mixing experiment. The bottom mass spectrum was collected before the addition of SOA and the middle spectra was collected immediately after SOA was mixed into the chamber. The top mass spectrum was collected some hours after the SOA was introduced to the chamber and photochemistry was induced by the UV lights.

introduced into the chamber already filled with biomass smoke. Single-particle mass spectra were detected during different stages of the mixing experiment and classified using fuzzy clustering. The mass spectrum from a biomass burning particle (Figure 4.8c) shows initial members of an elemental carbon ion series  $C_1$  and  $C_2$ , consistent with a particle containing black carbon. The  $\alpha$ -pinene SOA particle (Figure 4.8b) shows two peaks likely from oxidized organics,  $C_2H_3O^+$  and  $CO^+$ . Finally, the internally mixed soot and SOA particle (Figure 4.8a) has a peak at  $m/z$  39 as well as oxidized organic fragments. Potassium ( $^{39}K^+$ ) is a common feature in biomass-burning aerosol for SP-MS, and the isotopic peak at  $m/z$  41 ( $^{41}K^+$ ) corroborates the identification of  $m/z$  39 as  $^{39}K^+$  (Silva et al., 1999).

Although potassium is a prevalent marker for biomass burning, it is not present in all biomass burning particles (Silva et al., 1999), and thus not all biomass burning particles will have potassium ion markers, as shown in Figure 4.8. Whether or not one can reliably expect that all soot particles will have the strong potassium peak will require further analysis. In the FLAME-IV mixing experiment we observed that the K-deficient organic rich particles rapidly decayed after the introduction of K-rich particles, suggesting that the SOA particles were coagulating with the primary soot particles that also contain potassium.

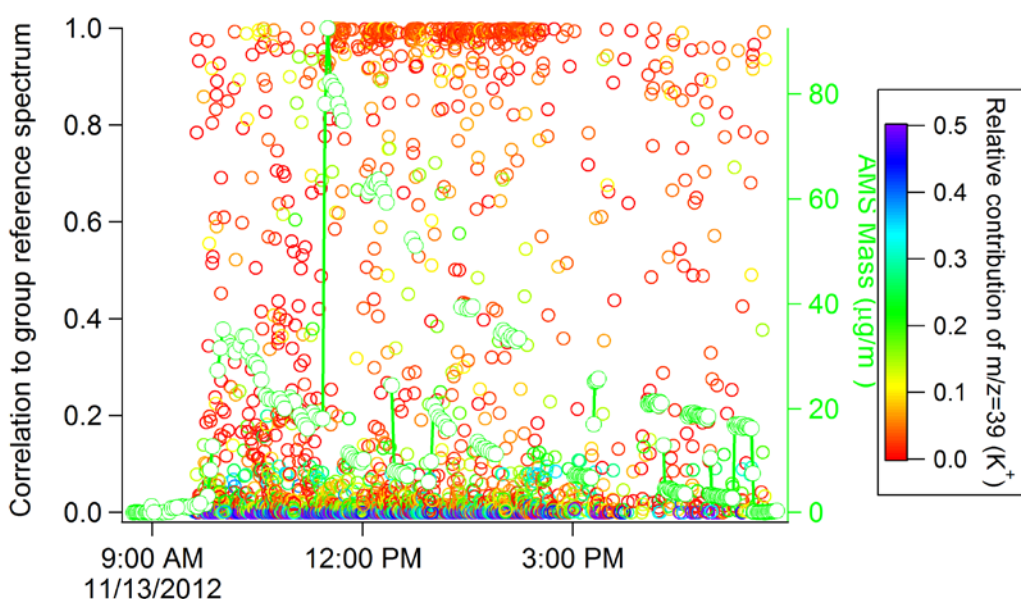


Figure 4.16. The correlation of single particle mass spectra to cluster center output from a fuzzy cluster algorithm. Values close to one are similar to the mass spectrum in Fig. 4.8b. When  $\alpha$ -pinene SOA is introduced into the chamber at time = 11:30AM, more particles with a high correlation with this SOA-like cluster appear. This cluster is characterized by the absence of  $K^+$  (indicated by color scale) and the presence of organic fragments.

Fuzzy clustering was run on the mass spectra obtained from the mixing experiment and a cluster was identified that had little contribution at  $m/z$  39 and strong contributions of oxidized organics. The temporal trace (Figure 4.9) shows that the particles that correlate strongly with this cluster's weight matrix coincide with

the introduction of pure SOA particles, which occurred at time = 11:30AM. The presence of particles before the introduction of SOA that also match this mixed cluster suggests that the clustering may not be perfect. The relative contribution of the  $K^+$  ion signal (color scale in Figure 4.8) indicates that the clustering algorithm did successfully identify a group of particles that does not have a strong potassium signal.

Fuzzy clustering analysis is useful a useful tool for sorting through the large variability between individual particle mass spectra. Manually looking for trends in the large numbers of mass spectra would be impractical, and categorizing particles using peak searches based on strict rules for can be misleading due to large variability in the sources and compositions of particles, and their resulting mass spectra.

#### 4.4. LAAPTOF development

Since the execution of these original experiments, a number of improvements have been made to the LAAPTOF, particularly with respect to increasing the particle mass spectra collection rate. At the time of the experiments shown above, the light scattering units delivered were not working. There were a number of issues including insufficient cooling of the laser diodes and thermal deformation of the laser light shaping elements (lenses and baffles). These issues resulted in decreased laser power and increased background noise, respectively. Thus, mass spectra were collected by free-firing the excimer at 10 Hz and collecting the resulting spectra, whether a particle was ablated or not. The data was analysed after the fact to remove blank spectra and to isolate particle ablation events. During the end of the experiment shown in Figure 4.4, we obtained mass spectra from fewer than 0.002% of the particles sampled by the instrument, recording mass spectra from  $\sim 5$  particles  $\text{min}^{-1}$  for high sample loadings of  $3000$  particles  $\text{cm}^{-3}$ . To obtain a sufficient number of mass spectra to measure the changes in particle composition on the timescale of minutes, the instrument must operate with light scattering units to trigger the excimer.

The AeroMegt-designed light scattering units were engineered to ensure that if a light-scattering event were detected, then the excimer would be triggered and could not miss the particle. This was confirmed by Marsden et al. (2016) using the

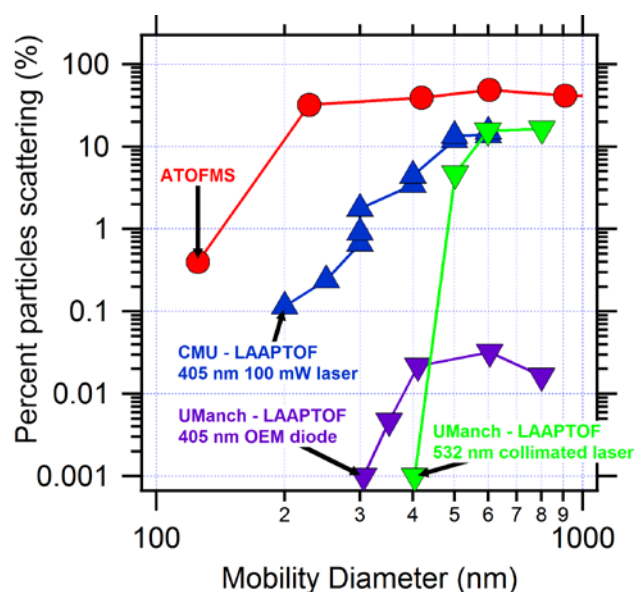


Figure 4.10. Percent of particles that scattered light as a function of mobility diameter. ATOFMS measurements are shown in red circles from Pratt et al. (2009). Upside down triangles are LAAPTOF scattering efficiencies reported by Marsden et al. (2016) from the University of Manchester. Purple triangles show the AeroMegt system with laser diodes, and the green show a collimated 532 nm laser beam with a custom optical system. The system described in this work is reported as blue triangles.

second generation of LAAPTOF laser diode light scattering units, which included more robust optical components and better cooling. Marsden et al. (2016) also showed that a limiting factor for the fraction of particles detected was the very small overlap between the particle beam and the scattering laser cross section, similar to what we show in Figure 4.2. The AeroMegt-designed focussed diode laser has a measured second moment width ( $4D\sigma$ ) of 51.2  $\mu\text{m}$ , compared to the particle beam width (represented as a 1D Gaussian) which can range from 0.25 mm to 0.77 mm (Huffman et. al, 2005, Marsden et al. 2016). The means that although every particle that scatters light will be hit by the excimer, only a small fraction of the total particles sampled will scatter light. Marsden et al. (2016) increased the fraction of particles that scattered light by using a different laser and optics system on the University of Manchester LAAPTOF. The new 532 nm laser beam they implemented exited through an aspherical fiberport resulting in a specified beam output that has a collimated

profile. The Gaussian laser beam has a much larger cross-section with the particle beam,  $1/e^2 = 330 \mu\text{m}$  according to the manufacturer (model PAF-X-2A, Thorlabs.)

Figure 4.10 shows the percent of sampled particles that trigger the excimer laser by scattering light as a function of size. The purple triangles show the 2<sup>nd</sup> generation AeroMegt design (focused 405 nm laser diode), and the green triangles show the collimated 532 nm beam. Although the collimated beam does increase the fraction of scattered particles by an order of magnitude for particles with a mobility diameter  $> 400 \text{ nm}$ , the AeroMegt system has a smaller minimum detection diameter of  $\sim 350 \text{ nm}$ , due to the shorter light wavelength of 405 nm, despite the reduced intensity compared to the collimated 532 nm beam (40 mW vs 300 mW). This is because the scattering cross section of the particle is proportional to  $\lambda^{-4}$  in the Raleigh regime for small particles, and thus shorter wavelengths scatter more efficiently for smaller particles. In the Mie regime, the relationship between scattering cross section and wavelength is more complex, but the trend is generally consistent; small particles scatter shorter wavelengths of light more efficiently than longer wavelengths.

For this reason, we redesigned our new laser light scattering system to use 405 nm laser light, shown as upward pointing blue triangles in Figure 4.10. The use of 100 mW diode-pumped solid state Coherent Obis lasers and the custom laser shaping optics shown in Figure 4.11, allows us to a) use most of the original 100 mW beam power ( $\sim 70 \text{ mW}$  measured after beam shaping), b) increase the overlap of the scattering laser with the particle beam,  $1/e^2 = 61 \mu\text{m}$ , and c) scatter light effectively at small particle sizes  $< 400 \text{ nm}$ . This beam diameter was calculated using the Focal Spot Size Calculator for Gaussian Laser Beams available on the Ophir Optronics website (2017), based on the formulas in Self (1983). However, fundamental challenges still exist for the laser shaping system shown in Figure 4.11. While Marsden et al. introduce their laser via a fiber optic, the Obis laser is mount on and guided by optomechanical components into the Carnegie Mellon University (CMU) LAAPTOF. This means that alignment of the lasers must be meticulous, and are susceptible to internal and external vibrations. These vibrations may cause the laser to clip an element of the beam-shaping optics and scatter light into the mass

spectrometer, thus increasing the background noise and limiting how high the gain on the photomultipliers can be set without saturating the component.

Key improvement for increased particle detection would be a wider collection angle for light collection. Marsden et al. (2016) stated that this would not only increase the sensitivity of the system, it would also reduce the size-dependent effects at larger particle diameters. Furthermore, improved light collection over a much larger range of light scattering angles (e.g. use of an ellipsoid mirror) could reduce the sensitivity of the detectors to stray light from misaligned optics or window glow. The ATOFMS, as described by Pratt et al. (2009) uses an ellipsoid and thus has a more robust alignment method as well as a high degree of overlap with the particle beam. Shown as red circles in Figure 4.10, the ellipsoid mirror allows a very high scattering efficiency and a very small lower particle size limit due to its wide light collection angle, effective removal of scattered light, and lack of laser beam focusing, despite the use of the longer wavelength 532 nm laser.

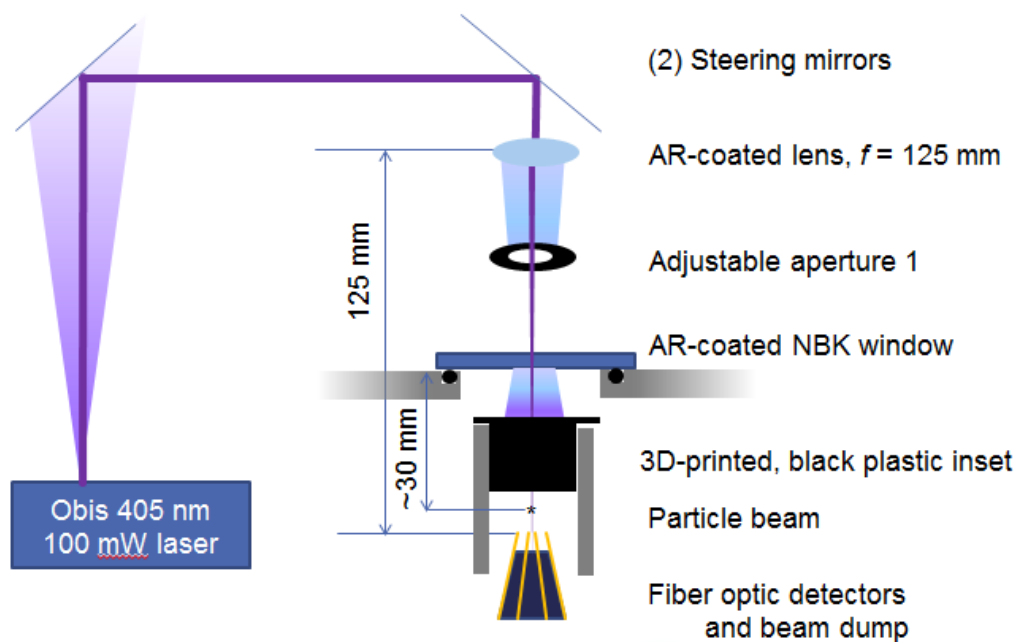


Figure 4.11. A schematic of the improved CMU LAAPTOF scattering laser shaping system. The schematic is not drawn to scale.

Another enhancement to the Carnegie Mellon University LAAPTOF is the introduction of the Aerodyne Research Inc. high-pressure aerodynamic lens inlet (Williams et al., 2013). Besides focusing submicron particles into a tighter particle beam (increasing scattering efficiency), this new high-pressure lens efficiently transmits particles up to a diameter of about 2.5  $\mu\text{m}$  ( $\text{PM}_{2.5}$ ), as opposed to the current low-pressure lens's upper limit of approximately 700 nm.  $\text{PM}_{2.5}$  concentration and composition is of particular interest because of its ability to penetrate into human lungs.  $\text{PM}_{2.5}$  mass is one of the National Air Quality Standards enforced by the EPA. The ability to measure supermicron particles with the LAAPTOF would enable the efficient sampling and transmission of a wider range of particle sizes and compositions, including dust and marine aerosol that are typically maximized in supermicron particle size ranges (Sullivan et al., 2007).

Another potential area for improvement for the LAAPTOF is increasing the uniformity by which the instrument exposes particles to excimer laser pulses. Future work will include reducing the variability in shot-to-shot laser power, or at least recording said laser power for each shot, indexing the laser shot power with each particle's mass spectrum, and homogenizing the excimer laser pulse profile to produce a flat-top laser profile (Steele et al., 2003; Wenzel and Prather, 2004). A laser power meter would measure 10% of each excimer laser pulse, using a beam splitter, and the laser power would be recorded along with each particle's mass spectrum. This will allow the analysis of variations in particle mass spectra as a function of the laser power with which the particle was ablated.

It is important to know that a particle was exposed to sufficient energy to ionize a component of interest before positing that an undetected component wasn't in fact present in the particle. Higher laser power could be maintained for particles expected to contain difficult to ionize components. The mixing experiment shown in Figure 4.5 is a good example of internally mixed particles that appear to be purely inorganic because there was likely insufficient power to ionize the organic components. Operating at a lower laser power, which will reduce fragmentation and provide more molecular information, as opposed to molecule fragmentation, carries

the inherent risk of not detecting hard to ionize components. Having the ability to record and control laser power with great precision will allow such a decision to be made, and may even lead to a protocol of systematically varying LDI laser power during measurement cycles.

Along similar lines, an attenuation method will be developed to reduce the laser power that is transmitted to the particle while still operating the laser at high output power. This has been shown to produce more consistent shot-to-shot laser power (Figure 4.6a). A number of attenuation methods are available, including neutral density filters and half-wave plates combined with polarized filters. The laser will also be attenuated by the various techniques available for homogenizing the excimer pulse profile. Proven methods for beam homogenization that result in a flat-top laser profile will be utilized to transform the pseudo-Gaussian profile into a flat-top shape. The methods we are considering implementing and testing include mixing optics or fiber optics that use reflective surfaces to separate, mix, and recombine the light; and gold-plated apertures, which block the less intense shoulders of a pseudo-Gaussian profile (Steele et al., 2003; Wenzel and Prather, 2004). This will further reduce the variability in the amount of energy transferred to a particle. With the present pseudo-Gaussian excimer beam profile, the particle can be ablated in the low-energy shoulder of the beam, in the higher-energy peak, or in a localized hot-spot of very high laser power. Once laser power is a logged shot-to-shot parameter, a flat-top profile will ensure all ionized particles were exposed to the same laser energy.

By homogenizing the laser profile, and reducing shot-to-shot laser variability, we should measure similar mass spectra, including absolute ion signal, for identical particle compositions. This is the first critical step towards improving the quantitative abilities of the LAAPTOF. Once a relatively consistent signal is generated for identical particles, one may begin to calibrate for the complex ionization mechanisms that are the result of internally mixed particles containing multiple components. Atmospherically common systems of interest include primary particles (e.g. elemental carbon, dust, sea spray) coated with secondary species (e.g. oxidation products from volatile organic compounds, or nitrogen or sulfur oxides). The AMS



will provide a mass quantitative measure of the complex mixed aerosol composition for comparison to and calibration of the signal and fragmentation patterns observed with the LAAPTOF.

## 4.5. Conclusion

Laser desorption/ionization single particle mass spectrometers (LDI-SP-MS) generate a wealth of information about complex aerosol populations by measuring individual particle sizes and composition. Although most LDI-SP-MS instruments operate using similar principles, variation in particle detection, excimer laser, and data analysis methods makes characterization of each instrument critical for translating the data acquired to an accurate understanding of the aerosol measured. Laboratory characterization experiments with the new LAAPTOF have shown that the instrument has a larger minimum particle cutoff size than the AMS, likely due to the smaller cross sectional area for particle detection (i.e. the LAAPTOF excimer beam profile vs. the surface area of the AMS thermal vaporizer). Particles of known composition, both pure and mixed, displayed a high degree of variability between individual particle mass spectra measured by the LAAPTOF. This is likely due to beam inhomogeneity and shot-to-shot laser power variation. A fuzzy clustering algorithm was shown to effectively identify particle mass spectra with similar ions. During the FLAME-IV campaign, the LAAPTOF detected particles that could be identified as containing elemental carbon, oxidized organic carbon, and also trace marker ions like potassium. These particle types are expected for photochemically aged biomass smoke aerosol. The LAAPTOF also provided valuable measurement of the mixing between pure SOA and the biomass burning smoke, showing that after mixing SOA tracer ions existed on biomass burning particles. However, we cannot discount the potential that ozone from the SOA-containing secondary vessel induced SOA condensation on the biomass burning aerosol, which was then detected by the LAAPTOF. More experiments will need to be conducted to evaluate the potential of fresh SOA formation to mix through the gas phase with fresh biomass-burning emissions.

The continued development and characterization of the LAAPTOF and its comparison with the AMS will result in a powerful tool for investigating the physiochemical characteristics of PM<sub>2.5</sub> in real-time at the single-particle level. This is at a time when the atmospheric chemistry community is actively searching for improved means to determine the physical phase of aerosol particles, their individual ice nucleating potential, and the fate of refractory black carbon following atmospheric aging, to name just a few important topics where understanding can be advanced by quantitative single-particle mass spectrometry. The LAAPTOF's insensitivity to particle bounce, high sensitivity to trace particle components, and ability to measure refractory components will play an important part in addressing these outstanding questions in atmospheric chemistry.

## 4.6. References

- Bond, T. C., Doherty, S. J., Fahey, D. W., Forster, P. M., Berntsen, T., DeAngelo, B. J., Flanner, M. G., Ghan, S., Kärcher, B., Koch, D., Kinne, S., Kondo, Y., Quinn, P. K., Sarofim, M. C., Schultz, M. G., Schulz, M., Venkataraman, C., Zhang, H., Zhang, S., Bellouin, N., Guttikunda, S. K., Hopke, P. K., Jacobson, M. Z., Kaiser, J. W., Klimont, Z., Lohmann, U., Schwarz, J. P., Shindell, D., Storelvmo, T., Warren, S. G. and Zender, C. S.: Bounding the role of black carbon in the climate system: A scientific assessment, *J. Geophys. Res. Atmos.*, 118(11), 5380–5552, doi:10.1002/jgrd.50171, 2013.
- Brock, C. A., Hudson, P. K., Lovejoy, E. R., Sullivan, A., Nowak, J. B., Huey, L. G., Cooper, O. R., Cziczo, D. J., de Gouw, J., Fehsenfeld, F. C., Holloway, J. S., Hubler, G., Lafleur, B. G., Murphy, D. M., Neuman, J. A., Nicks, D. K., Orsini, D. A., Parrish, D. D., Ryerson, T. B., Tanner, D. J., Warneke, C., Weber, R. J. and Wilson, J. C.: Particle characteristics following cloud-modified transport from Asia to North America, *J. Geophys. Res.*, 109(D23), D23S26, doi:10.1029/2003JD004198, 2004.
- Cappa, C. D., Onasch, T. B., Massoli, P., Worsnop, D. R., Bates, T. S., Cross, E. S., Davidovits, P., Hakala, J., Hayden, K. L., Jobson, B. T., Kolesar, K. R., Lack, D. A., Lerner, B. M., Li, S.-M., Mellon, D., Nuaaman, I., Olfert, J. S., Petaja, T., Quinn, P. K., Song, C., Subramanian, R., Williams, E. J. and Zaveri, R. A.: Radiative Absorption Enhancements Due to the Mixing State of Atmospheric Black Carbon, *Science* (80-. ), 337(6098), 1078–1081, doi:10.1126/science.1223447, 2012.
- Carbone, S., Onasch, T., Saarikoski, S., Timonen, H., Saarnio, K., Sueper, D., Rönkkö, T., Pirjola, L., Häyrynen, A., Worsnop, D. and Hillamo, R.: Characterization of trace metals on soot aerosol particles with the SP-AMS: detection and quantification, *Atmos. Meas. Tech.*, 8, 4803–4815, doi:10.5194/amt-8-4803-2015, 2015.
- Carson, P. G., Neubauer, K., Johnston, M. and Wexler, A.: Online chemical analysis of aerosols by rapid single-particle mass spectrometry, *J. Aerosol Sci.*, 26(4), 535–545, doi:10.1016/0168-1176(95)04312-8, 1995.
- Change, I. P. on C.: IPCC5 - Chapter 7 - Clouds and Aeorsols, , (January 2014), 2013.

Creamean, J. M., Suski, K. J., Rosenfeld, D., Cazorla, A., DeMott, P. J., Sullivan, R. C., White, A. B., Ralph, F. M., Minnis, P., Comstock, J. M., Tomlinson, J. M. and Prather, K. A.: Dust and Biological Aerosols from the Sahara and Asia Influence Precipitation in the Western U.S., *Science*, 339(6127), 1572–1578, doi:10.1126/science.1227279, 2013.

Cross, E. S., Slowik, J. G., Davidovits, P., Allan, J. D., Worsnop, D. R., Jayne, J. T., Lewis †, D. K., Canagaratna, M. and Onasch, T. B.: Laboratory and Ambient Particle Density Determinations using Light Scattering in Conjunction with Aerosol Mass Spectrometry, *Aerosol Sci. Technol.*, 41(4), 343–359, doi:10.1080/02786820701199736, 2007.

Dall'Osto, M., Beddows, D. C. S., Kinnersley, R. P., Harrison, R. M., Donovan, R. J. and Heal, M. R.: Characterization of individual airborne particles by using aerosol time-of-flight mass spectrometry at Mace Head, Ireland, *J. Geophys. Res. D Atmos.*, 109, D21302, doi:10.1029/2004JD004747, 2004.

DeCarlo, P. F., Slowik, J. G., Worsnop, D. R., Davidovits, P. and Jimenez, J. L.: Particle Morphology and Density Characterization by Combined Mobility and Aerodynamic Diameter Measurements. Part 1: Theory, *Aerosol Sci. Technol.*, 38(12), 1185–1205, doi:10.1080/027868290903907, 2004.

DeCarlo, P. F., Kimmel, J. R., Trimborn, A., Northway, M. J., Jayne, J. T., Aiken, A. C., Gonin, M., Fuhrer, K., Horvath, T., Docherty, K. S., Worsnop, D. R. and Jimenez, J. L.: Field-Deployable, High-Resolution, Time-of-Flight Aerosol Mass Spectrometer, *Anal. Chem.*, 78(24), 8281–8289, doi:10.1021/ac061249n, 2006.

Dockery, D. W., Pope, C. A., Xu, X., Spengler, J. D., Ware, J. H., Fay, M. E., Ferris, B. G. and Speizer, F. E.: An Association between Air Pollution and Mortality in Six U.S. Cities, *N. Engl. J. Med.*, 329(24), 1753–1759, doi:10.1056/NEJM199312093292401, 1993.

Finlayson-Pitts, B. J.: Tropospheric Air Pollution: Ozone, Airborne Toxics, Polycyclic Aromatic Hydrocarbons, and Particles, *Science* (80-. ), 276(5315), 1045–1051, doi:10.1126/science.276.5315.1045, 1997.

Gard, E., Mayer, J. E., Morrical, B. D., Dienes, T., Fergenson, D. P. and Prather, K. A.: Real-Time Analysis of Individual Atmospheric Aerosol Particles: Design and Performance

of a Portable ATOFMS, *Anal. Chem.*, 69(20), 4083–4091, doi:10.1021/ac970540n, 1997.

Gemayel, R., Hellebust, S., Temime-Roussel, B., Hayeck, N., Van Elteren, J. T., Wortham, H. and Gligorovski, S.: The performance and the characterization of laser ablation aerosol particle time-of-flight mass spectrometry (LAAP-ToF-MS), *Atmos. Meas. Tech.*, 9(4), 1947–1959, doi:10.5194/amt-9-1947-2016, 2016.

Healy, R. M., Hellebust, S., Kourtchev, I., Allanic, A., O'Connor, I. P., Bell, J. M., Healy, D. A., Sodeau, J. R. and Wenger, J. C.: Source apportionment of PM<sub>2.5</sub> in Cork Harbour, Ireland using a combination of single particle mass spectrometry and quantitative semi-continuous measurements, *Atmos. Chem. Phys.*, 10(19), 9593–9613, doi:10.5194/acp-10-9593-2010, 2010.

Hennigan, C. J., Miracolo, M. A., Engelhart, G. J., May, A. A., Presto, A. A., Lee, T., Sullivan, A. P., McMeeking, G. R., Coe, H., Wold, C. E., Hao, W.-M., Gilman, J. B., Kuster, W. C., de Gouw, J. A., Schichtel, B. A., Kreidenweis, S. M. and Robinson, A. L.: Chemical and physical transformations of organic aerosol from the photo-oxidation of open biomass burning emissions in an environmental chamber, *Atmos. Chem. Phys.*, 11(15), 7669–7686, doi:10.5194/acp-11-7669-2011, 2011.

Hinz, K.-P., Kaufmann, R. and Spengler, B.: Simultaneous Detection of Positive and Negative Ions From Single Airborne Particles by Real-time Laser Mass Spectrometry, *Aerosol Sci. Technol.*, 24(4), 233–242, doi:10.1080/02786829608965368, 1996.

Huffman, J. A., Jayne, J. T., Drewnick, F., Aiken, A. C., Onasch, T., Worsnop, D. R. and Jimenez, J. L.: Design, Modeling, Optimization, and Experimental Tests of a Particle Beam Width Probe for the Aerodyne Aerosol Mass Spectrometer, *Aerosol Sci. Technol.*, 39(12), 1143–1163, doi:10.1080/02786820500423782, 2005.

Jayne, J. T., Leard, D. C., Zhang, X., Davidovits, P., Smith, K. A., Kolb, C. E. and Worsnop, D. R.: Development of an Aerosol Mass Spectrometer for Size and Composition Analysis of Submicron Particles, *Aerosol Sci. Technol.*, 33(1–2), 49–70, doi:10.1080/027868200410840, 2000.

Kreuter, J., Alyautdin, R. N., Kharkevich, D. A. and Ivanov, A. A.: Passage of peptides through the blood-brain barrier with colloidal polymer particles (nanoparticles), *Brain Res.*, 674(1), 171–174, doi:10.1016/0006-8993(95)00023-J, 1995.

Lack, D. A., Cappa, C. D., Cross, E. S., Massoli, P., Ahern, A. T., Davidovits, P. and Onasch, T. B.: Absorption Enhancement of Coated Absorbing Aerosols: Validation of the Photo-Acoustic Technique for Measuring the Enhancement, *Aerosol Sci. Technol.*, 43(10), 1006–1012, doi:10.1080/02786820903117932, 2009.

Liu, P., Ziemann, P. J., Kittelson, D. B. and McMurry, P. H.: Generating Particle Beams of Controlled Dimensions and Divergence: II. Experimental Evaluation of Particle Motion in Aerodynamic Lenses and Nozzle Expansions, *Aerosol Sci. Technol.*, 22(3), 314–324, doi:10.1080/02786829408959749, 1995.

Liu, P. S. K., Deng, R., Smith, K. A., Williams, L. R., Jayne, J. T., Canagaratna, M. R., Moore, K., Onasch, T. B., Worsnop, D. R. and Deshler, T.: Transmission Efficiency of an Aerodynamic Focusing Lens System: Comparison of Model Calculations and Laboratory Measurements for the Aerodyne Aerosol Mass Spectrometer, *Aerosol Sci. Technol.*, 41(8), 721–733, doi:10.1080/02786820701422278, 2007.

Marsden, N., Flynn, M. J., Taylor, J. W., Allan, J. D. and Coe, H.: Evaluating the influence of laser wavelength and detection stage geometry on optical detection efficiency in a single particle mass spectrometer, *Atmos. Meas. Tech. Discuss.*, 1–25, doi:10.5194/amt-2016-150, 2016.

Middlebrook, A. M., Bahreini, R., Jimenez, J. L. and Canagaratna, M. R.: Evaluation of Composition-Dependent Collection Efficiencies for the Aerodyne Aerosol Mass Spectrometer using Field Data, *Aerosol Sci. Technol.*, 46(3), 258–271, doi:10.1080/02786826.2011.620041, 2012.

Moffet, R. C., de Foy, B., Molina, L. T., Molina, M. J. and Prather, K. A.: Measurement of ambient aerosols in northern Mexico City by single particle mass spectrometry, *Atmos. Chem. Phys.*, 8(16), 4499–4516, doi:10.5194/acp-8-4499-2008, 2008.

Murphy, D. M.: The design of single particle laser mass spectrometers, *Mass Spectrom. Rev.*, 26(2), 150–165, doi:10.1002/mas.20113, 2007.

Murphy, D. M., Thomson, D. S. and Mahoney, M. J.: In Situ Measurements of Organics, Meteoritic Material, Mercury, and Other Elements in Aerosols at 5 to 19 Kilometers, *Science* (80-. ), 282(5394), 1998a.

Murphy, D. M., Thomson, D. S., Middlebrook, A. M. and Schein, M. E.: In situ single-particle characterization at Cape Grim, *J. Geophys. Res.*, 103(D13), 16485–16491, 1998b.

Murphy, D. M., Cziczo, D. J., Froyd, K. D., Hudson, P. K., Matthew, B. M., Middlebrook, A. M., Peltier, R. E., Sullivan, A., Thomson, D. S. and Weber, R. J.: Single-particle mass spectrometry of tropospheric aerosol particles, *J. Geophys. Res.*, 111(D23), D23S32, doi:10.1029/2006JD007340, 2006.

Ophir Optronics Solutions, Ltd.: Focal Spot Size Calculator for Gaussian Laser Beams, 2017 <http://www.ophiropt.com/laser-measurement-instruments/laser-power-energy-meters/services/focal-spot-size-calculator-for-gaussian-beams> (Accessed 15 February 2017), 201

Pratt, K. A., Mayer, J. E., Holecek, J. C., Moffet, R. C., Sanchez, R. O., Rebotier, T. P., Furutani, H., Gonin, M., Fuhrer, K., Su, Y., Guazzotti, S. and Prather, K. A.: Development and Characterization of an Aircraft Aerosol Time-of-Flight Mass Spectrometer, *Anal. Chem.*, 81(5), 1792–1800, doi:10.1021/ac801942r, 2009.

Pratt, K. A. and Prather, K. A.: Mass spectrometry of atmospheric aerosols-Recent developments and applications. Part II: On-line mass spectrometry techniques, *Mass Spectrom. Rev.*, 31(1), 17–48, doi:10.1002/mas.20330, 2012.

Qin, X., Bhawe, P. V. and Prather, K. A.: Comparison of two methods for obtaining quantitative mass concentrations from aerosol time-of-flight mass spectrometry measurements, *Anal. Chem.*, 78(17), 6169–6178, doi:10.1021/ac060395q, 2006.

Rebotier, T. P. and Prather, K. A.: Aerosol time-of-flight mass spectrometry data analysis: a benchmark of clustering algorithms., *Anal. Chim. Acta*, 585(1), 38–54, doi:10.1016/j.aca.2006.12.009, 2007.

Robinson, E. S., Saleh, R. and Donahue, N. M.: Organic Aerosol Mixing Observed by Single-Particle Mass Spectrometry, *J. Phys. Chem. A*, 117(51), 13935–13945, doi:10.1021/jp405789t, 2013.

Robinson, E. S., Onasch, T. B., Worsnop, D. and Donahue, N. M.: Collection efficiency of alpha-pinene secondary organic aerosol particles explored via light scattering single particle aerosol mass spectrometry, *Atmos. Meas. Tech. Discuss.*, 1–29, doi:10.5194/amt-2016-271, 2016.

Schwartz, J., Laden, F. and Zanobetti, A.: The Concentration-Response Relation between PM<sub>2.5</sub> and Daily Deaths, *Environ. Health Perspect.*, 110(10), 1025–1029, doi:10.1289/ehp.021101025, 2002.

Self, S. A.: Focusing of spherical Gaussian beams, *Appl. Opt.*, 22(5), 658, doi:10.1364/AO.22.000658, 1983.

Shields, L. G., Qin, X., Toner, S. M. and Prather, K. A.: Detection of Ambient Ultrafine Aerosols by Single Particle Techniques During the SOAR 2005 Campaign, *Aerosol Sci. Technol.*, 42(8), 674–684, doi:10.1080/02786820802227378, 2008.

Silva, P. J., Liu, D.-Y., Noble, C. A. and Prather, K. A.: Size and Chemical Characterization of Individual Particles Resulting from Biomass Burning of Local Southern California Species, *Environ. Sci. Technol.*, 33(18), 3068–3076, doi:10.1021/es980544p, 1999.

Steele, P. T., Tobias, H. J., Fergenson, D. P., Pitesky, M. E., Horn, J. M., Czerwieniec, G. A., Russell, S. C., Lebrilla, C. B., Gard, E. E. and Frank, M.: Laser Power Dependence of Mass Spectral Signatures from Individual Bacterial Spores in Bioaerosol Mass Spectrometry, *Anal. Chem.*, 75(20), 5480–5487, doi:10.1021/ac034419u, 2003.

Stockwell, C. E., Yokelson, R. J., Kreidenweis, S. M., Robinson, A. L., DeMott, P. J., Sullivan, R. C., Reardon, J., Ryan, K. C., Griffith, D. W. T. and Stevens, L.: Trace gas emissions from combustion of peat, crop residue, domestic biofuels, grasses, and other fuels: configuration and Fourier transform infrared (FTIR) component of the fourth Fire Lab at Missoula Experiment (FLAME-4), *Atmos. Chem. Phys.*, 14(18), 9727–9754, doi:10.5194/acp-14-9727-2014, 2014.



Su, Y., Sipin, M., Furutani, H. and Prather, K.: Development and characterization of an aerosol time-of-flight mass spectrometer with increased detection efficiency, *Anal. Chem.*, 23(3), 712–719, doi:10.1029/2001JD001211.(12), 2004.

Sullivan, R. C. and Prather, K. A.: Recent Advances in Our Understanding of Atmospheric Chemistry and Climate Made Possible by On-Line Aerosol Analysis Instrumentation, *Anal. Chem.*, 77(12), 3861–3886, doi:10.1021/ac050716i, 2005.

Sullivan, R. C., Guazzotti, S. A., Sodeman, D. A., Tang, Y., Carmichael, G. R. and Prather, K. A.: Mineral dust is a sink for chlorine in the marine boundary layer, *Atmos. Environ.*, 41(34), 7166–7179, doi:10.1016/j.atmosenv.2007.05.047, 2007.

Thomson, D. S., Middlebrook, A. M. and Murphy, D. M.: Thresholds for Laser-Induced Ion Formation from Aerosols in a Vacuum Using Ultraviolet and Vacuum-Ultraviolet Laser Wavelengths, *Aerosol Sci. Technol.*, 26(6), 544–559, doi:10.1080/02786829708965452, 1997.

Tkacik, D. S., Robinson, E. S., Ahern, A. T., Saleh, R., Stockwell, C. E., Simpson, I., Meinardi, S., Blake, D. R., Yokelson, R. J., Presto, A. A., Sullivan, R. C., Donahue, N. M. and Robinson, A. L.: A dual-chamber enhancement method for quantifying effects of atmospheric perturbations on secondary organic aerosol formation from biomass burning emissions, *J. Geophys. Res.*, submitted 2017.

Wenzel, R. J. and Prather, K. A.: Improvements in ion signal reproducibility obtained using a homogeneous laser beam for on-line laser desorption/ionization of single particles, *Rapid Commun. Mass Spectrom.*, 18(13), 1525–1533, doi:10.1002/rcm.1509, 2004.

Williams, L. R., Gonzalez, L.A., Peck, J., Trimborn, D., McInnis, J., Farrar, M. R., Moore, K. D. , Jayne, J. T. , Robinson, W. A. , Lewis, D. K. , Onasch, T. B., Canagaratna, M. R., Trimborn, A., Timko, M. T., Magoon, G. , Deng, R., Tang, D., Blanco, E., Prévôt, A. S. H., Smith, K. A., and Worsnop, D. R. Characterization of an Aerodynamic Lens for Transmitting Particles Greater Than 1 Micrometer in Diameter into the Aerodyne Aerosol Mass Spectrometer. *Atmos. Meas. Tech.*, 6(11), 3271–3280, doi:10.5194/amt-6-3271-2013, 2013.

White, W. H. and Roberts, P. T.: On the nature and origins of visibility-reducing aerosols in the los angeles air basin, *Atmos. Environ.*, 11(9), 803–812, doi:10.1016/0004-6981(77)90042-7, 1977.

Ye, Q., Robinson, E. S., Ding, X., Ye, P., Sullivan, R. C. and Donahue, N. M.: Mixing of secondary organic aerosols versus relative humidity., *Proc. Natl. Acad. Sci. U. S. A.*, 113(45), 12649–12654, doi:10.1073/pnas.1604536113, 2016.

Zelenyuk, A. and Imre, D.: Single Particle Laser Ablation Time-of-Flight Mass Spectrometer: An Introduction to SPLAT, *Aerosol Sci. Technol.*, 39(6), 554–568, doi:10.1080/027868291009242, 2005.

Zelenyuk, A., Yang, J., Song, C., Zaveri, R. A. and Imre, D.: A New Real-Time Method for Determining Particles' Sphericity and Density: Application to Secondary Organic Aerosol Formed by Ozonolysis of  $\alpha$ -Pinene, *Environ. Sci. Technol.*, 42(21), 8033–8038, doi:10.1021/es8013562, 2008a.

Zelenyuk, A., Imre, D., Nam, E. J., Han, Y. and Mueller, K.: ClusterSculptor: Software for expert-steered classification of single particle mass spectra, *Int. J. Mass Spectrom.*, 275(1–3), 1–10, doi:10.1016/j.ijms.2008.04.033, 2008b.

# 5. EFFECT OF SECONDARY ORGANIC AEROSOL COATING THICKNESS ON THE REAL-TIME DETECTION AND CHARACTERIZATION OF BIOMASS BURNING SOOT BY TWO PARTICLE MASS SPECTROMETERS

This chapter contains material reproduced from my work published in *Atmospheric Measurement Techniques* (Ahern et al., 2016).

Biomass burning is a large source of light-absorbing refractory black carbon (rBC) particles with a wide range of morphologies and sizes. The net radiative forcing from these particles is strongly dependent on the amount and composition of non-light absorbing material internally mixed with the rBC, and on the morphology of the mixed particles. Understanding how the mixing state and

morphology of biomass-burning aerosol evolves in the atmosphere is critical for constraining the influence of these particles on radiative forcing and climate. We investigated the response of two commercial laser-based particle mass spectrometers, the VUV ablation LAAPTOF and the IR vaporization SP-AMS, to monodisperse biomass-burning particles as we sequentially coated the particles with secondary organic aerosol (SOA) from  $\alpha$ -pinene ozonolysis. We studied three mobility-selected soot core sizes, each with a number of successively thicker coatings of SOA applied. Using IR laser vaporization, the SP-AMS had different changes in sensitivity to rBC compared to potassium as a function of applied SOA coatings. We show that this is due to different effective beam widths for the IR laser vaporization region of potassium versus black carbon. The SP-AMS's sensitivity to BC mass was not observed to plateau following successive SOA coatings, despite achieving high OA:BC mass ratios  $> 9$ . We also measured the ion fragmentation pattern of biomass-burning rBC and found it changed only slightly with increasing SOA mass. The average organic matter ion signal measured by the LAAPTOF demonstrated a positive correlation with the condensed SOA mass on individual particles, despite the inhomogeneity of the particle core compositions. This demonstrates that the LAAPTOF can obtain quantitative mass measurements of aged soot particle composition from realistic biomass-burning particles with complex morphologies and composition.

## 5.1. Introduction

Particles containing black carbon (BC) are largely anthropogenic and have the third largest warming effect on the planet, after CO<sub>2</sub> and methane (Bond et al., 2013; Ramanathan and Carmichael, 2008). This makes BC-containing particles a likely target for climate change mitigation policy (Anenberg et al., 2012). However, there is high uncertainty regarding the climate forcing of BC, and thus any potential benefits from BC control technologies and policies (Jacobson, 2001). The uncertainty stems from the variable optical, chemical, and physical properties of BC, which affect particle radiative properties and lifetime, respectively. The properties of BC-containing particles can change as atmospheric oxidants react with gas-phase vapors; the products of these reactions can condense onto the light-absorbing aerosol. Although this condensed material may not absorb light itself, it can affect the lifetime and cloud-nucleation ability of the BC-containing particle, and increase the internally mixed BC absorption of sunlight by as much as a factor of two (Bond et al., 2013; Chung and Seinfeld, 2002; Jacobson, 2001; Lack et al., 2009; Moffet et al., 2008; Ramanathan and Carmichael, 2008).

The burning of non-fossil-fuel biomass, either as biofuel, agricultural refuse, or in wildfires, is the largest source of light-absorbing BC-containing particles

globally. However, the effect of aging on the biomass burning aerosol (BBA) is not well characterized (Bond et al., 2013). In some cases, co-emitted organic gases become oxidized and condense on the BBA, simultaneously reducing BBA atmospheric lifetime and increasing BBA light absorptivity (Lack et al., 2009; Mikhailov et al., 2006; Yokelson et al., 2009). In other smoke plumes, there has been no observed increase in organic matter (OM) with aging, and in a few cases a decrease in OM has been reported, likely due to dilution-induced evaporation (Cubison et al., 2011; May et al., 2013). In order to identify the contribution of various chemical processes to the compositional changes in BC-containing particles, measurements of particle composition must be carried out with a temporal resolution similar to or faster than the timescale of the chemical processes. Improved mass measurements of BC and internally mixed material will enable more accurate model simulations that constrain the climate forcing by black carbon and other aerosol components.

Particle mass spectrometers provide information about the chemical composition of atmospheric aerosols with a time resolution comparable to their transformation processes. In this paper we investigate the response of two commercial laser-based particle mass spectrometers to the systematic condensation of secondary organic aerosol (SOA) onto complex biomass-burning soot particles. One instrument is an infrared laser vaporization soot-particle aerosol mass spectrometer (SP-AMS, Aerodyne Research Inc.), while the other is a laser desorption ionization single-particle mass spectrometer (LDI-SP-MS) known as the laser ablation aerosol particle time of flight mass spectrometer (LAAPTOF, Aeromegt GmbH). Both instruments provide compositional information regarding the core composition of BBA particles as well as secondary condensed components on a time scale of ten minutes or less. However, each has quantitative challenges related to particle mixing state and morphology that are the subject of ongoing research (Corbin et al., 2014; Onasch et al., 2015; Spencer and Prather, 2006; Willis et al., 2014). Herein we evaluate the ability of the two instruments to measure the composition of BBA composed of both a BC core and SOA coating, as we simulate atmospheric aging by

coating primary BBA particles with complex secondary organic material in a chamber reactor.

We confirm that significant SOA coatings on BC cause only small changes in the ion fragmentation patterns of elemental carbon (EC) in the SP-AMS. EC is defined as ions detected by mass spectrometry that consist of only carbon ions. We show that the infrared laser beam in the SP-AMS has a different effective beam width and therefore different detection efficiency for alkali metals versus BC. The feasibility of quantitative measurements of organic matter (OM) by the LAAPTOF in complex and realistic particles containing inorganic salts, rBC, and SOA was also investigated. We demonstrate that there is a positive correlation between the LAAPTOF measured OM ion signal and the SOA mass condensed on BBA particles. This is significant given the especially complex composition of BBA, and is highly encouraging for achieving mass quantitative single-particle measurements of other complex ambient particle matrices. In this work, we will use the term “SOA” to describe the condensed phase organic material that was formed from  $\alpha$ -pinene ozonolysis. We will use “OM” to discuss all condensed organic matter, including mass that is primary or secondary in nature. Organic ions measured by mass spectrometry will be identified as OM because in this work we cannot strictly differentiate between primary and secondary organic material.

#### 5.1.1. Characterization of carbonaceous aerosol by SP-AMS

The SP-AMS is a variant of the conventional aerosol mass spectrometer that includes an intracavity infrared (IR) laser that can vaporize light-absorbing refractory material. A conventional AMS includes a 600 °C heater to vaporize aerosol particles in a vacuum before ionization (Decarlo et al., 2006; Jayne et al., 2000). Two species of interest are difficult and impossible to detect, respectively, with a conventional AMS: potassium and refractory black carbon (rBC). Refractory is an operationally defined term describing any material not readily vaporized, such as by the 600 °C heater in a conventional AMS. Potassium and rBC are chemical species that are used as inert, non-volatile tracers for biomass burning (Andreae, 1983; Hennigan

et al., 2011; Lee et al., 2016). The sensitivity of the SP-AMS to rBC has been shown to increase with the addition of organic coatings to rBC-containing particles. Willis et al. (2014) showed that the increased sensitivity was due to increased overlap between the particle beam and the IR beam that vaporizes the particles. The particles become more tightly focused by the aerodynamic lens inlet with increasing coating thickness and thus sphericity, causing a larger portion of the particle beam to intersect with the IR laser beam. The fraction of rBC-containing particles that are vaporized by the IR laser is defined by Onasch et al. (2012) as the shape-dependent collection efficiency,  $E_{IR}$ , and is the determining factor for the sensitivity of the SP-AMS to rBC. Willis et al. (2014) measured the  $E_{IR}$  for rBC using a beam-width probe with a rBC aerosol calibration standard (Regal Black, Cabot) coated to varying degrees with dioctyl sebacate (DOS), a surrogate for primary or hydrocarbon-like OM. They observed that the  $E_{IR}$  was less than unity for uncoated, collapsed rBC particles such as Regal Black, but that for urban ambient particles and DOS-coated Regal Black,  $E_{IR}$  was close to unity. However, real-world BBA has a different composition than Regal Black, with particles that are less spherical and that contain inorganic salts (e.g. potassium chloride) that may be internally or externally mixed with rBC (Huffman et al., 2005; Li et al., 2003; Onasch et al., 2012). We will show that as BBA is coated with OM, the SP-AMS ion signal response to the mass of potassium and rBC increases. Furthermore, we will show that the SP-AMS response to potassium increases more rapidly than that for rBC for equivalent amounts of OM coating, despite the species being internally mixed. We believe that this is in part due to the ability of components with low ionization energy to be ionized directly upon vaporization (Carbone et al., 2015; Drewnick et al., 2006). However, most chemical components in the SP-AMS undergo sequential vaporization followed by 70 eV electron ionization of the neutral vapors. This allows for extensive but reproducible molecular fragmentation and subsequent classification and detection of the resulting ions in the high-resolution time-of-flight mass spectrometer. The IR laser vaporization enables the subsequent ionization and thus detection of refractory material in particles containing rBC that strongly absorbs the IR laser energy. The vapors produced by the IR laser are ionized by the same

electron source used when vaporization is performed only with the 600 °C heater. The reproducibility of the ion fragmentation by electron ionization has led researchers to investigate the possibility of using the ratios of the various detected elemental carbon (EC) fragments ( $C_x^+$ ) to perform source apportionment of rBC. Corbin et al. (2014) showed that fullerene-rich particles produced a higher ratio of  $C_4^+$ -to- $C_3^+$  than did particles from higher temperature combustion, which did not contain substantial fullerenes. Onasch et al. (2015) confirmed that fragmentation of larger graphitic molecules was a minor source of  $C_4^+$  cations in addition to the direct ionization of vaporized rBC. This suggests that the elemental carbon (EC) fragmentation pattern could be used to differentiate between rBC generated from different types of combustion (e.g. diesel vs. biomass combustion). Here we investigate the effect of atmospheric aging in the form of OM coatings on these EC ion ratios.

#### 5.1.2. Characterization of carbonaceous aerosol by LDI-SP-MS

The LAAPTOF is a laser desorption/ionization single-particle mass spectrometer (LDI-SP-MS) using a VUV excimer laser pulse to ablate and ionize individual particles simultaneously. This enables the analysis of a wider range of particle compositions and types than is possible with the AMS, even when the IR laser is used. High time resolution measurements of individual particles are achieved; an aerodynamic size and bipolar mass spectrum can be obtained for each particle. LDI-SP-MS also provides much greater mass sensitivity compared to the less efficient electron ionization scheme because the laser ionization produces many more ions than electron ionization per mole of analyte (Farmer and Jimenez, 2010; Murphy, 2007; Pratt and Prather, 2012; Sullivan and Prather, 2005). However, the large number of ions produced per particle can result in poor MS resolution and/or ion plume chemistry after desorption/ionization. The molecular fragmentation is also less reproducible compared to 70 eV electron ionization due to laser shot-to-shot variability, inhomogeneity of the laser pulse, and varying optical properties of individual particles. Generation of ions directly from each particle introduces



important matrix effects where the particle's composition and properties strongly dictate its interaction with the VUV laser pulse, the distribution of laser energy to the particle's constituents, and the resulting ion signal and fragmentation (Gross et al., 2000; Mansoori et al., 1996; Reinard and Johnston, 2008; Steele et al., 2005; Thomson et al., 1997; Wenzel and Prather, 2004).

Despite these challenges, LDI-SP-MS can obtain quantitative measurements of individual particle composition and its evolution. Effective demonstrations of data analysis strategies for achieving quantitative LDI-SP-MS measurements include restricting the analysis to particles of a similar particle type based on their mass spectrum, normalization of ion peak areas to total ion signal, the use of ion peak area ratios, sensitivity calibration by comparison to co-located speciated mass measurements, and signal averaging over numerous individual measurements (Bhave et al., 2002; Fergenson et al., 2001; Gross et al., 2000; Healy et al., 2013; Jeong et al., 2011; Pratt and Prather, 2012; Spencer and Prather, 2006; Sullivan et al., 2009; Sullivan and Prather, 2005). Although the ion plume chemistry can complicate analysis, the species known to cause ion-plume effects (e.g. water, inorganic salts) are generally present in the mass spectra and can thereby inform the analysis (Murphy, 2007; Murray and Russell, 1994; Neubauer et al., 1998). In this study, we account for laser shot-to-shot inconsistencies by averaging over particles of similar size and composition.

Spencer and Prather (2006) used graphite spark-generated elemental carbon (EC) with condensed unleaded fuel to calibrate the ATOFMS LDI-SP-MS and found a linear relationship between the ratio of summed select OM cation signals to summed select EC cation signals, as the mass of OM condensed on the EC was increased. However, as pointed out by Gysel et al. (2012), EC from graphite spark discharge has different optical properties than combustion soot. Before such analysis can be used with confidence on realistic combustion BBA and complex SOA, two key differences between soot and BBA must be addressed, namely the variable morphology of BBA and the presence of inorganic salts. Inorganic salts, such as the potassium chloride observed in BBA, are very readily ionized (Li et al., 2003; Reid et

al., 2005; Zauscher et al., 2013). They therefore can generate a dense ion cloud that may reduce MS resolution and can interfere with the formation/detection of other ions (Murphy, 2007). The presence of potassium, the irregular shape, and strongly light-absorbing nature of BBA presents an especially complex matrix for LDI-SP-MS. We evaluated the ability of the LAAPTOF with its 193 nm laser to generate and detect OM ion signal proportional to the mass of realistic SOA condensed on a BBA particle.

## 5.2. Experimental Methods

### 5.2.1. Experimental particle generation and conditioning

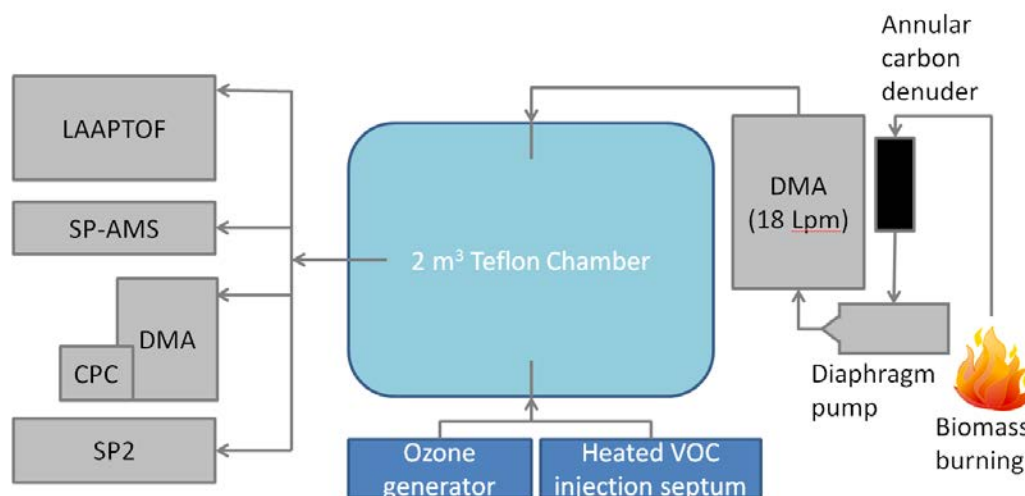


Figure 5.1. Experimental setup including size-selected biomass-burning aerosol generation, environmental aging chamber for sequential coating with  $\alpha$ -pinene SOA, and subsequent online characterization with particle instrumentation.

In Figure 5.1 we display the experimental setup for the generation, coating, and characterization of monodisperse biomass-burning aerosol particles. For these experiments, we burned European white birch bark in a cookstove and sampled the smoke from the flaming phase 1 m above the fire through 1/2" o.d. stainless-steel tubing. We removed the gas-phase organics from the smoke by pulling polydisperse smoke through a 20 °C annular activated-carbon denuder with a diaphragm pump.

The same pump then pushed the denuded aerosol sample through a series of  $^{85}\text{Kr}$  neutralizers and a differential mobility analyzer (DMA; TSI, model 3081) with a sample flow of 4.0 Lpm and a non-circulating sheath flow of 18 Lpm to select a narrow range of mobility particle diameters. We then injected the monodisperse soot particles into a 2 m<sup>3</sup> Teflon chamber at a rate of 4.0 Lpm until the concentration was between 2,000 and 14,000 particles cm<sup>-3</sup>. This typically took less than 30 minutes. During this time, we continuously fueled the fire to maintain flaming conditions. Before soot injection, we partially filled the chamber with clean filtered dry air. Although the diaphragm pump generated some small particles (with mobility diameters less than 50 nm), they were smaller than the selected soot particles (143 nm to 220 nm mobility diameter) and thus not transmitted through the DMA into the chamber.

We characterized the nascent soot particles with a suite of particle instruments described below and confirmed that the particles were nearly monodisperse; doubly-charged particles were always less than 10% by number. We then injected precursor gases for SOA formation. We generated ozone by flowing oxygen through a corona-discharge ozone generator (Azco, HTU500AC) until the chamber concentration reached ~300 ppb. We measured the ozone concentration with a UV photometric ozone monitor (Dasibi, 1008-PC). We injected 0.1 or 0.2  $\mu\text{L}$  aliquots of  $\alpha$ -pinene (Sigma Aldrich, >99%) through an air-tight heated septum flushed with clean air. We used serial injections of  $\alpha$ -pinene to generate successively thicker SOA coatings on the soot cores. Chamber experiments with several steps of SOA production typically lasted 3-4 hours, stopping after homogenous nucleation prevented additional coating of soot seeds.

### 5.2.2. Particle component mass measurements

We characterized the soot and the SOA coatings using a number of different methods. We used three instruments to measure the refractory black carbon (rBC): a Droplet Measurement Technologies Single Particle Soot Photometer (SP2) (Schwarz et al., 2010; Stephens et al., 2003); a laser desorption/ionization single-particle mass

spectrometer (LDI-SP-MS) – the Laser Ablation Aerosol Particle Time-Of-Flight (LAAPTOF) mass spectrometer; and an Aerodyne Soot-Particle High Resolution Aerosol Mass Spectrometer (SP-AMS) (Onasch et al., 2012). Extensive descriptions of the SP2 and SP-AMS instruments are available elsewhere and thus we provide only a brief overview. For the LAAPTOF we describe the salient features below; a more detailed discussion of the LDI-SP-MS technique is available in the form of a review article by Murphy (2007), and literature descriptions of other closely related instruments (Marsden et al., 2016; Pratt et al., 2009; Sullivan and Prather, 2005; Thomson et al., 2000; Zelenyuk et al., 2009).

The LAAPTOF is a commercially available single-particle mass spectrometer (Aeromegt, GmbH) that uses laser desorption/ionization to generate positive and negative ions from individual particles that are subsequently detected by a bipolar time-of-flight mass spectrometer (TOFWerk, AG) (Gemayel et al., 2016; Marsden et al., 2016). The particles are focused into the ionization region by an aerodynamic lens. Normally the particle time-of-flight is measured by light scattering between two 405 nm continuous-wave lasers (OBIS, Coherent Inc.) to determine the velocity of each particle and thus its vacuum aerodynamic diameter. The particle is then ablated and ionized with an 8 ns pulse from a VUV 193 nm excimer laser (EX5, GAM Laser, Inc.) that is triggered immediately by the second particle light scattering event. The VUV pulse travels coaxially up the particle beam and hits the particle in the ion extraction region, coincident with and orthogonal to the second light scattering laser beam. During these experiments, the 405 nm scattering lasers were not operational, and instead we free-fired the excimer laser at 10 Hz with an average laser pulse energy of 2.0 mJ, and an average laser fluence of  $\sim 1.1 \times 10^5 \text{ J m}^{-2}$ . We set and periodically confirmed the VUV laser power using a laser power meter (EnergyMax, Coherent, Inc.). The SP2 rapidly heats individual rBC-containing particles as they pass through an intracavity IR laser beam, and then measures the intensity of emitted thermal radiation resulting from particle incandescence. The rBC mass of each particle is proportional to this light intensity. We calibrated the SP2 rBC mass response with fullerene soot that we size-selected using a DMA. We previously measured the batch-

specific effective density of this soot sample using a Cambustion Centrifugal Particle Mass Analyzer (Gysel et al., 2011; Slowik et al., 2007). We measured the particle concentration during these calibrations using a Condensation Particle Counter (TSI model 3772). Further details are provided by Saliba et al. (2016), where the optical properties of the coated rBC particles produced in these experiments are presented.

Both the SP-AMS and the LAAPTOF use the same aerodynamic lens inlet design (Huffman et al., 2005; Liu et al., 2007). The aerodynamic lens these instruments use efficiently transmit particles with vacuum aerodynamic diameters ( $d_{va}$ ) between 150 nm and 700 nm. Particles smaller than 150 nm tend to be removed with the excess gas, while particles greater than 700 nm may be impacted on the lens' critical orifices. For the measurements presented here, some particles start smaller than 150 nm  $d_{va}$  and then grow into the ideal lens transmission regime. This is very important for mass-based measurements like the SP-AMS, but less so for individual particle analysis for the LAAPTOF. We will discuss how this affects our results in 5.3.3.

The aerodynamic lens focuses particles into a collimated beam for transmission into the SP-AMS detection region. The SP-AMS uses the same IR laser as the SP2 to vaporize rBC along with any internally mixed components; the vapors are then ionized by 70 eV electrons from a tungsten filament and the ions analyzed by time-of-flight mass spectrometry (Canagaratna et al., 2015; Onasch et al., 2012). The SP-AMS also contains a tungsten heater kept at 600 °C for particle thermal desorption, identical to the conventional AMS design. Unless stated otherwise, we operated the SP-AMS with both the IR laser and the conventional heater on for all experiments described here. The largest uncertainty in mass measurements of rBC by the SP-AMS is the particle collection efficiency, which is determined by the particle shape and size. The fraction of particles that pass through the laser beam and are vaporized ( $E_{IR}$ ) has been shown to be the largest uncertainty for SP-AMS mass measurements using the IR laser. It is caused by the incomplete overlap of the particle beam and the IR laser beam (Huffman et al., 2005; Onasch et al., 2012; Willis et al., 2014). A perfectly collimated particle beam would result in all of the rBC-containing particles passing through the center of the Gaussian IR laser beam energy profile, where it is most

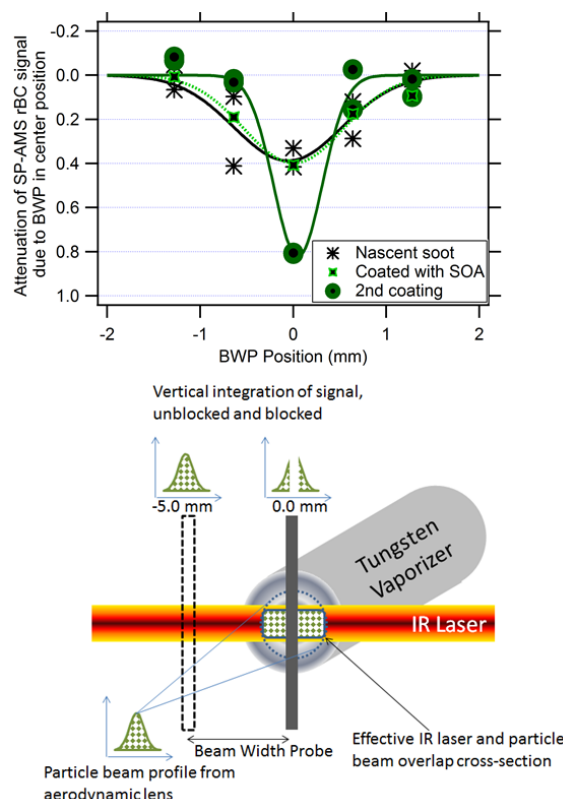


Figure 5.2 The particle beam-width probe blocks a fraction of the particles that would have been vaporized by the IR laser and thus the probe attenuates the elemental carbon ion signal ( $C_x^+$ ) for rBC containing particles. We used six probe positions to establish the particle-beam width. The measured ion signal is the integrated Gaussian profile shown at the top of the schematic. The difference between the unblocked ( $x = -5.0$  mm) and blocked (0.0 mm) green integrated Gaussian profile plots is the attenuation for that beam width probe blocking-position, plotted as the y-axis on the top figure. The top panel shows the attenuation of nascent uncoated soot (black asterisks), soot with a single coating of SOA (black and light green crosses), and soot with a second coating of SOA (black and dark green circles). A wider Gaussian particle beam shape determined by the beam-width probe analysis indicates the aerosol has a small diameter and therefore  $E_{IR} < 1$ .

intense. However, the particle beam can spread because small and/or irregularly shaped particles diverge from an ideal beam profile. This divergence is due to Brownian diffusion or uneven drag distribution on the particles as they leave the aerodynamic lens (Huffman et al., 2005; Liu et al., 1995). The collection efficiency for

non-refractory material not mixed with IR-laser absorbing rBC (components that promptly evaporate at 600 °C) is determined by the particle bounce off of the heater. Note that the cross-sectional area of the heater is much larger than that of the IR laser beam. Therefore, particle detection of refractory components such as rBC in the SP-AMS by IR vaporization is more sensitive to particle shape than is the detection of non-refractory components vaporized by the 600 °C heater.

We determined the fraction of total particle mass undetected by the SP-AMS due to diverging, light-absorbing particles missing the IR laser beam. We did this by measuring the ion signal from refractory species (elemental carbon or potassium) while sequentially blocking portions of the particle beam with a thin piece of wire ( $\varnothing = 0.41$  mm), called the beam-width probe. We compared the signal with the beam-width probe in place to the signal observed when the wire was not obstructing any of the particle beam (Huffman et al., 2005; Willis et al., 2014). We show this schematically in Figure 5.2 for the carbon cation signal,  $C_x^+$  (where  $x$  is a positive integer). The ratio of the partially blocked signal to the unblocked signal, hereafter referred to as the attenuation with the beam-width probe, indicates how narrow the particle beam is. If the measured attenuation is high, then in the absence of the beam-width probe, most of the particles will pass through the most intense IR laser region and be vaporized. If the attenuation is low, then some of the particles will miss the laser and the refractory material will not be detected. The IR laser intensity was measured by Willis et al. (2014) to have a Gaussian distribution with a  $\sigma \approx 0.18$  mm, although this may vary with IR laser power. As the beam-width probe is wider than the effective width of the IR laser for rBC, anything less than complete attenuation of the measured ion signal when the beam-width probe is at the center position indicates that some of the EC mass on particles containing rBC will not be detected. Therefore,  $E_{IR}$  will be  $< 1$  (Willis et al., 2014). However, as we will show, vaporization of potassium occurs with a larger effective IR beam width, and thus  $E_{IR}$  is larger for potassium than rBC.

### 5.2.3. Particle mobility measurements and calculations

During these experiments, there was evidence of subsampling in the aerosol sampling lines, resulting in different particle concentrations reaching some instruments. As a result, we do not compare the absolute concentration of aerosol species measured by the various instruments. Instead, we perform our analysis based on particle size measurements that are unaffected by the flow-splitting issues due to the monodisperse aerosol used here.

We classified the size distribution of the biomass-burning aerosol (BBA) with a Scanning Mobility Particle Sizer (SMPS; TSI Inc., model 3081 DMA and 3772 CPC) that measures particle mobility diameter ( $d_{mob}$ ) size distributions, and with the SP-AMS that measures particle vacuum aerodynamic diameter ( $d_{va}$ ) in addition to composition. The SP-AMS measures the vacuum aerodynamic diameter by accelerating particles into a vacuum and measuring the time to ion detection after a particle passes through a rotating 2% slit chopper. We calibrated the particle time of flight measurements using polystyrene latex spheres vaporized using the conventional tungsten heater in the SP-AMS (Jayne et al., 2000). It is important to note that for the fractal-like nascent soot particles, the terms  $d_{mob}$  and  $d_{va}$  do not fully describe the physical shape of a particle. Rather, they describe the relationship between the drag force on that particle compared to either a counterbalancing electrostatic force for  $d_{mob}$  or the acceleration modulated by the particle mass for  $d_{va}$  (DeCarlo et al., 2004).

In Figure 5.3 we show aerodynamic size distributions for particles originally selected with a DMA at 143 nm  $d_{mob}$ . Though the nascent particles were monodisperse in mobility space, the  $d_{va}$  distribution for the nascent soot particles was much wider than the  $d_{mob}$  distribution. This is probably due to the range of particle masses and shapes that can exist at a given  $d_{mob}$  for highly irregular nascent



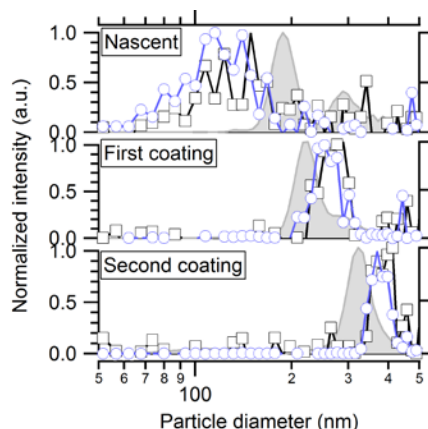


Figure 5.3. Normalized particle size distributions for coating experiments from two instruments. Traces are mass distributions vs. vacuum aerodynamic diameter ( $d_{va}$ ) for two refractory species measured by the SP-AMS, potassium (purple circles) and rBC (black squares). The filled-in gray curve is the volume distribution ( $d^3$ ) versus mobility diameter ( $d_{mob}$ ) measured by the SMPS. Measurements of the original uncoated nascent biomass-burning soot particles are shown in the top panel, while the middle and bottom panel show measurements after we applied the first and second SOA coatings, respectively. The uncoated particles had broad mass distributions with modes well below the mobility volume mode indicating fractal particles with a wide variability in particle shape. The mass distribution narrowed and overtook the volume distribution following condensation of SOA because the particles became more spherical and homogeneous with respect to shape and composition, with a density greater than  $1.0 \text{ g/cm}^3$ .

soot (Zelenyuk et al., 2008). The  $d_{va}$  size range narrowed following the addition of SOA coatings, likely reflecting the increasing uniformity as the irregularly shaped particles became coated with SOA. When measuring the mobility size distribution, we adjusted the sheath flow of the SMPS to ensure that we captured the complete aerosol size distribution, at times operating at sheath-to-sample flow ratios as low as 5:1. Although the lower sheath-to-sample flow ratio reduces the SMPS size resolution, it does not affect the accuracy of the mode size determination.

As a nascent soot particle becomes coated with SOA, the particle grows and gains organic mass. Thus  $d_{mob}$ ,  $d_{va}$ , and the organic mass per particle all increase. We

calculated the SOA mass per particle ( $m_{SOA}$ ) from mobility and mass measurements following the method described in Slowik et al. (2004), with some differences as described here. In addition to  $d_{mob}$  and  $d_{va}$ , we measured the single-particle black carbon mass ( $m_{rBC}$ ) with the SP2. The SP2 also confirmed that  $> 97\%$  of the nascent particles were composed of significant amounts of black carbon. We assumed that the black-carbon density ( $\rho_{rBC}$ ) was  $1.8 \text{ g/cm}^3$  (Park et al., 2004). For thickly coated particles, with  $m_{SOA} \gg m_{rBC}$ , we assumed that the particles were effectively spherical and determined the density of the SOA ( $\rho_{SOA}$ ) to be  $1.3 \text{ g/cm}^3$  by taking the ratio of  $d_{mob}$  and  $d_{va}$ . Knowing the two densities, we then iteratively solved for the particle dynamic shape factor ( $\chi$ ), volume equivalent diameter ( $d_{ve}$ ), and the average mass of SOA per particle ( $m_{SOA}$ ) using Eqs. (1), (2), and (3) below, taking into account the Cunningham slip correction factor ( $Cc$ ).

$$d_{mob} = \frac{d_{ve} Cc(d_{mob}) \chi}{Cc(d_{ve})} \quad (5.1)$$

$$d_{va} = \frac{d_{ve}}{\chi(\rho_0)} \left( \frac{m_{rBC} + m_{SOA}}{\frac{m_{rBC}}{\rho_{rBC}} + \frac{m_{SOA}}{\rho_{SOA}}} \right) \quad (5.2)$$

$$\frac{m_{rBC}}{\rho_{rBC}} + \frac{m_{SOA}}{\rho_{SOA}} = \frac{\pi}{6} * d_{ve}^3 \quad (5.3)$$

We neglected the contribution of ammonium, sulfate, and nitrate to particle mass and volume as they are small ( $< 10\%$ ) relative to rBC and SOA. Unless specified otherwise, SOA mass per particle is calculated in this manner.

The combustion of solid biomass fuel generates particles with shapes and compositions that vary more widely than those produced from controlled, well-mixed internal-combustion engines (Reid et al., 2005; Schwarz et al., 2008). Relative to engine exhaust soot, biomass-burning particles are typically larger and contain more non-carbonaceous components, such as inorganic salts (Bond et al., 2006; Li et al., 2003; Reid and Hobbs, 1998). Electron microscopy studies of aerosol particles have shown that biomass burning can result in a wide range of particle compositions and morphologies (Li et al., 2003; Pósfai and Buseck, 2010). For this work, based on our measurements it appears that that most of the particles initially consisted of mostly

rBC, with trace primary organic material and inorganic material, including potassium salts. The particles maintained their initial core composition mass as SOA was condensed onto them. This made the particles increasingly homogeneous in terms of composition and shape. Single particle measurements by the SP2 showed that > 97% of the particles detected by light scattering contained > 0.7 fg of rBC. In cases where the uncoated, non-BC containing particles were too small to be detected by the SP2 via light scattering, the fraction of rBC-containing particles was monitored after the particles were grown with SOA to detectable sizes. The fraction of rBC-containing particles did not change, except in cases where there was substantial and obvious new particle formation. We suspect that the largest variability in particles was with regard to the amount of potassium in a particle and with respect to particle shape. We do not have an estimate of variability in individual particle potassium content. Variability in particle shape is observed by the broad distribution in vacuum aerodynamic diameters. As the particles became coated, and therefore more uniform in shape and composition, the vacuum aerodynamic diameter distribution narrowed. The coating of fractal-like soot with organics has also been shown to cause structural collapse of the particle, potentially affecting its light absorption cross section (Cross et al., 2010; Ghazi and Olfert, 2013; Zhang et al., 2008).

## 5.3. Results and Discussion

### 5.3.1. Effect of SOA condensation on soot particle shape

Figure 5.4 shows the calculated dynamic shape factor,  $\chi$ , for particles as they were coated with SOA. Nascent soot particles are very fractal-like, with  $\chi > 1.6$ . This is within the range of previously observed soot from fuel-rich combustion (Slowik et al., 2004). For context, Schwarz et al. (2008) measured the thickness of coatings on ambient BBA using an SP2. The instrument was onboard an aircraft that transected a biomass-burning plume. They determined aged ambient particles with a rBC core mass equivalent diameter of 200 nm (BC mass of 8.4 fg) had a coating thickness of 79 nm ~1 hour after emission from the biomass burning source. For comparison, we

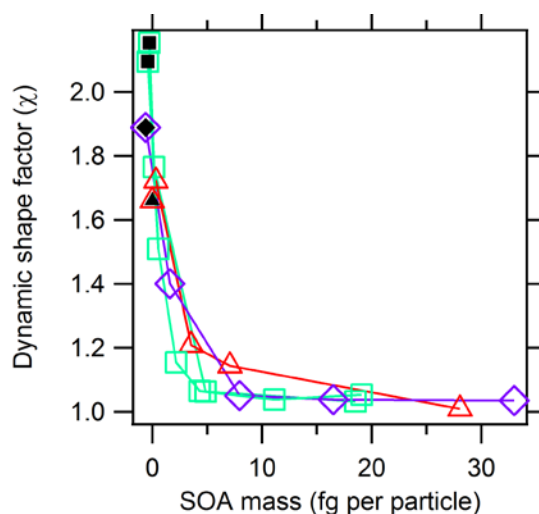


Figure 5.4. Dynamic shape factor ( $\chi$ ) of soot particles became more spherical ( $\chi \rightarrow 1$ ) with increasing SOA mass. Nascent particles (black) were coated sequentially, and after 5 fg of SOA per particle had condensed the particles are mostly spherical in shape. Additional coatings served to increase the diameter of the now effectively spherical particles. Different colored/shaped symbols indicate different initial selected soot core mobility diameters: red triangles were initially 142 nm, teal squares were 188 nm, and purple diamonds were 220 nm.

assume the BBA particles discussed in Schwarz et al. (2008) are coated with SOA with a density of 1.3 g/cm<sup>3</sup>. The SOA coating mass would then be 25.7 fg of OA mass per particle, and would result in a mostly spherical particle. Although we cannot say the particle coating observed by Schwarz et al. (2008) consisted entirely of OA mass, the volume equivalent of any secondary component such as sulfate would also result in a spherical particle shape, with a SOA to rBC mass ratio greater than > 3.2 (Ghazi and Olfert, 2013). As shown before, because the particle shape and size influences the particle beam profile and the beam width at the IR laser, the shape factor influences the total rBC signal detected by the SP-AMS.

### 5.3.2. Sequential coating of monodisperse soot in a smog chamber

In Figure 5.5 we display a time series from a particle coating experiment for initially monodisperse particles with  $d_{mob} = 143$  nm. All of the experiments followed this

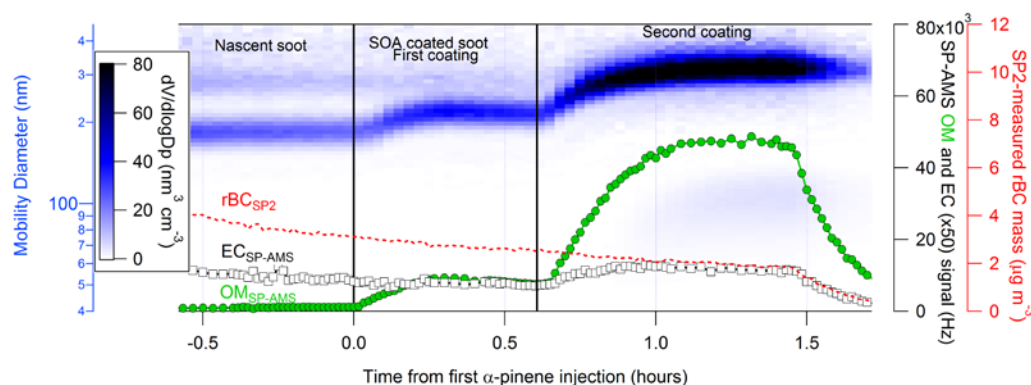


Figure 5.5. Monodisperse biomass soot particles to which two successive additions of SOA were applied. Fractal-like, monodisperse soot particles with initial mobility diameter of 143 nm grew via condensation of successive SOA coatings following discrete injections of  $\alpha$ -pinene vapor (indicated by vertical lines) into a chamber containing ozone. Particle growth is evident in the volume-weighted SMPS mobility size distribution (blue-black, top) and the SP-AMS measured OM (green closed circles) and EC (black open squares) ion signal as a function of time. SP2 rBC mass measurements (red dotted line) reveal the steady decay of soot-particle mass concentration due to chamber wall loss, followed by greater loss when we purged the chamber at  $t > 1.5$  hours.

general pattern. We show the particle mobility size distribution from the SMPS, the rBC mass from the SP2, and the SP-AMS signal for both rBC and organic material (OM). Prior to coating ( $t < 0$ ), the SP2 and SP-AMS rBC signals decreased as particles were lost to the chamber walls. After each  $\alpha$ -pinene vapor injection, which drove SOA coating, the particle mobility diameter increased and there was also an increase in the SP-AMS OM signal. After the second injection ( $t = 0.6$  hours), the SP-AMS rBC signal increased while the SP2-measured rBC mass concentration continued to decay, as expected due to particle wall loss. This difference demonstrates that the increase in SP-AMS rBC signal with thicker SOA coatings was almost certainly due to an increase in the IR laser beam particle collection efficiency ( $E_{IR}$ ) of the SP-AMS, and not an increase in the actual rBC mass present in the chamber.

### 5.3.3. Particle composition from mass spectrometry

In Figure 5.6 we show speciated high-resolution mass spectra from the SP-AMS for nascent and thickly coated biomass-burning particles, detected with the IR-laser on. The coating was SOA formed from  $\alpha$ -pinene ozonolysis. High-resolution peak fitting was done using PIKA version 1.15 (Decarlo et al., 2006). Highly resolved ions were classified into a species and are displayed at unit mass resolution according to the fragmentation table therein. With respect to this dataset, the fragmentation table was only used to adjust the apportioning of  $\text{CO}_2^+$  and  $\text{C}_1^+$  ions. To account for  $\text{CO}_2^+$  in the gas-phase vs. particle phase, the fragmentation table was adjusted using HEPA filter gas-only measurements. To account for  $\text{C}_1^+$  that may result from the fragmentation of non-refractory OM components, the fragmentation table specifies that the amount of  $\text{C}_1^+$  attributed to rBC is limited to  $0.625 \cdot \text{C}_3^+$ , the ratio observed for the rBC calibrant, Regal Black (Onasch et al., 2012). Recent studies have begun to investigate the degree to which non-refractory OM contributes to larger elemental-carbon ion fragments ( $\text{C}_x^+$ , where  $x > 1$ ) using IR laser vaporization. This has important implications for quantitative measurements of rBC using the SP-AMS and also for source apportionment based on the ion fragmentation pattern of rBC (Corbin et al., 2014).

We measured refractory and non-refractory material from nascent soot using the SP-AMS with the IR laser on. High-resolution analysis of non-refractory organic material showed significant contribution from aliphatic ions,  $^{55}[\text{C}_4\text{H}_7]^+$ ,  $^{57}[\text{C}_4\text{H}_9]^+$ ,  $^{69}[\text{C}_5\text{H}_9]^+$ , and  $^{81}[\text{C}_6\text{H}_9]^+$ . This is consistent with other AMS measurements of fresh, flaming-phase biomass-burning emissions (Corbin et al., 2015; Cubison et al., 2011; Hennigan et al., 2011). We also observed the highly oxygenated ions  $\text{C}_2\text{H}_3\text{O}_2^+$  ( $m/z + 60$ ) and  $\text{C}_3\text{H}_5\text{O}_2^+$  ( $m/z + 73$ ), which are common tracer ions for biomass burning. However,  $\text{C}_2\text{H}_3\text{O}_2^+$  was less than 0.5% of the total organic signal for nascent soot, much less than what has previously been reported in BBA measurements (Aiken et al., 2010; Corbin et al., 2015; Cubison et al., 2011; Hennigan et al., 2010, 2011; Lee et al., 2010). This is likely due to low cellulose content in the bark that we burned, resulting in less formation of the anhydrosugars including

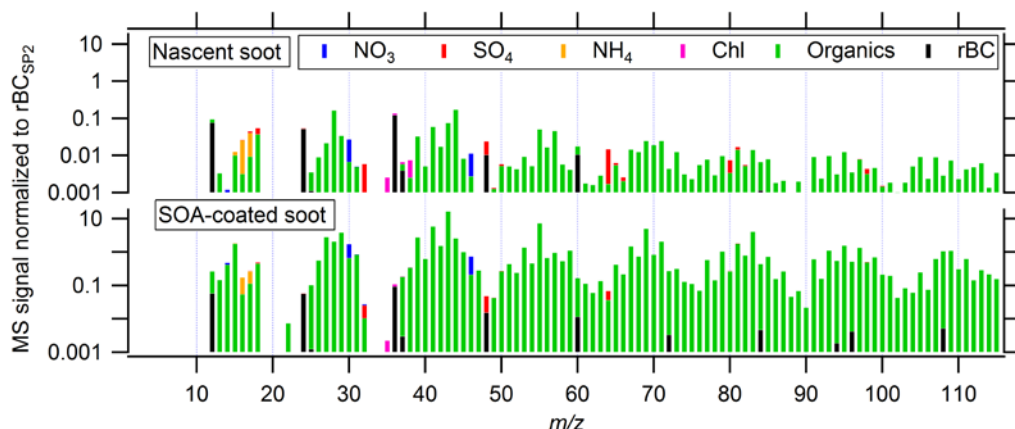


Figure 5.6. Stick integrated high-resolution mass spectra from the SP-AMS for nascent (top) and thickly SOA-coated soot (bottom). Mass spectra were collected with the IR laser on, and have been normalized by total rBC mass as measured by the SP2 to account for particle wall-loss. Peak bar colors correspond to the assigned chemical components for each unit  $m/z$  ion peak, based on analysis of the high-resolution mass spectra. The nascent soot spectrum is rich in refractory black carbon, inorganic ions, and organic fragments. The spectrum from the SOA-coated soot, on the other hand, is dominated by the OM from the secondary organic aerosol. However, increased sensitivity to larger EC fragments from rBC in the coated particles is obvious.

levoglucosan compared to burning wood (Branca et al., 2007). The average oxidation state of carbon ( $\overline{OS}_c = 2O:C - H:C$ ) for the organic fragments (including  $HO^+$ ,  $H_2O^+$ , and  $CO_2^+$ ) was  $-0.56 \pm 0.25$ . This low oxidation state is consistent with primary organic aerosol (Canagaratna et al., 2014; Kroll et al., 2011). We also observed refractory material, including elemental carbon series ( $C_1^+ - C_9^+$ ) and some metals including potassium, rubidium, and zinc. The alkali metals have very low ionization energies, and thus may become ionized by heating in the IR laser. This ionization mechanism is independent of the 70 eV electrons that usually ionize neutral vapors in the SP-AMS. A broad abnormal ion peak shape of the metals indicates that they underwent single-step thermal ionization in the IR beam, rather than conventional two-step thermal vaporization with subsequent electron ionization (Allan et al., 2004; Carbone et al., 2015; Corbin et al., 2015; Drewnick et al., 2006). Condensation

of SOA from  $\alpha$ -pinene ozonolysis increased the signal from most organic fragments. Especially notable was the signal increase for singly oxygenated organic fragments  $^{43}[\text{C}_2\text{H}_3\text{O}]^+$ ,  $^{55}[\text{C}_3\text{H}_3\text{O}]^+$ ,  $^{71}[\text{C}_4\text{H}_7\text{O}]^+$  and  $^{83}[\text{C}_5\text{H}_7\text{O}]^+$ . Reduced fragments such as  $^{69}[\text{C}_5\text{H}_9]^+$  also increased with SOA coating. After a thick coating (with an SOA:BC mass ratio of approximately 9) the average oxidation state of carbon was  $1.15 \pm 0.04$ . This is consistent with the  $\alpha$ -pinene ozonolysis SOA formed in smog chambers (Chhabra et al., 2010; Shilling et al., 2008); however, the SOA mass spectra we obtain show relatively less fragmentation than similar  $\alpha$ -pinene SOA mass spectra obtained with a conventional AMS using the 600 °C heater. This suggests that a significant fraction of the particles were vaporized by the IR laser ( $> 97\%$  of the BBA contained sufficient black carbon that could be measured by the SP2) and that this produced marginally less fragmentation; the much lower  $f_{44}$  (fraction of total ion signal at  $m/z + 44$ ) is also consistent with this hypothesis. Canagaratna et al. (2015) used near-threshold VUV ionization with a SP-AMS to confirm that ionization via the IR laser resulted in significantly less fragmentation for pure species, relative to when vaporized by the 600 °C heater.

Attribution of rBC in the SP-AMS mass spectrum would be straightforward if graphitic material had a consistent fragmentation pattern and if all elemental carbon fragments (the  $\text{C}_x^+$  family) arose only from rBC. However, studies using high-resolution transmission electron microscopy (HR-TEM) have shown that rBC can have varying degrees of disorder that result from formation conditions (Vander Wal and Tomasek, 2004). Onasch et al. (2015) showed the IR laser in the SP-AMS may cause restructuring of the rBC due to annealing. Annealing has been observed in other graphitic particle systems using HR-TEM and a pulsed laser (Vander Wal and Choi, 1999; Vander Wal and Jensen, 1998). It is also well known that organic aerosol produces  $\text{C}_1^+$  and  $\text{C}_2^+$  fragments following electron ionization (Alfarra, 2004; Corbin et al., 2014), but we have evidence that SOA either produces larger  $\text{C}_x^+$  fragments or that it changes the rBC fragmentation pattern. In Figure 5.7 we show the ion peak area ratios for  $\text{C}_4^+/\text{C}_3^+$  and  $\text{C}_{6-9^+}/\text{C}_3^+$  for size-selected soot particles as they became coated with OA. The SOA mass per particle on the x-axis is the mass calculated from particle



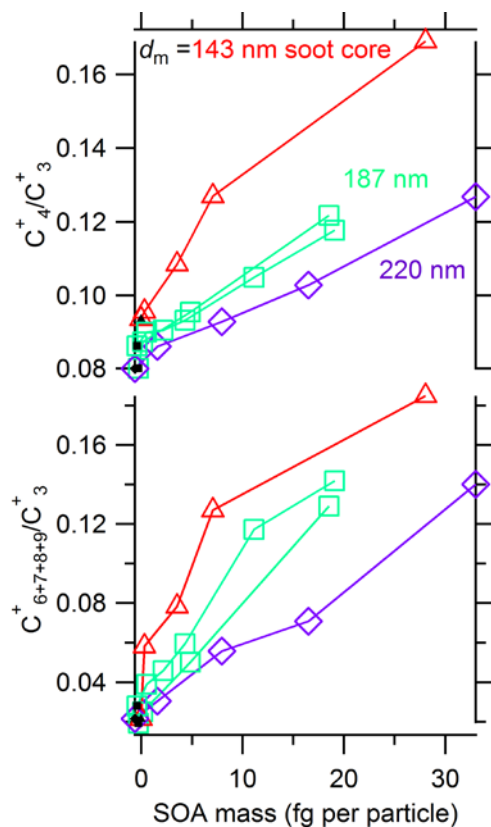


Figure 5.7. SP-AMS measurements of carbon ion family ( $C_x^+$ ) peak area ratios versus SOA coating mass on three different BBA soot-core sizes, indicated by symbol colors. SOA mass determined from SP-AMS measurements of all identified OM mass (as in Fig. 5.4). The ratio of  $C_4^+$  and  $C_{\Sigma 6-9}^+$  compared to  $C_3^+$ , increases with organic coating either due to contributions to the  $C_x^+$  family from non-refractory OM, and/or a decrease in relative fragmentation of EC to  $C_3^+$ .

size measurements, described in section 5.2.3. Both ratios increase consistently with coating mass, with a larger slope for smaller cores (with smaller  $m_{rBC}$ ). This is also apparent in Figure 5.6, where black sticks representing EC from rBC are evident for  $m/z \geq 72$  after SOA coating, while they were not detected in the nascent soot. We propose three possible explanations for these trends: 1) SOA coating changes the fragmentation pattern of EC to reduce the  $C_3^+$  signal, thereby enhancing the apparent ratio of other EC ions relative to it; 2) SOA generates significant signal for  $C_{>3}^+$ ; or 3) The abundant signal at the same nominal masses as  $C_{>5}^+$  causes the HR peak fitting

to incorrectly attribute some signal to  $C_{>5}^+$ . During HR peak fitting, the user decides whether to include an ion based on the residual signal. The residual signal is the amount of measured signal that is not reproduced by the fitted HR ion species. Although the addition of the higher  $C_x^+$  fragments appear to reduce the residual signal, the peak fitting without them is still very good (residual  $<0.05\%$ ). Furthermore, the signal at  $C_1^+$ - $C_5^+$  is much higher and better resolved in the peak fitting due to fewer available peaks to fit. Although the causes of these trends are not clear, the trends themselves indicate that soot source apportionment by the SP-AMS might be most meaningful for rBC that has been thermally denuded to remove any coatings as this would remove any effect of OM on the  $C_x^+$  ratios measured from the rBC.

We detected small amounts of non-refractory species other than OM, amounting to less than 10% of the total mass. Ammonium sulfate condensed onto the particles after they were injected into the chamber. This was probably caused by the formation of sulfuric acid from oxidation of  $SO_{2(g)}$ , and subsequent neutralization by ammonia in the dry chamber. We also detected nitrate ions after addition of ozone to the chamber, as well as after injections of  $\alpha$ -pinene, suggesting the formation of some organonitrates (Farmer et al., 2010; Zhang et al., 2006). The  $NO^+/NO_2^+$  ratio was 2.2, as opposed to 1.45 for ammonium nitrate calibration particles. We observed chloride with both SP-AMS vaporizer modes (IR laser on and off), while the potassium signal was much larger when we operated the SP-AMS with the laser on. This is further evidence that the potassium is internally mixed with black carbon, and that it underwent one-step thermal ionization in the IR beam (Corbin et al., 2015; Drewnick et al., 2006; Lee et al., 2016). Sulfur dioxide, ammonia, nitrogen oxides, hydrogen chloride, and other chloride salts are known common primary emissions from biomass burning (Levin et al., 2010; Li et al., 2003; Reid et al., 2005; Stockwell et al., 2015; Zauscher et al., 2013).

Figure 5.8 shows single-polarity mass spectra obtained by the LAAPTOF for individual particles before and after coating with SOA. The characteristic ion series for elemental carbon included  $C_1^+$ ,  $C_2^+$ , and  $C_3^+$ . We also observed anions  $C_1^-$  and  $C_2^-$ .

for some particles, but not as consistently. We observed  $\text{NO}^+$  in both coated and uncoated particles. We believe that this may be the result of  $\text{NO}_x$  and  $\text{O}_3$  combining in the chamber and forming  $\text{NO}_3$  radicals. These  $\text{NO}_3$  radicals may then react with water or organic vapors to form  $\text{HNO}_3$  or organonitrates, respectively. Either species could then condense onto the existing particles and fragment to  $\text{NO}^+$  in the mass spectrometers.  $\text{K}^+$  was readily identified by its isotopic abundance at  $m/z$  +39 and +41 (Ba(Bahadur et al., 2010)hadur et al., 2010; Healy et al., 2012; Silva et al., 1999). OM fragments tentatively identified as  $\text{CO}^+$  at  $m/z$  +28 and  $\text{C}_2\text{H}_3\text{O}^+$  at  $m/z$  +43 were measured from both nascent and oxidized particles. We also observed sulfur and sulfate ions ( $\text{S}^+$ ,  $\text{SO}^+$ , and  $\text{HSO}_4^-$ ), likely fragments of sulfates.  $\text{Zn}^+$  was observed and identified by its isotopic fingerprint.

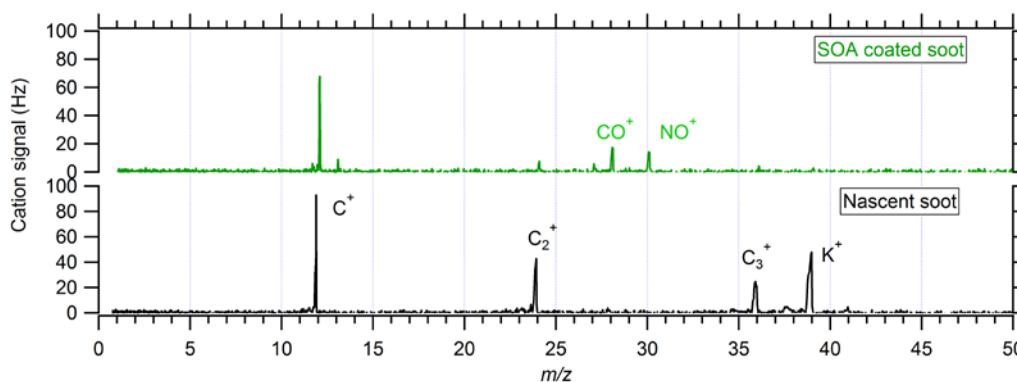


Figure 5.8. Positive polarity mass spectra and ion assignments for two representative particles analyzed by the LAAPTOF. The elemental carbon fragment series ( $\text{C}_x^+$ ) dominates the nascent soot spectra in the bottom, while the contribution from oxidized organic matter is increased in the top panel for a soot particle that was coated with  $\alpha$ -pinene SOA.

As previously stated, for these experiments the instrument was operated in UV laser free-fire mode, without the aid of light scattering modules to more efficiently detect particles and trigger the excimer. As a result, only 454 individual mass spectra were collected by the LAAPTOF across the four experiments. 31 of 454 particles contained only potassium and inorganic species, with no detectable elemental carbon. 4 of 454 particles contained  $\text{S}^+$  or  $\text{SO}^+$ . 11 of the 454 had a negative ion mass

spectrum in addition to a positive ion mass spectrum. 5 of these negative ion spectra contained only  $\text{HSO}_4^-$ , 2 were only  $\text{C}_1^-$ , and the remaining were a richer spectrum of elemental carbon with larger signal from even carbon number anions, consistent with previous observations (Bloomfield et al., 1985; Onasch et al., 2015). 104 of 454 particles contained  $\text{Zn}^+$ . 281 particles contained  $\text{NO}^+$ .

#### 5.3.4. SP-AMS sensitivity to refractory species

We determined the ion response of the SP-AMS to biomass-burning particles as a function of SOA coating mass using two ions produced from refractory biomass-burning material –  $\text{K}^+$  and  $\text{C}_3^+$  – normalized by the rBC mass concentration measured by the SP2 ( $\text{rBC}_{\text{SP2}}$ ). In Fig. 5.9 we show the  $\text{K}^+$  and  $\text{C}_3^+$  SP-AMS ion signal per  $\text{rBC}_{\text{SP2}}$  mass during progressive SOA coating experiments. The plotted points are ten-minute averages for four batch chamber experiments using different initial soot core sizes. We determined the SOA mass per particle using the method described in section 5.2.3. Different colored and shaped traces indicate the mobility mode diameter of the initial soot core injected into the chamber, and the black dots indicate the initial nascent soot, prior to SOA coating. We used the SP2-measured rBC mass to correct for particle wall loss in the chamber because the rBC mass measurement of the SP2 is insensitive to particle shape and coating thickness for particles with at least 0.7 fg of rBC present (Schwarz et al., 2010). The smallest particle mode measured in these experiments was 1.1 fg of rBC, well above detection limits for the SP2. All of the wall loss corrected ion signals in Fig. 5.9 were also normalized to the uncoated soot conditions. This was done for three reasons. First, the inherent variability in biomass burning limits how much one can expect uncoated soot particles to have similar amounts of K or rBC. However, within a given coating experiment, the average composition of the soot particle core is guaranteed to be the same. Second, it allows for ready comparison of the data in Figs. 5.9 and 5.10, which compares the changes in the two ions directly. Finally, the normalization is a small change relative to the effect induced by coating the soot particles with SOA, which is the focus of this work. Prior to normalization, initial wall-loss corrected values for  $\text{C}_3^+$  ( $\text{K}^+$ ) for nascent conditions

agreed within 30% (20%), compared to the sometimes 300% (600%) change due to coating the particles with SOA.

Potassium is a useful marker for refractory BBA material because it has a high signal-to-noise ratio, it is not produced by fragmentation of non-refractory OM, and it is a non-volatile unreactive conserved tracer. By turning off the IR laser we confirmed that very little of the potassium signal resulted from particles that hit the conventional 600 °C heater ( $< 1\%$  of total  $K^+$  signal with IR laser on). Therefore, the potassium we observed with the IR laser on was internally mixed with rBC. We selected  $C_3^+$  at  $m/z$  36 as an ion of interest because of its large contribution to the total rBC  $C_x^+$  family signal (Fig. 5.4), and the very low contribution from OM. The  $C_3^+$  signal from OM is less than 0.08% of the total OM signal when the IR laser is off and particles are vaporized by the heater. One important difference between the two measured species,  $K^+$  and  $C_3^+$ , is the method of ion formation within the SP-AMS. rBC undergoes the conventional process of IR vaporization followed by 70 eV electron ionization of neutral vapors. Potassium, however, has a very low ionization energy and at high temperatures can undergo one-step, thermal ionization, without interacting with 70 eV electrons to become ionized (Corbin et al., 2015; Drewnick et al., 2006; Svane et al., 2004; Zandberg, 1995). Furthermore, rBC particles approach  $\sim 4000$  K in the IR laser before vaporizing, while potassium may vaporize/ionize at temperatures less than 1500 K (Svane et al., 2004).

Panels (a) and (e) in Figure 5.9 reveal an increasing SP-AMS response to both potassium and rBC as the SOA coating grew. Panels (b) and (f) show the attenuation of the  $K^+$  or  $C_3^+$  ion signal normalized to SP2-measured rBC, that resulted from moving the beam-width probe into the center of the particle beam. The attenuation increased as the SOA coating thickened because the particle beam narrowed. The increased response of the SP-AMS with successive coatings of SOA is thus due to an increase in the SP-AMS IR-beam particle collection efficiency,  $E_{IR}$ . However, the attenuation of  $K^+$  rises steeply, whereas the attenuation of  $C_3^+$  steadily continues to rise more shallowly with coating thickness.

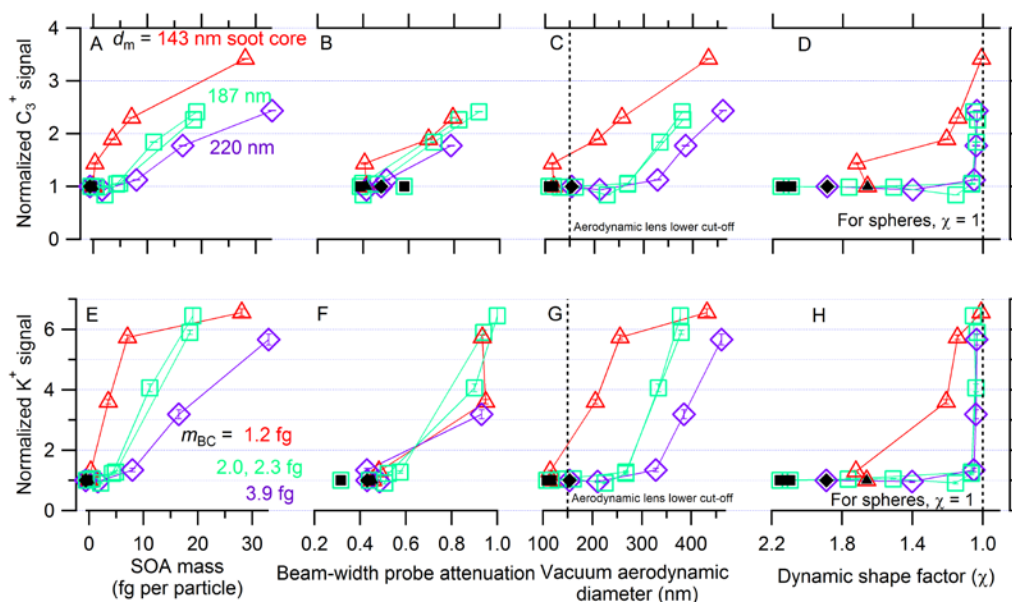


Figure 5.9. SP-AMS-measured biomass-burning ion signals for  $C_3^+$  (top) and  $K^+$  (bottom) for three mobility selected core particle sizes versus four different metrics. These signals are corrected for particle wall-loss using SP2-measured rBC, and then normalized to values obtained from the uncoated nascent soot. Symbols are colored/shaped by their initial soot core mobility diameter (SP2-measured rBC mass per particle), prior to SOA coating, where red triangles = 143 nm (1.2 fg), teal squares = 187 nm (2.0, 2.3 fg, two replicate experiments), and purple diamonds = 220 nm (3.9 fg). The nascent particles are indicated by black dots, and the lines connect them with the data points following subsequent SOA coatings. The left panels (a and e) display the normalized ratio of the SP-AMS-measured  $C_3^+$  and  $K^+$  ion signals, respectively, to the SP2-measured black carbon mass concentration as a function of the mass of SOA per particle. The SP-AMS-measured ion to SP2-measured rBC mass ratio is normalized to the uncoated soot values. Panels (b and f) display the attenuation of the SP-AMS ion signal caused by the beam-width probe in the center of the particle beam. Panels (c and g) display the mode mobility diameter of the particles that produced either the  $C_3^+$  or  $K^+$  ion signal. The vertical dashed line indicates the lower size cutoff for the aerodynamic lens. Panels (d and h) display the particle dynamic shape factor; particles start as less spherical ( $\chi > 1.0$ ) and move towards sphericity ( $\chi = 1$ ) as more SOA mass is added. The measurement uncertainties are indicated by the vertical error bars and represent the standard deviation of one-minute AMS integration time from the ten-minute averages presented by each symbol.

The IR laser beam cross-section that vaporizes particles has a roughly Gaussian intensity profile. The difference we observe between  $C_3^+$  and  $K^+$  attenuation suggests that the effective IR beam for vaporizing rBC, described by Willis et al. (2014), is narrower than the effective beam for thermal ionization of potassium. That is, rBC must pass through a region of higher laser energy density near the center of the IR beam to be vaporized, ionized by the electron source, and then detected than is required for thermal ionization of potassium. If an internally mixed particle containing potassium and rBC passes through the center of the laser, two processes will take place. rBC will become vaporized and ionized, and potassium will be thermally ionized. Since turning off the IR laser reduced the potassium signal to  $< 1\%$  of that when the laser was on, we know that the observed changes in K signal result from rBC particles internally mixed with some K. Thus, our measurements show that particles may pass through the potassium thermal ionization region of the IR beam but miss the smaller rBC vaporization region.

The ability of an aerodynamic lens, such as that used on the SP-AMS, to effectively focus a particle depends on particle morphology. Panels (c) and (g) in Fig. 5.9 illustrate the increasing response of the SP-AMS to coated rBC as a function of vacuum aerodynamic diameter. The increasing response is likely due to the product of the aerodynamic lens transmission efficiency and the overlap between the particle beam and the IR laser,  $E_{IR}$ . However, it appears that the largest increase in particle sensitivity occurs when the particle  $d_{va}$  increases beyond 200 nm. The lower size cutoff of the aerodynamic lens is 150 nm, as discussed in section 5.2.2 and illustrated by a black dotted line in Figs. 5.9c and 5.9g. Any changes in sensitivity for  $d_{va} > 150$  nm are therefore minimally affected by particle lens transmission. The particles grow as more SOA mass is condensed, and the larger particles are focused more efficiently by the aerodynamic lens towards the center of the IR laser, resulting in a larger instrument ion signal response with both increasing particle size and increasing SOA mass. The other factor that influences effective focusing of the particles in an aerodynamic lens is particle shape, reported as a calculated dynamic shape factor,  $\chi$ . As seen in panels (d) and (h), the shape factor decreases towards unity ( $\chi = 1$  for

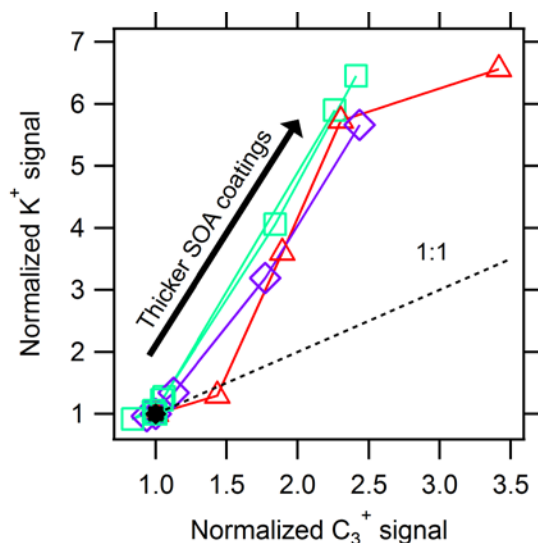


Figure 5.10. Correlation of refractory ion signals from the SP-AMS during SOA coating experiments. Colored symbols represent the relative enhancement of  $K^+$  and  $C_3^+$ , as in Figure 5.9. All four traces, indicating different coating experiments, begin at (1,1) and generally increase with increasing SOA coating. The increase in measured  $K^+$  compared to  $C_3^+$  ion signal for the same coatings shows that there are two different effective laser widths for the processes, thermal ionization of  $K^+$  and two-step vaporization-ionization of rBC, respectively.

spheres) as the particles become more thickly coated with SOA. Although the particles become nearly spherical after a few coatings, they still need to grow to a sufficiently large diameter to be successfully focused into the IR laser beam of the SP-AMS. Neither particle shape nor diameter alone is sufficient to describe  $E_{IR}$ . Even at  $d_{va} = 250$  nm there is a factor of two difference in response to particles with different dynamic shape factors. However, the largest increase in instrument response occurs after the particles are mostly spherical ( $\chi < 1.2$ ), which as we discussed in section 5.2.3 may describe the state of rBC particles in ambient biomass burning plumes after less than 1 hour of aging. This increase in instrument signal is driven by growth from condensation of additional SOA. Panels (d) and (h) demonstrate this by plotting the refractory ion signal ratios versus the dynamic shape factor ( $\chi$ ) calculated as described in section 5.2.3.



Figure 5.10 shows the same normalized  $K^+$  and  $C_3^+$  signals from Fig. 5.9, accounting for particle wall-loss and normalized to the ion response under nascent conditions. The differently shaped and colored traces show the relative enhancement of ion signals, measured for the same SOA coating conditions. The greater increase in the  $K^+$  signal compared to the increase in the  $C_3^+$  ion signal for the same coatings is attributed to two distinct ion formation mechanisms that the two species experienced. As the IR laser has a Gaussian intensity profile, the different mechanisms occur in different regions of the IR beam. Evidently, a higher intensity is necessary for the vaporization of rBC, but a lower intensity can still drive thermal vaporization/ionization of alkali metals, such as potassium and sodium. The Gaussian IR beam thus has a greater effective width for alkali metals than for rBC.

Figure 5.11 displays the wall-loss corrected  $K^+$  and  $C_x^+$  signal measured by the SP-AMS as a function of wall-loss corrected OM signal. We corrected the SP-AMS signal for wall losses using the rBC mass measurement from the SP2, and we normalized the signals from each experiment to the signals for the nascent soot particles. We smoothed the traces using a 3-point boxcar moving average to clarify trends. The OM signal is not quantitative due to unknown relative ionization and collection efficiencies for organics detected with both the IR laser and heater operating simultaneously. However, it provides a high time resolution relative metric of the amount of condensed SOA. It shows that even at our highest achieved coating thickness the signals from both  $K^+$  and  $C_x^+$  continued to increase; neither signal saturated. This is different from what is expected based on the results of Willis et al. (2014). When they coated Regal Black with OM in the form of DOS, they observed that both OM ions and EC ions reached a maximum enhancement after coating the Regal Black with a thick coating of DOS (OM mass:EC mass > 3.) Although we cannot rule out the effect of  $E_{IR}$ , the continued increase merits investigation of other causes for increased ion signals with additional SOA coating.

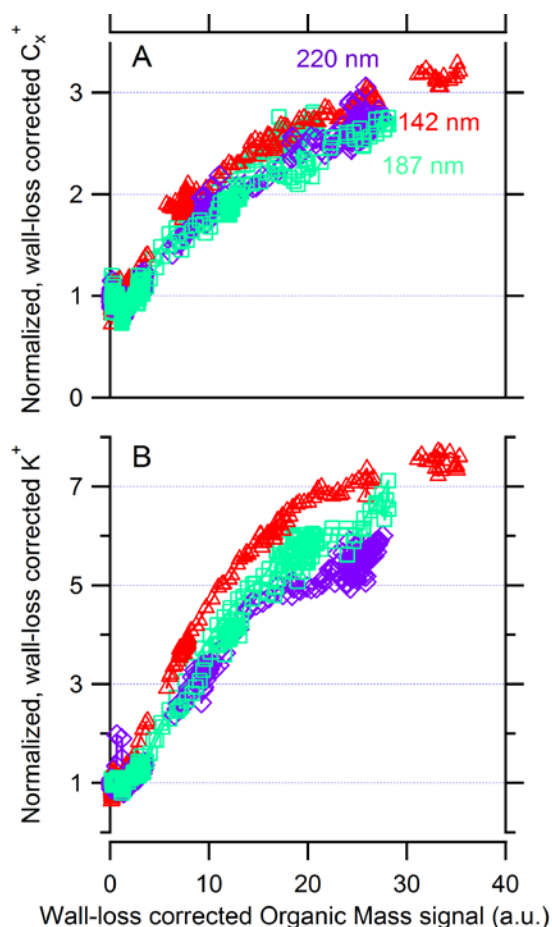


Figure 5.11. Wall-loss corrected SP-AMS signal from rBC  $C_x^+$  (panel A) and  $K^+$  (panel B) have been normalized to their nascent values (before SOA coating) and are shown as a function of wall-loss corrected SP-AMS OM signal. Marker shapes and sizes indicate the initial soot core mobility diameter for a given experiment. One-minute averages show that the evolution of the particle sensitivity is continuous, and that even at our thickest SOA coating, we continue to see an increase in instrument sensitivity to both rBC and K refractory material.

The continuous increase in  $K^+$  ion signal may potentially be explained by changes in the thermal ionization efficiency, described by the Saha-Langmuir equation (Vandburg and Ionov, 1973). This states that the probability of thermal ionization of a species will increase if the surface it vaporizes from has a higher work function or reaches a higher temperature. One explanation is that the highly oxygenated SOA possesses a higher work function than the rBC, and thus as the

particle is coated it may generate potassium ions more efficiently. However, it seems unlikely that K would vaporize before all the SOA, as is seen in similar, albeit ambient pressure, IR laser systems (Moteki and Kondo, 2007; Schwarz et al., 2010; Stephens et al., 2003). An alternative explanation is that thicker SOA coatings may cause the particle to penetrate deeper into Gaussian profile of the IR laser before the K vaporizes and it subsequently vaporizes from a hotter surface, thus generating more ions thermally.

With respect to the increasing  $C_x^+$  signal with increasing coating thickness, a potential explanation includes the fragmentation of SOA to contribute significantly to  $C_x^+$  mass. As stated in section 5.3.4, laser-off measurements of the SOA showed that  $C_3^+$  accounted for 0.08% of the SOA mass. With an OM mass increase of ten times the rBC present in a particle, and assumed relative ionization efficiencies for rBC and OM of 0.2 and 1.4, respectively, the perceived increase in EC that would be attributed incorrectly would be 1.1%. This is much smaller than the observed relative increase in  $C_3^+$  for OM:rBC > 3, ~63% for the change in the last two data points for  $d_{mob} = 220$  in Fig. 5.9a. Furthermore, with the increased fraction of particles being vaporized by the IR laser, it has been shown that fragmentation would decrease, thereby decreasing the contribution of SOA to  $C_3^+$  (Canagaratna et al., 2015). Alternative explanations may include instrument differences and variability in IR laser beam width. This illustrates that particle beam width is an important metric for quantitative measurements of BBA, even with a high SOA:rBC mass ratio > 9, and particle vacuum aerodynamic diameters greater than 400 nm.

### 5.3.5. LAAPTOF quantification of OM on externally mixed soot particles

Single-particle analysis provides valuable insight into the physical and chemical evolution of biomass-burning plumes as they are diluted by entrainment of background air, and undergo transformation processes during transport. Single-particle analysis also facilitates the determination of contributions from biomass-burning particles to aerosol loading for source apportionment, and can reveal changes in the mixing state of biomass-burning particles as they age (Chen et al.,

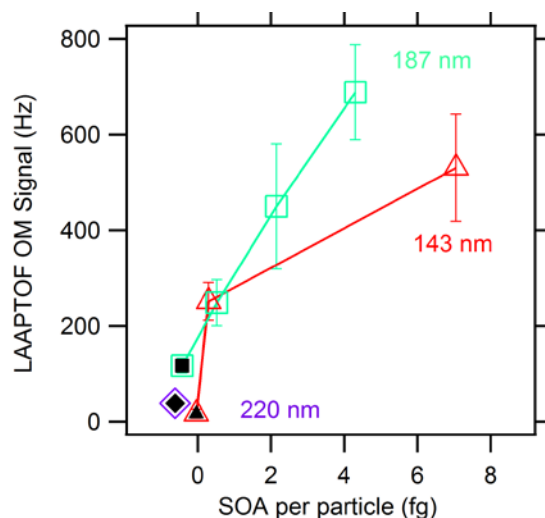


Figure 5.12. Averaged OM signal ( $m/z+28$ ;  $\text{CO}^+$ ) from nascent and SOA-coated soot particles measured by the LAAPTOF during SOA coating experiments vs. SOA mass per particle. Error bars indicate the standard error. There is a strong positive correlation despite the complex biomass-burning aerosol matrix. Open marker colors/shapes indicate the initial  $d_{\text{mob}}$  of the size-selected soot core, and black markers indicate nascent, uncoated soot particles.

2014; Moffet et al., 2008; Silva et al., 1999; Zauscher et al., 2013). Although laser desorption/ionization (LDI), such as that used by the LAAPTOF, is often regarded as a semi-quantitative method, there are numerous examples demonstrating that it can be mass quantitative for constrained systems where similar particle matrices are studied (Healy et al., 2013; Jeong et al., 2011; Mansoori et al., 1994; Spencer and Prather, 2006; Sullivan et al., 2007, 2009). Quantitative mass measurements using (LDI-SP-MS) are difficult because of the particle matrix effects that influence how much energy is absorbed by a given particle and subsequently the production and fate of the generated ions (Murphy, 2007; Steele et al., 2005; Sullivan and Prather, 2005). Calibration of the LDI-SP-MS ion-signal response to particles of known composition is also required to yield mass-quantitative component measurements. The SOA-coated soot experiments we present here provide a unique opportunity to characterize the response of the LAAPTOF to realistic biomass-burning cores coated

with complex and realistic biogenic SOA, where the masses of rBC and OM are well constrained.

We show the average OM signal per particle measured by the LAAPTOF in Figure 5.12. We observed a large degree of molecular fragmentation; most of the OM signal appeared at  $m/z + 28$ , which we attribute to  $\text{CO}^+$ . All data points represent the average of at least five particles with a minimum of 100 Hz of total EC ion signal at  $m/z + 24$ ,  $+36$ ,  $+48$ , and  $+60$ , representing  $\text{C}_{2-5}^+$ . This excludes any homogeneously nucleated SOA particles and low-signal particles from the analysis. 160 particles of the 454 total particles detected met the above criteria. A linear regression fit of all LAAPTOF OM ion signal as a function of SOA mass per particle results in a  $R^2 = 0.72$  ( $\text{OM signal (Hz)} = 75(\text{fg SOA}) + 167$ ). This may be due to different light absorption and laser energy distribution properties of different sized soot cores. Narrowing the analysis to the experiment with 187 nm soot cores results in a highly linear fit with a  $R^2 = 0.998$  ( $\text{OM signal (Hz)} = 120(\text{fg SOA}) + 179$ ). SOA from a single precursor can still contain hundreds or thousands of organic compounds, with a broad range of molecular weights, degrees of functionalization, and optical properties (Zhang et al., 2015). Despite the complex nature of the SOA coating and biomass-burning aerosol core, we observed a strong linear relationship between the amount of SOA condensed on the particle and the OM signal from the LAAPTOF. It is important to note that although other LDI-SP-MS studies have found a good correlation between OM signal and reference measurements, this work shows that an even better correlation can be obtained if the analysis can be informed by the chemical information provided by the mass spectra. In this case we show that, with some improvements in excimer laser homogeneity, it may be possible for an algorithm to isolate rBC-containing particles and identify the necessary function to convert OM signal into SOA mass per particle.

Figure 5.13 shows the same OM ion signal measured by the LAAPTOF plotted in Fig. 5.12, now normalized by the concurrent LAAPTOF EC ion signal. This parallels the analysis by ATOFMS of spark-generated EC particles coated by the condensation of diesel fuel presented by Spencer and Prather (2006), but using

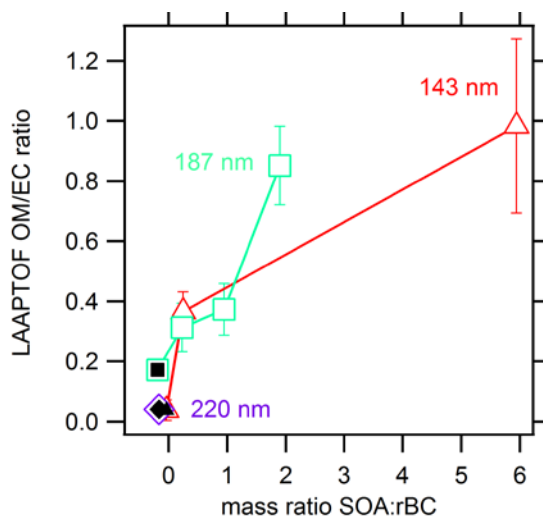


Figure 5.13. LAAPTOF-measured OM ion signal ( $m/z + 28$ ;  $\text{CO}^+$ ) normalized by LAAPTOF EC ion signal (sum of  $m/z + 24$ ,  $+36$ ,  $+48$ ,  $+60$ ;  $\text{C}_{2-5}^+$ ) for uncoated and SOA coated soot particles. Error bars indicate the standard error. Here the OM:EC ratio is shown as a function of the ratio of mobility-derived SOA mass to SP2-measured rBC. The LAAPTOF EC signal serves as an internal standard to normalize for the actual amount of laser energy the particle absorbed, which can change with increased rBC mass or SOA coating, and particle size and shape. Marker colors/shapes indicate the initial size-selected soot core  $d_{mob}$  for each experiment.

more complex and realistic particle EC and OM components. EC fragments used included  $\text{C}_{2-5}^+$  but excluded  $\text{C}_{1}^+$  because we have observed that OM can also be charred to  $\text{C}_{1}^+$  and thus produce an interference to the quantification of EC at  $m/z$  12. The OM:EC ion ratio used here is thus  $\text{CO}^+:\text{C}_{2-5}^+$ . We use the ratio of OM/EC ions to account for laser shot-to-shot variability, where more ions may be generated due to increased laser fluence or increased absorption of laser energy. We sampled biomass-burning particles that contained potassium salts, which ionize readily, as well as strongly light-absorbing rBC (Gross et al., 2000). This represents the complex composition of realistic aged BBA. Initial particles were composed mostly of black carbon, with initially variable shapes, and with an unknown distribution of potassium salts per particle. Despite the variability in the soot core composition of individual particles, a positive correlation between the amount of SOA mass per particle and the

LAAPTOF ion signal from oxidized organics was still observed from these mixed rBC and inorganic salt particles, when averaged over the many particles we sampled.

Other LDI-SP-MS instruments that use longer ionization wavelengths, such as 266 nm used in the ATOFMS, do not typically fragment oxidized organics to  $\text{CO}^+$ ; instead their major oxidized OM ion fragment is observed at  $m/z +43$ , presumably from  $\text{C}_2\text{H}_3\text{O}^+$  (Moffet and Prather, 2009; Spencer and Prather, 2006). We operated the LAAPTOF's excimer laser at a moderate pulse energy of 2.0 mJ, as a tradeoff between increased sensitivity while avoiding excessive decomposition or fragmentation of OM into EC  $\text{C}_n^+$  fragments. In the work described in Spencer and Prather (2006), graphitic soot particles with no condensed organics had an OM:EC ion signal ratio of  $\sim 0$ , and those coated with a mass of condensed fuel equal to the EC mass had an OM:EC ion signal ratio of 2.25. For a similar OM:EC mass ratio  $\sim 1$  in our experiments, we saw a more modest LAAPTOF OM:EC ratio of  $\sim 0.35$ . This difference may be caused by differences in instrument operation and chemical composition of the refractory EC core and OM coating. The LAAPTOF uses an exciplex VUV laser at 193 nm (compared to the "softer" 266 nm Nd:YAG laser in the ATOFMS) and we observe more extensive molecular fragmentation of the OM. Thus, we quantified OM with a single ion ( $\text{CO}^+$ ), compared to the various ions used by Spencer and Prather (i.e.  $m/z +27$ ,  $+29$ ,  $+37$ ,  $+43$ ). A softer ionization might have resulted in less charring of SOA to  $\text{C}_1^+$  in the LAAPTOF, and thus increased the slope of the LAAPTOF-measured OM:EC ions versus mass fraction of SOA. Spencer and Prather used condensed diesel fuel vapors as their source of OM, while we used SOA from the ozonolysis of  $\alpha$ -pinene. Therefore, the OM used in the prior study was unoxidized primary organic aerosol, while our OM was highly oxidized complex secondary organic aerosol.

## 5.4. Conclusions

We investigated the response of two particle mass spectrometers to biomass-burning particles with carefully controlled amounts of organic matter and well characterized particle properties. Our analysis revealed a variety of particle morphologies and compositions, leading to a broad distribution of vacuum

aerodynamic diameters at a single selected mobility diameter. As these particles of various compositions and shapes became coated with SOA, measurements using the beam-width probe of the SP-AMS revealed that the effective IR laser beam width for thermal ionization of potassium is larger than for vaporization of rBC. Future measurements using the SP-AMS would do well to quantify the particle-beam and effective IR-laser beam overlap for the species of interest using beam width probe measurements. The fraction of rBC-containing particles that experience sufficient laser fluence to vaporize the non-refractory coating should always be greater than or equal to the fraction of particles whose refractory material is also vaporized. The use of optical components to change the IR laser from a Gaussian to a uniform flat-top energy profile would greatly simplify the analysis of rBC-containing soot particles by the SP-AMS by ensuring that all particles passing through the laser experience the same amount of energy. This would eliminate the difference given above regarding the fraction of rBC-containing particles whose non-refractory versus refractory components are detected.

Although these measurements explored thick SOA coatings and large particle sizes, we did not observe a plateau in instrument response to potassium or black carbon as the coating was increased. These findings have important implications for obtaining quantitative mass measurements, and can help to better inform the analysis and interpretation of SP-AMS measurements of the emissions and specifically aging biomass-burning aerosol (Corbin et al., 2015; Dallmann et al., 2014; Fortner et al., 2012; Lee et al., 2016; Massoli et al., 2015). We would like to add however, that although changes in  $d_{va}$  may result in varying  $E_{IR}$ , SP-AMS measurements of rBC have been shown to correlate with reference measurements (Fortner et al., 2012; Willis et al., 2014). This suggests that the changes in secondary aerosol mass required to cause large changes in  $E_{IR}$  for rBC did not happen on the timescale of those measurements.

Mass spectral analysis with the SP-AMS also revealed that increased SOA coatings on the biomass-burning soot changed the relative abundance of elemental-carbon clusters. Specifically, as the particles became more thickly coated with SOA, the ratio of  $C_{>3}^+$  to  $C_3^+$  increased. The degree of change for the ratio of  $C_4^+$  to  $C_3^+$  was



smaller than the precision suggested Corbin et al. (2014) for identifying soot-particle source types using ratios of the elemental carbon ion family,  $C_x^+$ . However, the observed ratio of  $C_4^+$  to  $C_3^+$  was inconsistent with that previously observed from quenched-combustion flame soot (Corbin et al., 2014; Maricq, 2014). This reinforces the need for thermal denuding of ambient soot samples before attempting source analysis using EC ratios.

Despite the challenges presented by complex particle composition and shape for laser desorption ionization single-particle mass spectrometry, there is a strong correlation between the average OM ion signal measured by the LAAPTOF and the SOA mass per particle. Although this quantitative relationship has been shown previously for LDI-SP-MS analysis of graphite spark discharge soot coated by diesel fuel condensation (Spencer and Prather, 2006), this is the first time it has been explored with realistic combustion soot in the presence of inorganic components and complex realistic SOA. This opens the way for more quantitative single-particle measurements using techniques such as laser-beam homogenization and particle type informed ion sensitivity calibrations. Additional work is required to investigate the response of single-particle mass spectrometry to other atmospherically relevant core-shell combinations.

## 5.5. References

Ahern, A. T., Subramanian, R., Saliba, G., Lipsky, E. M., Donahue, N. M. and Sullivan, R. C.: Effect of secondary organic aerosol coating thickness on the real-time detection and characterization of biomass-burning soot by two particle mass spectrometers, *Atmos. Meas. Tech.*, 9(12), 6117–6137, doi:10.5194/amt-9-6117-2016, 2016.

Aiken, A. C., de Foy, B., Wiedinmyer, C., DeCarlo, P. F., Ulbrich, I. M., Wehrli, M. N., Szidat, S., Prevot, A. S. H., Noda, J., Wacker, L., Volkamer, R., Fortner, E., Wang, J., Laskin, A., Shutthanandan, V., Zheng, J., Zhang, R., Paredes-Miranda, G., Arnott, W. P., Molina, L. T., Sosa, G., Querol, X. and Jimenez, J. L.: Mexico city aerosol analysis during MILAGRO using high resolution aerosol mass spectrometry at the urban supersite (T0) – Part 2: Analysis of the biomass burning contribution and the non-fossil carbon fraction, *Atmos. Chem. Phys.*, 10(12), 5315–5341, doi:10.5194/acp-10-5315-2010, 2010.

Alfarra, M. R.: Insights Into Atmospheric Organic Aerosols Using An Aerosol Mass Spectrometer, University of Manchester., 2004.

Allan, J. D., Delia, A. E., Coe, H., Bower, K. N., Rami Alfarra, M., Jimenez, J. L., Middlebrook, A. M., Drewnick, F., Onasch, T. B., Canagaratna, M. R., Jayne, J. T., Worsnop, D. R. and Allan, J. D.: A generalised method for the extraction of chemically resolved mass spectra from Aerodyne aerosol mass spectrometer data, *Aerosol Sci.*, 35(35), 909–922, doi:10.1016/j.jaerosci.2004.02.007, 2004.

Andreae, M. O.: Soot carbon and excess fine potassium: long-range transport of combustion-derived aerosols., *Science*, 220(4602), 1148–51, doi:10.1126/science.220.4602.1148, 1983.

Anenberg, S. C., Schwartz, J., Shindell, D., Amann, M., Faluvegi, G., Klimont, Z., Janssens-Maenhout, G., Pozzoli, L., Van Dingenen, R., Vignati, E., Emberson, L., Muller, N. Z., West, J. J., Williams, M., Demkine, V., Hicks, W. K., Kuylensstierna, J., Raes, F. and Ramanathan, V.: Global Air Quality and Health Co-benefits of Mitigating Near-Term

Climate Change through Methane and Black Carbon Emission Controls, *Environ. Health Perspect.*, 120(6), 831–839, doi:10.1289/ehp.1104301, 2012.

Bahadur, R., Russell, L. M. and Prather, K. A.: Composition and Morphology of Individual Combustion, Biomass Burning, and Secondary Organic Particle Types Obtained Using Urban and Coastal ATOFMS and STXM-NEXAFS Measurements, *Aerosol Sci. Technol.*, 44(7), 551–562, doi:10.1080/02786821003786048, 2010.

Bhave, P. V, Allen, J. O., Morrical, B. D., Fergenson, D. P., Cass, G. R. and Prather, K. A.: A Field-Based Approach for Determining ATOFMS Instrument Sensitivities to Ammonium and Nitrate, *Environ. Sci. Technol.*, 36(22), 4868–4879, doi:10.1021/es015823i, 2002.

Bloomfield, L. A., Geusic, M. E., Freeman, R. R. and Brown, W. L.: Negative and positive cluster ions of carbon and silicon, *Chem. Phys. Lett.*, 121(1), 33–37, doi:10.1016/0009-2614(85)87149-9, 1985.

Bond, T. C., Habib, G. and Bergstrom, R. W.: Limitations in the enhancement of visible light absorption due to mixing state, *J. Geophys. Res. Atmos.*, 111(20), 1–13, doi:10.1029/2006JD007315, 2006.

Bond, T. C., Doherty, S. J., Fahey, D. W., Forster, P. M., Berntsen, T., DeAngelo, B. J., Flanner, M. G., Ghan, S., Kärcher, B., Koch, D., Kinne, S., Kondo, Y., Quinn, P. K., Sarofim, M. C., Schultz, M. G., Schulz, M., Venkataraman, C., Zhang, H., Zhang, S., Bellouin, N., Guttikunda, S. K., Hopke, P. K., Jacobson, M. Z., Kaiser, J. W., Klimont, Z., Lohmann, U., Schwarz, J. P., Shindell, D., Storelvmo, T., Warren, S. G. and Zender, C. S.: Bounding the role of black carbon in the climate system: A scientific assessment, *J. Geophys. Res. Atmos.*, 118(11), 5380–5552, doi:10.1002/jgrd.50171, 2013.

Branca, C., Iannace, A. and Di Blasi, C.: Devolatilization and Combustion Kinetics of *Quercus cerris* Bark, *Energy & Fuels*, 21(2), 1078–1084, doi:10.1021/ef060537j, 2007.

Canagaratna, M. R., Jimenez, J. L., Kroll, J. H., Chen, Q., Kessler, S. H., Massoli, P., Hildebrandt Ruiz, L., Fortner, E., Williams, L. R., Wilson, K. R., Surratt, J. D., Donahue,

N. M., Jayne, J. T. and Worsnop, D. R.: Elemental ratio measurements of organic compounds using aerosol mass spectrometry: characterization, improved calibration, and implications, *Atmos. Chem. Phys.*, 14(13), 19791–19835, doi:10.5194/acpd-14-19791-2014, 2014.

Canagaratna, M. R., Massoli, P., Browne, E. C., Franklin, J. P., Wilson, K. R., Onasch, T. B., Kirchstetter, T. W., Fortner, E. C., Kolb, C. E., Jayne, J. T., Kroll, J. H. and Worsnop, D. R.: Chemical Compositions of Black Carbon Particle Cores and Coatings via Soot Particle Aerosol Mass Spectrometry with Photoionization and Electron Ionization, *J. Phys. Chem. A*, 119(19), 4589–4599, doi:10.1021/jp510711u, 2015.

Carbone, S., Onasch, T., Saarikoski, S., Timonen, H., Saarnio, K., Sueper, D., Rönkkö, T., Pirjola, L., Häyrynen, A., Worsnop, D. and Hillamo, R.: Characterization of trace metals on soot aerosol particles with the SP-AMS: detection and quantification, *Atmos. Meas. Tech.*, 8, 4803–4815, doi:10.5194/amt-8-4803-2015, 2015.

Chen, K., Yin, Y., Kong, S., Xiao, H., Wu, Y., Chen, J. and Li, A.: Size-resolved chemical composition of atmospheric particles during a straw burning period at Mt . Huang ( the Yellow Mountain ) of China, *Atmos. Environ.*, 84, 380–389, doi:10.1016/j.atmosenv.2013.11.040, 2014.

Chhabra, P. S., Flagan, R. C. and Seinfeld, J. H.: Elemental analysis of chamber organic aerosol using an aerodyne high-resolution aerosol mass spectrometer, *Atmos. Chem. Phys.*, 10(9), 4111–4131, doi:10.5194/acp-10-4111-2010, 2010.

Chung, S. H. and Seinfeld, J. H.: Global distribution and climate forcing of carbonaceous aerosols, *J. Geophys. Res.*, 107(D19), 4407, doi:10.1029/2001JD001397, 2002.

Corbin, J. C., Sierau, B., Gysel, M., Laborde, M., Keller, A., Kim, J., Petzold, A., Onasch, T. B., Lohmann, U. and Mensah, A. A.: Mass spectrometry of refractory black carbon particles from six sources: Carbon-cluster and oxygenated ions, *Atmos. Chem. Phys.*, 14(5), 2591–2603, doi:10.5194/acp-14-2591-2014, 2014.

Corbin, J. C., Lohmann, U., Sierau, B., Keller, A., Burtscher, H. and Mensah, A. A.: Black-carbon-surface oxidation and organic composition of beech-wood soot aerosols,

Atmos. Chem. Phys. Discuss., 15(6), 9573–9629, doi:10.5194/acpd-15-9573-2015, 2015.

Cross, E. S., Onasch, T. B., Ahern, A., Wrobel, W., Slowik, J. G., Olfert, J., Lack, D. A., Massoli, P., Cappa, C. D., Schwarz, J. P., Spackman, J. R., Fahey, D. W., Sedlacek, A., Trimborn, A., Jayne, J. T., Freedman, A., Williams, L. R., Ng, N. L., Mazzoleni, C., Dubey, M., Brem, B., Kok, G., Subramanian, R., Freitag, S., Clarke, A., Thornhill, D., Marr, L. C., Kolb, C. E., Worsnop, D. R. and Davidovits, P.: Soot Particle Studies—Instrument Inter-Comparison—Project Overview, *Aerosol Sci. Technol.*, 44(8), 592–611, doi:10.1080/02786826.2010.482113, 2010.

Cubison, M. J., Ortega, A. M., Hayes, P. L., Farmer, D. K., Day, D., Lechner, M. J., Brune, W. H., Apel, E., Diskin, G. S., Fisher, J. A., Fuelberg, H. E., Hecobian, A., Knapp, D. J., Mikoviny, T., Riemer, D., Sachse, G. W., Sessions, W., Weber, R. J., Weinheimer, A. J., Wisthaler, A. and Jimenez, J. L.: Effects of aging on organic aerosol from open biomass burning smoke in aircraft and laboratory studies, *Atmos. Chem. Phys.*, 11(23), 12049–12064, doi:10.5194/acp-11-12049-2011, 2011.

Dallmann, T. R., Onasch, T. B., Kirchstetter, T. W., Worton, D. R., Fortner, E. C., Herndon, S. C., Wood, E. C., Franklin, J. P., Worsnop, D. R., Goldstein, A. H. and Harley, R. A.: Characterization of particulate matter emissions from on-road gasoline and diesel vehicles using a soot particle aerosol mass spectrometer, *Atmos. Chem. Phys.*, 14(14), 7585–7599, doi:10.5194/acp-14-7585-2014, 2014.

DeCarlo, P. F., Slowik, J. G., Worsnop, D. R., Davidovits, P. and Jimenez, J. L.: Particle Morphology and Density Characterization by Combined Mobility and Aerodynamic Diameter Measurements. Part 1: Theory, *Aerosol Sci. Technol.*, 38(12), 1185–1205, doi:10.1080/027868290903907, 2004.

Decarlo, P. F., Kimmel, J. R., Trimborn, A., Northway, M. J., Jayne, J. T., Aiken, A. C., Gonin, M., Fuhrer, K., Horvath, T., Docherty, K. S., Worsnop, D. R. and Jimenez, J. L.: Field-deployable, high-resolution, time-of-flight aerosol mass spectrometer, *Anal. Chem.*, 78(24), 8281–8289, doi:8410.1029/2001JD001213, 2006.

- Drewnick, F., Hings, S. S., Curtius, J., Eerdekens, G. and Williams, J.: Measurement of fine particulate and gas-phase species during the New Year's fireworks 2005 in Mainz, Germany, *Atmos. Environ.*, 40(23), 4316–4327, doi:10.1016/j.atmosenv.2006.03.040, 2006.
- Farmer, D. K. and Jimenez, J. L.: Real-time Atmospheric Chemistry Field Instrumentation †, *Anal. Chem.*, 82(19), 7879–7884, doi:10.1021/ac1010603, 2010.
- Farmer, D. K., Matsunaga, A., Docherty, K. S., Surratt, J. D., Seinfeld, J. H., Ziemann, P. J. and Jimenez, J. L.: Response of an aerosol mass spectrometer to organonitrates and organosulfates and implications for atmospheric chemistry, *Proc. Natl. Acad. Sci.*, 107(15), 6670–6675, doi:10.1073/pnas.0912340107, 2010.
- Ferguson, D. P., Song, X.-H., Ramadan, Z., Allen, J. O., Hughes, L. S., Cass, G. R., Hopke, P. K. and Prather, K. A.: Quantification of ATOFMS Data by Multivariate Methods, *Anal. Chem.*, 73(15), 3535–3541, doi:10.1021/ac010022j, 2001.
- Fortner, E. C., Brooks, W. A., Onasch, T. B., Canagaratna, M. R., Massoli, P., Jayne, J. T., Franklin, J. P., Knighton, W. B., Wormhoudt, J., Worsnop, D. R., Kolb, C. E. and Herndon, S. C.: Particulate Emissions Measured During the TCEQ Comprehensive Flare Emission Study, *Ind. Eng. Chem. Res.*, 51(39), 12586–12592, doi:10.1021/ie202692y, 2012.
- Gemayel, R., Hellebust, S., Temime-Roussel, B., Hayeck, N., Van Elteren, J. T., Wortham, H. and Gligorovski, S.: The performance and the characterization of laser ablation aerosol particle time-of-flight mass spectrometry (LAAP-ToF-MS), *Atmos. Meas. Tech.*, 9(4), 1947–1959, doi:10.5194/amt-9-1947-2016, 2016.
- Ghazi, R. and Olfert, J. S.: Coating Mass Dependence of Soot Aggregate Restructuring due to Coatings of Oleic Acid and Dioctyl Sebacate, *Aerosol Sci. Technol.*, 47(2), 192–200, doi:10.1080/02786826.2012.741273, 2013.
- Gross, D. S., Gälli, M. E., Silva, P. J. and Prather, K. A.: Relative Sensitivity Factors for Alkali Metal and Ammonium Cations in Single-Particle Aerosol Time-of-Flight Mass Spectra, *Anal. Chem.*, 72(2), 416–422, doi:10.1021/ac990434g, 2000.

Gysel, M., Laborde, M., Olfert, J. S., Subramanian, R. and Gröhn, A. J.: Effective density of Aquadag and fullerene soot black carbon reference materials used for SP2 calibration, *Atmos. Meas. Tech.*, 4(12), 2851–2858, doi:10.5194/amt-4-2851-2011, 2011.

Gysel, M., Laborde, M., Mensah, A. A., Corbin, J. C., Keller, A., Kim, J., Petzold, A. and Sierau, B.: Technical Note: The single particle soot photometer fails to reliably detect PALAS soot nanoparticles, *Atmos. Meas. Tech.*, 5(12), 3099–3107, doi:10.5194/amt-5-3099-2012, 2012.

Healy, R. M., Sciare, J., Poulain, L., Crippa, M., Wiedensohler, A., Prévôt, A. S. H., Baltensperger, U., Sarda-Estève, R., McGuire, M. L., Jeong, C.-H., McGillicuddy, E., O'Connor, I. P., Sodeau, J. R., Evans, G. J. and Wenger, J. C.: Quantitative determination of carbonaceous particle mixing state in Paris using single particle mass spectrometer and aerosol mass spectrometer measurements, *Atmos. Chem. Phys. Discuss.*, 13(4), 10345–10393, doi:10.5194/acpd-13-10345-2013, 2013.

Hennigan, C. J., Sullivan, A. P., Collett, J. L. and Robinson, A. L.: Levoglucosan stability in biomass burning particles exposed to hydroxyl radicals, *Geophys. Res. Lett.*, 37(9), 2–5, doi:10.1029/2010GL043088, 2010.

Hennigan, C. J., Miracolo, M. A., Engelhart, G. J., May, A. A., Presto, A. A., Lee, T., Sullivan, A. P., McMeeking, G. R., Coe, H., Wold, C. E., Hao, W.-M., Gilman, J. B., Kuster, W. C., de Gouw, J. A., Schichtel, B. A., Kreidenweis, S. M. and Robinson, A. L.: Chemical and physical transformations of organic aerosol from the photo-oxidation of open biomass burning emissions in an environmental chamber, *Atmos. Chem. Phys.*, 11(15), 7669–7686, doi:10.5194/acp-11-7669-2011, 2011.

Huffman, J. A., Jayne, J. T., Drewnick, F., Aiken, A. C., Onasch, T., Worsnop, D. R. and Jimenez, J. L.: Design, Modeling, Optimization, and Experimental Tests of a Particle Beam Width Probe for the Aerodyne Aerosol Mass Spectrometer, *Aerosol Sci. Technol.*, 39(12), 1143–1163, doi:10.1080/02786820500423782, 2005.

Jacobson, M. Z.: Strong radiative heating due to the mixing state of black carbon in atmospheric aerosols, *Nature*, 409(6821), 695–697, doi:10.1038/35055518, 2001.

Jayne, J. T., Leard, D. C., Zhang, X., Davidovits, P., Smith, K. A., Kolb, C. E. and Worsnop, D. R.: Development of an Aerosol Mass Spectrometer for Size and Composition Analysis of Submicron Particles, *Aerosol Sci. Technol.*, 33(1-2), 49-70, doi:10.1080/027868200410840, 2000.

Jeong, C.-H., McGuire, M. L., Godri, K. J., Slowik, J. G., Rehbein, P. J. G. and Evans, G. J.: Quantification of aerosol chemical composition using continuous single particle measurements, *Atmos. Chem. Phys.*, 11(14), 7027-7044, doi:10.5194/acp-11-7027-2011, 2011.

Kroll, J. H., Donahue, N. M., Jimenez, J. L., Kessler, S. H., Canagaratna, M. R., Wilson, K. R., Altieri, K. E., Mazzoleni, L. R., Wozniak, A. S., Bluhm, H., Mysak, E. R., Smith, J. D., Kolb, C. E. and Worsnop, D. R.: Carbon oxidation state as a metric for describing the chemistry of atmospheric organic aerosol, *Nat. Chem.*, 3(2), 133-139, doi:10.1038/nchem.948, 2011.

Lack, D. A., Cappa, C. D., Cross, E. S., Massoli, P., Ahern, A. T., Davidovits, P. and Onasch, T. B.: Absorption Enhancement of Coated Absorbing Aerosols: Validation of the Photo-Acoustic Technique for Measuring the Enhancement, *Aerosol Sci. Technol.*, 43(10), 1006-1012, doi:10.1080/02786820903117932, 2009.

Lee, A. K. Y., Willis, M. D., Healy, R. M., Wang, J. M., Jeong, C.-H., Wenger, J. C., Evans, G. J. and Abbatt, J. P. D.: Single-particle characterization of biomass burning organic aerosol (BBOA): evidence for non-uniform mixing of high molecular weight organics and potassium, *Atmos. Chem. Phys.*, 16(9), 5561-5572, doi:10.5194/acp-16-5561-2016, 2016.

Lee, T., Sullivan, A. P., Mack, L., Jimenez, J. L., Kreidenweis, S. M., Onasch, T. B., Worsnop, D. R., Malm, W., Wold, C. E., Hao, W. M. and Collett, J. L.: Chemical Smoke Marker Emissions During Flaming and Smoldering Phases of Laboratory Open Burning of Wildland Fuels, *Aerosol Sci. Technol.*, 44(9), i-v, doi:10.1080/02786826.2010.499884, 2010.

Levin, E. J. T., McMeeking, G. R., Carrico, C. M., Mack, L. E., Kreidenweis, S. M., Wold, C. E., Moosmüller, H., Arnott, W. P., Hao, W. M., Collett, J. L. and Malm, W. C.: Biomass



burning smoke aerosol properties measured during Fire Laboratory at Missoula Experiments (FLAME), J. Geophys. Res., 115(D18), 1–15, doi:10.1029/2009JD013601, 2010.

Li, J., Posfai, M., Hobbs, P. V. and Buseck, P. R.: Individual Aerosol Particles from Biomass Burning in Southern Africa Compositions and Aging of Inorganic Particles, , 108, 1–12, doi:10.1029/2002JD002310, 2003.

Liu, P., Ziemann, P. J., Kittelson, D. B. and McMurry, P. H.: Generating Particle Beams of Controlled Dimensions and Divergence: II. Experimental Evaluation of Particle Motion in Aerodynamic Lenses and Nozzle Expansions, Aerosol Sci. Technol., 22(3), 314–324, doi:10.1080/02786829408959749, 1995.

Liu, P. S. K., Deng, R., Smith, K. A., Williams, L. R., Jayne, J. T., Canagaratna, M. R., Moore, K., Onasch, T. B., Worsnop, D. R. and Deshler, T.: Transmission Efficiency of an Aerodynamic Focusing Lens System: Comparison of Model Calculations and Laboratory Measurements for the Aerodyne Aerosol Mass Spectrometer, Aerosol Sci. Technol., 41(8), 721–733, doi:10.1080/02786820701422278, 2007.

Mansoori, B. A., Johnston, M. V. and Wexler, A. S.: Quantitation of Ionic Species in Single Microdroplets by Online Laser Desorption/Ionization, Anal. Chem., 66(21), 3681–3687, doi:10.1021/ac00093a023, 1994.

Mansoori, B. A., Johnston, M. V. and Wexler, A. S.: Matrix-Assisted Laser Desorption/Ionization of Size- and Composition-Selected Aerosol Particles, Anal. Chem., 68(20), 3595–3601, doi:10.1021/ac9603385, 1996.

Maricq, M. M.: Examining the Relationship Between Black Carbon and Soot in Flames and Engine Exhaust, Aerosol Sci. Technol., 48(6), 620–629, doi:10.1080/02786826.2014.904961, 2014.

Marsden, N., Flynn, M. J., Taylor, J. W., Allan, J. D. and Coe, H.: Evaluating the influence of laser wavelength and detection stage geometry on optical detection efficiency in a single particle mass spectrometer, Atmos. Meas. Tech. Discuss., 1–25, doi:10.5194/amt-2016-150, 2016.

- Massoli, P., Onasch, T. B., Cappa, C. D., Nuamaan, I., Hakala, J., Hayden, K., Li, S.-M., Sueper, D. T., Bates, T. S., Quinn, P. K., Jayne, J. T. and Worsnop, D. R.: Characterization of black carbon-containing particles from soot particle aerosol mass spectrometer measurements on the R/V *Atlantis* during CalNex 2010, *J. Geophys. Res. Atmos.*, 120(6), 2575–2593, doi:10.1002/2014JD022834, 2015.
- May, A. A., Levin, E. J. T., Hennigan, C. J., Riipinen, I., Lee, T., Collett, J. L., Jimenez, J. L., Kreidenweis, S. M. and Robinson, A. L.: Gas-particle partitioning of primary organic aerosol emissions: 3. Biomass burning, *J. Geophys. Res. Atmos.*, 118(19), 11,327–11,338, doi:10.1002/jgrd.50828, 2013.
- Mikhailov, E. F., Vlasenko, S. S., Podgorny, I. A., Ramanathan, V. and Corrigan, C. E.: Optical properties of soot–water drop agglomerates: An experimental study, *J. Geophys. Res.*, 111(D7), D07209, doi:10.1029/2005JD006389, 2006.
- Moffet, R. C. and Prather, K. A.: In-situ measurements of the mixing state and optical properties of soot with implications for radiative forcing estimates, *Proc. Natl. Acad. Sci.*, 106(29), 11872–11877, doi:10.1073/pnas.0900040106, 2009.
- Moffet, R. C., de Foy, B., Molina, L. T., Molina, M. J. and Prather, K. A.: Measurement of ambient aerosols in northern Mexico City by single particle mass spectrometry, *Atmos. Chem. Phys.*, 8(16), 4499–4516, doi:10.5194/acp-8-4499-2008, 2008.
- Moteki, N. and Kondo, Y.: Effects of Mixing State on Black Carbon Measurements by Laser-Induced Incandescence, *Aerosol Sci. Technol.*, 41(4), 398–417, doi:10.1080/02786820701199728, 2007.
- Murphy, D.: The design of single particle laser mass spectrometers, *Mass Spectrom. Rev.*, (26), 150–165, doi:10.1002/mas, 2007.
- Murray, K. K. and Russell, D. H.: Aerosol matrix-assisted laser desorption ionization mass spectrometry., *J. Am. Soc. Mass Spectrom.*, 5(1), 1–9, doi:10.1016/1044-0305(94)85077-1, 1994.

Neubauer, K. R., Johnston, M. V and Wexler, A. S.: Humidity effects on the mass spectra of single aerosol particles, *Atmos. Environ.*, 32(14–15), 2521–2529, doi:10.1016/S1352-2310(98)00005-3, 1998.

Onasch, T. B., Trimborn, A., Fortner, E. C., Jayne, J. T., Kok, G. L., Williams, L. R., Davidovits, P. and Worsnop, D. R.: Soot Particle Aerosol Mass Spectrometer: Development, Validation, and Initial Application, *Aerosol Sci. Technol.*, 46(7), 804–817, doi:10.1080/02786826.2012.663948, 2012.

Onasch, T. B., Fortner, E. C., Trimborn, A. M., Lambe, A. T., Tiwari, A. J., Marr, L. C., Corbin, J. C., Mensah, A. A., Williams, L. R., Davidovits, P. and Worsnop, D. R.: Investigations of SP-AMS Carbon Ion Distributions as a Function of Refractory Black Carbon Particle Type, *Aerosol Sci. Technol.*, 49(6), 409–422, doi:10.1080/02786826.2015.1039959, 2015.

Park, K., Kittelson, D. B., Zachariah, M. R. and McMurry, P. H.: Measurement of Inherent Material Density of Nanoparticle Agglomerates, *J. Nanoparticle Res.*, 6(2/3), 267–272, doi:10.1023/B:NANO.0000034657.71309.e6, 2004.

Pósfai, M. and Buseck, P. R.: Nature and Climate Effects of Individual Tropospheric Aerosol Particles, *Annu. Rev. Earth Planet. Sci.*, 38(1), 17–43, doi:10.1146/annurev.earth.031208.100032, 2010.

Pratt, K., Mayer, J. and Holecek, J.: Development and characterization of an aircraft aerosol time-of-flight mass spectrometer, *Anal. Chem.*, 81(5), 1792–1800, doi:10.1029/2003JD004198.(11), 2009.

Pratt, K. A. and Prather, K. A.: Mass spectrometry of atmospheric aerosols-Recent developments and applications. Part II: On-line mass spectrometry techniques, *Mass Spectrom. Rev.*, 31(1), 17–48, doi:10.1002/mas.20330, 2012.

Ramanathan, V. and Carmichael, G.: Global and regional climate changes due to black carbon, *Nat. Geosci.*, 1(4), 221–227, doi:10.1038/ngeo156, 2008.

Reid, J. S. and Hobbs, P. V.: Physical and optical properties of young smoke from individual biomass fires in Brazil, *J. Geophys. Res. Atmos.*, 103(D24), 32013–32030, doi:10.1029/98JD00159, 1998.

Reid, J. S., Koppmann, R., Eck, T. F. and Eleuterio, D. P.: A review of biomass burning emissions part II: intensive physical properties of biomass burning particles, *Atmos. Chem. Phys.*, 5(3), 799–825, doi:10.5194/acp-5-799-2005, 2005.

Reinard, M. S. and Johnston, M. V: Ion formation mechanism in laser desorption ionization of individual nanoparticles., *J. Am. Soc. Mass Spectrom.*, 19(3), 389–99, doi:10.1016/j.jasms.2007.11.017, 2008.

Saliba, G., Subramanian, R., Saleh, R., Ahern, A. T., Lipsky, E., Tasoglou, A., Sullivan, R. C., Bhandari, J., Mazzoleni, C. and Robinson, A. L.: Optical properties of black carbon in cook stove emissions coated with secondary organic aerosols: Measurements and modeling, *Aerosol Sci. Technol.*, Submitted, 2016.

Schwarz, J. P., Gao, R. S., Spackman, J. R., Watts, L. A., Thomson, D. S., Fahey, D. W., Ryerson, T. B., Peischl, J., Holloway, J. S., Trainer, M., Frost, G. J., Baynard, T., Lack, D. A., de Gouw, J. A., Warneke, C. and Del Negro, L. A.: Measurement of the mixing state, mass, and optical size of individual black carbon particles in urban and biomass burning emissions, *Geophys. Res. Lett.*, 35(13), L13810, doi:10.1029/2008GL033968, 2008.

Schwarz, J. P., Spackman, J. R., Gao, R. S., Perring, A. E., Cross, E., Onasch, T. B., Ahern, A., Wrobel, W., Davidovits, P., Olfert, J., Dubey, M. K., Mazzoleni, C. and Fahey, D. W.: The Detection Efficiency of the Single Particle Soot Photometer, *Aerosol Sci. Technol.*, 44(8), 612–628, doi:10.1080/02786826.2010.481298, 2010.

Shilling, J. E., Chen, Q., King, S. M., Rosenoern, T., Kroll, J. H., Worsnop, D. R., McKinney, K. A. and Martin, S. T.: Particle mass yield in secondary organic aerosol formed by the dark ozonolysis of  $\alpha$ -pinene, *Atmos. Chem. Phys.*, 8(7), 2073–2088, doi:10.5194/acp-8-2073-2008, 2008.

Silva, P. J., Liu, D.-Y., Noble, C. A. and Prather, K. A.: Size and Chemical Characterization of Individual Particles Resulting from Biomass Burning of Local Southern California Species, *Environ. Sci. Technol.*, 33(18), 3068–3076, doi:10.1021/es980544p, 1999.

Slowik, J., Stainken, K., Davidovits, P., Williams, L. R., Jayne, J. T., Kolb, C. E., Worsnop, D., Rudich, Y., DeCarlo, P. and Jimenez, J.: Particle Morphology and Density Characterization by Combined Mobility and Aerodynamic Diameter Measurements. Part 2: Application to Combustion-Generated Soot Aerosols as a Function of Fuel Equivalence Ratio, *Aerosol Sci. Technol.*, 38(12), 1206–1222, doi:10.1080/02786826.2004.10399462, 2004.

Slowik, J. G., Cross, E. S., Han, J.-H., Davidovits, P., Onasch, T. B., Jayne, J. T., Williams, L. R., Canagaratna, M. R., Worsnop, D. R., Chakrabarty, R. K., Moosmüller, H., Arnott, W. P., Schwarz, J. P., Gao, R.-S., Fahey, D. W., Kok, G. L. and Petzold, A.: An Inter-Comparison of Instruments Measuring Black Carbon Content of Soot Particles, *Aerosol Sci. Technol.*, 41(3), 295–314, doi:10.1080/02786820701197078, 2007.

Spencer, M. T. and Prather, K. A.: Using ATOFMS to Determine OC/EC Mass Fractions in Particles, *Aerosol Sci. Technol.*, 40(8), 585–594, doi:10.1080/02786820600729138, 2006.

Steele, P. T., Srivastava, A., Pitesky, M. E., Fergenson, D. P., Tobias, H. J., Gard, E. E. and Frank, M.: Desorption/ionization fluence thresholds and improved mass spectral consistency measured using a flat-top laser profile in the bioaerosol mass spectrometry of single *Bacillus endospores.*, *Anal. Chem.*, 77(22), 7448–54, doi:10.1021/ac051329b, 2005.

Stephens, M., Turner, N. and Sandberg, J.: Particle identification by laser-induced incandescence in a solid-state laser cavity., *Appl. Opt.*, 42(19), 3726–3736, doi:10.1364/AO.42.003726, 2003.

Stockwell, C. E., Veres, P. R., Williams, J. and Yokelson, R. J.: Characterization of biomass burning emissions from cooking fires, peat, crop residue, and other fuels with high-resolution proton-transfer-reaction time-of-flight mass spectrometry, *Atmos. Chem. Phys.*, 15(2), 845–865, doi:10.5194/acp-15-845-2015, 2015.

Sullivan, R. C. and Prather, K. A.: Recent Advances in Our Understanding of Atmospheric Chemistry and Climate Made Possible by On-Line Aerosol Analysis Instrumentation, *Anal. Chem.*, 77(12), 3861–3886, doi:10.1021/ac050716i, 2005.

Sullivan, R. C., Guazzotti, S. A., Sodeman, D. A. and Prather, K. A.: Direct observations of the atmospheric processing of Asian mineral dust, *Atmos. Chem. Phys.*, 7(5), 1213–1236, doi:10.5194/acp-7-1213-2007, 2007.

Sullivan, R. C., Moore, M. J. K., Petters, M. D., Kreidenweis, S. M., Roberts, G. C. and Prather, K. A.: Timescale for hygroscopic conversion of calcite mineral particles through heterogeneous reaction with nitric acid, *Phys. Chem. Chem. Phys.*, 11(36), 7826, doi:10.1039/b904217b, 2009.

Svane, M., Hagström, M. and Pettersson, J.: Chemical Analysis of Individual Alkali-Containing Aerosol Particles: Design and Performance of a Surface Ionization Particle Beam Mass Spectrometer, *Aerosol Sci. Technol.*, 38(7), 655–663, doi:10.1080/02786820490485944, 2004.

Thomson, D. S., Middlebrook, A. M. and Murphy, D. M.: Thresholds for Laser-Induced Ion Formation from Aerosols in a Vacuum Using Ultraviolet and Vacuum-Ultraviolet Laser Wavelengths, *Aerosol Sci. Technol.*, 26(6), 544–559, doi:10.1080/02786829708965452, 1997.

Thomson, D. S., Schein, M. E. and Murphy, D. M.: Particle Analysis by Laser Mass Spectrometry WB-57F Instrument Overview, *Aerosol Sci. Technol.*, 33(1–2), 153–169, doi:10.1080/027868200410903, 2000.

Vander Wal, R. L. and Choi, M. Y.: Pulsed laser heating of soot: morphological changes, *Carbon N. Y.*, 37(2), 231–239, doi:10.1016/S0008-6223(98)00169-9, 1999.

Vander Wal, R. L. and Jensen, K. A.: Laser-induced incandescence: excitation intensity, *Appl. Opt.*, 37(9), 1607, doi:10.1364/AO.37.001607, 1998.

Vander Wal, R. L. and Tomasek, A. J.: Soot nanostructure: dependence upon synthesis conditions, *Combust. Flame*, 136(1), 129–140, doi:10.1016/j.combustflame.2003.09.008, 2004.

Wenzel, R. J. and Prather, K. A.: Improvements in ion signal reproducibility obtained using a homogeneous laser beam for on-line laser desorption/ionization of single particles., *Rapid Commun. Mass Spectrom.*, 18(13), 1525–33, doi:10.1002/rcm.1509, 2004.

Willis, M. D., Lee, A. K. Y., Onasch, T. B., Fortner, E. C., Williams, L. R., Lambe, A. T., Worsnop, D. R. and Abbatt, J. P. D.: Collection efficiency of the soot-particle aerosol mass spectrometer (SP-AMS) for internally mixed particulate black carbon, *Atmos. Meas. Tech.*, 7(12), 4507–4516, doi:10.5194/amt-7-4507-2014, 2014.

Yokelson, R. J., Crounse, J. D., DeCarlo, P. F., Karl, T., Urbanski, S., Atlas, E., Campos, T., Shinozuka, Y., Kapustin, V., Clarke, A. D., Weinheimer, A., Knapp, D. J., Montzka, D. D., Holloway, J., Weibring, P., Flocke, F., Zheng, W., Toohey, D., Wennberg, P. O., Wiedinmyer, C., Mauldin, L., Fried, A., Richter, D., Walega, J., Jimenez, J. L., Adachi, K., Buseck, P. R., Hall, S. R. and Shetter, R.: Emissions from biomass burning in the Yucatan, *Atmos. Chem. Phys.*, 9(15), 5785–5812, doi:10.5194/acp-9-5785-2009, 2009.

Zandberg, E. Y.: Surface Ionization Detection of Particles, *Tech. Phys.*, 40, 865–884, 1995.

Zauscher, M. D., Wang, Y., Moore, M. J. K., Gaston, C. J. and Prather, K. A.: Air quality impact and physicochemical aging of biomass burning aerosols during the 2007 San Diego wildfires, *Environ. Sci. Technol.*, 47(14), 7633–7643, doi:10.1021/es4004137, 2013.

Zelenyuk, A., Yang, J., Song, C., Zaveri, R. A. and Imre, D.: A New Real-Time Method for Determining Particles' Sphericity and Density: Application to Secondary Organic Aerosol Formed by Ozonolysis of  $\alpha$ -Pinene, *Environ. Sci. Technol.*, 42(21), 8033–8038, doi:10.1021/es8013562, 2008.

Zelenyuk, A., Yang, J., Choi, E. and Imre, D.: SPLAT II: An Aircraft Compatible, Ultra-Sensitive, High Precision Instrument for In-Situ Characterization of the Size and Composition of Fine and Ultrafine Particles, *Aerosol Sci. Technol.*, 43(5), 411–424, doi:10.1080/02786820802709243, 2009.

Zhang, J., Huff Hartz, K. E., Pandis, S. N. and Donahue, N. M.: Secondary Organic Aerosol Formation from Limonene Ozonolysis: Homogeneous and Heterogeneous Influences as a Function of NO<sub>x</sub>, J. Phys. Chem. A, 110(38), 11053–11063, doi:10.1021/jp062836f, 2006.

Zhang, R., Khalizov, A. F., Pagels, J., Zhang, D., Xue, H. and McMurry, P. H.: Variability in morphology, hygroscopicity, and optical properties of soot aerosols during atmospheric processing, Proc. Natl. Acad. Sci. U. S. A., 105(30), 10291–6, doi:10.1073/pnas.0804860105, 2008.

Zhang, X., McVay, R. C., Huang, D. D., Dalleska, N. F., Aumont, B., Flagan, R. C. and Seinfeld, J. H.: Formation and evolution of molecular products in  $\alpha$ -pinene secondary organic aerosol, Proc. Natl. Acad. Sci. U. S. A., 112(46), 14168–73, doi:10.1073/pnas.1517742112, 2015.



## 6. CONCLUSIONS

The fine particle and gas-phase emissions of biomass burning have large but uncertain effects on the global climate (Bond et al., 2013; Solomon et al., 2007). They are a significant source globally of small, long-lived particles as well as light absorbing black carbon. Dilution, photochemical oxidation, and reaction with nocturnal oxidants, are some of the mechanisms which I collectively refer to as “atmospheric aging.” Atmospheric aging affects the physical and chemical properties of the biomass-burning aerosol and are poorly constrained. This directly translates to an inability to predict the full magnitude of changes to the atmospheric aerosol population – and therefore climate – that would result from attempts at mitigating global warming using policies targeting biomass burning.

The uncertainty associated with atmospheric aging of biomass burning stems from many aspects of the physical and chemical processing that are addressed in this thesis. In Chapter 2, I used simulated atmospheric aging of smoke emissions from specific fuels to address two aspects of the atmospheric aging of organic aerosols: multi-phase evaporation/oxidation of primary organic aerosol (POA) and condensation of secondary organic aerosol (SOA). To do so, I proposed a new method for measuring the fraction of POA which remains in a biomass-burning particle as it ages in the atmosphere, using composition measurements from the aerosol mass

spectrometer. I identified a POA tracer ion,  $C_7H_{11}^+$  ( $m/z$  95), that was unlikely to be produced by secondary organic aerosol and that was associated with POA compounds that low volatility. The fractional contribution of that POA tracer ion ( $f_{C_7H_{11}^+}$ ) to the total organic signal in a conventional (without the infrared laser) aerosol mass spectrometer was used to show that multi-phase evaporation/oxidation was relatively unimportant in the total mass changes that were observed when biomass-burning emissions were aged in smog chambers. Rather, burn-to-burn variability in the total amount of VOCs emitted from the burn had the most significant effect on total aerosol mass change following chemical aging in the chamber experiments. The highly resolved VOC emission profiles measured by Hatch et al. (2015) using 2D-GC-MS proved effective at predicting the amount of SOA that would be formed in a given chamber experiment. Furthermore, it was showed that the VOCs that contributed to the majority of the SOA mass produced were compounds previously studied (i.e. monoterpenes) and known to be major SOA precursors, rather than unidentified, unmeasured, or unknown intermediate volatility organic compounds. Future work in this area should include an investigation of the lesser known SOA precursors, furans, which appear to be important in the modest SOA formation observed in grass burning. Furthermore, the identification of a conserved POA tracer ion in biomass-burning emissions allows for the analysis of past field campaign AMS datasets to compare the observations made in the lab with what has been measured in ambient biomass burning plumes to better quantify the SOA produced through atmospheric aging, as well to re-analyze other laboratory studies where an AMS was used to measure particle composition (Cubison et al., 2011; Hennigan et al., 2011; Yokelson et al., 2009).

Having established the dominance of VOC oxidation to the change in total organic mass observed in aging smoke plumes, I attempted to better constrain the effect of biomass-burning emissions on the atmospheric oxidant budget in Chapter 3. I showed that for biomass-burning plumes that mix with ambient air masses where  $O_3$  is present,  $N_2O_5$  will form readily. The formation of  $N_2O_5$  is part of the mechanism by which the ozone production catalyst  $NO_x$  ( $NO_x = NO + NO_2$ ) is removed from the

atmosphere at night. Our observation the formation of  $\text{N}_2\text{O}_5$  in biomass-burning smoke is noteworthy in itself. To form  $\text{N}_2\text{O}_5$ ,  $\text{NO}_3$  radicals must react with  $\text{NO}_2$ . Since VOCs react readily with  $\text{NO}_3$  and are abundant in smoke plumes, it is important to note that the  $\text{NO}_3$  survived long enough to react with  $\text{NO}_2$ , and therefore form  $\text{N}_2\text{O}_5$ . Consistent with other internally mixed organic particles, the biomass-burning aerosol was fairly ineffective at causing heterogeneous hydrolysis of  $\text{N}_2\text{O}_5$  (Gaston et al., 2014; McNeill et al., 2006). This suggests that despite the abundant  $\text{NO}_x$  and particles emitted from biomass burning, the  $\text{N}_2\text{O}_5$  reservoir will be less effectively removed by conversion to  $\text{HNO}_3$  on biomass-burning particles than it would on an equivalent surface area concentration of inorganic aerosols (e.g. ammonium bisulfate). Furthermore, the high-chloride content particles I observed from burning tall grasses appeared to effectively convert what  $\text{N}_2\text{O}_5$  they did hydrolyze rapidly into  $\text{ClNO}_2$  which subsequently evaporated from the particles.  $\text{ClNO}_2$  formation, and subsequent photolysis come daylight, contributes to tropospheric  $\text{O}_3$  production by restoring  $\text{NO}_x$  and forming the potent oxidant, atomic chlorine radicals (Osthoff et al., 2008). I also observed that nitric acid plays an important role in this  $\text{ClNO}_2$  formation, although not as was initially thought. Suppression of  $\text{ClNO}_2$  formation appears to be minimal in the presence of the abundant chloride in some biomass burning particles, but the displacement of particulate chloride as  $\text{HCl(g)}$  by the uptake of the stronger acid  $\text{HNO}_3\text{(g)}$  has a marked effect on the ability of the particles to convert  $\text{N}_2\text{O}_5$  into  $\text{ClNO}_2$  (Mentel et al., 1999; Song and Carmichael, 2001). The evaporated  $\text{HCl(g)}$  can still become neutralized however by  $\text{NH}_3\text{(g)}$ , and condense on other particles. The chloride that was emitted in the particle phase of biomass-burning aerosol—aerosol which was relatively ineffective at hydrolyzing  $\text{N}_2\text{O}_5$ —may transfer onto a particle which does rapidly uptake  $\text{N}_2\text{O}_5$ . Thus, the chloride salt that undergoes acid displacement to  $\text{HCl(g)}$ , is neutralized in the gas phase, and then recondenses as a chloride salt on a different particle may theoretically produce more  $\text{ClNO}_2$  than the same chloride mass would have if it remained in the biomass burning particle.

The smog chamber experiments described in Chapter 3 show that the ability to convert  $\text{N}_2\text{O}_5$  is positively correlated with chloride content in biomass burning,

either by increasing reactive uptake of  $\text{N}_2\text{O}_5$  or by increasing the yield of  $\text{ClNO}_2$  from however much  $\text{N}_2\text{O}_5$  is hydrolyzed. However, the measurements in Chapters 3 & 4, as well as other studies that use an aerosol mass spectrometer for aggregate particle composition measurements, reveal relatively little about the aerosol mixing state. This can have an important effect on particle chloride content, as the chloride fraction of an individual particle is the relevant parameter, rather than the chloride content of the aggregate or ensemble particle population, as measured by the Aerodyne aerosol mass spectrometer.

Although the AMS does provide size-dependent measurements of composition, there is still significant uncertainty about the makeup of the individual particles. For example, the AMS can report that the aggregate particle mass for all particles with a vacuum aerodynamic diameter of 200 nm is 50% black carbon, and 50% organic material. However, the aggregate measurement from the AMS will not tell us if this means that 100% of the particles are each composed of 50% black carbon, and 50% organic material, or if 50% of the particle number are entirely black carbon, and 50% of the particles are entirely organic carbon. More likely there is some distribution of compositions between particles with very few being composed of single compounds, and these particle-to-particle variations can be important, especially for biomass-burning emissions that simultaneously emit a wide variety of particle types via different combustion conditions. For example, the same wood log can be smoldering on one end (producing particles of mostly organic material) and flaming on the other (producing almost mostly black carbon and inorganic ash particles). Instrumentation that can measure single particle composition is key in advancing our understanding of the aging processes and atmospheric properties (e.g. ice nucleation ability) of biomass-burning aerosol.

Thus, the development of the Aeromegt LAAPTOF, a new single particle mass spectrometer was discussed in Chapter 4. If the ultimate goal is to use laser/desorption ionization single particle mass spectrometry quantitatively, then there are key performance characteristics that need to be addressed. In Chapter 4 I used particles of known composition to evaluate the ability of the aerodynamic lens

to focus particles of different sizes into the ionization region of the mass spectrometer. This is a critical feature to understand in terms of understanding the inherent limitations of the laser light-scattering particle detection unit. The light-scattering detection is used to determine the size of each particle that was detected by laser velocimetry, to trigger the firing of the particle ablation laser, and also informs the data inversion that will be used to transform the number of particles of a given size detected into the number of particles that were actually present in the air parcel sampled. I also illustrated the effect of particle composition on ionization and subsequent detection of a particle. Some particles like dihydroxybenzoic acid (DHBA) may absorb the VUV ( $\lambda = 193$ ) laser effectively, but can be difficult to ionize. If no ions are formed, then no mass spectrum will be recorded. By adding the readily ionizable species potassium chloride (KCl) to the DHBA particles, I increased the rate of detection significantly. The mixed particles interacted with the VUV laser *and* generated a spectrum containing ion fragments from both DHBA and KCl. This illustrates the importance of laboratory studies of particles with a known range of particle compositions for their ability to both absorb the VUV laser light and also generate ions. The ability of particles to rely on the laser energy absorption by one component, and the ionizability of another component to generate ion signals which includes fragments from both components is critical to the broad versatility of this method, and should be quantified for both organic and inorganic particle systems.

In Chapter 5 I focused on evaluating the ability of the LAAPTOF to quantitatively measure organic material on black carbon, a very different material than the KCl studies in the previous chapter. Black carbon absorbs the VUV laser very effectively, and can also contain potassium salts when emitted from biomass-burning. Potassium is very readily ionized, and can therefore have ion plume effects when a particle is ablated. This may result in a particle of mixed composition (i.e. containing black carbon, organic material, and potassium salts) producing a mass spectra that contains only potassium ions. The positive correlation shown in Chapter 5 between LAAPTOF-measured organic material ion signal and the single particle secondary organic aerosol mass shows that even for this extreme system, and over a wide range

of organic aerosol coating thicknesses and multiple black-carbon core sizes, there exists a monotonic relationship between the OA analyte and measured organic ion signal. This is the fundamental property required for the calibration of a system, and I confirmed it using a highly heterogeneous and realistic calibration aerosol. Future work should investigate particles with a broader array of binary and ternary mixtures of complex particle components. Past field measurements using single-particle mass spectrometry have shown that some species are ubiquitous and therefore should be targeted first for these calibration experiments. Particle cores should include black carbon and dust while important coatings include sulfate, nitrates, chloride, and hydrocarbon-like and humic-like organics.

During the experiments conducted in pursuit of quantitative single particle aerosol mass spectrometry, I also investigated in Chapter 5 the ability of another commercial aerosol mass spectrometer to measure the composition of biomass-burning aerosol. The Aerodyne soot-particle aerosol mass spectrometer (SP-AMS) can measure two conserved biomass-burning aerosol tracers, potassium and black carbon (Lee et al., 2016; Onasch et al., 2012). However, I showed that increasing the vacuum aerodynamic diameter of these particles also increases the collection efficiency of species interacting with the infrared (IR) laser, in agreement with past observation by Willis et al. (2014). However, I also showed black-carbon containing particles may interact with portions of the IR laser beam that are not intensive enough to vaporize black carbon, but can vaporize nonrefractory material, like potassium and potentially organic material. As internally mixed particles containing black carbon and potassium grow in size, the instrument sensitivity to each species increases. However, for the same particle growth, the increase in sensitivity for potassium can be three time greater compared to the same sensitivity increase observed for black carbon.

Improving the reliability of measurements of biomass-burning aerosol composition is critical in the process of understanding the full impact of biomass burning on climate and human health. There is still a great deal that is unconstrained regarding the evolution of organic material in the atmosphere. Chapters

2 & 3 both investigated the precursors (VOCs and oxidants) to secondary organic aerosol formation in a constrained setting. The methods developed in Chapters 4 & 5 will improve measurements in the field and lab to make sure what is observed in the lab is representative of what occurs in the atmosphere. The ability of humans to affect intentional change on air quality depends on having an accurate understanding of the anthropogenic effect on atmospheric particle budgets. By improving our understanding of the processes that lead to the formation or removal of particles from the atmosphere, I can make better decisions affecting the environment and our own well-being.

## 6.1. References

Bond, T. C., Doherty, S. J., Fahey, D. W., Forster, P. M., Berntsen, T., DeAngelo, B. J., Flanner, M. G., Ghan, S., Kärcher, B., Koch, D., Kinne, S., Kondo, Y., Quinn, P. K., Sarofim, M. C., Schultz, M. G., Schulz, M., Venkataraman, C., Zhang, H., Zhang, S., Bellouin, N., Guttikunda, S. K., Hopke, P. K., Jacobson, M. Z., Kaiser, J. W., Klimont, Z., Lohmann, U., Schwarz, J. P., Shindell, D., Storelvmo, T., Warren, S. G. and Zender, C. S.: Bounding the role of black carbon in the climate system: A scientific assessment, *J. Geophys. Res. Atmos.*, 118(11), 5380–5552, doi:10.1002/jgrd.50171, 2013.

Cubison, M. J., Ortega, A. M., Hayes, P. L., Farmer, D. K., Day, D., Lechner, M. J., Brune, W. H., Apel, E., Diskin, G. S., Fisher, J. A., Fuelberg, H. E., Hecobian, A., Knapp, D. J., Mikoviny, T., Riemer, D., Sachse, G. W., Sessions, W., Weber, R. J., Weinheimer, A. J., Wisthaler, A. and Jimenez, J. L.: Effects of aging on organic aerosol from open biomass burning smoke in aircraft and laboratory studies, *Atmos. Chem. Phys.*, 11(23), 12049–12064, doi:10.5194/acp-11-12049-2011, 2011.

Gaston, C. J., Thornton, J. A. and Ng, N. L.: Reactive uptake of N<sub>2</sub>O<sub>5</sub> to internally mixed inorganic and organic particles: The role of organic carbon oxidation state and inferred organic phase separations, *Atmos. Chem. Phys.*, 14(11), 5693–5707, doi:10.5194/acp-14-5693-2014, 2014.

Hatch, L. E., Luo, W., Pankow, J. F., Yokelson, R. J., Stockwell, C. E. and Barsanti, K. C.: Identification and quantification of gaseous organic compounds emitted from biomass burning using two-dimensional gas chromatography–time-of-flight mass spectrometry, *Atmos. Chem. Phys.*, 15(4), 1865–1899, doi:10.5194/acp-15-1865-2015, 2015.

Hennigan, C. J., Miracolo, M. A., Engelhart, G. J., May, A. A., Presto, A. A., Lee, T., Sullivan, A. P., McMeeking, G. R., Coe, H., Wold, C. E., Hao, W.-M., Gilman, J. B., Kuster, W. C., de Gouw, J. A., Schichtel, B. A., Kreidenweis, S. M. and Robinson, A. L.: Chemical and physical transformations of organic aerosol from the photo-oxidation of open biomass burning emissions in an environmental chamber, *Atmos. Chem. Phys.*, 11(15), 7669–7686, doi:10.5194/acp-11-7669-2011, 2011.



Lee, A. K. Y., Willis, M. D., Healy, R. M., Wang, J. M., Jeong, C.-H., Wenger, J. C., Evans, G. J. and Abbatt, J. P. D.: Single-particle characterization of biomass burning organic aerosol (BBOA): evidence for non-uniform mixing of high molecular weight organics and potassium, *Atmos. Chem. Phys.*, 16(9), 5561–5572, doi:10.5194/acp-16-5561-2016, 2016.

McNeill, V. F., Patterson, J., Wolfe, G. M. and Thornton, J. A.: The effect of varying levels of surfactant on the reactive uptake of  $\text{N}_2\text{O}_5$  to aqueous aerosol, *Atmos. Chem. Phys.*, 6(6), 1635–1644, doi:10.5194/acp-6-1635-2006, 2006.

Mentel, T. F., Sohn, M. and Wahner, A.: Nitrate effect in the heterogeneous hydrolysis of dinitrogen pentoxide on aqueous aerosols, *Phys. Chem. Chem. Phys.*, 1(24), 5451–5457, doi:10.1039/a905338g, 1999.

Onasch, T. B., Trimborn, A., Fortner, E. C., Jayne, J. T., Kok, G. L., Williams, L. R., Davidovits, P. and Worsnop, D. R.: Soot Particle Aerosol Mass Spectrometer: Development, Validation, and Initial Application, *Aerosol Sci. Technol.*, 46(7), 804–817, doi:10.1080/02786826.2012.663948, 2012.

Osthoff, H. D., Roberts, J. M., Ravishankara, A. R., Williams, E. J., Lerner, B. M., Sommariva, R., Bates, T. S., Coffman, D., Quinn, P. K., Dibb, J. E., Stark, H., Burkholder, J. B., Talukdar, R. K., Meagher, J., Fehsenfeld, F. C. and Brown, S. S.: High levels of nitryl chloride in the polluted subtropical marine boundary layer, *Nat. Geosci.*, 1(5), 324–328, doi:10.1038/ngeo177, 2008.

Solomon, S., Qin, D., Manning, M., Chen, Z., Marquis, M., Averyt, K. B., Tignor, M. and Miller, H. L.: *Climate change 2007: The physical science basis, contribution of working group 1 to the fourth assessment report of the Intergovernmental Panel on Climate Change*, Cambridge University Press, Cambridge, United Kingdom and New York, NY, USA, 2007.

Song, C. H. and Carmichael, G. R.: Gas-Particle Partitioning of Nitric Acid Modulated by Alkaline Aerosol, *J. Atmos. Chem.*, 40(1), 1–22, doi:10.1023/A:1010657929716, 2001.

Willis, M. D., Lee, A. K. Y., Onasch, T. B., Fortner, E. C., Williams, L. R., Lambe, A. T., Worsnop, D. R. and Abbatt, J. P. D.: Collection efficiency of the soot-particle aerosol mass spectrometer (SP-AMS) for internally mixed particulate black carbon, *Atmos. Meas. Tech.*, 7(12), 4507–4516, doi:10.5194/amt-7-4507-2014, 2014.

Yokelson, R. J., Crounse, J. D., DeCarlo, P. F., Karl, T., Urbanski, S., Atlas, E., Campos, T., Shinozuka, Y., Kapustin, V., Clarke, A. D., Weinheimer, A., Knapp, D. J., Montzka, D. D., Holloway, J., Weibring, P., Flocke, F., Zheng, W., Toohey, D., Wennberg, P. O., Wiedinmyer, C., Mauldin, L., Fried, A., Richter, D., Walega, J., Jimenez, J. L., Adachi, K., Buseck, P. R., Hall, S. R. and Shetter, R.: Emissions from biomass burning in the Yucatan, *Atmos. Chem. Phys.*, 9(15), 5785–5812, doi:10.5194/acp-9-5785-2009, 2009.